



FACHBEREICH MATHEMATIK UND NATURWISSENSCHAFTEN  
FACHGRUPPE PHYSIK  
BERGISCHE UNIVERSITÄT WUPPERTAL

# **Computer Simulation of the Stockmayer Fluid**

**Dissertation by  
Jörg Bartke**

March 2008

Diese Dissertation kann wie folgt zitiert werden:

urn:nbn:de:hbz:468-20080158

[<http://nbn-resolving.de/urn/resolver.pl?urn=urn%3Anbn%3Ade%3Ahbz%3A468-20080158>]

# Contents

<b>Abbreviations</b>	<b>13</b>
<b>1 Introduction</b>	<b>15</b>
Bibliography	19
<b>2 Models of polar fluids</b>	<b>21</b>
2.1 The Stockmayer interaction potential with and without polarizability	21
2.1.1 Pair interaction	21
2.1.2 Many-body interaction	26
2.2 The modified Stockmayer interaction potential	27
2.3 The dipolar soft sphere and dipolar hard sphere model	28
Bibliography	30
<b>3 Molecular dynamics simulations</b>	<b>31</b>
3.1 The molecular dynamics method	31
3.2 Calculating forces and torques	31
3.3 Integration of the equations of motion	33
3.4 Periodic boundary conditions and minimum image convention	35
3.5 Calculating thermodynamic quantities	36
3.5.1 Ergodicity	36
3.5.2 Internal energy and enthalpy	37
3.5.3 Calculating the temperature and pressure from the equipartition theorem	39
3.6 Control of temperature and pressure	41
3.6.1 The Berendsen thermostat	41
3.6.2 The Berendsen barostat	43
3.7 Long-range corrections	44
3.7.1 Pair correlations	45
3.7.2 Corrections for the Lennard-Jones potential	46
3.7.3 Reaction field corrections	47
3.8 Iteration scheme to calculate the induced dipole moments	49
3.9 Acceleration methods: cell and neighbor list	50
Bibliography	55
<b>4 The Stockmayer fluid in literature</b>	<b>57</b>

4.1	Gas-liquid phase coexistence . . . . .	57
4.2	Clusters, droplets and chains . . . . .	60
4.3	Dielectric properties and ferroelectric transition . . . . .	61
	Bibliography . . . . .	69
<b>5</b>	<b>Low density structure of the Stockmayer fluid</b>	<b>71</b>
5.1	Introduction . . . . .	71
5.2	Simulation results for low densities . . . . .	71
5.2.1	Comparison to a second-order virial expansion . . . . .	71
5.2.2	Comparison to a third-order virial expansion . . . . .	74
5.3	Chains and droplets . . . . .	74
5.3.1	Single droplet simulations . . . . .	74
5.3.2	Coexisting clusters in the dilute phase . . . . .	85
5.4	Conclusion . . . . .	93
	Bibliography . . . . .	96
<b>6</b>	<b>Gas-liquid coexistence in the Stockmayer fluid via computer simulation</b>	<b>97</b>
6.1	Introduction . . . . .	97
6.2	Determination of gas-liquid coexistence curves . . . . .	99
6.2.1	The Maxwell construction method . . . . .	99
6.2.2	Kofke's thermodynamic integration method . . . . .	102
6.2.3	Scaling laws for the critical point . . . . .	104
6.3	Results for gas-liquid coexistence from molecular dynamics . . . . .	105
6.3.1	The non polarizable case . . . . .	105
6.3.2	Checking the cut off radius . . . . .	115
6.3.3	The polarizable case . . . . .	118
6.3.4	Gas-liquid transition for the dipolar soft sphere fluid . . . . .	120
6.4	Conclusion . . . . .	124
	Bibliography . . . . .	129
<b>7</b>	<b>Equilibrium polymerization and gas-liquid critical behavior</b>	<b>131</b>
7.1	Introduction . . . . .	131
7.2	Flory-Huggins lattice model for reversibly assembling polymers . . . . .	132
7.2.1	The Helmholtz free energy . . . . .	132
7.2.2	Calculating critical properties from the lattice model . . . . .	138
7.2.3	Including ferroelectric order . . . . .	147
7.3	Comparison to molecular dynamics simulation results . . . . .	150
7.3.1	Gas-liquid critical behaviour . . . . .	150
7.3.2	Gas-liquid coexistence curves and ferroelectric order . . . . .	159
7.3.3	Relative Stability of chains and rings . . . . .	164
7.4	Conclusion . . . . .	166
	Bibliography . . . . .	171
<b>8</b>	<b>Dielectric properties and the ferroelectric transition of the Stockmayer fluid</b>	<b>173</b>

---

8.1	Introduction . . . . .	173
8.2	Methods for determining the static dielectric constant in fluids . . . . .	175
8.2.1	The Onsager equation . . . . .	175
8.2.2	The Debye equation . . . . .	177
8.2.3	The fluctuation equation . . . . .	179
8.3	Results for vanishing polarizability . . . . .	181
8.3.1	Static dielectric constant from different approaches . . . . .	181
8.3.2	Inverse susceptibility and the ferroelectric transition . . . . .	183
8.3.3	The local electric field . . . . .	188
8.3.4	The self diffusion coefficient . . . . .	193
8.4	Results for positive polarizability . . . . .	197
8.5	Conclusion . . . . .	199
	Bibliography . . . . .	204
<b>9</b>	<b>Summary discussion</b>	<b>205</b>
	Bibliography . . . . .	208
<b>A</b>	<b>Second virial coefficient for polarizable Stockmayer particles</b>	<b>209</b>
	Bibliography . . . . .	213
<b>B</b>	<b>Description of supplementary information and programs included on DVD</b>	<b>215</b>
	<b>Acknowledgments</b>	<b>217</b>



# List of Tables

0.1	Abbreviations used in the text . . . . .	13
2.1	Conversion of common units to Lennard-Jones units . . . . .	22
5.1	Critical parameters for the radius of gyration scaling. . . . .	90
6.1	Predictor-corrector formulas for the Kofke integration method . . . . .	104
6.2	Gas-liquid critical parameters for the Stockmayer and polarizable Stockmayer system . . . . .	111
A.1	Additional terms in the expression for the second virial coefficient . . . . .	211



# List of Figures

2.1	Angular coordinates of two interacting dipoles . . . . .	23
2.2	The orientation function in the Stockmayer interaction potential . . . . .	24
2.3	Values of the orientational function for some selected dipole orientations . . . . .	25
2.4	Comparison of the Lennard-Jones and Stockmayer potential dependend on pair separation . . . . .	25
3.1	Periodic boundary conditions and minimum image convention in two dimensions . . . . .	35
3.2	Long-range corrections for the Stockmayer fluid . . . . .	45
3.3	The Verlet neighbor list . . . . .	51
3.4	Combined cell and neighbor list . . . . .	52
5.1	Comparison of the pressure of the Stockmayer fluid from simulation for $\mu^2 = 1, 2, 3$ and second-order virial expansion . . . . .	72
5.2	Comparison of pressure of the polarizable Stockmayer fluid for $\mu^2 = 3$ from simulation and second-order virial expansion . . . . .	73
5.3	Comparison of the pressure of the Stockmayer fluid for $\mu^2 = 3$ and 36 from simulation and third-order virial expansion . . . . .	75
5.4	Simulation snapshots for $\mu^2 = 3$ and 36 in the gas phase . . . . .	76
5.5	Time evolution of the principal moments of inertia for a single cluster for $\mu^2 = 5$ and 36 . . . . .	78
5.6	Radius of gyration and principal moments of inertia for a single cluster vs. particle number . . . . .	80
5.7	Snapshots from single droplet simulations for $\mu^2 = 5, 16$ and 36 . . . . .	82
5.8	Snapshot from single droplet simulation with crystalline structure for $\mu^2 = 3$ . . . . .	83
5.9	The nematic order parameter vs. particle number for single cluster simulations . . . . .	84
5.10	Examples for the three classes of clusters: chains, rings and mutants . . . . .	86
5.11	Scaling of radius of gyration with chain length for coexisting clusters . . . . .	88
5.12	Chain length of the scaling transition and persistence length vs. reciprocal temperature for $\mu^2 = 16, 30$ and 36 . . . . .	89
5.13	Average bond length, radius of gyration, persistence length and fraction number per cluster size . . . . .	91
5.14	Average chain length vs. density for $\mu^2 = 36$ . . . . .	92

6.1	Phase diagram for a simple one component system in the $P$ - $T$ and $P$ - $V$ plane. . . . .	98
6.2	The Maxwell construction method . . . . .	99
6.3	Gibbs free energy vs. pressure for a compression path . . . . .	100
6.4	Phase separation in huge Stockmayer systems with $\mu^2 = 3$ and 36 . . . . .	102
6.5	Comparison of the results from the Maxwell construction and GEMC method for $\mu^2 = 1, 2, 3, 4$ and 5 . . . . .	106
6.6	Comparison of results from Maxwell construction and Kofke integration for $\mu^2 = 5$ and 16 . . . . .	107
6.7	Logarithmic saturation pressure vs. reciprocal temperature for $\mu^2 = 5$ and 16 . . . . .	108
6.8	Nematic order parameter on gas-liquid coexistence curves for $\mu^2 = 5$ and 16 . . . . .	109
6.9	Gas-liquid coexistence curves for $\mu^2 = 0, \dots, 60$ in LJ and critical units . . . . .	110
6.10	Gas-liquid coexistence curves for $\mu^2 = 30, 36$ and 60 . . . . .	112
6.11	Dipole-dipole correlation and radial pair distribution function for $\mu^2 = 60$ . . . . .	113
6.12	Simulation snapshot for $\mu^2 = 60$ with rings as predominant cluster species . . . . .	114
6.13	Isotherm for $\mu^2 = 60$ for different particle numbers . . . . .	115
6.14	Isotherms from simulation for $\mu^2 = 5, 16, 30, 36$ and 60 . . . . .	116
6.15	Nematic order parameter vs. density, radial distribution function and dipole-dipole correlation for $\mu^2 = 4$ . . . . .	117
6.16	Isotherms for dipole strength $\mu^2 = 30$ and different cut offs . . . . .	118
6.17	Radial pair distribution and dipole-dipole correlation for $\mu^2 = 30$ and different cut offs . . . . .	119
6.18	Average chain length and number fraction of different species vs. density for $\mu^2 = 30$ . . . . .	119
6.19	Gas-liquid coexistence curves in critical units for the polarizable Stockmayer fluid with $\mu^2 = 1$ . . . . .	120
6.20	Gas-liquid coexistence curves for the polarizable Stockmayer fluid with $\mu^2 = 2$ and 3 . . . . .	121
6.21	Pressure and average chain length vs. density for the dipolar soft sphere fluid . . . . .	122
6.22	Pressure vs. density for the dipolar soft sphere fluid in a region where a phase transition is expected . . . . .	123
6.23	Dependence of a Stockmayer system with $\mu^2 = 7.563$ on the cut off . . . . .	124
7.1	Schematic illustration of the Flory-Huggins lattice model for a mixture of polydispers polymers in two dimensions . . . . .	133
7.2	Intra-aggregate interaction parameter vs. bond length . . . . .	145
7.3	Simple approximation for $\varepsilon_i$ . . . . .	146
7.4	Orientational free energy from the Debye approach vs. order parameter $d$ for the ferroelectric phase . . . . .	149
7.5	Gas-liquid critical temperature and density vs. dipole strength . . . . .	151
7.6	Simulation snapshots near the critical density for $\mu^2 = 36$ . . . . .	153

7.7	Mean critical aggregation number vs. dipole strength . . . . .	154
7.8	The critical point of $n$ -alkanes as function of chain length . . . . .	155
7.9	Critical properties of the modified Stockmayer fluid depend on $\lambda$ . . . . .	157
7.10	Gas-liquid critical temperature vs. polarizability for $\mu^2 = 1, 2$ and $3$ . . . . .	158
7.11	Comparison between gas-liquid coexistence curves obtained by simulation and lattice theory . . . . .	160
7.12	Simulation snapshots for $\mu^2 = 5$ with ferroelectric order . . . . .	161
7.13	Mean aggregation number vs. particle number density along the gas-liquid coexistence curve for $\mu^2 = 16$ . . . . .	162
7.14	Heat capacity vs. reduced temperature from lattice theory and simulation .	163
7.15	Number fraction of species and cluster lengths for a system with $\mu^2 = 60$ .	165
7.16	Snapshots of mutants from a simulation with $\mu^2 = 60$ . . . . .	166
8.1	Static dielectric constant from the different approaches vs. temperature for $\mu^2 = 0.5, 1$ and $3$ . . . . .	182
8.2	Inverse susceptibility vs. reduced temperature from simulation . . . . .	184
8.3	Local electric field contributed by dipoles within a sphere of certain radius	189
8.4	Magnitude of the instantaneous local field strength vs. density for $\mu^2 = 4$ .	190
8.5	Instantaneous local field strength vs. temperature for $\mu^2 = 0.5, 1, 3,$ and $10$	191
8.6	Comparison of the autocorrelation functions for single dipoles, local electric field and total dipole moment . . . . .	194
8.7	comparison of $\langle \cos(\vec{\mu}(t), \vec{E}_{loc}(t)) \rangle$ with $\mathcal{L}(\mu E_{loc}/T)$ as functions of temperature	195
8.8	Self diffusion coefficient vs. temperature for dipole strengths $\mu^2 = 0.5, 1,$ $3, 16$ and $36$ . . . . .	196
8.9	Reduced local field vs. polarizability for $\mu^2 = 0.5, 1$ and $3$ . . . . .	197
8.10	Static dielectric constant vs. polarizability for $\mu^2 = 0.5, 1$ and $3$ . . . . .	198



# Abbreviations

Table 0.1: Abbreviations used in the text

Abbreviation	Meaning
LJ	Lennard-Jones
ST	Stockmayer
pST	polarizable Stockmayer
vLS	van Leeuwen Smit (modified Stockmayer)
DHS	dipolar hard sphere
DSS	dipolar soft sphere
GL	gas-liquid
DD	dipole-dipole
MD	molecular dynamics
MC	Monte Carlo
GEMC	Gibbs ensemble Monte Carlo
GCMC	grand canonical Monte Carlo
MBWR	modified Benedict-Webb-Rubin
DFT	density functional theory
HNC	hypernetted chain
LHNC	linearized hypernetted chain
QHNC	quadratic hypernetted chain
RHNC	reference hypernetted chain
SSCA	single super chain approximation
2CLJD	two-centre Lennard-Jones plus point dipole
RG	renormalization group



# 1 Introduction

Ultimately, intermolecular forces must be derived from quantum theory. Nevertheless, structural and dynamic properties of molecular systems can often be described via simple phenomenological models. Two molecules for instance attract at large distances and repel each other at close range. Based on this concept, the first microscopic theory of phase change, i.e. gas-liquid transition, was developed by van der Waals. This simple picture of molecular interaction may be extended to complex phenomenological force fields which, if properly parametrized, yield precise descriptions of many molecular and thermodynamic properties exhibited by real systems (an overview on force fields is provided by reference [5]). An important ingredient, largely responsible for phase changes in molecular systems, is the description of long-range interaction in terms of a power series expansion of dispersion attraction combined with Coulomb interaction between partial charges formed due to the difference in electron affinity of the atoms. Partial charges may be static or, which is less of an approximation, dynamically induced. The latter results in non-pairwise additive interactions.

This thesis describes the investigation of the phase behaviour of a simple molecular model, the Stockmayer potential with and without polarization, both via computer simulation and mean-field theory. The Stockmayer potential, originally designed as a simple approximation of molecular water or similar low molecular weight fluids, is one of the prototypical models in the context of ferrofluids. The original Stockmayer potential consists of a Lennard-Jones potential,  $u = 4(r^{-12} - r^{-6})$ , where  $u$  and  $r$  are the potential energy and the intermolecular separation in reduced units, plus a point dipole-point dipole interaction, where the dipole moments  $\vec{\mu}$  are located on the Lennard-Jones sites.

Ferrofluids become strongly polarized in the presence of a magnetic field. They are normally colloidal suspensions of solid, ferromagnetic nanoparticles, such as Iron (Fe), cobalt (Co), nickel (Ni) or magnetite ( $\text{Fe}_3\text{O}_4$ ) and a carrier liquid like water or oil. In ferrofluids agglomeration of the particles is usually unwanted and prevented by coating the ferromagnetic particles with stabilizing surfactants or silica layers. The size of the particles (5-15nm) is smaller than the size of magnetic domains making sure that the particles are magnetized homogeneously. The particles of modern ferrofluids produced by chemical reaction are almost of perfect spherical shape [6]. Since the magnetic field of a homogeneously magnetized sphere is an exactly dipolar one, the Stockmayer potential is a very good model to investigate the phase behaviour of ferrofluids. There is an analogy between the gas-liquid phase transition of polar molecules and the dilute-dense transition of ferrofluids which affects only the magnetic subsystem, the carrier system remains always

liquid [7, 8]. This results in clusters of ferromagnetic particles which form droplets in the carrier liquid.

Ferrofluids are already used in a wide range of applications. They are adopted as active liquid coolants for example in loud speakers to dissipate the heat from the voice coil and to cushion the membrane. They are used as liquid seals around spinning drive shafts, especially for vacuum chambers. The rotating shaft is surrounded by magnets to hold the ferrofluid in position. This principle is applied in hard disk drives of computers. Furthermore they are used for magnetohydrostatic separation, a method to separate substances like metal particles by density. An inhomogeneous magnetic field is varied and so the lifting force on the particles can be adjusted. Ferrofluids are constituents of Radar Absorbent Material (RAM) paint, an important part of the stealth technology to make aircrafts invisible for radar. In medicine ferrofluids are useful for cancer therapy. The concentration of drugs bonded to ferromagnetic particles can be increased in special parts of the body by applying an external magnetic field. Another approach is to heat the tumor by injecting a ferrofluid and then applying a fast varying magnetic field, but this is still a point of research. The last big area of applications is optics, due to the refractive properties of ferrofluids, so they are used in wave plates and polarizers.

The Stockmayer potential can be taken as a model potential for particles of magnetorheological liquids, too. These are very similar to ferrofluids, the main difference is the size of the ferromagnetic particles which is for magnetorheological liquids on the micrometer scale. If an external magnetic field is applied to these liquids, the ferromagnetic particles begin to form chains which lengths depend on the field strength. For ferrofluids this behaviour is disliked, for magnetorheological liquids one wants to influence the rheological properties like viscosity or elasticity. Magnetorheological liquids are used in dampers, shock absorbers, clutches and brakes. Electrorheological liquids are analogous to magnetorheological, but the particles consist of a ferroelectric or high polarizable material. The areas of applications are the same.

Another field of application of dipolar model fluids like the Stockmayer fluid are self assembling polymers. This is because dipolar interaction may lead to the reversible formation of polydisperse chains from molecules or colloidal particles [9] (cf. in particular Ref. [10] and the references therein) whose physical behavior is similar to ordinary polymer systems [11]. The chain formation in turns strongly affects the behavior of the monomer systems. Examples for reversibly self assembling polymers are the already mentioned ferrofluids [12] and surfactants. The latter form micelles with shapes dependend on the molecular shape. Another example are mesogens which show a liquid crystalline phase. The Stockmayer fluid can be taken as a model for dipolar liquid crystals, but models with an extended rigid body are here more favorable, since the liquid crystalline phase is caused by the rigid shape of the molecules, too.

Because of the perfect analogy between systems of magnetical and electrical dipolar particles, our results are applicable to both. Each electric physical quantity has an analog magnetic one. For reasons of simplicity we will always use the electric terminology in the equations, because most of the first articles on the Stockmayer fluid and other dipolar model potentials use this. If we refer to the literature, we will adopt the terminology used

there.

The main results of the present work are the path of the gas-liquid critical point in the  $T$ - $\rho$ -plane parametrized by  $\mu$ , the magnitude of the dipole moment [2,3] and the dependence of the isotropic liquid-to-ferroelectric liquid transition on  $T$ ,  $\rho$  and  $\mu$  [1].  $T$  and  $\rho$  denote temperature and number density, respectively. A major conclusion is the absence of a sudden disappearance of the gas-liquid critical point beyond a certain value of the dipole moment as proposed previously. This leads to the conclusion that dipolar interaction as the sole source of molecular attraction does not lead to gas-liquid phase separation [4].



# Bibliography

- [1] J. Bartke and R. Hentschke. Dielectric properties and the ferroelectric transition of the Stockmayer-fluid via computer simulation. *Molecular Physics*, 104(19):3057–3068, 2006.
- [2] R. Hentschke, J. Bartke, and F. Pesth. Equilibrium polymerization and gas-liquid critical behavior in the Stockmayer fluid. *Physical Review E*, 75:011506, 2007.
- [3] J. Bartke and R. Hentschke. Phase behavior of the Stockmayer fluid via molecular dynamics simulation. *Physical Review E*, 75:061503, 2007.
- [4] R. Hentschke and J. Bartke. Reply to "Comment on 'Equilibrium polymerization and gas-liquid critical behavior in the Stockmayer fluid'". *Physical Review E*, 77:013502, 2008.
- [5] J.W. Ponder and D.A. Case. Force fields for protein simulations. *Advances in Protein Chemistry*, 66:27–85, 2003.
- [6] R.E. Rosensweig. *Ferrohydrodynamics*. Cambridge University Press, 1985.
- [7] V. Russier and M. Douzi. On the utilization of the Stockmayer model for ferrocolloids: Phase transition at zero external field. *Journal of Colloid and Interface Science*, 162:356–371, 1994.
- [8] J.-C. Bacri, R. Perzynski, and D. Salin. Ionic ferrofluids: A crossing of chemistry and physics. *Journal of Magnetism and Magnetic Materials*, 85(1-3):27–32, 1990.
- [9] P.G. de Gennes and P.A. Pincus. Pair correlations in a ferromagnetic colloid. *Zeitschrift für Physik B*, 11(3):189–198, 1970.
- [10] P.I.C. Teixeira, J.M. Tavares, and M.M. Telo da Gama. The effect of dipolar forces on the structure and thermodynamics of classical fluids. *Journal of Physics: Condensed Matter*, (33):R411–R434, 2000.
- [11] P.J. Flory. *Principles of Polymer Chemistry*. Cornell University Press, Ithaca, 1953.
- [12] L.N. Donselaar, P.M. Frederik, P. Bomans, P.A. Buining, B.M. Humbel, and A.P. Philipse. Visualisation of particle association in magnetic fluids in zero-field. *Journal of Magnetism and Magnetic Materials*, 201(1-3):58–61, 1999.



## 2 Models of polar fluids

Here we discuss three simple models frequently studied in the context of dipolar liquids: the dipolar hard sphere (DHS) model, the dipolar soft sphere (DSS) model and the Stockmayer (ST) model. Also included in this discussion are the polarizable Stockmayer (pST) model and the modified Stockmayer (vLS) model by van Leeuwen and Smit [1]. Common to the aforementioned three models is the description of long-range anisotropic interaction in terms of a point dipole-point dipole potential. They differ with respect to their short range interaction. The DHS model employs hard core repulsion, whereas the ST potential employs the Lennard-Jones (LJ) potential. The intermediate DSS model adopts the soft repulsive core of the LJ potential. Here we do not investigate the DHS model explicitly, which is often discussed in literature for analytic calculations (see for instance references [2–8]), but it is expected to show a phase behaviour like the DSS model [9]. The fields of applications for these three model potentials are the same. They are used as simple models for polar molecules, ferrofluids or other self assembling systems as discussed for the ST potential in chapter 1. Other models for polar molecules like charged hard dumbbells [10] or model potentials for liquid crystals like hard spheroids [11] or hard rods [12] are not discussed here.

All three models, DHS, DSS and ST, exhibit a transition from an isotropic liquid to an orientationally ordered liquid and show quite similar dielectric properties, whereas a gas-liquid (GL) transition is established for the ST fluid only (e.g., [9, 13–15]) and is for the DHS or DSS still a matter of debate as discussed in chapter 6. One has to be aware of this fundamental different behaviour of these model fluids, if properties of real systems, for instance ferrofluids, should be obtained.

### 2.1 The Stockmayer interaction potential with and without polarizability

#### 2.1.1 Pair interaction

In 1941 ST introduced a model potential to describe the interaction between the particles in a polar gas [16]. One part of his potential is an isotropic interaction which is independent

of the orientations of the particles  $i$  and  $j$  and depends only on their separation  $r_{ij} = |\vec{r}_i - \vec{r}_j|$ . The isotropic part consists of a repulsive interaction due to Pauli's exclusion principle of the electron shells of the different particles and an attractive interaction which should describe the dispersion and induction energies. In the model ST employed every term of this interaction was adjustable to adapt the potential as close as possible to real systems. We will follow the literature afterwards on the ST fluid and use the well known LJ potential

$$u_{LJ}(r_{ij}) = 4\varepsilon \left[ \left( \frac{\sigma}{r_{ij}} \right)^{12} - \left( \frac{\sigma}{r_{ij}} \right)^6 \right], \quad (2.1.1)$$

in which the repulsive part depends on inverse order twelve of the distance and the attractive part on inverse order six. In this work we use LJ units (cf. table 2.1). In particular

Table 2.1: Conversion of common units to LJ units

Quantity	Conversion
length	$l^* = l/\sigma$
time	$t^* = \frac{t}{\sqrt{m\sigma^2/\varepsilon}}$
density	$\rho^* = \sigma^3 N/V$
energy	$E^* = E/\varepsilon$
temperature	$T^* = k_B T/\varepsilon$
pressure	$P^* = P\sigma^3/\varepsilon$
dipole moment	$\mu^* = \sqrt{\mu^2/(4\pi\epsilon_0\sigma^3\varepsilon)}$
force	$\vec{F}^* = \vec{F}\sigma/\varepsilon$
torque	$\vec{N}^* = \vec{N}/\varepsilon$

we set  $\varepsilon = \sigma = m = 1$ . LJ units are usually indicated by a star  $(\dots)^*$  which we omit in the following. Additionally we use  $4\pi\epsilon_0 = 1$ . ST added a permanent point-dipole  $\vec{\mu}$  to the particles to describe the electrostatic interactions between them. Every point-dipole  $i$  gives rise to a dipole potential  $\varphi(\vec{r})$  (see e.g. [17]) at position  $\vec{r}$ ,

$$\varphi(\vec{r}) = \frac{\vec{r} \cdot \vec{\mu}_i}{r^3}, \quad (2.1.2)$$

which results in the electric field

$$\vec{E}(\vec{r}) = -\vec{\nabla}\varphi = \frac{3(\vec{r} \cdot \vec{\mu}_i)\vec{r}}{r^5} - \frac{\vec{\mu}_i}{r^3}. \quad (2.1.3)$$

This leads to the point dipole-point dipole (DD) pair interaction

$$u_{DD}(\vec{r}_{ij}, \vec{\mu}_i, \vec{\mu}_j) = -\vec{\mu}_i \cdot \vec{E}_i(\vec{r}_{ij}) = \frac{\vec{\mu}_i \cdot \vec{\mu}_j}{r_{ij}^3} - \frac{3(\vec{r}_{ij} \cdot \vec{\mu}_i)(\vec{r}_{ij} \cdot \vec{\mu}_j)}{r_{ij}^5}, \quad (2.1.4)$$

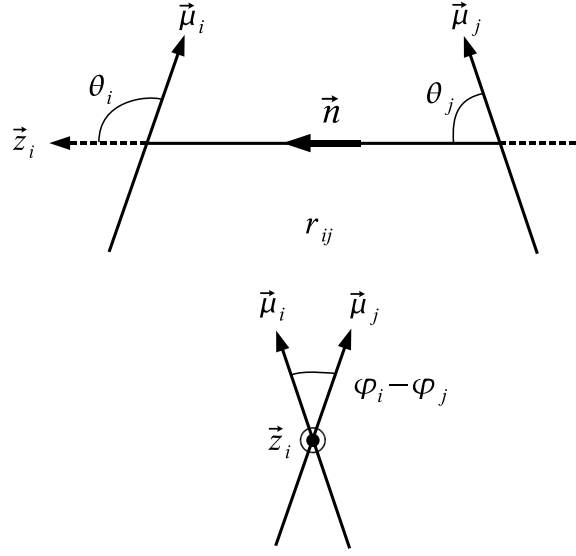


Figure 2.1: The angular coordinates of two interacting dipoles  $\vec{\mu}_i$  and  $\vec{\mu}_j$  with separation  $r_{ij}$ . The  $z$ -axis is set parallel to  $\vec{n} = \vec{r}_{ij}/r_{ij}$ . The bottom picture is the top one rotated  $90^\circ$  around the vertical axis.

whereas  $\vec{E}_i(\vec{r}_{ij})$  is the electric field evoked by dipole  $j$  affecting dipole  $i$  and  $\vec{r}_{ij} = \vec{r}_i - \vec{r}_j$ . In the following we will call this field  $\vec{E}(\vec{r}_i)$  for simplicity. Adding equations (2.1.1) and (2.1.4) yields the ST pair potential

$$u_{ST}(\vec{r}_{ij}, \vec{\mu}_i, \vec{\mu}_j) = u_{LJ}(r_{ij}) + u_{DD}(\vec{r}_{ij}, \vec{\mu}_i, \vec{\mu}_j). \quad (2.1.5)$$

ST used this potential in a form depending on the angles between the dipoles (cf. figure 2.1)

$$u_{ST}(r_{ij}, \theta_i, \theta_j, \varphi_i - \varphi_j) = 4 \left( \frac{1}{r_{ij}^{12}} - \frac{1}{r_{ij}^6} \right) + \frac{\mu^2}{r_{ij}^3} (\vec{s}_i \cdot \vec{s}_j - 3(\vec{n} \cdot \vec{s}_i)(\vec{n} \cdot \vec{s}_j)) \quad (2.1.6)$$

$$= 4 \left( \frac{1}{r_{ij}^{12}} - \frac{1}{r_{ij}^6} \right) + \frac{\mu^2}{r_{ij}^3} f(\theta_i, \theta_j, \varphi_i - \varphi_j), \quad (2.1.7)$$

where  $\mu = |\vec{\mu}|$  is the dipole strength and

$$\vec{s}_i = \frac{\vec{\mu}_i}{\mu} = \begin{pmatrix} \sin \theta_i \cos \varphi_i \\ \sin \theta_i \sin \varphi_i \\ \cos \theta_i \end{pmatrix}. \quad (2.1.8)$$

Without loss of generality we chose the  $z$ -axis parallel to  $\vec{n}$ . Evaluating the dot products in equation (2.1.6) we get the orientation function

$$f(\theta_i, \theta_j, \varphi_i - \varphi_j) = \sin \theta_i \sin \theta_j \cos(\varphi_i - \varphi_j) - 2 \cos \theta_i \cos \theta_j, \quad (2.1.9)$$

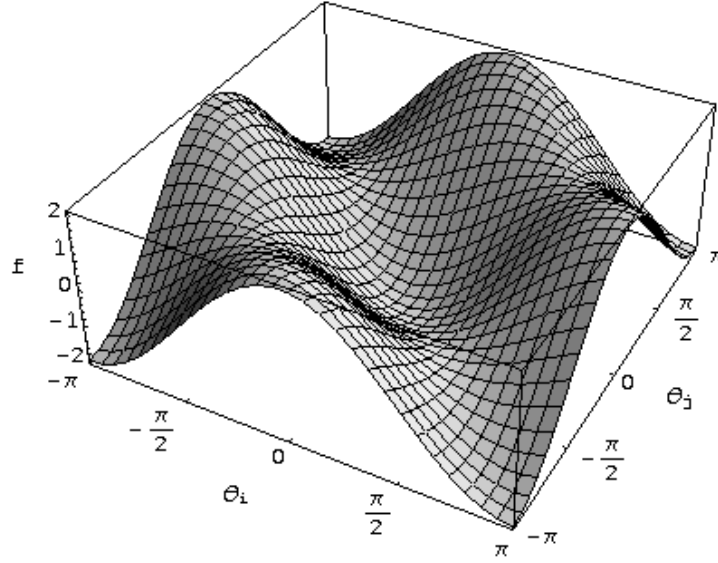


Figure 2.2: The orientation function  $f(\theta_i, \theta_j, \varphi_i - \varphi_j)$  in the ST interaction potential (2.1.7). To get a better impression  $f$  is plotted for  $\theta_i, \theta_j \in [-\pi, \pi]$ , nevertheless the domain of both is  $[0, \pi]$ . The region with a negative  $\theta$  can be realized with  $\varphi_i - \varphi_j = \pi$  instead of  $\varphi_i - \varphi_j = 0$ . In figure 2.3 values of  $f$  for some selected orientations are given.

which depends on the angular coordinates only.  $\theta_i$  and  $\theta_j$  are the inclinations of the two dipole axes to the intermolecular axis, and  $(\varphi_i - \varphi_j)$  is the azimuthal angle between them as shown in figure 2.1. Figure 2.2 shows  $f(\theta_i, \theta_j, \varphi_i - \varphi_j)$  versus  $\theta_i$  and  $\theta_j$ . For parallel orientation of the dipoles there is the strongest attractive interaction, i.e.  $f(0, 0, 0) = -2$ ; for antiparallel orientation there is the strongest repulsive interaction, i.e.  $f(0, \pi, 0) = 2$ . The values of  $f(\theta_i, \theta_j, \varphi_i - \varphi_j)$  for selected orientations are shown in figure 2.3. The dependency of the ST potential on the pair separation for head-to-tail and head-to-head orientation is compared in figure 2.4 with the LJ potential.

ST defined his system only for particles with permanent dipole moments. We add an isotropic point polarizability  $\alpha$  which gives an additional contribution to the total dipole moment, i.e.

$$\vec{m}_i(\vec{\mu}_i, \vec{p}_i) = \vec{\mu}_i + \vec{p}_i = \vec{\mu}_i + \alpha \vec{E}(\vec{r}_i). \quad (2.1.10)$$

The induced dipole moment  $\vec{p}_i$  is evoked by the electric field  $\vec{E}(\vec{r}_i)$ , produced by the dipole moments of the surrounding particles. For simplicity we only use the linear approximation for small electric fields  $\vec{E}(\vec{r}_i)$ . With polarizability the DD pair interaction (2.1.6) of the pST fluid becomes

$$u_{pST}(r_{ij}, \vec{m}_i, \vec{m}_j) = 4 \left( \frac{1}{r_{ij}^{12}} - \frac{1}{r_{ij}^6} \right) - \frac{1}{2} \left( \vec{\mu}_i \cdot \vec{E}(\vec{r}_i) + \vec{\mu}_j \cdot \vec{E}(\vec{r}_j) \right) \quad (2.1.11)$$

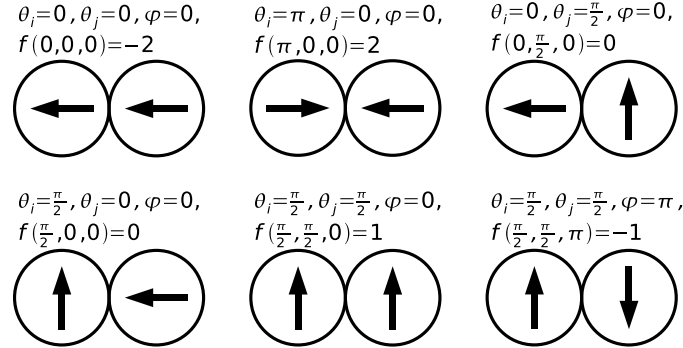


Figure 2.3: Values of the orientational function  $f(\theta_i, \theta_j, \varphi_i - \varphi_j)$  for some selected dipole orientations. Head-to-tail orientation of the dipoles gives the minimum of the dipolar energy, head-to-head orientation gives the strongest repulsive dipolar energy and perpendicular orientation causes no dipolar energy.

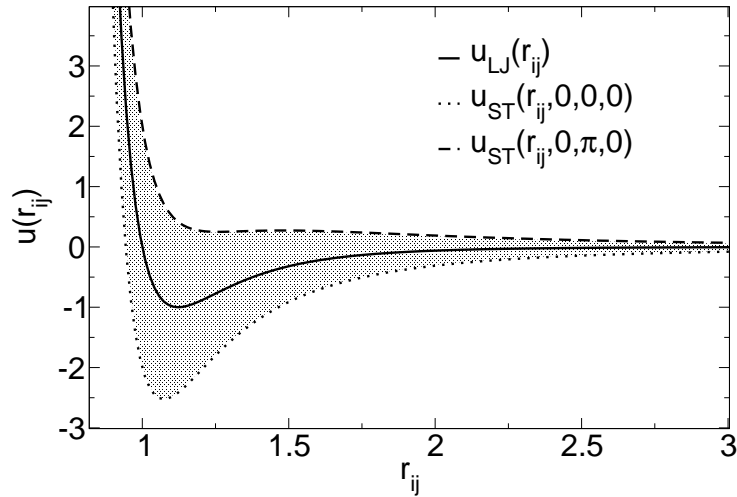


Figure 2.4: The LJ pair potential compared with the ST pair potential for dipole strength  $\mu = 1$  versus the pair separation  $r_{ij}$ . The dotted (dashed) line is for head-to-tail (head) orientation of the dipoles. At given distances the ST potential can assume every value in the shaded region due to orientation of the particles.

with

$$\vec{E}(\vec{r}_i) = \frac{3(\vec{r}_{ij} \cdot \vec{m}_j) \vec{r}_{ij}}{r_{ij}^5} - \frac{\vec{m}_j}{r_{ij}^3}. \quad (2.1.12)$$

For a simpler notation of the DD interactions we introduce the dipole tensor

$$\mathbb{T}_{ij} = \frac{\mathbb{1}}{r_{ij}^3} - \frac{3\vec{r}_{ij} \vec{r}_{ij}}{r_{ij}^5}. \quad (2.1.13)$$

Notice that  $ij$  refers to the interacting particles. The elements of the tensor which are given by

$$(\mathbb{T}_{ij})_{\alpha\beta} = \frac{1}{r_{ij}^3} (\delta_{\alpha\beta} - 3n_\alpha n_\beta). \quad (2.1.14)$$

The  $n_\alpha$ 's are the components of the unit vector in direction of the intermolecular axes (2.1.6). Now we can rewrite the electric field (2.1.12)

$$\vec{E}(\vec{r}_i) = -\mathbb{T}_{ij} \vec{m}_j, \quad (2.1.15)$$

the DD pair interaction for permanent dipoles (2.1.6)

$$u_{ST}(r_{ij}, \vec{\mu}_i, \vec{\mu}_j) = 4 \left( \frac{1}{r_{ij}^{12}} - \frac{1}{r_{ij}^6} \right) + \vec{\mu}_i \mathbb{T}_{ij} \vec{\mu}_j \quad (2.1.16)$$

and for the polarizable case (2.1.11)

$$u_{pST}(r_{ij}, \vec{m}_i, \vec{m}_j) = 4 \left( \frac{1}{r_{ij}^{12}} - \frac{1}{r_{ij}^6} \right) + \frac{1}{2} \left( \vec{\mu}_i \mathbb{T}_{ij} \vec{m}_j + \vec{m}_i \mathbb{T}_{ij} \vec{\mu}_j \right) \quad (2.1.17)$$

$$= 4 \left( \frac{1}{r_{ij}^{12}} - \frac{1}{r_{ij}^6} \right) + \vec{m}_i \mathbb{T}_{ij} \vec{m}_j + \frac{\alpha}{2} \left( \vec{E}(\vec{r}_i) + \vec{E}(\vec{r}_j) \right) \quad (2.1.18)$$

where the term

$$u_{pol} = \frac{\alpha}{2} \left( \vec{E}(\vec{r}_i) + \vec{E}(\vec{r}_j) \right) \quad (2.1.19)$$

denotes the reversible work required to create induced dipoles [18].

## 2.1.2 Many-body interaction

If we now consider a system of  $N$  ST particles, the total potential energy for the non-polarizable and polarizable case is

$$U_{ST}(\vec{r}_1, \dots, \vec{r}_N, \vec{s}_1, \dots, \vec{s}_N) = U_{ST}(\{\vec{r}_i\}, \{\theta_i\}, \{\varphi_i\}) = U_{LJ} + U_{DD} \quad (2.1.20)$$

$$= 4 \sum_{i < j}^N \left( \frac{1}{r_{ij}^{12}} - \frac{1}{r_{ij}^6} \right) - \frac{1}{2} \sum_{i=1}^N \vec{\mu}_i \cdot \vec{E}(\vec{r}_i) \quad (2.1.21)$$

Here we use the notation

$$\sum_{i < j}^N = \sum_{i=1}^{N-1} \sum_{j=i+1}^N, \quad (2.1.22)$$

i.e. pairs are counted only once and self-interaction is excluded.

The first term in equation (2.1.21) is the total LJ potential and the second term is the total DD interaction [18]

$$U_{DD} = -\frac{1}{2} \sum_{i=1}^N \vec{\mu}_i \cdot \vec{E}(\vec{r}_i) = \sum_{i < j}^N \vec{m}_i \mathbb{T}_{ij} \vec{m}_j + \frac{\alpha}{2} \sum_{i=1}^N \vec{E}(\vec{r}_i)^2, \quad (2.1.23)$$

where

$$U_{pol} = \frac{\alpha}{2} \sum_{i=1}^N \vec{E}(\vec{r}_i)^2 \quad (2.1.24)$$

is the reversible work of formation of the induced dipoles. Notice that equation (2.1.21) is valid for both the ST and pST fluid. For the ST fluid  $U_{pol}$  in equation (2.1.23) vanishes. The total electric field at the position of particle  $i$  is given by

$$\vec{E}(\vec{r}_i) = - \sum_{\substack{j=1 \\ j \neq i}}^N \mathbb{T}_{ij} \vec{m}_j. \quad (2.1.25)$$

## 2.2 The modified Stockmayer interaction potential

In 1993 van Leeuwen and Smit defined a modified version of the ST potential [1] multiplying the isotropic dispersion interaction by a parameter  $\lambda$ , i.e.

$$u_{vLS}(r_{ij}, \vec{\mu}_i, \vec{\mu}_j) = 4 \left( \frac{1}{r_{ij}^{12}} - \lambda \frac{1}{r_{ij}^6} \right) + \vec{\mu}_i \mathbb{T}_{ij} \vec{\mu}_j, \quad (2.2.1)$$

where  $0 \leq \lambda \leq 1$ . Notice that  $\lambda = 0$  corresponds to the DSS and  $\lambda = 1$  to the ST potential. Stevens and Grest showed that this system can be mapped onto the ordinary ST system [19] via the following scaling relations for energy, temperature, density, dipole moment, length and pressure

$$E_{ST} = \lambda^{-2} E_{vLS} \quad (2.2.2)$$

$$T_{ST} = \lambda^{-2} T_{vLS} \quad (2.2.3)$$

$$\rho_{ST} = \lambda^{-1/2} \rho_{vLS} \quad (2.2.4)$$

$$\mu_{ST} = \lambda^{-3/4} \mu_{vLS} \quad (2.2.5)$$

$$r_{ST} = \lambda^{1/6} r_{vLS} \quad (2.2.6)$$

$$P_{ST} = \lambda^{-5/2} P_{vLS}. \quad (2.2.7)$$

If we write the vLS potential (2.3.1) in a dimensionless form, i.e.

$$\frac{U_{vLS}(r_{vLS}, \mu_{vLS})}{T_{vLS}} = \frac{4}{T_{vLS}} \left( \frac{1}{r_{vLS}^{12}} - \lambda \frac{1}{r_{vLS}^6} \right) - \frac{\mu_{vLS}^2}{T_{vLS} r_{vLS}^3} f, \quad (2.2.8)$$

the scaling relations transform this to the dimensionless ST potential, i.e.

$$\frac{U_{ST}(r_{ST}, \mu_{ST})}{T_{ST}} = \frac{4}{T_{ST}} \left( \frac{1}{r_{ST}^{12}} - \frac{1}{r_{ST}^6} \right) - \frac{\mu_{ST}^2}{T_{ST} r_{ST}^3} f. \quad (2.2.9)$$

Notice that the Boltzmann weight  $\exp(-U/T)$  determines configurational averages in the NVT ensemble. So the equivalence of the two potentials is not only a mathematical formal one, there is a physical argument. The consequence is that for every choice of  $\lambda$  in the vLS model, there exists a corresponding ST model which properties can be obtained by applying the scaling relations to the properties of the vLS system. On the other hand we can map the ordinary ST system onto a vLS system with given  $\lambda$ . This is used in subsection 7.3.1 to investigate the GL critical behaviour for the limit  $\lambda \rightarrow 0$  (DSS model) which corresponds to the large dipole limit in the ST system.

## 2.3 The dipolar soft sphere and dipolar hard sphere model

Both the DSS and DHS model are dipolar interaction potentials without attractive dispersion interaction. The systems are similar and should in general show similar phase behaviour. The DSS interaction potential is a DD interaction, in addition with the soft repulsive core of the LJ potential. It can directly be obtained from the vLS potential (2.3.1) for  $\lambda = 0$ .

$$u_{DSS}(r_{ij}, \vec{\mu}_i, \vec{\mu}_j) = \frac{4}{r_{ij}^{12}} + \vec{\mu}_i \cdot \vec{T}_{ij} \vec{\mu}_j \quad (2.3.1)$$

Different to the ST and the DSS, the DHS model employs hard core repulsion and the potential looks as follows

$$u_{DHS}(r_{ij}, \vec{\mu}_i, \vec{\mu}_j) = \begin{cases} \vec{\mu}_i \cdot \vec{T}_{ij} \vec{\mu}_j & \text{for } r_{ij} > \sigma \\ \infty & \text{for } r_{ij} < \sigma \end{cases} \quad (2.3.2)$$

with  $\sigma$  as the diameter of the hard sphere. The DHS system was often discussed in literature (cf. [9, 15]). In this work it is only interesting because the phase behaviour of the vLS and so the DSS system allows considerations about the phase behaviour of the DHS, due to its strong similarity.

# Bibliography

- [1] M.E. van Leeuwen and B. Smit. What makes a polar liquid a liquid? *Physical Review Letters*, 71(24):3991–3994, 1993.
- [2] G.N. Patey. An integral equation theory for the dense dipolar hard-sphere fluid. *Molecular Physics*, 34(2):427–440, 1977.
- [3] R.P. Sear. Low-density fluid phase of dipolar hard spheres. *Physical Review Letters*, 76(13):2310–2313, 1996.
- [4] C.G. Joslin. The third dielectric and pressure virial coefficients of dipolar hard sphere fluids. *Molecular Physics*, 42(6):1507–1518, 1981.
- [5] M. Kasch and F. Forstmann. An orientational instability and the liquid-vapor interface of a dipolar hard sphere fluid. *Journal of Chemical Physics*, 99(4):3037–3048, 1993.
- [6] P.T. Cummings and L. Blum. Dielectric constant of dipolar hard sphere mixtures. *Journal of Chemical Physics*, 85(1):6658–6667, 1986.
- [7] G.S. Rushbrooke. On the dielectric constant of dipolar hard spheres. *Molecular Physics*, 37(3):761–778, 1979.
- [8] A.D. Buckingham and C.G. Joslin. The second virial coefficient of dipolar hard-sphere fluids. *Molecular Physics*, 40(6):1513–1516, 1980.
- [9] P.I.C. Teixeira, J.M. Tavares, and M.M. Telo da Gama. The effect of dipolar forces on the structure and thermodynamics of classical fluids. *Journal of Physics: Condensed Matter*, (33):R411–R434, 2000.
- [10] G. Ganzenmüller and P.J. Camp. Vapor-liquid coexistence in fluids of charged hard dumbbells. *Journal of Chemical Physics*, 126:191104, 2007.
- [11] J.W. Perram, M.S. Wertheim, J.L. Lebowitz, and G.O. Williams. Monte Carlo simulation of hard spheroids. *Chemical Physics Letters*, 105(3):277–280, 1984.
- [12] D. Frenkel and J.F. Maguire. Molecular dynamics study of the dynamical properties of an assembly of infinitely thin hard rods. *Molecular Physics*, 49(3):503–541, 1983.
- [13] C. Holm and J.J. Weis. The structure of ferrofluids: A status report. *Current Opinion in Colloid & Interface Science*, 10(3-4):133–140, 2005.

- 
- [14] J.J. Weis and D. Levesque. *Advanced Computer Simulation Approaches for Soft Matter Sciences II*, volume 185 of *Advances in Polymer Science*, chapter Simple dipolar fluids as generic models for soft matter. Springer, New York, 2005.
  - [15] B. Huke and M. Lücke. Magnetic properties of colloidal suspensions of interacting magnetic particles. *Reports on Progress in Physics*, 67:1731–1768, 2004.
  - [16] W.H. Stockmayer. Second virial coefficients of polar gases. *Journal of Chemical Physics*, 9(5):398–402, May 1941.
  - [17] J.D. Jackson. *Classical Electrodynamics*. Wiley & Sons, 1962.
  - [18] F.J. Vesely. N-particle dynamics of polarizable Stockmayer-type molecules. *Journal of Computational Physics*, 24:361–371, 1976.
  - [19] M.J. Stevens and G.S. Grest. Phase coexistence of a Stockmayer fluid in an applied field. *Physical Review E*, 51(6):5976 – 5983, 1995.

# 3 Molecular dynamics simulations

## 3.1 The molecular dynamics method

The aim of this work is to investigate the thermodynamic properties of the ST fluid via computer simulation. We chose the molecular dynamics (MD) method<sup>1</sup> to perform these simulations<sup>2</sup>. In MD the classical equations of motion

$$\frac{d}{dt} \vec{p}_i = \vec{F}_i \quad (3.1.1)$$

and

$$\frac{d}{dt} \vec{L}_i = \vec{N}_i \quad (3.1.2)$$

of a  $N$ -particle system are solved numerically to obtain the trajectories for all particles. Here  $\vec{p}_i$  is the momentum of particle  $i$  and  $\vec{F}_i$  is the total force acting on this particle. In contrast to ordinary LJ systems we now include the orientational motion of the dipoles.  $\vec{L}_i$  is the angular momentum of dipole  $i$  and  $\vec{N}_i$  is the total torque acting on it.

## 3.2 Calculating forces and torques

The force on dipole  $i$  is

$$\vec{F}(\vec{r}_i) = \vec{F}_{LJ}(\vec{r}_i) + \vec{F}_{DD}(\vec{r}_i) = -\vec{\nabla}_i U_{ST}(\{\vec{r}_i\}, \{\theta_i\}, \{\varphi_i\}) \quad (3.2.1)$$

---

<sup>1</sup>Detailed introductions to the MD method and its connection to statistical mechanics are given in [1–4].

We present here only the techniques and fundamentals applied in our work on our special problems. Many equations are taken from the literature above and many pictures are similar to pictures in there. we abstain from citing these references every time. The interested reader will have a careful look at these references anyway.

<sup>2</sup>It turns out that the ST fluid exhibits pronounced formation of linear aggregates (dipole chains) under certain thermodynamic conditions. Efficient Monte Carlo sampling techniques are difficult to design for these conditions.

with (2.1.20). The LJ and the DD contribution to the total force on the  $i$ -th particle can be calculated separately. For the LJ part we get

$$\vec{F}_{LJ}(\vec{r}_i) = -\vec{\nabla}_i U_{LJ} = 48 \sum_{\substack{j=1 \\ j \neq i}}^N \left[ \left( \frac{\sigma}{r_{ij}} \right)^{14} - \frac{1}{2} \left( \frac{\sigma}{r_{ij}} \right)^8 \right] \vec{r}_{ij} \quad (3.2.2)$$

and for the DD part

$$\vec{F}_{DD}(\vec{r}_i) = -\vec{\nabla}_i U_{DD} = \vec{\nabla}_i \left( \vec{\mu}_i \cdot \vec{E}(\vec{r}_i) \right) = \left( \vec{\mu}_i \cdot \vec{\nabla}_i \right) \vec{E}(\vec{r}_i) + \vec{\mu}_i \times \underbrace{\left( \vec{\nabla}_i \times \vec{E}(\vec{r}_i) \right)}_{=-\frac{1}{c} \dot{\vec{H}}(\vec{r}_i)=0} \quad (3.2.3)$$

$$= \sum_{\substack{j=1 \\ j \neq i}}^N \left[ \frac{3}{r_{ij}^5} \left( \vec{m}_i (\vec{r}_{ij} \cdot \vec{m}_j) + \vec{m}_j (\vec{r}_{ij} \cdot \vec{m}_i) + \vec{r}_{ij} (\vec{m}_i \cdot \vec{m}_j) \right) - \frac{15 (\vec{r}_{ij} \cdot \vec{m}_i) (\vec{r}_{ij} \cdot \vec{m}_j) \vec{r}_{ij}}{r_{ij}^7} \right] \quad (3.2.4)$$

The  $\vec{\nabla}_i \times \vec{E}(\vec{r}_i)$ -term in equation (3.2.3) is zero, since at any snapshot of time evolution of the system this is an electrostatic problem, thus the time derivative of the magnetic field  $\vec{H}$  vanishes. With the knowledge of the forces we are able to integrate the translational motion.

Additional to the force there is a torque

$$\vec{N}_i = \vec{\mu}_i \times \vec{E}(\vec{r}_i) = \vec{s}_i \times \vec{G}_i, \quad (3.2.5)$$

with  $\vec{G}_i = \mu_i \vec{E}(\vec{r}_i)$ , acting on the dipole moment due to the electric field. We consider the ST particles to be linear molecules with angular momentum

$$\vec{L}_i = I \vec{\omega}_i, \quad (3.2.6)$$

where  $I$  is the moment of inertia with respect to the momentary axis of rotation and  $\vec{\omega}_i$  the angular velocity of the  $i$ -th particle. This leads via  $\dot{\vec{L}}_i = \vec{N}_i$  to the equations of the rotational motion

$$I \dot{\vec{\omega}}_i = \vec{s}_i \times \vec{G}_i \quad (3.2.7)$$

$$\dot{\vec{s}}_i = \vec{\omega}_i \times \vec{s}_i \quad (3.2.8)$$

and by differentiating the second one with respect to time, we can combine both to get the angular acceleration

$$\ddot{\vec{s}} = \dot{\vec{\omega}} \times \vec{s} + \vec{\omega} \times \dot{\vec{s}} \quad (3.2.9)$$

$$= \frac{1}{I} \left( \vec{s} \times \vec{G} \right) \times \vec{s} + \vec{\omega} \times (\vec{\omega} \times \vec{s}) \quad (3.2.10)$$

$$= \frac{1}{I} \left[ \vec{G} - \vec{s} \left( \vec{s} \cdot \vec{G} \right) \right] - \vec{s} \omega^2. \quad (3.2.11)$$

With

$$\dot{s}^2 = (\vec{\omega} \times \vec{s})^2 = \omega^2 s^2 - (\vec{\omega} \cdot \vec{s})^2 = \omega^2, \quad (3.2.12)$$

since  $\vec{\omega} \perp \vec{s}$  and  $s^2 = 1$ , follows

$$\ddot{\vec{s}} = \frac{1}{I} \vec{G} - \left( \frac{1}{I} \vec{s} \cdot \vec{G} + \dot{s}^2 \right) \vec{s}. \quad (3.2.13)$$

With the knowledge of the translational and angular acceleration we can now think on an integration scheme for the equations of motion.

### 3.3 Integration of the equations of motion

To integrate the equations of motion numerically, we will use a method traced back to Störmer [5], but initially adopted by Verlet [6] to MD. Verlet's algorithm can be derived from the Taylor expansion about  $\vec{r}_i(t)$ , i.e.

$$\begin{aligned} \vec{r}_i(t + \Delta t) &= \vec{r}_i(t) + \Delta t \vec{v}_i(t) + \frac{1}{2} \Delta t^2 \vec{a}_i(t) + \dots \\ \vec{r}_i(t - \Delta t) &= \vec{r}_i(t) - \Delta t \vec{v}_i(t) + \frac{1}{2} \Delta t^2 \vec{a}_i(t) - \dots \end{aligned} \quad (3.3.1)$$

at finite time steps  $\Delta t$ . Here  $\vec{v}_i(t) = \dot{\vec{r}}_i(t)$  is the instantaneous velocity of the particle  $i$ . Addition of these two equations yields to the original Verlet algorithm

$$\vec{r}_i(t + \Delta t) = 2\vec{r}_i(t) - \vec{r}_i(t - \Delta t) + \Delta t^2 \vec{a}_i(t) + \mathcal{O}(\Delta t^4) \quad (3.3.2)$$

which is a discrete solution for times  $m\Delta t$ , where  $m$  is an integer. The solution is based on the positions  $\vec{r}_i(t)$  and  $\vec{r}_i(t - \Delta t)$  from the previous step and the accelerations  $\vec{a}_i(t)$  connected to the force  $\vec{F}_i$  via (3.1.1) for each particle  $i$ . The Verlet algorithm is the perhaps most widely used in molecular dynamics, because of the big advantages for this application. Different to algorithms like the Runge-Kutta method, the computational effort of the Verlet algorithm is much less, since only one force calculation per time step is needed. In the simulation program the force is evaluated by a double loop over all particle pairs (which can be decreased with acceleration methods later), so it is the most CPU expensive task in MD. Compared to other integrators with only one force evaluation like the Euler method with error of order  $\Delta t^2$ , the numerical stability of the Verlet algorithm is much higher and the errors are of order  $\Delta t^4$ . From a physical point of view the time reversibility and area preserving properties are very important.

The algorithm itself does not provide the velocities  $\vec{v}_i(t)$  which leads to the biggest disadvantage of the algorithm, because they are needed to calculate the kinetic energy and other thermodynamic values. They can be estimated from the formula

$$\vec{v}_i(t) = \dot{\vec{r}}_i(t) = \frac{\vec{r}_i(t + \Delta t) - \vec{r}_i(t - \Delta t)}{2\Delta t} + \mathcal{O}(\Delta t^2). \quad (3.3.3)$$

To avoid this problem of the original Verlet algorithm we use for our simulations the velocity Verlet version of the algorithm [7]

$$\vec{r}_i(t + \Delta t) = \vec{r}_i(t) + \Delta t \vec{v}_i(t) + \frac{1}{2} \Delta t^2 \vec{a}_i(t) \quad (3.3.4)$$

$$\vec{v}_i(t + \frac{1}{2} \Delta t) = \vec{v}_i(t) + \frac{1}{2} \Delta t \vec{a}_i(t) \quad (3.3.5)$$

$$\vec{v}_i(t + \Delta t) = \vec{v}_i(t + \frac{1}{2} \Delta t) + \frac{1}{2} \Delta t \vec{a}_i(t + \Delta t), \quad (3.3.6)$$

where the velocities and forces are provided at the same time as the positions. Eliminating the velocities in these equations will trace back to the original Verlet algorithm, so the original and the velocity version are completely equivalent. To calculate the trajectories  $\vec{r}_i(t)$  the three equations (3.3.4)-(3.3.6) are processed gradually by the simulation program. In the past this method had computational disadvantages, because in the equation for the positions terms of very different values are added. This is not a problem any longer, since we perform our simulations on computers with a precision for floating point numbers which is sufficient.

For integration of the rotational motion we employ the velocity Verlet algorithm, too. It is exactly analog to the translational motion.

$$\vec{s}_i(t + \Delta t) = \vec{s}_i(t) + \Delta t \dot{\vec{s}}_i(t) + \frac{1}{2} \Delta t^2 \ddot{\vec{s}}_i(t) \quad (3.3.7)$$

$$\dot{\vec{s}}_i(t + \frac{1}{2} \Delta t) = \dot{\vec{s}}_i(t) + \frac{1}{2} \Delta t \ddot{\vec{s}}_i(t) \quad (3.3.8)$$

$$\dot{\vec{s}}_i(t + \Delta t) = \dot{\vec{s}}_i(t + \frac{1}{2} \Delta t) + \frac{1}{2} \Delta t \ddot{\vec{s}}_i(t + \Delta t) \quad (3.3.9)$$

Here  $\vec{s}_i$  is the in (2.1.8) introduced orientation of the dipole moment of particle  $i$ . With equation (3.2.13) we can directly evaluate the first two steps of the algorithm (3.3.7) and (3.3.8), but in the last step (3.3.9) there is a problem due to the dependence of the angular acceleration  $\ddot{\vec{s}}_i(t + \Delta t)$  on the angular velocity  $\dot{\vec{s}}_i(t + \Delta t)$  which is at this time unknown, but applying the approximation

$$\dot{\vec{s}}_i(t + \Delta t) = \dot{\vec{s}}_i(t + \frac{1}{2} \Delta t) + \frac{1}{2} \Delta t \ddot{\vec{s}}_i(t), \quad (3.3.10)$$

we can calculate the angular acceleration

$$\begin{aligned} \ddot{\vec{s}}_i(t + \Delta t) = \frac{1}{I} \vec{G}_i(t + \Delta t) - \left[ \frac{1}{I} \vec{s}_i(t + \Delta t) \cdot \vec{G}_i(t + \Delta t) \right. \\ \left. + \left( \dot{\vec{s}}_i(t + \frac{1}{2} \Delta t) + \frac{1}{2} \Delta t \ddot{\vec{s}}_i(t) \right)^2 \right] \vec{s}_i(t) \end{aligned} \quad (3.3.11)$$

with sufficient precision, since the simulation is numerically stable. In references [1, 8] the velocity term in (3.3.11) is completely neglected, but stability seems even in this case not to be effected.

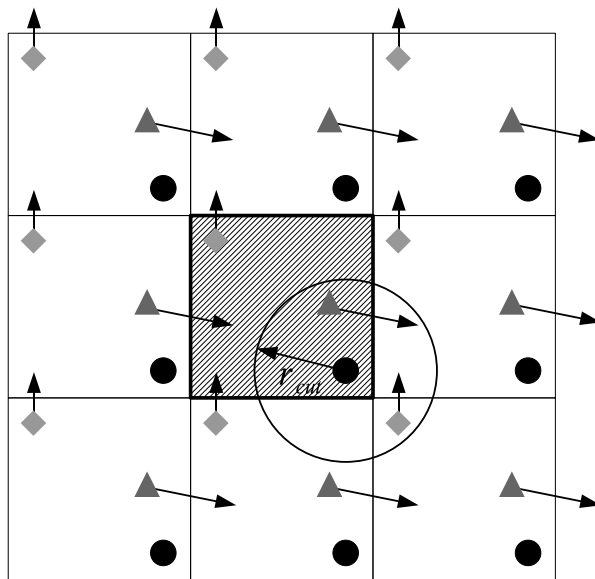


Figure 3.1: Visualisation of periodic boundary conditions and the minimum image convention in two dimensions. The central, cubic simulation box (shaded) is surrounded by replicas. If a particle leaves the central box an image of its own directly reenters on the opposite side. Interactions are only calculated to nearest copies of particles within a cut off sphere.

### 3.4 Periodic boundary conditions and minimum image convention

Despite the rise of computing power since adoption of the MD simulation method, the simulations are still usually performed for a small number of particles. Almost all simulations for this work were done on systems with at most 5000 particles, most simulations were done with fewer particle numbers. Simulations with more particles were only done as a check for finite size effects. The reason for the small number of particles is not the lack of memory of computers, it is rather the computational power spent on evaluating the forces between the particles which is proportional to  $N^2$ , or at best of order  $N$  with special acceleration techniques discussed in section 3.9. Because we are interested in the thermodynamic properties of the bulk phases, it is not satisfactory to simulate the system as a closed box. In such a simulation box of a system of 1000 particles, arranged on a simple cubic lattice, 50% of the particles are in contact with the surface of the box. These particles will experience quite different forces as particles inside the bulk. This problem can be overcome by implementing periodic boundary conditions. The small system of particles is expanded to infinity by surrounding the central simulation box with identical copies till an infinite space-filling array is obtained. For this work, only simulations with

a cubic simulation box were performed. An visualisation for the two dimensional case is given in figure 3.1. If particles leave the central simulation box, an image of their own will reenter it directly through the opposite face. Nevertheless, even with periodic boundary conditions finite size effects are still present. On the one hand structures bigger than the central simulation box cannot be formed. For instance this may be a problem in two phase coexistence regions, or if the particles aggregate to chains or clusters of size comparable to the box size. On the other hand there are correlations between particles and fluctuations of physical quantities. As a minimal requirement, the size of the box should exceed the range of any significant correlations to prevent self correlation of the particles. Fluctuations of the density for example can propagate around the system and eventually return to affect the source of the fluctuation itself. Long-wavelength fluctuations with a wavelength greater than the box length will be inhibited at all. This might cause problems for simulations near the gas-liquid critical point, where the range of fluctuations critical quantities is macroscopic. Furthermore, phase transitions which are known to be of first order often appear as transitions of higher order in a small simulation box like the nematic-to-isotropic transition, shown for liquid crystals in [9].

A direct consequence of periodic boundary conditions is the minimum image convention first used by Metropolis *et al.* in Monte Carlo (MC) simulations [10]. If all interactions between a central particle and the other particles in the box should be calculated in periodic systems, we have to take into account that some copies of particles are closer to the central one, than the particle itself (c.f. figure 3.1, the image of the diamond particle is closer to the circle particle than the diamond itself). We calculate the components of the separation vector  $\vec{r}_{ij}$  in the minimum image convention by

$$(\vec{r}_{ij})_{\alpha}^{(min)} = (\vec{r}_{ij})_{\alpha} - L \left\lfloor \frac{(\vec{r}_{ij})_{\alpha}}{L} + 0.5 \right\rfloor, \quad (3.4.1)$$

where  $\alpha \in \{x, y, z\}$  and  $L$  is the length of the cubic box. Usually the interactions are only calculated with particles, within a definite cut off distance  $r_{cut}$ , because neighboring particles give the largest contribution to the potential energy and the force. To prevent self interaction of the particles the cut off distance should be at maximum half the box length  $L$  ( $r_{cut} < L/2$ ). The contributions to potential energy and force from particles outside the cut off sphere are discussed in section 3.7.

## 3.5 Calculating thermodynamic quantities

### 3.5.1 Ergodicity

MD simulations provide knowledge of the classical microscopic states of the system. Every microstate is represented by a particular point in phase space corresponding to a full

set of generalized coordinates  $q_j$  and conjugate momenta  $p_j$ ,  $\Gamma = (q_1, \dots, q_{6N}, p_1, \dots, p_{6N})$ . However, a thermodynamic state of the system is characterized by macroscopic quantities like pressure  $P$ , temperature  $T$ , internal energy  $E$ , etc. Statistical mechanics allows to connect the microscopic information to these macroscopic quantities.

In conventional statistical mechanics a macroscopic quantity  $A$ , depending on the microstate  $\Gamma$ , is given by the ensemble average

$$\langle A \rangle = \frac{\int d\Gamma A(\Gamma) \rho(\Gamma)}{\int d\Gamma \rho(\Gamma)}, \quad (3.5.1)$$

where  $\rho(\Gamma)$  is the so called phase space density. From a single system configuration/snapshot produced by molecular dynamics simulation we can determine the instantaneous value  $A(\Gamma)$ . With running simulation the system evolves in time, so that a trajectory in phase space  $\Gamma(t)$  is produced and  $A(\Gamma(t))$  will change. To measure the observable macroscopic property  $A_{obs}$  from simulation, we determine the time average over a definite time period  $t_{obs}$

$$A_{obs} = \overline{A(\Gamma(t))} = \lim_{t_{obs} \rightarrow \infty} \frac{1}{t_{obs}} \int_0^{t_{obs}} dt A(\Gamma(t)) = \frac{1}{M} \sum_{m=1}^M A(\Gamma(m\Delta t)). \quad (3.5.2)$$

The overline implies the time average of a physical quantity. In general, time averaging should be done over infinite times to get macroscopic quantities, but in practice this might be satisfied with long enough finite times  $t_{obs}$ . Since MD simulation do not provide continuous time development of the system, we have to sum the instantaneous values of  $A$  at integer multiples of the time step  $\Delta t$ . The observed time interval is then  $t_{obs} = M\Delta t$ . Provided the considered system is ergodic, we can identify the time average (3.5.2) with the ensemble average (3.5.1)

$$A_{obs} = \overline{A(\Gamma(t))} = \langle A \rangle, \quad (3.5.3)$$

i.e. if we simulate the system for a long enough time, the system can access every possible point  $\Gamma$  in phase space. This is based on the ergodic hypothesis originally traced back to Boltzmann. In general the ergodicity of a system has always to be proved for a definite set of parameters, but this is hard to do. In MD ergodicity is often destroyed by metastable states trapping the system for extended periods of time. This problem can be avoided by comparing averages of observables from different simulations with the same simulation parameters, but different initial configurations. Even in this case one cannot be sure, however, to reach every region in phase space.

### 3.5.2 Internal energy and enthalpy

The internal energy  $E$  of a thermodynamic system is the sum of the total kinetic energy  $K$  due to the motion of the particles and the total potential energy  $U$  due to the interaction

of the different particles. For a system of ST particles there are contributions from the translational motion,  $K_{trans}$ , and the rotational motion,  $K_{rot}$ , to the total kinetic energy

$$K = K_{trans} + K_{rot}, \quad (3.5.4)$$

with

$$K_{trans} = \frac{1}{2}m \sum_{i=1}^N |\vec{v}_i|^2 = \frac{1}{2}m \sum_{i=1}^N (v_{x_i}^2 + v_{y_i}^2 + v_{z_i}^2) \quad (3.5.5)$$

and

$$K_{rot} = \frac{1}{2}I \sum_{i=1}^N |\dot{\vec{s}}_i|^2 = \frac{1}{2}I \sum_{i=1}^N (\dot{s}_{x_i}^2 + \dot{s}_{y_i}^2 + \dot{s}_{z_i}^2) = \frac{1}{2}I \sum_{i=1}^N (\dot{\theta}_i^2 + \dot{\varphi}_i^2 \sin^2 \theta_i). \quad (3.5.6)$$

In general all masses and moments of inertia of the ST particles are set to one ( $m = I = 1$ ), but we will show them explicitly to represent the physical context. In equation (3.5.5)  $v_{x_i}, v_{y_i}$  and  $v_{z_i}$  are the Cartesian components of the translational velocities which are independent of each other, i.e. in a system of  $N$  particles there are  $3N$  independent velocity components. In equation (3.5.6)  $\vec{s}_i$  is the orientation of the dipole moment, which can be expressed by the angles via (2.1.8). The potential energy was already given in (2.1.20).

With knowledge of kinetic and potential energy we can write down the Lagrangian of the system in terms of coordinates and velocities

$$\mathcal{L} = K - U \quad (3.5.7)$$

$$= \sum_{i=1}^N \left[ \frac{m}{2} (v_{x_i}^2 + v_{y_i}^2 + v_{z_i}^2) + \frac{I}{2} (\dot{\theta}_i^2 + \dot{\varphi}_i^2 \sin^2 \theta_i) \right] - U_{ST}(\{\vec{r}_i\}, \{\theta_i\}, \{\varphi_i\}). \quad (3.5.8)$$

To be able to write down the Hamiltonian of the system, first the generalized momenta have to be determined via

$$p_{x_i} = \frac{\partial \mathcal{L}}{\partial v_{x_i}} = mv_{x_i} \quad (3.5.9)$$

$$p_{y_i} = \frac{\partial \mathcal{L}}{\partial v_{y_i}} = mv_{y_i} \quad (3.5.10)$$

$$p_{z_i} = \frac{\partial \mathcal{L}}{\partial v_{z_i}} = mv_{z_i} \quad (3.5.11)$$

$$p_{\theta_i} = \frac{\partial \mathcal{L}}{\partial \dot{\theta}_i} = I\dot{\theta}_i \quad (3.5.12)$$

$$p_{\varphi_i} = \frac{\partial \mathcal{L}}{\partial \dot{\varphi}_i} = I\dot{\varphi}_i \sin^2 \theta. \quad (3.5.13)$$

In the following we will use

$$\{q_i\} = \{\{x_i\}, \{y_i\}, \{z_i\}, \{\theta_i\}, \{\varphi_i\}\} \quad (3.5.14)$$

as an abbreviation for the generalized coordinates and

$$\{p_i\} = \{\{p_{x_i}\}, \{p_{y_i}\}, \{p_{z_i}\}, \{p_{\theta_i}\}, \{p_{\varphi_i}\}\} \quad (3.5.15)$$

for the generalized momenta.

The Hamiltonian, dependend on the generalized coordinates and momenta, can be derived from the Lagrangian via the Legendre transformation

$$\mathcal{H} = \sum_j \dot{q}_j p_j - \mathcal{L} \quad (3.5.16)$$

$$= \sum_{i=1}^N \left[ \frac{1}{2m} (p_{x_i}^2 + p_{y_i}^2 + p_{z_i}^2) + \frac{1}{2I} (p_{\theta_i}^2 + p_{\varphi_i}^2) \right] + U_{ST}(\{\vec{r}_i\}, \{\theta_i\}, \{\varphi_i\}) \quad (3.5.17)$$

$$= E \quad (3.5.18)$$

and is equal to the total energy  $E$  of the system or the "instantaneous" internal energy.

Besides the internal energy, the enthalpy is another important thermodynamic potential, which we will need in section 6.2 for thermodynamic integration along the GL phase boundaries, and can be calculated from the simulation data via the relation

$$H = E + PV. \quad (3.5.19)$$

To use this equation, we must be able to determine the pressure  $P$ , which is explained in the next subsection.  $V$  is the volume of the simulation box.

### 3.5.3 Calculating the temperature and pressure from the equipartition theorem

With knowledge of the phase space trajectory  $\Gamma(t)$  the thermodynamic quantities temperature  $T$  and pressure  $P$  can be calculated from the general formulation of the equipartition theorem

$$\left\langle x_i \frac{\partial \mathcal{H}}{\partial x_j} \right\rangle = \delta_{ij} T \quad (3.5.20)$$

(in LJ units). Here  $x_j$  can either be the generalized coordinates  $q_j$  or momenta  $p_j$ . Due to the Kronecker delta  $\delta_{ij}$ , the ensemble average vanishes for  $i \neq j$ . If  $x_j$  is set to  $p_j$ , we can calculate the temperature. With Hamilton's equation of motion

$$\dot{q}_j = \frac{\partial \mathcal{H}}{\partial p_j} \quad (3.5.21)$$

and (3.5.17), (3.5.9)-(3.5.13) follows

$$\left\langle \sum_{i=1}^f p_j \dot{q}_j \right\rangle = \left\langle \sum_{i=1}^N (p_{x_i} v_{x_i} + p_{y_i} v_{y_i} + p_{z_i} v_{z_i} + p_{\theta_i} \dot{\theta}_i + p_{\varphi_i} \dot{\varphi}_i) \right\rangle \quad (3.5.22)$$

$$= 2 \langle K \rangle = 5NT. \quad (3.5.23)$$

On the right hand side of equation (3.5.22) it can be easily seen that the system of linear ST particles has  $5N$  degrees of freedom,  $3N$  for translation and  $2N$  for rotation. Equation (3.5.23), without the ensemble average on the left hand side, gives something like an "instantaneous temperature". For our purpose we do not distinguish between them explicitly. So we are able to calculate the temperature from the simulation data by

$$T = \frac{2}{5N}K. \quad (3.5.24)$$

Anyway, this formula has to be used carefully in MD simulation, because global constraints can reduce the number of degrees of freedom. In our simulations we set the center of mass motion to zero to prevent "the flying ice cube" problem [11]. This reduces the number of degrees of freedom by  $N_c = 3$ . So for simulations with few particles we have to use the formula

$$T = \frac{2}{(5N - N_c)}K. \quad (3.5.25)$$

instead of (3.5.24), but this can be neglected for big particle numbers ( $N \gg N_c$ ). A similar procedure for the rotation of the particles is not necessary, due to the cubic shape of the simulation box which prevents a global rotation of the system. If we are interested in the different contributions to the temperature by the translation and rotation we can directly determine them from equation (3.5.22) resulting in

$$T_{rot} = \frac{1}{N}K_{rot} \quad (3.5.26)$$

$$T_{trans} = \frac{2}{3N}K_{trans}. \quad (3.5.27)$$

We will call these quantities translational and rotational temperature in the following. Note that they should be equal in equilibrium  $T = T_{trans} = T_{rot}$ .

The pressure,  $P$ , can be calculated from the equipartition theorem by choosing Cartesian coordinates  $q_j$  in equation (3.5.20) and Hamilton's second equation of motion

$$\dot{p}_j = -\frac{\partial \mathcal{H}}{\partial q_j}, \quad (3.5.28)$$

resulting in

$$-\left\langle \sum_{i=1}^N (x_i \dot{p}_{x_i} + y_i \dot{p}_{y_i} + z_i \dot{p}_{z_i}) \right\rangle = 3NT \quad (3.5.29)$$

$$\Leftrightarrow \mathcal{V} = \left\langle \sum_{i=1}^N \vec{r}_i \cdot \vec{F}_i^{tot} \right\rangle = -3NT \quad (3.5.30)$$

Here  $\vec{F}_i^{tot}$  is the sum of internal forces between the particles  $\vec{F}_i^{int}$  and external forces  $\vec{F}_i^{ext}$  evoked by the container walls which border the volume  $V$ . Notice that we may avoid the

inclusion of the torques. Like the forces we can split the virial  $\mathcal{V}$  in an internal  $\mathcal{V}_{int}$  and external  $\mathcal{V}_{ext}$  one with

$$\mathcal{V} = \mathcal{V}_{int} + \mathcal{V}_{ext} = \left\langle \sum_{i=1}^N \vec{r}_i \cdot \vec{F}_i^{int} \right\rangle + \left\langle \sum_{i=1}^N \vec{r}_i \cdot \vec{F}_i^{ext} \right\rangle. \quad (3.5.31)$$

To get the pressure we substitute the external virial for an isotropic fluid by

$$\mathcal{V}_{ext} = -P \int_A dA (\vec{n} \cdot \vec{r}) = -P \int_V dV \vec{\nabla}_{\vec{r}} \cdot \vec{r} = -3PV. \quad (3.5.32)$$

Here  $\vec{n}$  is a unit vector perpendicular to the surface element  $dA$ , pointing outwards and  $A$  is the surface bordering the volume  $V$ . The combination of equations (3.5.30), (3.5.31) and (3.5.32) leads to the pressure

$$P = \frac{NT}{V} + \frac{1}{3V} \mathcal{V}_{int} \quad (3.5.33)$$

$$= \frac{NT}{V} + \frac{1}{3V} (\mathcal{V}_{LJ} + \mathcal{V}_{DD}) \quad (3.5.34)$$

with the LJ and DD contributions

$$\mathcal{V}_{LJ} = \left\langle \sum_{i=1}^N \vec{r}_i \cdot \vec{F}_i^{LJ} \right\rangle = \left\langle \sum_{i<j} \vec{r}_{ij} \cdot \vec{F}_{ij}^{LJ} \right\rangle \quad (3.5.35)$$

$$\mathcal{V}_{DD} = \left\langle \sum_{i=1}^N \vec{r}_i \cdot \vec{F}_i^{DD} \right\rangle = \left\langle \sum_{i<j} \vec{r}_{ij} \cdot \vec{F}_{ij}^{DD} \right\rangle = 3(U_{DD} - U_{pol}). \quad (3.5.36)$$

$\vec{F}_{ij}$  denotes the force between the  $i$ -th and the  $j$ -th particle. Equations (3.5.35) and (3.5.36) are only valid, because of the pairwise additivity of the forces [12]. From these equations we are now able to calculate the pressure from the simulation data.

## 3.6 Control of temperature and pressure

### 3.6.1 The Berendsen thermostat

To be able to adjust the temperature of the system during the simulations and not by choice of the initial conditions, we used the method proposed by Berendsen *et al.* [4, 13]. This method is a rescaling of the velocities  $\vec{v}_i$  and  $\vec{s}_i$  with a factor  $\lambda_{trans}$  and  $\lambda_{rot}$  every time step, since the temperature is only dependent on the kinetic energy (cf. equation (3.5.24)). We apply the thermostat to both, the translational and the rotational motion.

In general to apply it to one should be enough, because translational and rotational motion of the particles are coupled, but for systems with small dipole strength or very dilute ones equilibrium is reached much faster in this way. From a physical point of view, this is a coupling of the system to a huge external heat bath. The heat current between system and heat bath is given by

$$J_Q = \frac{\Delta Q}{\Delta t} = N c_V \frac{\Delta T}{\Delta t} = \alpha_T (T_B - T) . \quad (3.6.1)$$

Here  $\Delta Q$  is the exchanged heat quantity per time step  $\Delta t$ ,  $c_V$  is the heat capacity per particle at constant volume,  $\Delta T$  is the temperature change of the system per time step,  $T_B$  is the temperature of the heat bath (or supposed temperature of the system) and  $T$  the actual temperature of the system. The heat current couples to the system via the kinetic energy

$$\Delta Q = \Delta K = \frac{1}{2} (\lambda^2 - 1) \sum_{i=1}^N \left( m |\vec{v}_i|^2 + I |\dot{\vec{s}}_i|^2 \right) \quad (3.6.2)$$

$$= \frac{1}{2} \sum_{i=1}^N \left[ m |\vec{v}_i|^2 (\lambda_{trans}^2 - 1) + I |\dot{\vec{s}}_i|^2 (\lambda_{rot}^2 - 1) \right] \quad (3.6.3)$$

$$= \frac{3}{2} N T_{trans} (\lambda_{trans}^2 - 1) + N T_{rot} (\lambda_{rot}^2 - 1) \quad (3.6.4)$$

Notice that the differences between  $\lambda$ ,  $\lambda_{trans}$  and  $\lambda_{rot}$  is only a technical one due to the discrepancies of the instantaneous values of  $T$ ,  $T_{trans}$  and  $T_{rot}$ . In equation (3.6.1)  $\alpha_T$  is a constant related with the relaxation time  $\tau_T$  through

$$\tau = \frac{3N}{2\alpha_T} = \frac{N c_V}{\alpha_T} . \quad (3.6.5)$$

If we combine equations (3.6.1), (3.6.2), (3.6.4) and (3.6.5) we get

$$\lambda = \sqrt{1 + \frac{\Delta t}{\tau_T} \left( \frac{T_B}{T} - 1 \right)} \approx 1 + \frac{\Delta t}{2\tau_T} \left( \frac{T_B}{T} - 1 \right) , \quad (3.6.6)$$

or splitted in translational and rotational parts

$$\lambda_{trans} \approx 1 + \frac{\Delta t}{2\tau_T} \left( \frac{3NT_B}{2K_{trans}} - 1 \right) \quad (3.6.7)$$

$$\lambda_{rot} \approx 1 + \frac{\Delta t}{2\tau_T} \left( \frac{NT_B}{K_{rot}} - 1 \right) , \quad (3.6.8)$$

to scale the velocities and angular velocities

$$\vec{v}_i \longrightarrow \lambda_{trans} \vec{v}_i \quad (3.6.9)$$

$$\dot{\vec{s}}_i \longrightarrow \lambda_{rot} \dot{\vec{s}}_i . \quad (3.6.10)$$

More physical consistent would be a scaling by introducing a term of friction in the equations of motion

$$\ddot{\vec{r}}_i = \frac{1}{m} \vec{F}_i - \zeta \dot{\vec{r}}_i \quad (3.6.11)$$

with  $\zeta = (1 - \lambda)/\Delta t$  and including the solution of this equation directly in the Verlet algorithm. Due to the much simpler structure of the simulation program with a separated analysis of the thermostat and the equations of motion, we prefer the more simple velocities scaling method (3.6.9) and (3.6.10). Nevertheless, for weak couplings ( $\zeta \sim \mathcal{O}(\Delta t)$ ) both methods are completely equivalent. The special feature of the Berendsen thermostat compared to the constraint method [1,4] is the exponential adjustment of the temperature with time  $t$

$$T = T_B - (T_B - T_0) \exp\left(-\frac{t}{\tau_T}\right), \quad (3.6.12)$$

with  $T_0$  as the starting temperature. The system is effected by the thermostat in a less stronger way, than for the constraint method and has higher numerical stability. We chose for all simulations  $\tau_T \in [0.1, 1]$ . For simulations of systems of dipoles with a cut off radius, the thermostat is not only necessary to adjust the temperature, these systems do not conserve energy, so without thermostat there would be a drift in internal energy and temperature during the simulation. There are methods to improve the situation like smoothing the forces at the cut off distances, but we are only interested in properties at given temperature, so we do not employ such methods.

### 3.6.2 The Berendsen barostat

With Berendsen's method we are also able to adjust the pressure of the system, if this is necessary, as for example for Kofke's thermodynamic integration method. The box volume of the simulated system and the particle positions are scaled as the velocities with the thermostat

$$L \longrightarrow \mu L \quad (3.6.13)$$

$$\vec{r}_i \longrightarrow \mu \vec{r}_i \quad (3.6.14)$$

with  $V = L^3$ . The system can now exchange volume with its environment via the "volume current"

$$J_V = -\alpha_P (P_B - P) = \frac{\dot{V}}{V} = 3 \frac{\dot{L}}{L} = 3\eta \quad (3.6.15)$$

with the supposed pressure  $P_B$ , the actual pressure  $P$  and  $\eta = (\mu - 1)/\Delta t$ . The equivalent effect on the equations of motion like in (3.6.11) is

$$\dot{\vec{r}}_i = \vec{v}_i + \eta \vec{r}_i, \quad (3.6.16)$$

with  $\vec{v}_i = \vec{p}_i/m$  as the "real" kinetic velocities of the particles, but we prefer to apply the scaling (3.6.13) and (3.6.14) with

$$\mu = 1 - \frac{1}{3}\alpha_P (P_B - P) \Delta t \quad (3.6.17)$$

to the system for the same reason as in the case of the thermostat. The relaxation time is given by  $\tau_P = \kappa_T/\alpha_P$ , where

$$\kappa_T = -\left. \frac{1}{V} \frac{dV}{dP} \right|_T \quad (3.6.18)$$

is the compressibility at constant temperature. Because we cannot calculate the compressibility easily for the system, we set  $\alpha_P$  instead of  $\tau_P$  as parameter for the simulation. We choose  $\alpha_P$  small to make sure that the coupling to the "volume bath" is only weak. Like in the case of the thermostat the pressure is adjusted exponentially in time

$$P = P_B - (P_B - P_0) \exp\left(-\frac{t}{\tau_P}\right). \quad (3.6.19)$$

Both Berendsen's thermostat and barostat can be applied to the system at the same time to adjust pressure and temperature. One has always to be aware of the fact that neither the NVT nor the NPT ensemble can be produced by the Berendsen thermostat or barostat. To calculate quantities which depend strongly on the existing ensemble of the system, one has to make sure carefully that the thermodynamic limit is reached.

### 3.7 Long-range corrections

Since our simulations are performed with a cut off radius, we calculate the interactions only between particle pairs exactly, whose separations are smaller than a definite cut off radius ( $r_{ij} < r_{cut}$ ). The long range tail of the potentials, so the interactions between particles whose separations are greater than the cut off ( $r_{ij} \geq r_{cut}$ ) are not respected in this procedure and some physical quantities must be corrected. Hence, we have to choose the cut off radius in a way that the structure of the fluid outside the cut off sphere is negligible for the center particle, meaning the correlations between these pairs should not depend on the separation any longer. In the case of the ST fluid we have to observe two spatial correlation functions, on the one hand the radial pair distribution function  $g_2(r_{ij})$  and on the other hand the DD correlation  $\langle \vec{\mu}(0) \cdot \vec{\mu}(\vec{r}) \rangle / \mu^2$ . If this holds, we can interpret the matter outside the cut off sphere as a dielectric continuum as shown in figure 3.2 and we can calculate the corrections for the center particle. This cannot be handled in the same way for the LJ and the DD interaction due to the different symmetries of both. The LJ potential has radial symmetry, the DD potential not.

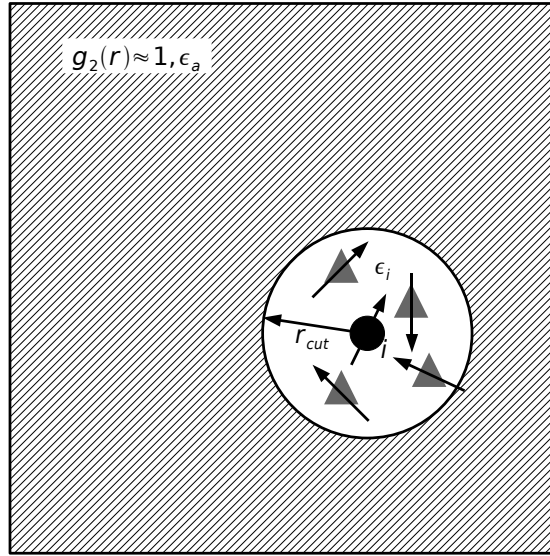


Figure 3.2: Long-range corrections for the ST fluid: Interactions of particle  $i$  and the particles within the cut off sphere (triangles) are calculated exactly. The medium, surrounding the cut off sphere, is considered to be a homogeneous dielectric continuum with dielectric constant  $\epsilon_a$ .

### 3.7.1 Pair correlations

A measurement for the structure of matter is the radial pair distribution function  $g_2(r_{ij})$ , dependent only on the pair separation  $r_{ij}$  for a translational invariant system of identical particles. It gives the probability of finding a pair of particles a distance  $r_{ij}$  apart, relative to the probability expected for a completely random distribution for the same density. We get the radial pair distribution function by the definition

$$g_2(r_{ij}) = \frac{V}{N^2} \left\langle \sum_i \sum_{j \neq i} \delta(r - r_{ij}) \right\rangle \quad (3.7.1)$$

from the simulation data. In practise the delta function is replaced by a discrete function which is not vanishing for a definite range of separations. To evaluate  $g_2(r_{ij})$  a histogram is compiled of all pair separations falling within each such range and normalized by the volume of the spherical shell covered by the separation range.

Ensemble averages of quantities which are only dependent on the pair separation  $r_{ij}$ ,  $\langle h(r_{ij}) \rangle$ , can now be calculated by

$$\langle h(r_{ij}) \rangle = \frac{1}{V} \int d^3r_{ij} h(r_{ij}) g_2(r_{ij}), \quad (3.7.2)$$

so the radial pair distribution function is something like a phase space density for particle pairs. If the matter for the considered range of separation has no structure, the radial pair distribution function should be constant  $g_2(r_{ij}) \equiv 1$  in this range, we are satisfied with  $g_2(r_{ij}) \approx 1$ .

The spatial DD correlation  $\langle \vec{\mu}(0) \cdot \vec{\mu}(r) \rangle / \mu^2$  is important for the ST fluid, too, since it can exhibit structure in the dipole orientation. It is easily determined from the simulation data by averaging the scalar products of all dipole orientations of particles  $r$  apart. To consider the matter as dielectric continuum, the spatial DD correlation should be constant with separation, it is not necessary to become zero (non-correlated pairs). In the case of ferroelectric order, the dipoles are strongly correlated with a not vanishing DD correlation function, but beyond a definite distance it doesn't depend on separation any longer and the matter can be interpreted as polarized dielectric continuum, too.

Examples of radial pair distribution functions and the spatial DD correlation with and without ferroelectric order are shown in figure 6.15 in section 6.3.

### 3.7.2 Corrections for the Lennard-Jones potential

Because the LJ part of the ST potential has radial symmetry and therefore depends only on the distance of the particles, we can directly apply equation (3.7.2) to calculate the long-range corrections for the internal energy and the virial. For the total LJ potential energy in (2.1.20) we get

$$U_{LJ} = \frac{1}{2} \frac{N^2}{V} \int_{r=0}^{\infty} d^3r u_{LJ}(r) g_2(r) = U_{LJ}^{r < r_{cut}} + U_{LJ}^{r \geq r_{cut}} \quad (3.7.3)$$

$$\approx U_{LJ}^{r < r_{cut}} + 2\pi N \rho \int_{r_{cut}}^{\infty} dr r^2 u_{LJ}(r) \quad (3.7.4)$$

$$= U_{LJ}^{r < r_{cut}} + \frac{8}{9} \pi \rho N \left( \frac{1}{r_{cut}^9} - 3 \frac{1}{r_{cut}^3} \right), \quad (3.7.5)$$

where  $U_{LJ}^{r < r_{cut}}$  is the exactly calculated and  $U_{LJ}^{r \geq r_{cut}}$  the long range part.

Applying the same procedure to the internal virial (3.5.35) we get the correction for the LJ part

$$\mathcal{V}_{LJ} \approx \mathcal{V}_{LJ,cut} + \frac{16}{9} \pi \rho N \left( 2 \frac{1}{r_{cut}^9} - 3 \frac{1}{r_{cut}^3} \right) \quad (3.7.6)$$

which has to be respected for the calculation of the pressure in equation (3.5.34). The correction of the total potential energy has no effect on other values.

### 3.7.3 Reaction field corrections

For the long-range corrections of the dipolar interactions we cannot employ the method used for the corrections of the LJ interactions. The dipolar interactions depend on the orientation of the particle, thus it has no spherical symmetry and equation (3.7.2) is not applicable. Another, perhaps more important difference to the LJ interaction is the long-range character of the DD interaction falling with  $r^{-3}$  instead of  $r^{-6}$  in the LJ case. Indeed, for a vanishing correlation of the dipoles at finite separation, the DD interactions diminishes effectively with  $r^{-6}$  for these separations (cf. equation (7.2.70)). But in a ferroelectric phase there is no separation for which the correlation vanishes and integral (3.7.3) would not converge for the DD case. Nevertheless, these phases of dipolar systems are stable, hence we have use special methods to calculate the long-range corrections for the DD interaction.

In our simulations we employ the theory of dielectric continua, the so called reaction field method [12, 14–16]. In this method the electric field acting on the observed dipole  $i$  in the center of the cut off sphere is splitted into two parts. The first part is the electric field produced by the dipoles of the other particles inside the cut off sphere, which can be calculated exactly, the second part arises from dipoles outside the cut off sphere considered to form a dielectric continuum with dielectric constant  $\epsilon_a$  as shown in figure 3.2. The reaction field method is suitable for the ferroelectric ordered phases, too, due to the afore mentioned reasons.

To explain the reaction field method, we consider the cut off sphere, centered on particle  $i$ , with volume  $V_{sphere} = (4\pi/3) r_{cut}^3$ , containing  $N_{sphere}$  other point dipoles and embedded in a dielectric continuum with dielectric constant  $\epsilon_a$ , cf. figure 3.2. The total dipole moment  $\vec{M}_{sphere}$  of the cut off sphere is calculated exactly by summing up all dipole moments with ( $j \in V_{sphere}$ )

$$\vec{M}_{sphere} = \sum_{j \in V_{sphere}} \vec{m}_j = V_{sphere} \vec{P}_{sphere}. \quad (3.7.7)$$

We consider the part of the system inside the sphere large enough to show macroscopic behaviour, so the sphere will appear to the surrounding dielectric as a cavity with a homogeneous polarization  $\vec{P}_{sphere}$ . This is one of the lacks of this theory, because the size of the cut off sphere in our simulations is not of macroscopic dimension, but we will discuss this later.

The electric field acting on the center particle can be obtained by applying the continuity relations of the tangential component of the electric field  $\vec{E}$  and the normal component of the dielectric displacement field  $\vec{D}$  at the surface of the cut off sphere on

$$\vec{D}_i = \vec{E}_i + 4\pi \vec{P}_{sphere} \quad (3.7.8)$$

$$\vec{D}_a = \epsilon_a \vec{E}_a, \quad (3.7.9)$$

where the index  $i$  denotes the quantities inside the sphere and  $a$  outside. The solution of this will give the total field inside the sphere caused by its own polarization and the

polarization of the surrounding dielectric [2, 14]

$$\vec{E}_i = -\frac{4\pi}{2\epsilon_a + 1} \vec{P}_{Sphere}. \quad (3.7.10)$$

Remembering that we are only interested in the contribution of the surrounding dielectric, since we are calculating the contribution of dipoles inside the sphere exactly, we have to remove this part from  $\vec{E}_i$ . Thus we have to subtract the field inside a sphere with polarization  $P_{sphere}$  surrounded by vacuum from equation (3.7.10). This is solved by setting  $\epsilon_a = 1$  in (3.7.9) and yields to the so called self-field

$$\vec{E}_s = -\frac{4\pi}{3} \vec{P}_{Sphere}, \quad (3.7.11)$$

which direction is opposite to  $\vec{P}_{Sphere}$ . Assuming that the fluid is a homogeneous dielectric with  $\epsilon_a = \epsilon_i = \epsilon$ , where  $\epsilon$  is the dielectric constant of the fluid, we can write down the reaction field as

$$\vec{E}_R(\vec{r}_i) = \vec{E}_i - \vec{E}_s = \frac{2(\epsilon - 1)}{2\epsilon + 1} \frac{4\pi}{3} \vec{P}_{Sphere} = \frac{2(\epsilon - 1)}{2\epsilon + 1} \frac{1}{r_{cut}^3} \vec{M}_{Sphere} \quad (3.7.12)$$

at the position  $\vec{r}_i$  of the particle  $i$ . The dielectric constant  $\epsilon$  of the system is still unknown, but can be obtained by the fluctuation equation

$$\frac{3}{4\pi\rho} \frac{(\epsilon - 1)(2\epsilon + 1)}{3\epsilon} = \frac{\langle \vec{M}_{sphere} \cdot \vec{M} \rangle_{\vec{E}_{ext}=0}}{TN_{sphere}} + \frac{3}{4\pi\rho} \frac{(\epsilon_\infty - 1)(2\epsilon_\infty + 1)}{3\epsilon_\infty}. \quad (3.7.13)$$

derived in subsection 8.2.3. Here  $\vec{M}$  is the total dipole moment of the entire simulation box and  $\rho$  is the particle number density. The index relation,  $\vec{E}_{ext} = 0$ , refers to a vanishing external field. The high-frequency dielectric constant  $\epsilon_\infty$  is in general related to  $\alpha$  via the Clausius-Mossotti relation

$$\frac{\epsilon_\infty - 1}{\epsilon_\infty + 2} = \frac{4\pi}{3} \rho \alpha \quad (3.7.14)$$

( $\epsilon_\infty = 1$  in the non polarizable case), adapted to the boundary conditions used here

$$\frac{(\epsilon_\infty - 1)(2\epsilon_\infty + 1)}{9\epsilon_\infty} = \frac{4\pi}{3} \rho \alpha. \quad (3.7.15)$$

Now we can give the expression for the total electric field acting on particle  $i$

$$\vec{E}'(\vec{r}_i) = - \sum_{\substack{j \in V_{cut} \\ j \neq i}} \mathbb{T}_{ij} \vec{m}_j + \vec{E}_R(\vec{r}_i). \quad (3.7.16)$$

In the simulation the reaction field must be respected in the calculation of the internal energy of the system and the torques on every particle. Thus the electric field  $\vec{E}(\vec{r}_i)$  in equations (2.1.20), (2.1.23) and (3.2.5) have to be substituted by  $\vec{E}'(\vec{r}_i)$ . Notice that

the reaction field is homogeneous, so it has neither effect on the dipole forces nor on the pressure or virial calculation.

An apparent disadvantage of the reaction field method often mentioned in literature [1] is that the static dielectric constant  $\epsilon$ , needed to evaluate (3.7.12), is *a priori* unknown and an expected value must be used. We prevent this problem by using the cumulative average of  $\epsilon$  obtained from (3.7.13) at run time of the simulation. If we choose several spheres at random to calculate the fluctuations of the total dipole moment the cumulative average will converge very soon. Furthermore, the total electric field depends only slightly on the dielectric constant (cf. equation (3.7.12) and (3.7.16))

The Ewald method, more often used in recent publications (for instance [17–20]), was originally developed in the study of ionic crystals [21]. The lattice sums in general, such as the Ewald sum, include the interaction of the dipoles with all its periodic images. But the use of these methods to calculate the long-range behaviour of DD interactions, especially in fluids, is not without controversy, too. Thus Valleau claimed [22] that the Ewald sum, working well for crystals, overemphasize the periodic nature of the model fluid. On the other hand, it was shown previously [17, 23–27] that simulations working with Ewald or reaction field method lead to almost the same results, so it seems that the problems of both methods are negligible. Especially reference [28] shows the equivalence of the reaction field and Ewald summation method for GL phase equilibria simulations. This should convince us that both methods are reasonable.

## 3.8 Iteration scheme to calculate the induced dipole moments

The induced dipole moments  $\vec{p}_i = \alpha \vec{E}'(\vec{r}_i)$  (cf. equation (2.1.10)) are calculated at every MD step using an iteration scheme, since it is dependend on the instantaneous electric field including the contribution of the induced dipoles of the neighboring particles. We follow the iteration scheme proposed by Vesely [12] with only minor improvements, here  $k$  denotes the iteration step:

$k = 0$  For the starting point of the iteration scheme to calculate the induced dipole moments and the resulting electric field, we have to distinguish two different cases: at the beginning of the simulation we set the initial value for the induced dipole moments to zero

$$\vec{p}_i^{(0)} = 0 , \quad (3.8.1)$$

for a running simulation we set it to the iteration result of the previous time step

$$\vec{p}_i^{(0)}(t) = \vec{p}_i(t - \Delta t) . \quad (3.8.2)$$

The initial value of the electric field  $\vec{E}'^{(0)}(\vec{r}_i)$  is now calculated via equation (3.7.16) with  $\vec{m}_i = \vec{\mu}_i + \vec{p}_i^{(0)}$ .

$k = 1$  At the first real iteration step the induced dipole moments are calculated from the initial electric field

$$\vec{p}_i^{(1)} = \alpha \vec{E}'^{(0)}(\vec{r}_i) \quad (3.8.3)$$

and with the result  $\vec{E}'^{(1)}(\vec{r}_i)$  as for  $k = 0$ .

$k$  This procedure is now repeated by applying

$$\vec{p}_i^{(k)} = \alpha \vec{E}'^{(k-1)}(\vec{r}_i) , \quad (3.8.4)$$

to calculate  $\vec{E}'^{(k)}(\vec{r}_i)$ , until the required precision is reached.

Following Vesely we take

$$R_E(k) = \frac{\sum_{i=1}^N \left| \vec{E}'^{(k)}(\vec{r}_i) - \vec{E}'^{(k-1)}(\vec{r}_i) \right|^2}{\sum_{i=1}^N \left| \vec{E}'^{(k-1)}(\vec{r}_i) \right|^2} \quad (3.8.5)$$

as measure for accuracy of the scheme. For our simulations, we chose  $R_E(k) \leq 10^{-4}$ . To use the results for the induced dipole moments of the previous time step as initial values for the iteration, causes a dramatic decrease of CPU time, in this way only 1-2 iterations per time step are necessary, instead of 5-6 starting with  $\vec{p}_i^{(0)} = 0$ .

A problem of the pST model is that for large polarizabilities and temperatures a polarization catastrophe may occur. If two very fast particles hit each other centrally, their minimal separation during the impact will be very small, so the electric field acting on the particles will become very large. The raise of the electric field will be even enforced by the polarizability and it may happen that the iteration scheme does not converge anymore. This will cause a crash of the simulation. Vesely gives as condition for this separations smaller than  $r_{ij} < (2\alpha)^{1/3}$ . We did not analyze this condition in our simulations, since if the polarization catastrophe occur, we will recognize the crash of the simulation. We found for intermediate dipole strengths ( $\mu^2 = 0.5, \dots, 5$ ) and a polarization of  $\alpha = 0, \dots, 0.08$  no problems for the simulated temperatures and densities, while for the larger dipole strengths ( $\mu^2 = 30$  and  $36$ ) polarizations of  $\alpha = 0, \dots, 0.04$  were manageable.

### 3.9 Acceleration methods: cell and neighbor list

Since we have to perform simulations of systems with a huge number of particles, we have to think about acceleration methods for our simulation program. The computing time of the original Verlet algorithm scales as  $N^2$ , because the separations of all particle pairs must be calculated for every time step in the minimum image convention. Only after doing this, all interactions whose separation exceeds  $r_{cut}$  can be neglected. Verlet

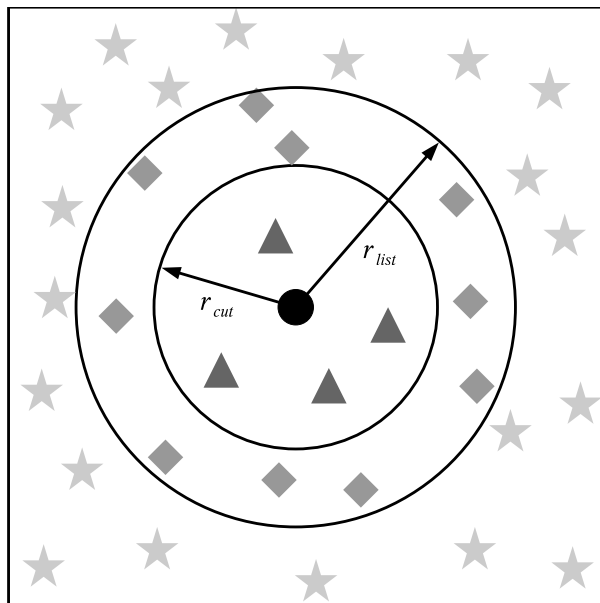


Figure 3.3: The Verlet neighbor list: The center particle (circle) is only interacting with the particles inside the cut off sphere with radius  $r_{cut}$  (triangles). All particles within the list sphere with radius  $r_{list}$  are stored in the neighbor list (diamonds + triangles) and the separations are calculated every time step. The distances to all other particles (stars) are only calculated for setting up and updating the neighbor list.

proposed a method to decrease the computer time by storing all particles with positions inside or close to the cut off sphere of the center particle in an array [6], the so called neighbor list. In practice the cut off sphere of every particle is surrounded by an additional sphere with radius  $r_{list} > r_{cut}$ , shown in figure 3.3. For setting up the list at the start of the simulation, we have to calculate all particle separations like for the pure Verlet algorithm. The simulation can now run for some steps by calculating only the separations of the neighboring particles, since only these particles are able to enter the cut off sphere. If the number of neighbors of one particle is small, compared to the total particle number, this method reduces the computation effort to order  $N$ . After a definite time particles from outside the list sphere will be able to enter the cut off sphere and the neighbor list has to be updated. For this reason the two largest displacements of every time step are stored and as soon as the sum of these exceeds the distance  $r_{list} - r_{cut}$ , the neighbor list is updated. The optimal choice of  $r_{list} - r_{cut}$  is dependend on almost all simulation parameters. We abstain from determining the optimal list radius for every simulation, as our experience shows a choice of  $r_{list} - r_{cut} = 0.5$  is always close to the optimum. The neighbor list method works well for simulation boxes bigger than the cut off sphere, but still of same magnitude. For huge systems of which the half box length  $L/2$  exceeds  $r_{cut}$  several times the set-up of the neighbor list becomes predominant and the computing time will scale again with order  $N^2$ . Hence, for huge systems we must think on another

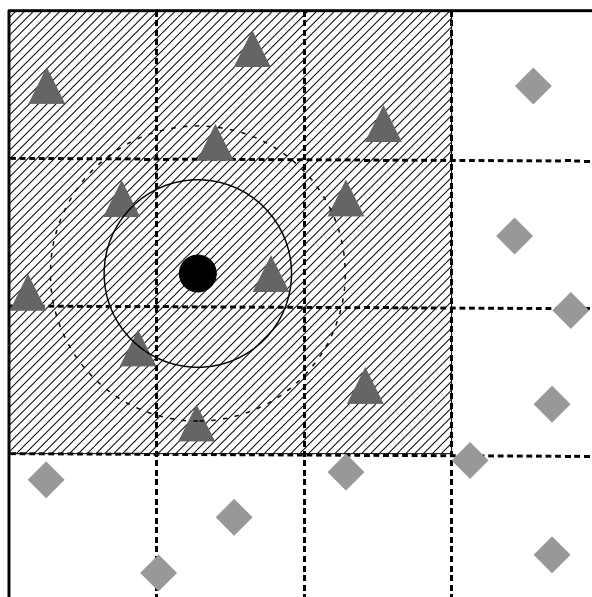


Figure 3.4: Combined cell and neighbor list: The simulation box is divided into cells at least of size  $r_{list}$ . For setting up the neighbor list, only particles in the same or neighboring cells of the considered particle have to be respected (shaded region), the diamonds outside can be neglected.

acceleration method.

Auerbach *et al.* proposed to combine the Verlet neighbor list with a cell list [29]. This allows to use it even for very huge systems and reduces the computing time to order  $N$  again. A schematic picture in two dimensions is given in figure 3.4. If the length of the simulation box exceeds at least four times  $r_{list}$ , the box is divided into cells with size equal to or slightly larger than the list radius  $r_{list}$ . Before setting up the neighbor list, we store the cell number for each particle in an additional array, so we have only to calculate the separations of particles within the same or neighboring cell (shaded cells). So we can save computer time neglecting the calculations of separations to particles in the non-shaded region from the outset, since the computational effort for setting up the cell list is of order  $N$ , too. This method is not only useful for systems with huge particle numbers, for very low densities this saves computer time even for smaller particle numbers.

# Bibliography

- [1] M.P. Allen and D.J. Tildesley. *Computer Simulation of Liquids*. Oxford University Press, 1989.
- [2] K. Binder and G. Ciccotti, editors. *Monte Carlo and Molecular Dynamics of Condensed Matter Systems*, volume 49 of *Conference Proceedings*. Italian Physical Society, July 1995.
- [3] D.C. Rapaport. *The Art of Molecular Dynamics Simulation*. Cambridge University Press, 2004.
- [4] R. Hentschke, E.M. Aydt, B. Fodi, and E. Stöckelmann. Molekulares Modellieren mit Kraftfeldern. <http://constanze.materials.uni-wuppertal.de>.
- [5] C.W. Gear. *Numerical Initial Value Problems in Ordinary Differential Equations*. Prentice-Hall Series in Automatic Computation, Engelwood Cliffs, 1971.
- [6] L. Verlet. Computer "experiments" on classical fluids. I. Thermodynamical properties of Lennard-Jones molecules. *Physical Review*, 159(1):98–103, 1967.
- [7] W. C. Swope, H. C. Andersen, P. H. Berens, and R. Wilson. A computer simulation method for the calculation of equilibrium constants for the formation of physical clusters of molecules: Application to small water clusters. *Journal of Chemical Physics*, 76(1):637–649, 1982.
- [8] K. Singer. Thermodynamic and structural properties of liquids modelled by 2-Lennard-Jones centres pair potentials. *Molecular Physics*, 33(6):1757–1795, 1977.
- [9] G.R. Luckhurst and P. Simpson. Computer simulation studies of anisotropic systems. VIII. The Lebwohl-Lasher model of nematogens revisited. *Molecular Physics*, 47(2):251–265, 1982.
- [10] N. Metropolis, A. W. Rosenbluth, M. N. Rosenbluth, A. H. Teller, and E. Teller. Equation of state calculations by fast computing machines. *Journal of Chemical Physics*, 21(6):1087–1092, 1953.
- [11] S. C. Harvey, R. K.-Z. Tan, and T. E. Cheatham. The flying ice cube: Velocity rescaling in molecular dynamics leads to violation of energy equipartition. *Journal of Computational Chemistry*, 19(7):726–740, 1998.
- [12] F.J. Vesely. N-particle dynamics of polarizable Stockmayer-type molecules. *Journal of Computational Physics*, 24:361–371, 1976.

- 
- [13] H.J.C. Berendsen, J.P.M. Postma, W.F. van Gunsteren, A. DiNola, and J.R. Haak. Molecular dynamics with coupling to an external bath. *Journal of Chemical Physics*, 81(8):3684–3690, 1984.
- [14] H. Fröhlich. *Theory of Dielectrics*. Clarendon Press, 1949.
- [15] J.A. Barker and R.O. Watts. Monte Carlo studies of the dielectric properties of water-like models. *Molecular Physics*, 26(3):789–792, 1973.
- [16] L. Onsager. Electric moments of molecules in liquids. *Journal of the American Chemical Society*, 58:1486–1493, 1936.
- [17] C. Millot, J.-C. Soetens, and M.T.C. Martins Costa. Static dielectric constant of the polarizable Stockmayer fluid. Comparison of the lattice summation and reaction field methods. *Molecular Simulation*, 18:367–383, 1997.
- [18] M. Valiskó, D. Boda, J. Liszi, and I. Szalai. A systematic Monte Carlo simulation and renormalized perturbation theoretical study of the dielectric constant of the polarizable Stockmayer fluid. *Molecular Physics*, 101(14):2309–2313, 2003.
- [19] M. Valiskó, D. Boda, J. Liszi, and I. Szalai. The dielectric constant of polarizable fluids from the renormalized perturbation theory. *Molecular Physics*, 100(20):3239–3243, 2002.
- [20] M. Valiskó, D. Boda, J. Liszi, and I. Szalai. Relative permittivity of dipolar liquids and their mixtures. Comparison of theory and experiment. *Physical Chemistry Chemical Physics*, 3:2995 – 3000, 2001.
- [21] P. Ewald. Die Berechnung optischer und elektrostatischer Gitterpotentiale. *Annalen der Physik*, 369:253–287, 1921.
- [22] J.P. Valleau. The problem of coulombic forces in computer simulation. volume 9 of *NRCC Workshop Proceedings*, pages 3–8, 1980.
- [23] C.G. Gray, Y.S. Sainger, C.G. Joslin, P.T. Cummings, and S.Goldman. Computer simulation of dipolar fluids. Dependence of the dielectric constant on system size: A comparative study of Ewald sum and reaction field approaches. *Journal of Chemical Physics*, 85(3):1502–1504, 1986.
- [24] M. Neumann. Dipole moment fluctuation in computer simulations of polar systems. *Molecular Physics*, 50(4):841–858, 1983.
- [25] M. Neumann and O. Steinhauser. The influence of boundary conditions used in machine simulations on the structure of polar systems. *Molecular Physics*, 39(2):437–454, 1980.
- [26] M. Neumann. Dielectric properties and the convergence of multipolar lattice sums. *Molecular Physics*, 60:225–235, 1987.
- [27] M. Neumann, O. Steinhauser, and G.S. Pawley. Consistent calculation of the static and frequency-dependent dielectric constant in computer simulations. *Molecular Physics*, 52(1):97–113, 1984.

- 
- [28] B. Garzón, S. Lago, and C. Vega. Reaction field simulations of the vapor-liquid equilibria of dipolar fluids. Does the reaction field dielectric constant affect the coexistence properties? *Chemical Physics Letters*, 231(4-6):366–372, 1994.
- [29] D. J. Auerbach, W. Paul, A. F. Bakker, C. Lutz, W. E. Rudge, and F. F. Abraham. A special purpose parallel computer for molecular dynamics: Motivation, design, implementation, and application. *Journal of Physical Chemistry*, 91:4881–4890, 1987.



## 4 The Stockmayer fluid in literature: Theory and computer simulation

In this chapter we give an overview over the literature published on the ST fluid. We report both theoretical works and results of computer simulation. Notice that the ST fluid has been investigated for more than 65 years. Therefore our main intention is not completeness with respect of the published works, but rather with respect to the different scientific aspects.

### 4.1 Gas-liquid phase coexistence

It is well known that at small dipole strength the ST fluid does exhibit a GL phase separation, mainly due to the isotropic dispersion interaction from the LJ potential. The first computer simulations on GL equilibria for the ST fluid were performed by Smit, Williams, Hendriks, de Leeuw and van Leeuwen [1–3]. They employed the Gibbs ensemble Monte Carlo method (GEMC), a technique proposed by Panagiotopoulos [4], to simulate GL equilibrium without explicit knowledge of the chemical potential. Two phases are simulated in two separate simulation boxes. The method employs MC steps with particle displacements and volume changes for each box including particle exchange between the two boxes, to impose internal and mutual equilibrium on the two phases. The long-range corrections were calculated by Ewald summation with 'tinfoil' boundary conditions (cf. equation (4.3.5)). They got GL phase coexistence curves for the ST fluid for dipole strengths up to  $\mu^2 = 6$  and compared them with curves obtained from first order perturbation theory [5] and first order perturbation theory with Padé approximation [6]. They found good agreement with first order perturbation theory only for GL coexistence curves with  $\mu^2 < 1$ , with Padé approximation up to  $\mu^2 < 4$ . Nevertheless in the critical region both methods are not satisfactory and overestimate the critical point.

In perturbation theory the Helmholtz free energy of the considered system is expressed in terms of a well known reference system and a perturbation of the reference system. In case of the ST fluid, the LJ fluid is an adequate reference system and an expansion in terms of the dipole moment  $\mu$  yields the perturbation. The Padé approximation includes an estimate for the higher order terms of the expansion. First order perturbation theory

for dipolar systems refers to expansions of order  $\mu^4$ . The next order estimated by Stell *et al.* via Padé approximation is  $\mathcal{O}(\mu^6)$ . As equation of state for the LJ system, the modified Benedict-Webb-Rubin (MBWR) equation [7] was used. Perturbation theory calculations using Padé approximation applied to the pST fluid were also carried out by Vesely [8]. He calculated the internal energy, the compressibility factor and the mean dipole moment for dipole strength  $\mu = 1$  and polarizabilities up to  $\alpha = 0.1$ . The results were also compared with values obtained from computer simulation [9]. He found substantial deviations for large polarizabilities, but his simulated systems were small ( $N = 108$ ).

In reference [3], van Leeuwen compared the critical properties obtained from GEMC with properties obtained from the virial equation of state [10–12], including the third virial coefficient, and density functional theory (DFT) [13], originally developed for higher dipole strengths. The former one does not even reproduce the critical behaviour qualitatively, because it is a low density theory and the critical densities for the investigated range of dipole strengths are close to 0.3. DFT shows an overly strong  $\mu$  dependence of the critical properties. Van Leeuwen showed the increasing deviation from the principle of corresponding states [14] for the ST fluid with increasing dipole strength, especially in the liquid phase.

DFT is based on the fact that the thermodynamic potential of an ensemble, for example the Helmholtz free energy, can be written as a functional of the microscopic density. This functional is minimal for the physical realized density. From the thermodynamic potential all other thermodynamic properties can be derived.

Garzón, Lago and Vega showed in reference [15] the equivalence of reaction field and Ewald summation simulations for GEMC simulations, by comparing their results for  $\mu^2 = 2$  and 4 obtained using the reaction field method with the ones of Smit *et al.* [1]. They found differences neither in the location of the phase coexistence region, nor in the structure of the gas and liquid by observing the pair correlation functions.

Van Leeuwen and Smit investigated the GL phase coexistence region for the vLS fluid (cf. equation (2.3.1)) with the same method employed in [16]. They performed simulations with dipole strength  $\mu^2 = 4$  and varied  $\lambda$  between 0 and 1. Most noticeably they found no coexistence region for  $\lambda \lesssim 0.3$  (especially for the DSS fluid ( $\lambda = 0$ )). They claimed chain formation, observed for small values of  $\lambda$ , prohibits the phase transition. Since the vLS fluid can be mapped onto the ST fluid according to (2.2.2)-(2.2.7), the phase transition should disappear for the ST fluid for dipole strengths  $\mu^2 \gtrsim 25$ . This seemed to be in line with a publication of Caillol [17], who performed GEMC and isothermal-isobaric MC simulations of the DHS fluid and was not able to observe a GL transition. This conclusion is quoted frequently in the subsequent literature (e.g. [18–24]), although, van Leeuwen and Smit reported problems with the GEMC method due to formation of reversible dipole chains resulting in too low acceptance rates for the MC steps (cf. reference [25]). They tried to solve these problems employing the configurational bias MC technique.

Tavares, Telo da Gama and Osipov [21] calculated the free energy of a strongly polar fluid as a mixture of self-assembled chains applying several approximations to calculate the phase coexistence region and critical properties. They compared their results to the simulation data for the vLS fluid of van Leeuwen and Smit and found qualitatively good

agreement for  $\lambda \geq 0.35$ . If  $\lambda$  is further decreased, the theory predicts coexistence for a fluid of chains, interacting via the isotropic dispersion interaction between the monomers. They suggest finite size effects as possible reason for the prevention of the phase transition in simulation, since the average chain length grows exponentially with decreasing  $\lambda$ . Their theory predicts the critical temperature and density to become zero for  $\lambda = 0$ .

Stevens and Grest performed GEMC simulations on the ST fluid with and without an applied electric field [18]. They provided GL coexistence curves without applied field up to dipole strength  $\mu^2 = 16$ , together with the values for the critical temperature and critical density. Additionally, they obtained the field dependence of the coexistence curves for  $\mu^2 = 1$  and 6.25. They provided the mapping laws of the vLS potential [16] onto the ordinary ST potential. To our knowledge they were the first who combined simulation data for GL coexistence with ferroelectric ordering. They found a ferroelectric phase in the dense liquid phase for  $\mu^2/T \gtrsim 4$ , but the isotropic gas-ferroelectric liquid coexistence, as predicted by a theory of Zhang and Widom [26], seemed to be unlikely, since the order parameter decreases strongly entering the phase coexistence region. They relied on the disappearance of the GL coexistence region for the ST fluid above the dipole strength  $\mu^2 \gtrsim 25$ , but it does not become clear if they checked this on their own or not.

Stoll *et al.* determined vapour-liquid equilibria properties of the two-centre LJ plus axial point dipole fluid (2CLJD) [27] from MD simulations using the reaction field method. The 2CLJD potential model is composed of two identical LJ sites at fixed distance and a point dipole  $\vec{\mu}_{2CLJD}$  placed in the geometric center of the molecule, pointing along the molecular axis. They employed the NPT plus test particle method introduced by Möller [28] to get GL coexistence curves. In the borderline case for vanishing LJ centre-centre distance, they provided GL phase coexistence and critical data for dipole strengths up to  $\mu_{2CLJD}^2 = 20$ , corresponding to  $\mu^2 = 5$  for the ST fluid.

Kiyohara, Gubbins and Panagiotopoulos, to the best of our knowledge, published the only phase coexistence data from simulation on the pST fluid [29]. They performed grand canonical Monte Carlo (GCMC) simulations [30] and calculated the thermodynamic properties from the histogram reweighting method [31]. They gave coexistence curves for dipole strengths  $\mu^2 = 1, 4$  and polarizabilities  $\alpha = 0, 0.03, 0.06$  and compared their results with Wertheim's perturbation theory [32], later improved by Kriebel and Winkelmann [33, 34]. Kiyohara *et al.* recognized an advantage of the GCMC method for phase equilibria in CPU time compared with the GEMC simulations.

As already mentioned Frodl, Groh and Dietrich provided various global phase diagrams for the ST fluid, obtained from DFT, including GL phase coexistence, ferroelectric order and the liquid-solid transition [13, 35–38]. The main focus of reference [13] was GL coexistence with small dipole strengths  $\mu^2 \leq 4$ . In [35, 36] Groh and Dietrich investigated the phase coexistence and the isotropic liquid-ferroelectric liquid transition for samples of different shapes. In [37, 38] they deal with the freezing of the ST system and the coexistence of ferroelectric liquid and ferroelectric solid. They found that for small dipole strengths  $\mu^2 < 1$ , the ferroelectric liquid is preempted completely by the freezing transition.

Russier and Douzi compared the GL phase transition of the ST fluid as a model for the dilute-dense phase transition of a colloidal ferrofluid [39]. They did not take the solvent

into account explicitly, thus they considered a one-component system whose interaction potential indirectly includes the influence of the solvent. They determined GL coexistence curves from a second order virial expansion via the Maxwell construction in the range of dipole strengths  $\mu^2 = 1 - 4$  and compare their results with MC simulation [1–3] and DFT [13]. With this simple method they got surprisingly good results.

Dudowicz, Freed and Douglas applied a Flory-Huggins mean field lattice model for reversibly associating polymers to the ST fluid to determine the GL phase coexistence region and the critical points for high dipole strengths [40]. In their model they found no evidence for the coexistence region to disappear for  $\mu^2 \gtrsim 25$ . The critical temperatures and densities they found were in good agreement with the existing data from GEMC [1–3, 16, 18].

## 4.2 Clusters, droplets and chains

The structure of compact clusters and droplets of ST particles has been investigated with computer simulation in [41–44]. In theoretical considerations by Zhang and Widom [26], phase coexistence of a isotropic gas and a magnetic liquid was expected. The droplets of magnetic liquid were expected to be highly prolate spheroids. But this could not be confirmed by MD and MC simulations [41, 42]. For small dipole strengths ( $\mu^2 = 1, 3$ ) the droplets are of spherical shape and the particles inside form chains in a circulating pattern with non-zero curl. The orientations of the dipoles are perpendicular to an axis through the center of mass and parallel to the surface of the droplet, contrary to DFT calculations by Talanquer and Oxtoby [45]. Clusters of ST particles with dipole strength  $\mu^2 = 16$  were investigated by ten Wolde *et al.* [43]. They observed that the nucleation process was initiated by chainlike clusters. When these clusters exceed a certain size, they condense to form compact droplet like nuclei. The shape of the droplets differ slightly from spheres and from a planar interface due to the high degree of chain formation. Toroidal shapes as predicted by DFT in [46] were not found. The shape of droplets were investigated in a diploma thesis by Florian Pesth from this group [47]. He found significant deviations from spherical shape of strongly polar droplets, but he performed simulations at very low temperatures, so that the droplets may be trapped in metastable states.

Equilibrium polymerization in the ST fluid was investigated by van Workum and Douglas [24]. They did MC simulations with a simple interaction truncation for dipole strength  $\mu^2 = 36$ . They chose this dipole strength to be sure that there is no GL phase coexistence [16, 18]. Their main interest was the polymerization transition which is characterized by a maximum of the constant volume heat capacity as function of temperature  $C_V(T)$  and an inflection point of the extend of polymerization  $\Phi(T)$  with  $\Phi = N_p/N$ , where  $N_p$  is the number of associated particles and  $N$  is the total number of particles. The criterion for determining clusters was simply based on distance. Furthermore, they investigated the frequency distribution of cluster types like chains, rings and mutants. Mutants they called branched chains and rings. They found a power law scaling for the radius of gyration with

particle number  $R_g \sim N^\nu$  with  $\nu \approx 0.68$ . For this they observed clusters with particle number  $10 \leq N \leq 70$ . It should be mentioned that they performed simulations only in the very dilute phase.

### 4.3 Dielectric properties and ferroelectric transition

Pollock and Alder [48] performed MD simulations of the ST fluid to calculate dielectric and structural properties as the total dipole moment fluctuations, static dielectric constant, radial pair distribution  $g_2(r)$  and the DD correlation functions  $h^{110}(r)$  and  $h^{112}(r)$  defined via

$$g(i, j) = g_2(r_{ij}) + h^{110}(r_{ij}) \vec{s}_i \cdot \vec{s}_j + h^{112}(r_{ij}) [3(\vec{s}_i \cdot \vec{n})(\vec{s}_j \cdot \vec{n}) - \vec{s}_i \cdot \vec{s}_j], \quad (4.3.1)$$

where  $g(i, j)$  is the total pair distribution function. They compared results obtained from simulations with the Ewald summation technique and a simple truncation of the potential at the cut off radius. For calculation of the static dielectric constant, they employed the Kirkwood relation for the fluctuation of the total dipole moment

$$\frac{(\epsilon_i - 1)(2\epsilon_a + 1)}{3(2\epsilon_a + \epsilon_i)} = gy, \quad (4.3.2)$$

with  $y = 4\pi\rho\mu^2\beta$ ,  $g$  is the so called Kirkwood factor and  $\epsilon_i/\epsilon_a$  the dielectric constant inside/outside a spherical system (cf. figure 3.2). Notice, that equation (3.7.13) is a special case of the Kirkwood relation. Pollock and Alder chose  $g = \langle M^2 \rangle / (N\mu^2)$ , where  $\langle M^2 \rangle$  denotes the fluctuation of the total dipole moment of the spherical system. Almost all later publications on the dielectric properties of the ST fluid from computer simulation refer to equation (4.3.2). They may differ in the boundary conditions, in the choice of  $\epsilon_a$ , and in the sample shape to which the fluctuation of the total dipole moment  $\langle M^2 \rangle$  refers. We will derive the equation for our conditions in subsection 8.2.3. In the case of Ewald summation Pollock and Alder adopted  $\epsilon = \epsilon_i = \epsilon_a$ , corresponding to a dielectric sphere surrounded by a continuum with the same dielectric constant, resulting in

$$\frac{(\epsilon - 1)(2\epsilon + 1)}{9\epsilon} = gy. \quad (4.3.3)$$

For the truncated system they used the formula for a spherical system surrounded by vacuum ( $\epsilon = \epsilon_i$ ,  $\epsilon_a = 1$ )

$$\frac{\epsilon - 1}{\epsilon + 2} = gy. \quad (4.3.4)$$

They compared the properties obtained for both systems and found significant differences in the DD correlation function  $h^{110}(r)$ , while the radial pair distribution function  $g_2(r)$  and  $h^{112}(r)$  coincidences.

So they showed that the complete truncation of the long-range tail of the potential will cause a change in the structure of the fluid. Furthermore, they compared their results from the Ewald method with the linearized hypernetted-chain approximation (LHNC) and the quadratic hypernetted-chain approximation (QHNC) predictions. They found good accordance for small dipolar coupling strengths,  $\mu^2/T < 2$ , only.

A detailed overview on the hypernetted-chain (HNC) theories like LHNC, QHNC and reference hypernetted-chain (RHNC) can be found in [49, 50]. The HNC theories are so called integral equation methods or correlation function expansions. The basic principle of these methods is to approach the molecular pair distribution function (4.3.1), containing all necessary information to calculate thermodynamic or dielectric properties, by means of different approximations. The HNC theory is based on the Ornstein-Zernike integral equation, which splits the pair distribution function in parts with direct and indirect correlations, and the HNC closure approximation, which connect the direct correlation function to the pair potential.

The molecular pair distribution function (4.3.1), or more likely  $h(i, j) = g(i, j) - 1$ , is calculated for the ST fluid with LHNC, QHNC and RHNC in [51, 52] by Patey, Levesque, Weis, Lee and Fries. The LHNC and QHNC hold only for small dipole strengths  $\mu^2 \lesssim 3$ , where the QHNC gives an improvement especially for low densities. Best results for the ST fluid gives the RHNC, where only the difference of the pair distribution function to a well known reference liquid, here the LJ fluid, is calculated. The different parts of the pair distribution function and the herefrom calculated dielectric constants are in very good agreement with MC simulations [52].

In reference [53] Pollock *et al.* investigated the dielectric properties of the pST fluid. They derived the equation for the polarizable case by adding a term for the high frequency dielectric constant  $\epsilon_\infty$  which is given by the Clausius-Mossotti formula. They observed the same quantities as in [48] and compared the results for the static dielectric constant with Wertheim's single super chain approximation (SSCA) [54]. Only poor accordance was found between simulation and theory.

In reference [55] Adams and Adams compared the Ewald-Kornfeld summation [56, 57], a special adaption of the Ewald summation for point dipoles, with the reaction field method. They compared dielectric and structural properties as Pollock and Alder did. In the case of the Ewald-Kornfeld summation they calculated the static dielectric constant from the Kirkwood fluctuation (4.3.2) formula with 'tinfoil' ( $\epsilon = \epsilon_i, \epsilon_a = \infty$ ) boundary conditions

$$\frac{\epsilon - 1}{3} = gy . \quad (4.3.5)$$

They used the fluctuation of the total dipole moment of the cubic simulation box to get the Kirkwood factor  $g$ . In the case of the reaction field method they applied equation (4.3.3) and used the fluctuation of the total dipole moment of the sphere beyond which the interactions are truncated. They pointed out that even the accordance of dielectric properties obtained from simulations with Ewald summation and reaction field method are no prove that the methods are adequate, because both suffer from the fact that macroscopic formulae are applied to a very small region of material. Comparing results

from MD and MC for different particle numbers, they found good accordance of the Ewald-Kornfeld and reaction field method in calculating  $h^{110}(r)$  for both, different to the simple spherical truncation method. The results for the dielectric constant differed slightly, but this is hard to judge, because they varied several simulation parameters like particle number, number of steps and cut off radius for the different methods. In the second part of the paper they investigated the influence of an external electric field on the dielectric properties.

Gray *et al.* [58] compared results from MC simulations with 'tin foil' (4.3.5) boundary conditions for both the reaction field and Ewald summation method. They calculated the Kirkwood factor  $g$  from the fluctuation of the total dipole moment of the simulation box. They found different finite size effects for the methods, but good accordance for sufficiently large particle numbers ( $N > 8$ ). However, their comparison involves only a single state point with a relative small dipole moment  $\mu^2 = 1$ .

Neumann *et al.* [59, 60] showed the equivalence of the reaction field and Ladd's lattice summation method [61, 62] with respect to dielectric properties and the structure of the ST fluid via MD simulation. They found only differences for small particle numbers. Millot *et al.* [63] repeated this comparison for the polarizable case and found deviations for high static dielectric constants ( $\epsilon > 200$ ) for relative small systems ( $N = 256$ ). They claim that both methods are equivalent for not too large dielectric constants and for sufficient sample size. The region of equivalence they found should increase with system size. In reference [64], Neumann compared the reaction field and Ewald summation method and found good agreement. Both Neumann *et al.* [59, 60, 64] and Millot *et al.* [63] used the total dipole moment of the simulation box.

MC simulations on the pST with reaction field method were done by Valiskó *et al.* [65, 66]. They compared the results for the dielectric constant with calculating it from perturbation theory by expanding the Kirkwood factor  $g = \langle M^2 \rangle / (N\mu^2)$ ,  $M^2$  is here the total dipole moment of the entire simulation box, with respect to the density. This is done with a convolution integral (cf. reference [67]), whose values have been tabulated for the ST fluid by Goldman [68]. They performed simulations with dipole strengths up to  $\mu^2 = 3$  and polarizabilities up to  $\alpha = 0.08$ . For these parameters they found excellent agreement with perturbation theory.



# Bibliography

- [1] B. Smit, C.P. Williams, E.M. Hendriks, and S.W. de Leeuw. Vapour-liquid equilibria for Stockmayer fluids. *Molecular Physics*, 68(3):765–769, 1989.
- [2] M.E. van Leeuwen, B. Smit, and E.M. Hendriks. Vapour-liquid equilibria of Stockmayer fluids, computersimulations and perturbation theory. *Molecular Physics*, 78(2):271–283, 1993.
- [3] M.E. van Leeuwen. Deviation from corresponding-states behaviour for polar fluids. *Molecular Physics*, 82(2):383–392, 1994.
- [4] A.Z. Panagiotopoulos. Direct determination of phase coexistence properties of fluids by Monte Carlo simulation in a new ensemble. *Molecular Physics*, 61(4):813–826, 1987.
- [5] G. Stell, J.C. Rasaiah, and H. Narang. Thermodynamic perturbation theory for simple polar fluids, I. *Molecular physics*, 23(2):393–406, 1972.
- [6] G. Stell, J.C. Rasaiah, and H. Narang. Thermodynamic perturbation theory for simple polar fluids, II. *Molecular physics*, 27(5):1393–1414, 1974.
- [7] J.J. Nicolas, K.E. Gubbins, W.B. Streett, and D.J. Tildesley. Equation of state for the Lennard-Jones fluid. *Molecular Physics*, 37(5):1429–1454, 1979.
- [8] F.J. Vesely. Thermodynamics of the polarizable Stockmayer fluid. *Chemical Physics Letters*, 56(2):390–394, 1978.
- [9] F.J. Vesely. N-particle dynamics of polarizable Stockmayer-type molecules. *Journal of Computational Physics*, 24:361–371, 1976.
- [10] J.S. Rowlinson. The second virial coefficients of polar gases. *Transactions of the Faraday Society*, 45:974 – 984, 1949.
- [11] J.S. Rowlinson. The third virial coefficients of polar gases. *Journal of Chemical Physics*, 19(7):827–831, 1951.
- [12] J.S. Rowlinson. The critical constants of polar gases. *Journal of Chemical Physics*, 19(7):831–833, 1951.
- [13] P. Frodl and S. Dietrich. Bulk and interfacial properties of polar and molecular fluids. *Physical Review A*, 45(10):7330–7354, 1992.
- [14] J.O. Hirschfelder, C.F. Curtiss, and R.B. Bird. *Molecular Theory of Gases and Liquids*. John Wiley & Sons, Inc., 8 edition, 1964.

- 
- [15] B. Garzón, S. Lago, and C. Vega. Reaction field simulations of the vapor-liquid equilibria of dipolar fluids. Does the reaction field dielectric constant affect the coexistence properties? *Chemical Physics Letters*, 231(4-6):366–372, 1994.
- [16] M.E. van Leeuwen and B. Smit. What makes a polar liquid a liquid? *Physical Review Letters*, 71(24):3991–3994, 1993.
- [17] J.-M. Caillol. Search of the gas-liquid transition of dipolar hard spheres. *Journal of Chemical Physics*, 98(12):9835–9849, 1993.
- [18] M.J. Stevens and G.S. Grest. Phase coexistence of a Stockmayer fluid in an applied field. *Physical Review E*, 51(6):5976 – 5983, 1995.
- [19] R.P. Sear. Low-density fluid phase of dipolar hard spheres. *Physical Review Letters*, 76(13):2310–2313, 1996.
- [20] R. van Roij. Theory of chain association versus liquid condensation. *Physical Review Letters*, 76(18):3348–3351, 1996.
- [21] J.M. Tavares, M.M. Telo da Gama, and M.A. Osipov. Criticality of dipolar fluids: Liquid-vapor condensation versus phase separation in systems of living polymers. *Physical Review E*, 56(6):6252–6255, 1997.
- [22] J.M. Tavares, J.J. Weis, and M.M. Telo da Gama. Strongly dipolar fluids at low densities compared to living polymers. *Physical Review E*, 59(4):4388–4395, 1999.
- [23] P.I.C. Teixeira, J.M. Tavares, and M.M. Telo da Gama. The effect of dipolar forces on the structure and thermodynamics of classical fluids. *Journal of Physics: Condensed Matter*, (33):R411–R434, 2000.
- [24] K. van Workum and J.F. Douglas. Equilibrium polymerization in the Stockmayer fluid as a model of supermolecular self-organization. *Physical Review E*, 71(031502), 2005.
- [25] P.J. Camp, J.C. Shelley, and G.N. Patey. Isotropic fluid phases of dipolar hard spheres. *Physical Review Letters*, 84(1):115–118, 2000.
- [26] H. Zhang and M. Widom. Global phase diagrams for dipolar fluids. *Physical Review E*, 49(5):3591–3593, 1994.
- [27] J. Stoll, J. Vrabec, and Hans Hasse. Comprehensive study of the vapour-liquid equilibria of the pure two-centre Lennard-Jones plus pointdipole fluid. *Fluid Phase Equilibria*, 209:29–30, 2003.
- [28] D. Möller and J. Fischer. Vapour liquid equilibrium of a pure fluid from test particle method in combination with NpT molecular dynamics simulations. *Molecular Physics*, 69(3):463–473, 1990.
- [29] K. Kiyohara, K.E. Gubbins, and A.Z. Panagiotopoulos. Phase coexistence properties of polarizable Stockmayer fluids. *Journal of Chemical Physics*, 106(8):3338–3347, 1997.

- [30] G.E. Norman and V.S. Filinov. Investigations of phase transitions by a Monte Carlo method. *High Temperature*, 7:216, 1969.
- [31] A.M. Ferrenberg and R.H. Swendsen. New Monte Carlo technique for studying phase transitions. *Physical Review Letters*, 61(23):2635–2638, 1988.
- [32] V. Venkatasubramanian, K.E. Gubbins, C.G. Gray, and C.G. Joslin. Induction effects in polar-polarizable liquid mixtures. *Molecular Physics*, 52(6):1411–1429, 1984.
- [33] C. Kriebel and J. Winkelmann. Thermodynamic properties of polarizable Stockmayer fluids: perturbation theory and simulation. *Molecular Physics*, 88(2):559–578, 1996.
- [34] C. Kriebel and J. Winkelmann. Vapour-liquid equilibria for Stockmayer fluids with rigid and polarizable dipoles. *Molecular Physics*, 90(2):297–301, 1997.
- [35] B. Groh and S. Dietrich. Long-ranged orientational order in dipolar fluids. *Physical Review Letters*, 72(15):2422–2425, 1994.
- [36] B. Groh and S. Dietrich. Ferroelectric phase in Stockmayer fluids. *Physical Review E*, 50(5):3814–3833, 1994.
- [37] B. Groh and S. Dietrich. Density-functional theory for the freezing of Stockmayer fluids. *Physical Review E*, 54(2):1687–1697, 1996.
- [38] B. Groh and S. Dietrich. Crystal structures and freezing of dipolar fluids. *Physical Review E*, 63(021203), 2001.
- [39] V. Russier and M. Douzi. On the utilization of the Stockmayer model for ferrocolloids: Phase transition at zero external field. *Journal of Colloid and Interface Science*, 162:356–371, 1994.
- [40] J. Dudowicz, K.F. Freed, and J.F. Douglas. Flory-Huggins model of equilibrium polymerization and phase separation in the Stockmayer fluid. *Physical Review Letters*, 92(4):045502, 2004.
- [41] H.B. Lavender, K.A. Iyer, and S.J. Singer. Global orientational order in model polar clusters. *Journal of Chemical Physics*, 101(9):7856–7867, 1994.
- [42] D. Lu and S.J. Singer. Orientational ordering and anisotropy in model polar clusters. *Journal of Chemical Physics*, 103(5):1913–1921, 1995.
- [43] P.R. ten Wolde, D.W. Oxtoby, and D. Frenkel. Coil-globule transition in gas-liquid nucleation of polar fluids. *Physical Review Letters*, 81(17):3695–3698, 1998.
- [44] A.P. Shreve, J.P.R.B. Walton, and K.E. Gubbins. Liquid drops of polar molecules. *Journal of Chemical Physics*, 85(4):2178–2186, 1986.
- [45] V. Talanquer and D.W. Oxtoby. Nucleation in dipolar fluids: Stockmayer fluids. *Journal of Chemical Physics*, 99(6):4670–4679, 1993.
- [46] S. Banerjee and M. Widom. Shapes and textures of ferromagnetic liquid droplets. *Brazilian Journal of Physics*, 31(3):360–365, 2001.
- [47] F. Pesth. Flüssig-Gas-Koexistenz in Stockmayer-Fluiden mittels Computersimulation. Diploma thesis, Bergische Universität Wuppertal, April 2006.

- [48] E.L. Pollock and B.J. Alder. Static dielectric properties of Stockmayer fluids. *Physica A*, 102(1):1–21, 1980.
- [49] J.P. Hansen and I.R. McDonald. *Theory of Simple Liquids*. Academic Press, 2 edition, 1986.
- [50] C.G. Gray and K.E. Gubbins. *Theory of Molecular Fluids*, volume 1 of *International Series of Monographs on Chemistry 9*. Clarendon Press Oxford, 1984.
- [51] G.N. Patey, D. Levesque, and J.J. Weis. Integral equation and approximations for dipolar fluids. *Molecular Physics*, 38(1):219–239, 1979.
- [52] L.Y. Lee, P.H. Fries, and G.N. Patey. The solution of the reference hypernetted-chain approximation for Stockmayer fluids. *Molecular Physics*, 55(4):751–762, 1985.
- [53] E.L. Pollock, B.J. Alder, and G.N. Patey. Static dielectric properties of polarizable Stockmayer fluids. *Physica A*, 108(1):14–26, 1981.
- [54] M.S. Wertheim. Dielectric constant of non-polar fluids. *Molecular Physics*, 25(1):211–223, 1973.
- [55] D.J. Adams. Static dielectric properties of the Stockmayer fluid from computer simulation. *Molecular Physics*, 42(4):907–926, 1981.
- [56] H. Kornfeld. Die Berechnung elektrostatischer Potentiale und der Energie von Dipol- und Quadrupolgittern. *Zeitschrift für Physik*, 22(1):27–43, 1924.
- [57] D.J. Adams and I.R. McDonald. Thermodynamic and dielectric properties of polar lattices. *Molecular Physics*, 32(4):931–947, 1976.
- [58] C.G. Gray, Y.S. Sainger, C.G. Joslin, P.T. Cummings, and S. Goldman. Computer simulation of dipolar fluids. Dependence of the dielectric constant on system size: A comparative study of Ewald sum and reaction field approaches. *Journal of Chemical Physics*, 85(3):1502–1504, 1986.
- [59] M. Neumann. Dielectric properties and the convergence of multipolar lattice sums. *Molecular Physics*, 60:225–235, 1987.
- [60] M. Neumann, O. Steinhauser, and G.S. Pawley. Consistent calculation of the static and frequency-dependent dielectric constant in computer simulations. *Molecular Physics*, 52(1):97–113, 1984.
- [61] A.J.C. Ladd. Monte-Carlo simulation of water. *Molecular Physics*, 33(4):1039–1050, 1977.
- [62] A.J.C. Ladd. Long-range dipolar interactions in computer simulations of polar liquids. *Molecular Physics*, 36(2):463 – 474, 1978.
- [63] C. Millot, J.-C. Soetens, and M.T.C. Martins Costa. Static dielectric constant of the polarizable Stockmayer fluid. Comparison of the lattice summation and reaction field methods. *Molecular Simulation*, 18:367–383, 1997.
- [64] M. Neumann. Dipole moment fluctuation in computer simulations of polar systems. *Molecular Physics*, 50(4):841–858, 1983.

- 
- [65] M. Valiskó, D. Boda, J. Liszi, and I. Szalai. A systematic Monte Carlo simulation and renormalized perturbation theoretical study of the dielectric constant of the polarizable Stockmayer fluid. *Molecular Physics*, 101(14):2309–2313, 2003.
- [66] M. Valiskó, D. Boda, J. Liszi, and I. Szalai. The dielectric constant of polarizable fluids from the renormalized perturbation theory. *Molecular Physics*, 100(20):3239–3243, 2002.
- [67] M. Valiskó, D. Boda, J. Liszi, and I. Szalai. Relative permittivity of dipolar liquids and their mixtures. Comparison of theory and experiment. *Physical Chemistry Chemical Physics*, 3:2995 – 3000, 2001.
- [68] S. Goldman. Determination of static dielectric constant-temperature-density surfaces of a Stockmayer fluid by perturbation theory. *Molecular Physics*, 71(3):491–507, 1990.



# 5 Low density structure of the Stockmayer fluid

## 5.1 Introduction

In this chapter the low density structure of the ST fluid is discussed. First, we will compare the results for the pressure obtained from MD simulation for intermediate dipole strengths  $\mu^2 = 1, 2$  and  $3$  with analytic results obtained from a second-order virial expansion for the ST fluid and for the pST fluid with  $\mu^2 = 3$ . This is primarily done as a check of accuracy for our MD program, because dipolar systems are rather complex and programming errors are not unlikely. We will show that a third-order virial expansion is neither for a very strongly dipolar ST fluid with  $\mu^2 = 36$  nor for an intermediate ST fluid with  $\mu^2 = 3$  sufficient to provide an adequate equation of state in the entire GL coexistence region. (Some authors have given estimates for the coexistence curves from a virial expansion [1]). In the last part of this chapter the focus lies on structures formed by strongly polar ST fluids in the very dilute phase and in the GL phase coexistence region. The strongly polar ST fluid is known to associate into chains. We give a short description of the algorithm, how to determine the clusters and quantities like frequency distributions and scaling laws of cluster sizes. We will also discuss the internal structure of droplets, since there are different predictions from theory in the present literature. In the following we set  $\alpha = 0$  unless stated, otherwise.

## 5.2 Simulation results for low densities

### 5.2.1 Comparison to a second-order virial expansion

To write a MD simulation program for the ST fluid is a quite effortful task, because the algorithm for the rotational movement with its constraints is complicated and a potential source of mistakes. Although, we checked our MD program versus data of other groups, for example reference [2], it is always recommendable to check the MD program versus

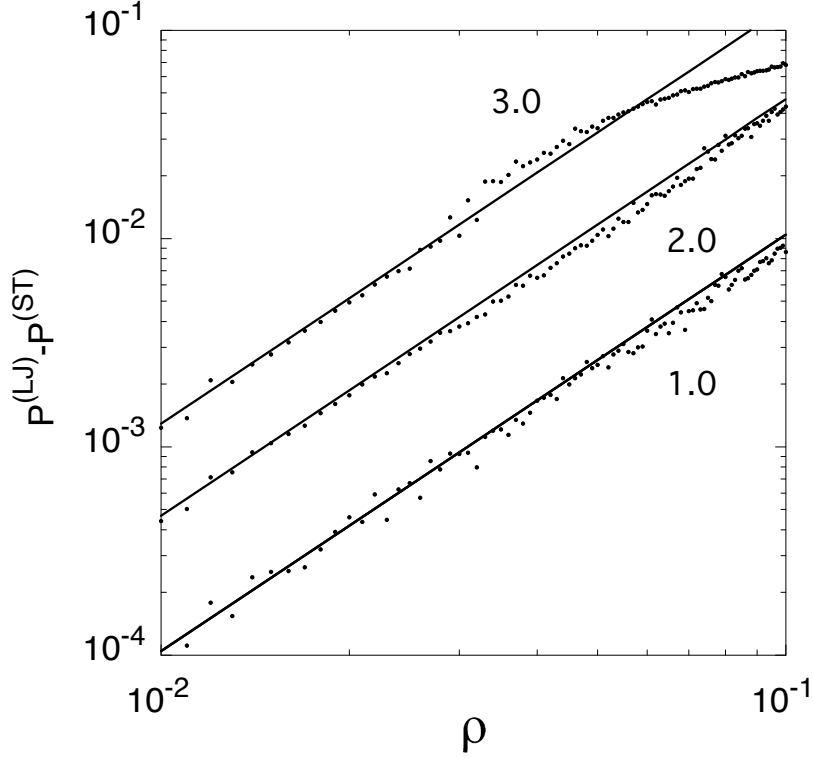


Figure 5.1: LJ pressure  $P^{(LJ)}$  minus the pressure of the corresponding ST fluid  $P^{(ST)}$  versus particle number density  $\rho$  at  $T = 1.2$ . Symbols: simulation data; lines: second-order virial approximation,  $\Delta P = T\rho^2 \left( B_2^{(LJ)}(T) - B_2(T, \mu^2, 0) \right)$ . Numbers are  $\mu^2$ -values.

exact analytic results when possible. This can be done for the pressure from simulation in the very dilute gas phase compared to a virial expansion

$$P = k_B T \rho \left( 1 + B_2(T, \mu^2, \alpha) \rho + B_3(T, \mu^2, \alpha) \rho^2 + \dots \right), \quad (5.2.1)$$

where  $B_2(T, \mu^2, \alpha)$  and  $B_3(T, \mu^2, \alpha)$  are the second and third-order virial coefficients. The virial expansion of the equation of state adds particle interactions to the ideal gas law. From this point of view,  $B_2$  corresponds to interactions between pairs of molecules and  $B_3$  between triplets. A detailed description of the calculation of  $B_2$  and  $B_3$  for the ST fluid can be found in appendix A. For the considered dipole strengths  $\mu^2 = 1, 2$  and  $3$  and temperature  $T = 1.2$  the system is an isotropic gas of monomers, i.e. no chains or clusters are formed. Therefore we can be sure that at least in the very dilute limit, the pressure should be described by a second-order virial expansion adequately. Figure 5.1 shows the difference of the LJ pressure  $P^{(LJ)}$  and the pressure of the corresponding ST fluid  $P^{(ST)}$ ,  $\Delta P = P^{(LJ)} - P^{(ST)}$ , versus number density  $\rho$ , from computer simulation (symbols) and from a second-order virial expansion (lines) for  $T = 1.2$  and  $\mu^2 = 1, 2$  and

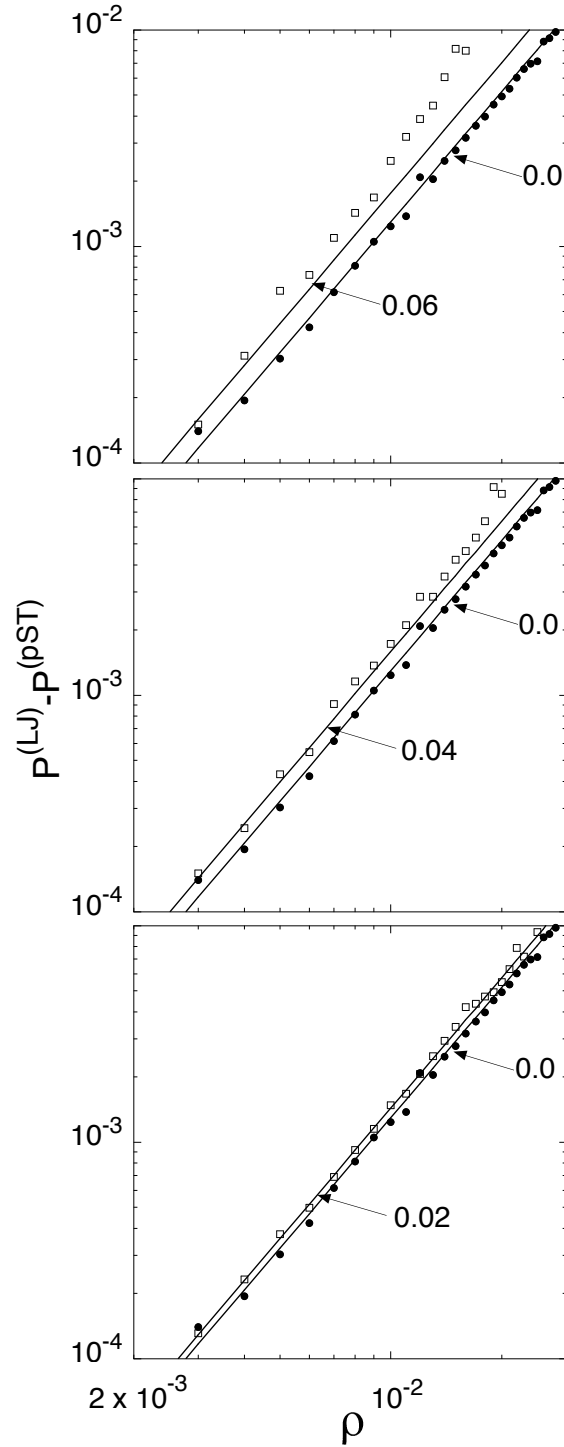


Figure 5.2: LJ pressure  $P^{(LJ)}$  minus pressure of the corresponding pST fluid  $P^{(pST)}$  versus particle number density  $\rho$ , for  $\mu^2 = 3.0$  and  $T = 1.2$ . Symbols: simulation data; lines: second-order virial approximation,  $\Delta P = T\rho^2 \left( B_2^{(LJ)}(T) - B_2(T, \mu^2, \alpha) \right)$ . Numbers with arrows indicate the  $\alpha$ -values.

3. The results are in very good accordance with each other, i.e. our MD program is able to reproduce the results of a second-order virial expansion at low densities. In figure 5.2 a similar comparison is shown for the case  $T = 1.2$ ,  $\mu^2 = 3$  and non-vanishing polarization  $\alpha = 0.02, 0.04$  and  $0.06$ . Here too we find good accordance for low densities.

## 5.2.2 Comparison to a third-order virial expansion

In the literature there are attempts to calculate the critical properties [3] or even whole coexistence curves [1] for the ST fluid from a virial expansion of the equation of state. In these publications third- and second-order expansions were employed. Figure 5.3 shows a comparison of the pressure  $P$  versus number density  $\rho$  of analytic results for the virial equation of state of different orders for intermediate  $\mu^2 = 3$  and strong  $\mu^2 = 36$  dipole strength and simulation data. The temperatures  $T$  are slightly below the respective critical temperatures. For  $\mu^2 = 36$  the third-order virial approximation fails already at low densities below the GL coexistence region. For dipole strength  $\mu^2 = 3$  at  $T = 1.8$ , the third-order approximation provides a significant improvement compared to the second-order one. Nevertheless, in this case the virial approximation fails on entering the GL phase coexistence region as indicated by the beginning van der Waals loop. So the third-order virial expansion works well in the gas phase for intermediate dipole strengths, while for strongly polar systems it fails already for dilute systems most likely due to chain formation. Simulation snapshots for number density  $\rho = 0.01$  are shown in figure 5.4. For  $\mu^2 = 3$  the particles are dispersed homogeneously over the entire simulation box, while for  $\mu^2 = 36$  the particles assemble to chains. So even at very low densities, there are many-particle interactions for  $\mu^2 = 36$  and the third-order virial expansion provides no adequate description of the equation of state.

## 5.3 Chains and droplets

### 5.3.1 Single droplet simulations

We want to give a global phase diagram of the ST fluid. In this part we investigate structures appearing in the GL phase coexistence region, the droplets. Zhang and Widom [4] predict with their phenomenological theory a coexistence of an isotropic-gas and a magnetic-liquid, meaning that droplets should show ferromagnetic order, located in the lower temperature range of the GL coexistence region. They assume the droplets should be of spheroidal shape due to their magnetization. Contrary Banerjee and Widom suggest in reference [5] a vortex like structure of the droplets with dipoles aligned parallel to the surface which leads to a toroidal or 'donut' shape. The vortex structure is in agreement

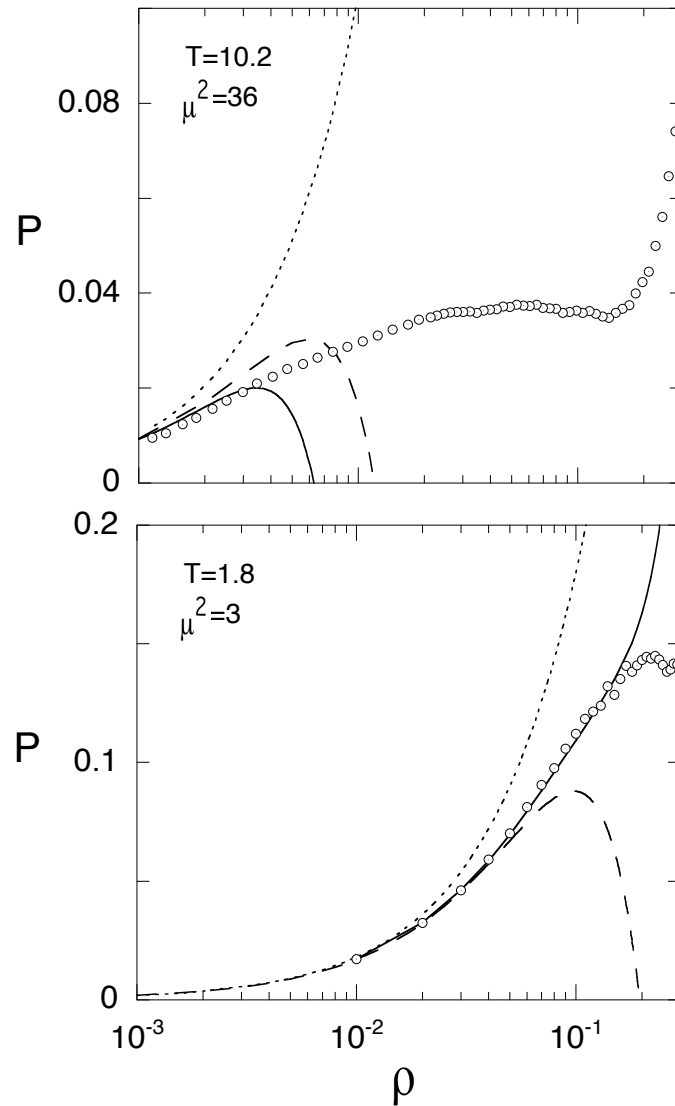


Figure 5.3: Pressure  $P$  versus number density  $\rho$  for the ST fluid. The lines are analytic results corresponding to the ideal gas equation of state (dotted line) and virial approximations including the second (dashed line) and third (solid line) virial coefficient, respectively. Temperatures and dipole moments are indicated in the plots.

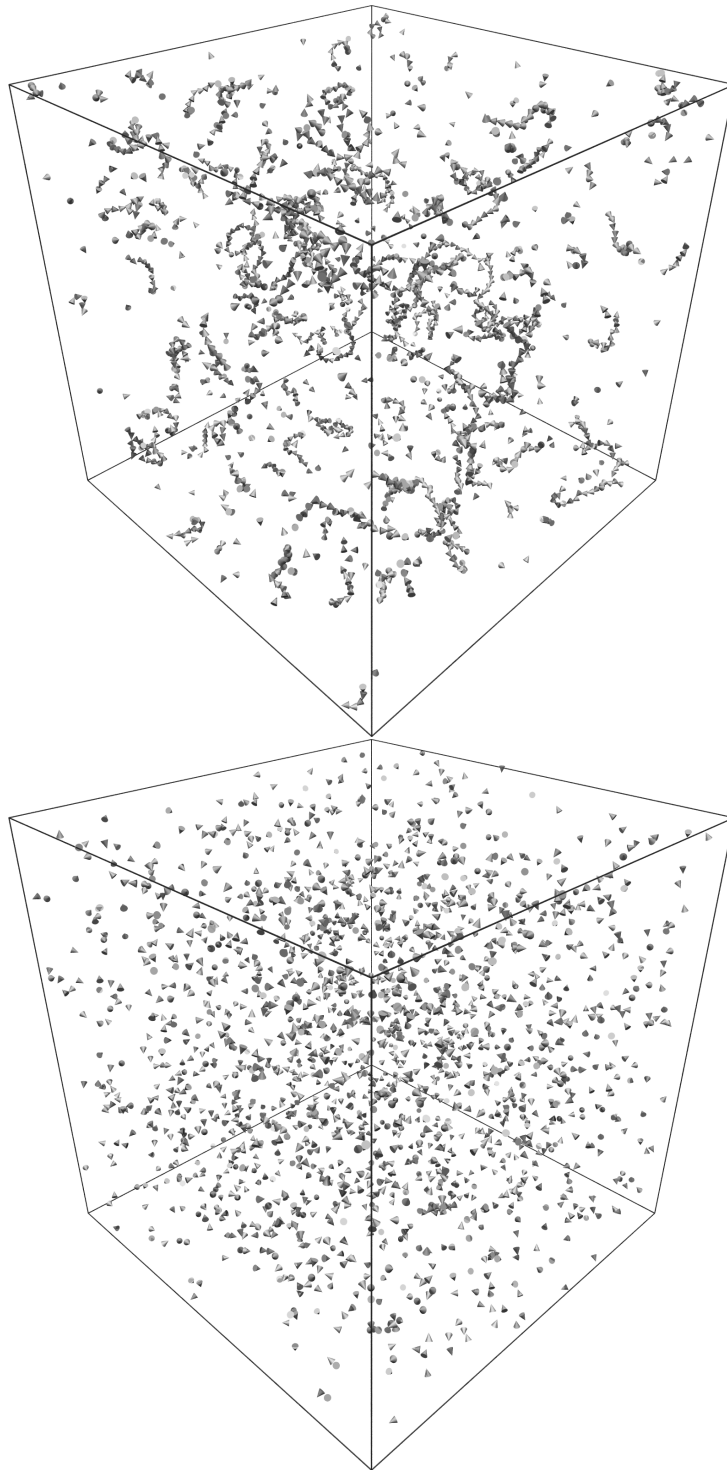


Figure 5.4: Simulation snapshots in the gas phase at density  $\rho = 0.01$  slightly below the critical temperature. Top:  $\mu^2 = 36$ ,  $T = 10.2$ ; bottom:  $\mu^2 = 3$ ,  $T = 1.8$ . Each ST particle is represented by a cone whose orientation gives the instantaneous direction of the particle's dipole moment. For the smaller dipole moment there is a homogeneous gas of monomers, while for the higher one single particles are coexisting with chains.

with simulation results by Lavender *et al.* [6] and Lu and Singer [7] for droplets consisting of 10 to 50 ST particles with dipole strengths  $\mu^2 = 1$  and 3. The particle numbers were too few to give a meaningful conclusion of the shape of the droplets, but the presented ones are sphere like. This confirms the observations of Shreve *et al.* [8] who performed MD simulations of ST droplets for  $\mu^2 = 4$  and particle numbers in the range from 50 to 896. Comparing the results of Shreve *et al.* with the ones of our group and references [6, 7] we have to take into account that their system was different. They trapped the droplets in a spherical container, while in the simulations of our group and [6, 7] the droplets were surrounded by vacuum. The simulations are in contradiction with DFT results from Talanquer and Oxtoby [9] who predict a perpendicular alignment of the dipoles to the surface of the droplet.

Here we report single droplet simulations. For this task the MD simulation program has to be changed only slightly. We turned off the periodic boundary conditions and minimum image convention, so we have a finite system and we can calculate the interactions between all particles exactly without long-range corrections. In general droplets are growing in the gas and particles are exchanged between the two phases in the GL phase coexistence region. These simulations were performed at temperatures low enough so that all particles of the system form one large metastable droplet surrounded by vacuum. For every system we chose the highest possible temperature, for which long simulations without evaporation were feasible.

### Total angular momentum and principal moments of inertia

Additionally, compared to simulations with periodic boundary conditions, we must take care of the 'rotating block of ice' [10] and remove the total angular momentum

$$\vec{L} = m \sum_{i=1}^N \vec{r}_i \times \vec{v}_i \quad (5.3.1)$$

from the system, because here we have no cubic box which prevents the system from rotating. This is done for every particle via

$$\vec{v}'_i = \vec{v}_i - \vec{\omega} \times \vec{r}_i \quad (5.3.2)$$

with

$$\vec{\omega} = \tilde{\mathbb{I}}^{-1} \vec{L}, \quad (5.3.3)$$

the instantaneous angular velocity of the system and the inverse moment of inertia tensor  $\tilde{\mathbb{I}}^{-1}$ . The moment of inertia tensor is a symmetric  $3 \times 3$  matrix with the elements  $\tilde{\mathbb{I}}_{\mu\mu} = m \sum_i (r_i^2 - \mu_i^2)$  and  $\tilde{\mathbb{I}}_{\mu\nu} = -m \sum_i \mu_i \nu_i$  with  $\mu \neq \nu$  and  $\mu, \nu \in \{x, y, z\}$  [11]. The inverse of  $\tilde{\mathbb{I}}$  can be obtained from

$$\tilde{\mathbb{I}}^{-1} = \frac{1}{\det(\tilde{\mathbb{I}})} \text{adj}(\tilde{\mathbb{I}}), \quad (5.3.4)$$

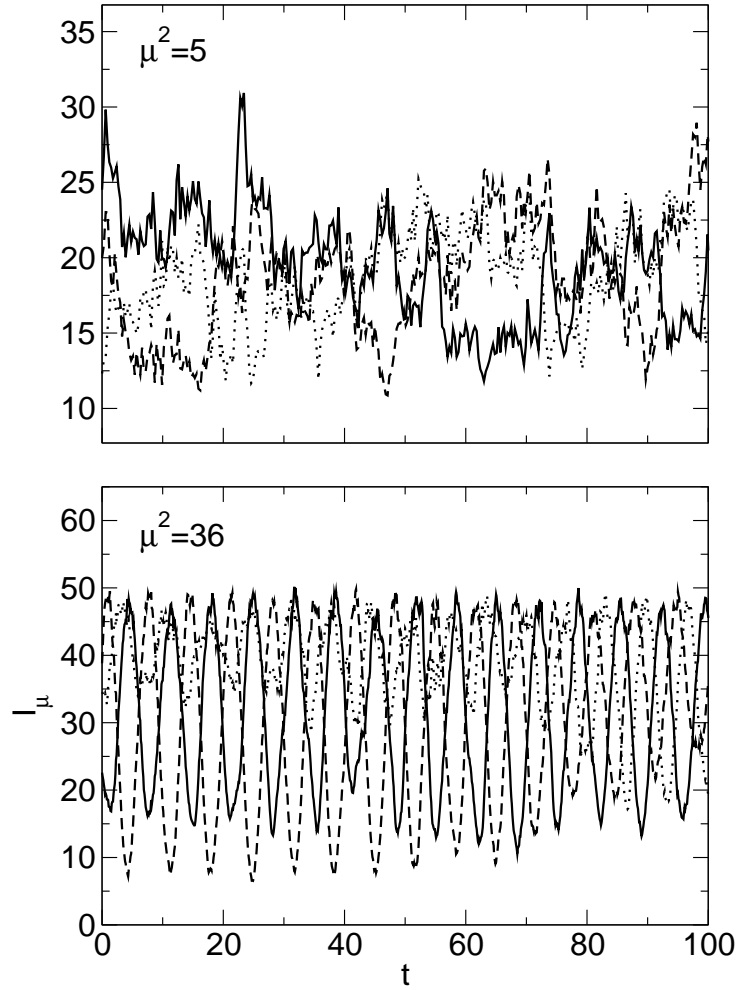


Figure 5.5: Time evolution of the principal moments of inertia  $I_1$ ,  $I_2$  and  $I_3$  for a  $N = 16$  cluster from single droplet simulation with  $\mu^2 = 5$ ,  $T = 0.7$  (top) and  $\mu^2 = 36$ ,  $T = 4$  (bottom). Different line types correspond to 1, 2 and 3.

where  $\det(\underline{\mathbf{I}})$  is the determinant and  $\text{adj}(\underline{\mathbf{I}})$  the adjoint of  $\underline{\mathbf{I}}$ . Moreover, we use the moment of inertia tensor to characterize the shape of the droplet. Because it depends on the origin and orientation of the coordinate system, we have to determine the eigenvalues. These are the principal moments of inertia  $I_\mu$  with respect to the axes of rotation for which the angular velocity and momentum are parallel ( $\vec{L} \parallel \vec{\omega}$ ). The three eigenvalues roughly characterize the shape of the droplet, i.e. for spheres all eigenvalues are equal, for spheroids two eigenvalues are equal and for prolate ellipsoids all eigenvalues differ. Nevertheless, there are many other shapes and generally visual inspection is necessary. A problem of this method is that the droplet changes shape with time and does not behave like a rigid body. For example if the principal moments of inertia, all have the same value on average, there is the possibility of a spherical shape, but

an ellipsoid, which is oscillating around a sphere, is possible also. To be able to distinguish the different cases, we calculate two kinds of averages of the principal moments of inertia. First we average the eigenvalues due to the same or only slightly changing eigenvectors and call them  $\langle I_1 \rangle$ ,  $\langle I_2 \rangle$  and  $\langle I_3 \rangle$ . We get the eigenvalues by diagonalizing the moment of inertia tensor numerically with Octave [12]. If some of these eigenvalues differ the shape of the droplet is likely a stable non spherical one. This should be observed for Zhang and Widoms spheroids. If all averages are equal, there is the possibility that the shape is stable highly symmetric, like for a sphere, but it can also oscillate around a sphere. To distinguish these cases we determine  $\langle I_{max} \rangle$ ,  $\langle I_{med} \rangle$  and  $\langle I_{min} \rangle$  corresponding to the averages of the instantaneous maximal, medium and minimal principal moment of inertia. These should differ for an oscillating shape. Figure 5.5 shows the time evolution of the instantaneous principal moments of inertia  $I_1$ ,  $I_2$  and  $I_3$  for a cluster with dipole strength  $\mu^2 = 5$  at temperature  $T = 0.7$ , and one with  $\mu^2 = 36$  at temperature  $T = 4$ . The fluctuations for  $\mu^2 = 5$  seem to be statistical, while the ones for  $\mu^2 = 36$  are highly correlated. So there is a systematic difference in the time evolution of the shape of a  $\mu^2 = 5$  and a  $\mu^2 = 36$  cluster. For the latter one the different kinds of averages should differ much.

### Radius of gyration

Another important quantity, often used in polymer physics, is the so called radius of gyration

$$R_g = \sqrt{\frac{1}{N} \sum_{i=1}^N \vec{r}_i^2 - \frac{1}{N^2} \left( \sum_{i=1}^N \vec{r}_i \right)^2}. \quad (5.3.5)$$

Here  $N$  is the number of particles inside the cluster or chain. The radius of gyration is the average distance of a particle to the center of mass of its cluster. From the scaling behaviour with increasing particle number

$$R_g \sim N^\nu \quad (5.3.6)$$

we can also get information of the cluster shape. A compact spherical object should scale with  $\nu_s = 1/3$  [13], an ideal chain (random walk) with  $\nu_{rw} = 1/2$ , a self-avoiding random walk with  $\nu_{srw} = 3/5$  and head-to-tail rings described by the XY model with  $\nu_{XY} = 0.67$  [14–16]. The critical exponent  $\nu$  for LJ clusters in the neighborhood of the critical point was found to be in the range  $\nu_{LJ} = 0.4 - 0.5$  [17–19] by computer simulation. From a modified cluster-cluster aggregation model with dipolar interactions [20], Mors *et al.* predict  $\nu_{ccd} = 0.75$  for the zero temperature limit.

To compare the principal moments of inertia with the radius of gyration, we introduce

$$R_{g\mu} = \sqrt{\frac{I_\mu}{N}} = \sqrt{m \sum_{i=1}^N r_i'^2} \quad (5.3.7)$$

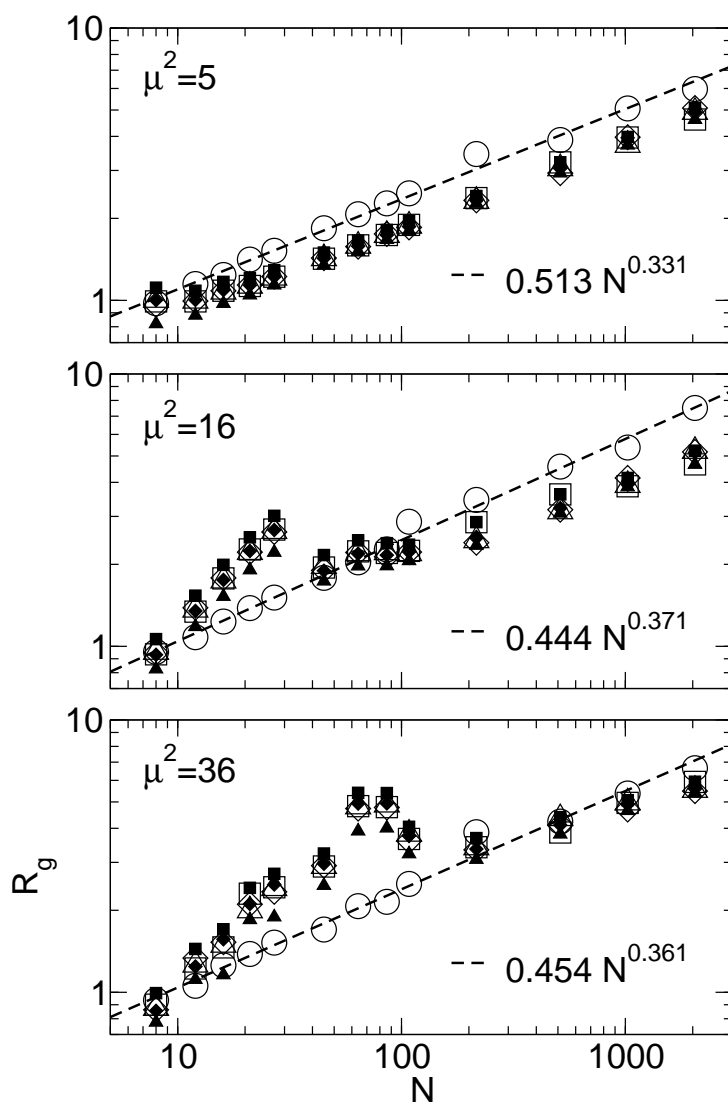


Figure 5.6: Radius of gyration  $R_g$  (hollow circles), and the averaged eigenvalues of the moment of inertia tensor  $R_{g_1}$  (hollow squares),  $R_{g_2}$  (hollow diamonds),  $R_{g_3}$  (hollow triangles),  $R_{g_{max}}$  (filled squares),  $R_{g_{med}}$  (filled diamonds) and  $R_{g_{min}}$  (filled triangles) for the indicated dipole strengths. For the two higher dipole strengths the scaling law changes with particle number most likely due to rigidity of formed chains.

(cf. [13]) where  $r'_i$  denotes the distance of the particle to the principal axis of rotation  $\mu$ .

Figure 5.6 shows the radius of gyration  $R_g$  and  $R_{g_1}$ ,  $R_{g_2}$ ,  $R_{g_3}$ ,  $R_{g_{max}}$ ,  $R_{g_{med}}$ ,  $R_{g_{min}}$ , calculated via (5.3.7) from  $\langle I_1 \rangle$ ,  $\langle I_2 \rangle$ ,  $\langle I_3 \rangle$ ,  $\langle I_{max} \rangle$ ,  $\langle I_{med} \rangle$  and  $\langle I_{min} \rangle$  versus particle number of the cluster for the dipole strengths  $\mu^2 = 5, 16$  and  $36$ . For all dipole strengths the radius of gyration scales with  $N^\nu$  and  $\nu$  close to  $1/3$ , that indicates a compact spherical growth of the cluster. The scaling law for the moments of inertia from the different averaging methods changes with particle number for the two higher dipole moments. This can be explained with the forming of stiff chains for small particle numbers which collapse at a definite particle number to a more compact shape, as already discussed by ten Wolde *et al.* and called coil-globule transition. For  $\mu^2 = 5$  it is similar to the scaling law of  $R_g$ , and the two averaging methods show only differences for the principal moments of inertia at very small particle numbers, since few particles cannot form ideal spheres. So we can assume a compact spherical shape for the droplets with  $\mu^2 = 5$ . For  $\mu^2 = 16, 36$  the averages  $\langle I_1 \rangle$ ,  $\langle I_2 \rangle$  and  $\langle I_3 \rangle$  coincide for small particle numbers, while  $\langle I_{max} \rangle$ ,  $\langle I_{med} \rangle$  and  $\langle I_{min} \rangle$  differ. This is an evidence that for these dipole strengths there is a non-stable not spherical shape for small particle numbers. For high particle numbers all averages are close to each other and the scaling law is similar to the one for  $R_g$ . It remains unclear, why the scaling law for  $R_g$  does not show a transition for  $\mu^2 = 16$  and  $36$  like for the  $R_{g_\mu}$ 's. Since  $R_{g_1}$ ,  $R_{g_2}$  and  $R_{g_3}$  are in quite good agreement for all dipole strengths and particle numbers there is no evidence for a significant stable spheroidal, ellipsoidal or toroidal shape, as predicted by [4, 5].

In figure 5.7 we show simulation snapshots of the single droplet simulations. The left column are droplets of ST particles with  $\mu^2 = 5$  and  $T = 0.7$ , the middle column with  $\mu^2 = 16$  and  $T = 2$  and the right column with  $\mu^2 = 36$  and  $T = 4$ . For every dipole strength clusters with  $N = 16, 64, 512$  and  $2048$  particles are shown. The temperatures were chosen as large as possible that no particles evaporate from the droplet for a long enough time period.

For the smallest dipole moment we can confirm a compact spherical shape for all particle numbers. For the two higher dipole moments and small particle numbers the systems form chains which compose to ring like structures. These structures collapse to a more compact globule for larger particle numbers, but the chain-characteristic remains obvious, especially for  $\mu^2 = 36$ .

On the other hand in all clusters, even for  $\mu^2 = 5$ , the particles are linked head-to-tail in chains. Their dipole orientations are forming a vortex like structure with arrangement parallel to the surface as predicted by [5] and already observed by [6, 7]. This become less obvious for increasing dipole strength at given particle number, but the reason for this can be the increasing temperature, too.

Lu and Singer [7] simulated droplets of 50 ST particles with dipole moment  $\mu^2 = 1, 3$  with MC at the temperature  $T = 0.28$  and found liquid behaviour. We were not able to reproduce these results via MD. In our simulations with these dipole strengths the particles were trapped to a lattice for an even larger temperature. An example is shown in figure 5.8 for  $\mu^2 = 3$  and  $T = 0.55$ .

However, our simulation procedure for single droplets holds many dangers. Because of

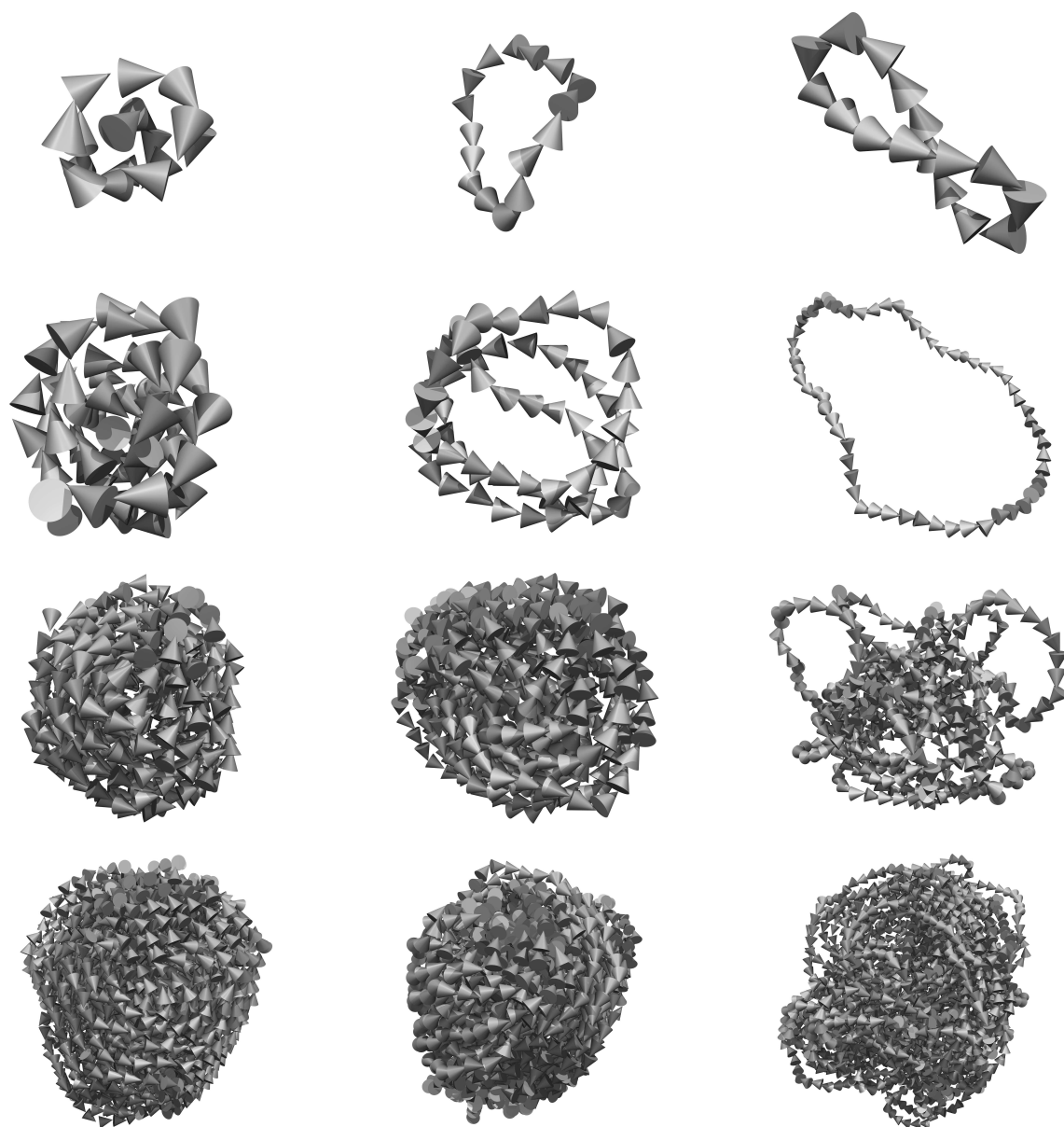


Figure 5.7: Snapshots from single droplet simulations for dipole strengths  $\mu^2 = 5, 16$  and  $36$  from left to right and particle numbers  $N = 15, 64, 512$  and  $2048$  from top to bottom. The temperatures are  $T = 0.7, 2$  and  $4$  for the increasing dipole strength. Inside the clusters the particles are linked head-to-tail in chains forming a globally circulating pattern. With increasing particle number the shape of the droplets become more spherical. For increasing dipole strengths the chain characteristic becomes more obvious.

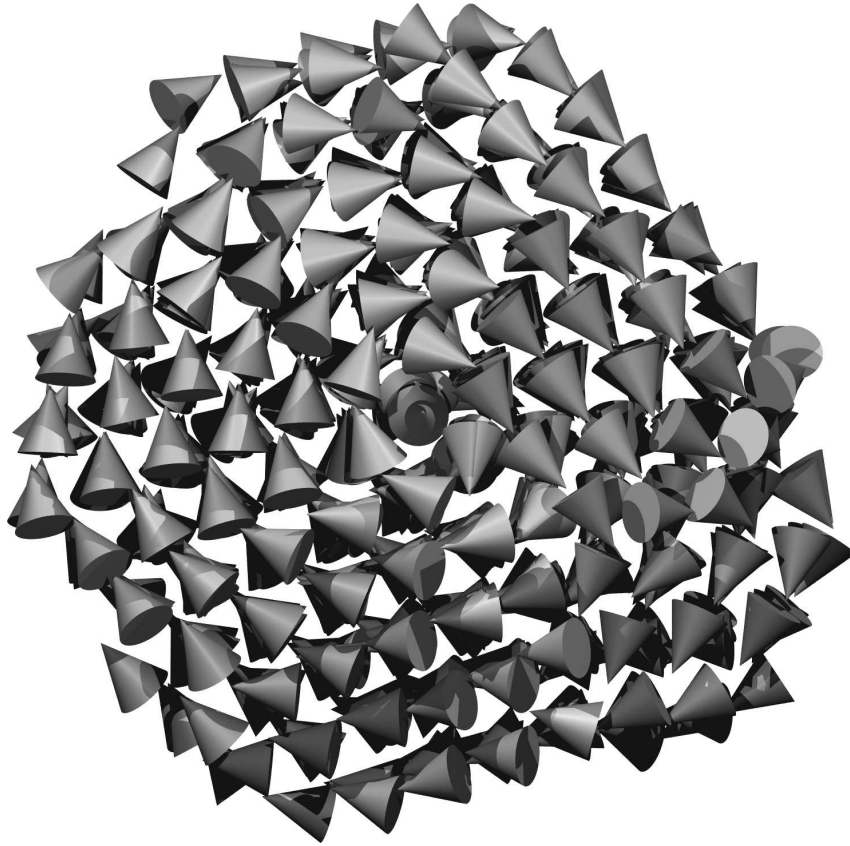


Figure 5.8: Snapshot from single droplet simulation for  $\mu^2 = 3$ ,  $T = 0.55$  and  $N = 512$ . The droplet freezes to a crystalline solid. The dipole orientations are arranged head-to-tail in an almost perfect circulating pattern. The perspective depth in this picture has been removed to make the lattice structure more obvious.

the low temperatures the systems can freeze or the shape of the droplets can be trapped in metastable states, so that it does not change any more. These problems were observed for simulations for  $\mu^2 < 5$ , so that no meaningful observations for these systems can be reported. It is worth mentioning that before we were aware of the 'rotating block of ice' problem, simulations of not evaporating droplets without crystalline structure were possible even for dipole strengths  $\mu^2 < 5$ . This problem may concern the investigations on droplets in reference [21]. Furthermore, droplets in the GL phase coexistence region are coexisting with gas particles and other droplets, so interaction between them may effect the shape and size. The results reported here can only be taken as a low temperature limit of the properties of droplets.

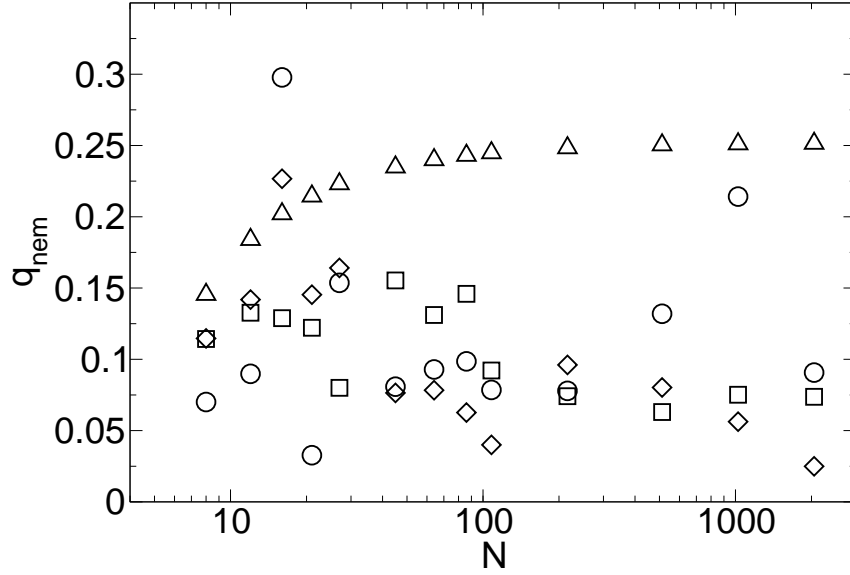


Figure 5.9: The nematic order parameter  $q_{nem}$  versus particle number  $N$  for droplets with  $\mu^2 = 5$  (circles),  $\mu^2 = 16$  (squares) and  $\mu^2 = 36$  (diamonds). The triangles show  $q_{nem}$  for an ideal chain. For increasing particle number in simulation there is a decreasing tendency for  $q_{nem}$ .

### The nematic order parameter

We have confirmed the vortex like structure of the dipole orientations by eye, but at last we want to amplify the degree of ferroelectric/-magnetic order inside the droplets by means of the nematic order parameter

$$q_{nem} = \frac{1}{(N-1)N} \left\langle \sum_{i<j}^N (3 \cos^2 \theta_{ij} - 1) \right\rangle = \frac{1}{(N-1)N} \left\langle \sum_{i<j}^N (3 (\vec{s}_i \cdot \vec{s}_j)^2 - 1) \right\rangle, \quad (5.3.8)$$

where  $\theta_{ij}$  is the angle between the two dipole orientations  $\vec{s}_i$  and  $\vec{s}_j$ . A system of completely parallel ordered dipoles would show  $q_{nem} = 1$ , while a completely randomly dispersed system would show  $q_{nem} = 0$ . Negative values to  $q_{nem} = -0.5$  are possible, but have not been observed. We will show here the nematic order parameter of the investigated droplets to check if there is a tendency of the droplet to form a ferroelectric ordered phase, as predicted by Zhang and Widom [4]. Doing this we have to be aware that  $q_{nem}$  of a vortex like structure is in general not zero, since for an ideal ring there exists for every particle at least one with parallel dipole orientation. Consider  $N$  particles arranged on an ideal ring. The angle between the dipole orientations of two particles positioned on sites  $i$  and  $j$  is given by

$$\theta_{ij} = \frac{2\pi}{N}(j-i) \quad (5.3.9)$$

and we can calculate for the ring

$$q_{nem}^{(ring)} = \frac{1}{(N-1)N} \sum_{i < j}^N \left[ 3 \cos^2 \left( \frac{2\pi}{N} (j-i) \right) - 1 \right]. \quad (5.3.10)$$

Figure 5.9 shows the nematic order parameter  $q_{nem}$  dependent on the particle number  $N$  of the droplet. Additionally shown is  $q_{nem}$  of an ideal ring calculated via (5.3.10) numerically, as an upper limit for a non-vanishing  $q_{nem}$  without real ferroelectric order. It is hard to judge the change of  $q_{nem}$  with particle number, because of the large scattering, but there seems to be an decreasing tendency of  $q_{nem}$  with increasing particle number. The more important information is that, except a few outliers, the highly symmetric ideal ring structure shows a larger  $q_{nem}$  than the investigated droplets. So the non-vanishing  $q_{nem}$  has not to be interpreted as starting ferroelectric ordering, it can be interpreted as a result of the ring structure inside the droplet. The crystalline cluster, shown in figure 5.8 has a order parameter  $q_{nem} = 0.1357$  for  $N = 512$ , more than all other droplets with this particle number.

### 5.3.2 Coexisting clusters in the dilute phase

In this part we want to investigate clusters at higher temperatures which are more relevant for the gas phase and GL coexistence region. At higher temperatures the droplets and clusters are no longer stable. Chains are formed and destroyed continuously due to equilibrium polymerization [14, 22] and in the phase coexistence region there is permanent evaporation and condensation, due to the dynamic equilibrium between the two phases. To investigate clusters in this temperature range we have to simulate large systems in which several chains or droplets can be formed. We use the simulations performed to determine the phase coexistence region in chapter 6 to search for clusters in the stored configurations. As already pointed out by van Workum and Douglas [14], in the very dilute phase there are reversible chains, rings and an intermediate species, the mutants. Examples are given in figure 5.10. Notice that the given illustration for mutants is a very schematic one. Branched chains and rings are rather rare during simulation. Most detected mutants are interlooped chains and rings with increasing frequency for increasing density.

#### Searching for clusters

Clusters are determined from the simulation configuration files containing all coordinates of the particles in the system. We determine the clusters with a simple distance argument: two particles, which are less than a definite distance  $r_n$  apart, are considered to belong to the same cluster. The most reasonable choice for  $r_n$  is the first minimum of the radial

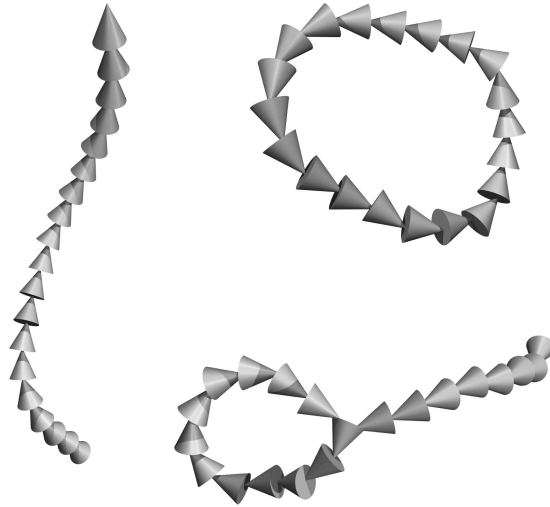


Figure 5.10: In the very dilute phase of the strongly dipolar ST fluid, we divide the clusters into three different classes: chains, rings and the intermediate mutants (similar to this example).

pair distribution function (3.7.1), but we also chose different ones, to compare results with literature, or to determine the dependence of the chain length on  $r_n$  in the more dense phase.

We employ an recursive algorithm to search for the clusters in a configuration, since this has turned out to be the fastest method. At the beginning we take one particle and define it as the cluster number one. Now we check if any of the other particles is inside a sphere of radius  $r_n$  around the first particle. As soon as we find one particle, we consider it to belong to the same cluster and start the search function for this particle. We repeat this procedure until we find a particle with no more neighbors. Then we return to the former particle and search for one more neighbor. If there is one we start the search for this particle, if there none we go again to the former particle in the row and so on. We continue this procedure until we reach again the first particle of the cluster and if no more neighbors are found, we have successfully determined the cluster and can continue with the next single particle. Particles which already belong to any cluster are not longer respected in the search.

The species of a cluster (cf. figure 5.10) is determined by storing the number of neighbors for every particle. If all particles of a cluster have exactly two neighbors the cluster is considered to be a ring, if all particles in the cluster have two neighbors except two, which have only one neighbor, the cluster is considered to be chain and if at least one particle has more than two neighbors the cluster is considered to be a mutant. Notice that compact droplets will be recognized as mutants, too.

### Characteristics of clusters

The radius of gyration, a significant characteristic of any type of cluster, was already introduced in equation 5.3.7. Another important characteristic for systems with equilibrium polymerization is the average chain length

$$n = \frac{\sum_{s=1}^N s N_s}{\sum_{s=1}^N N_s}, \quad (5.3.11)$$

where  $s$  is the number of particles in a given chain and  $N_s$  is the number of chains of length  $s$  in the system. Notice that  $N$  is here the total number of particles of the whole system. Different to mixtures of ordinary polymers the average chain length of a configuration is a dynamic property and changing with running simulation. For systems with chain formation one has to check carefully, if the system has reached equilibrium before producing data, since especially in the very dilute phase this can take an enormous long time. The average chain length  $n$  is often used in literature to show the degree of polymerization for a system of self-assembling particles. Although we call this quantity average 'chain' length, all clusters are respected for this quantity regardless of the cluster species.

The persistence length is a basic mechanical property quantifying the stiffness of a polymer and is given by

$$l_p = -\frac{1}{\ln \langle \vec{s}_i \cdot \vec{s}_{i+1} \rangle}, \quad (5.3.12)$$

where  $\vec{s}_i \cdot \vec{s}_{i+1}$  is the dot product of neighboring dipole orientations in a chain. The average is taken over all starting positions. The persistence length is defined as the length over which correlations in the direction of the tangent are lost. This can be interpreted that for pieces of the polymer, shorter than the persistence length, it behaves like an elastic rod, for pieces longer than the persistence length it is statistically described by a random walk. The persistence length is calculated for all species of clusters, but for mutants particles with more than two neighbors are neglected for the average in (5.3.12).

To analyze the distribution of chain lengths and species of a system, we give the number fraction

$$h^{(spec)}(s) = \frac{N_s^{(spec)}}{\sum_{spec} \sum_{s=1}^N N_s^{(spec)}}, \quad (5.3.13)$$

where  $N_s^{(spec)}$  is the number of chains of species  $spec$  with length  $s$ .

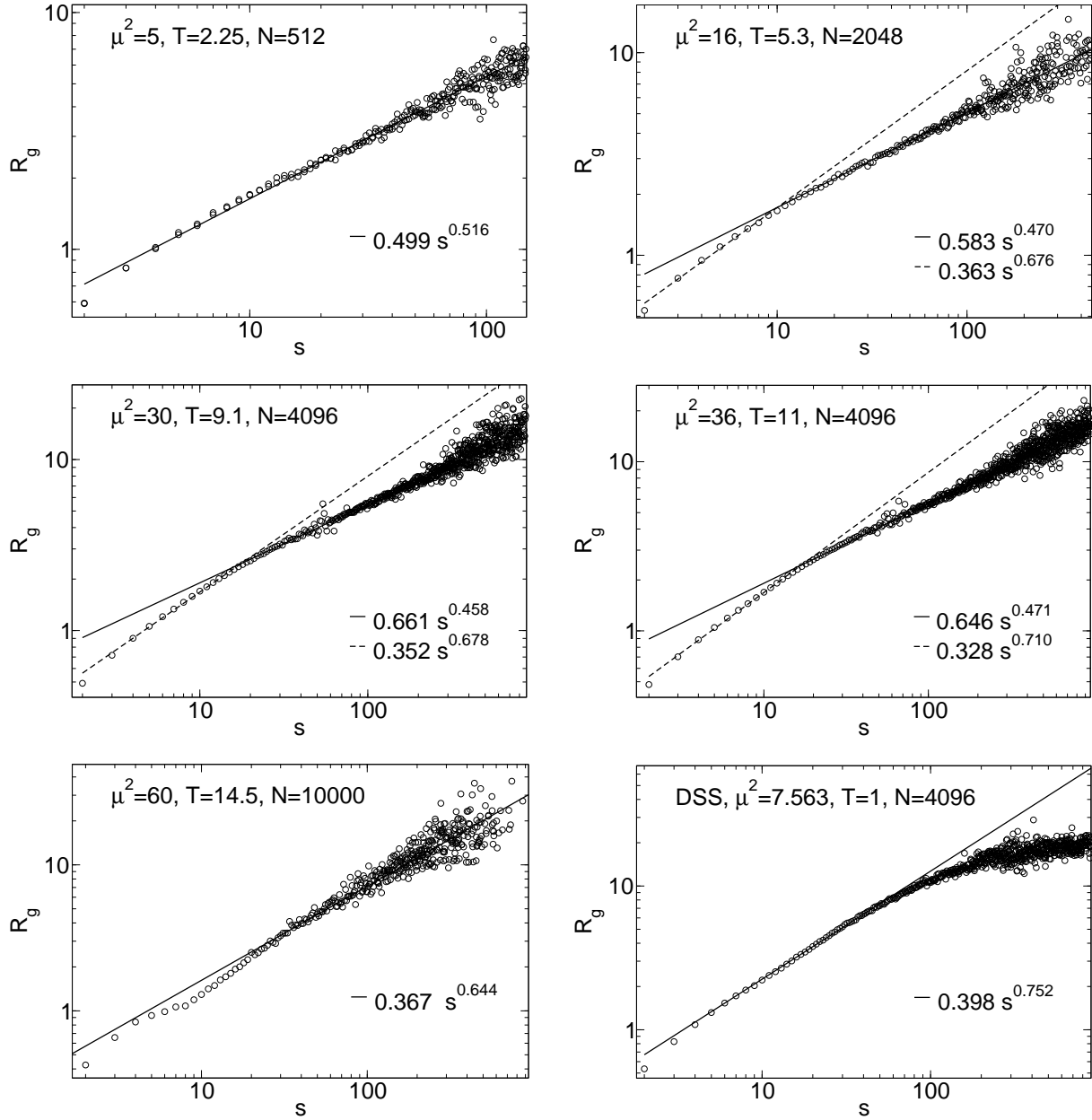


Figure 5.11: Scaling of the radius of gyration with chain length for coexisting clusters. The dipole strengths, temperatures and total particle numbers are indicated in the plots. The dashed and solid lines are fits to the data for different regions (dashed: small clusters; solid: large clusters). The density of the systems had no influence on the scalings, the system size affects only the largest observable clusters.

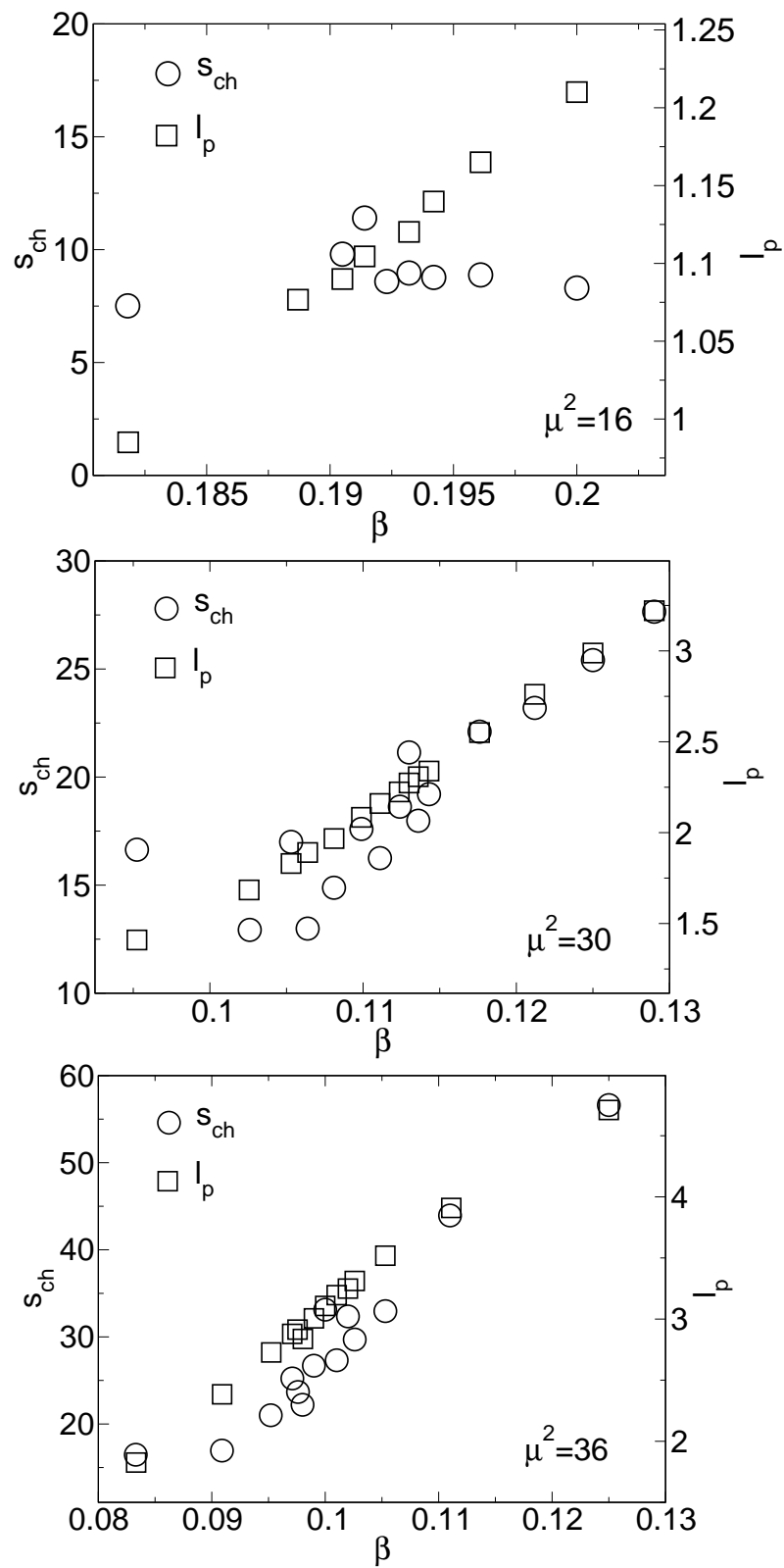


Figure 5.12: Chain length for the scaling law transition  $s_{ch}$  and persistence length  $l_p$  versus reciprocal temperature  $\beta$ . The persistence length is calculated for clusters at given temperatures with  $s > 100$ , for which it does not depend on chain length  $s$  anymore.

### Simulation results for coexisting clusters

In figure 5.11 we show some examples for the scaling laws of the radius of gyration with cluster length for different systems. For the smallest dipole moment  $\mu^2 = 5$  there is only one scaling law, valid in the whole range of cluster length. For dipole strengths  $16 \leq \mu^2 \leq 36$  there are two scaling laws for small and large particle numbers with a sharp transition for a definite cluster length. For  $\mu^2 = 60$  there is only one scaling law with variations in the small cluster limit. For the DSS fluid there is a scaling law only valid for small clusters with no sharp transition. The analyzed configurations for  $\mu^2 = 5, 16$  and  $60$  and the DSS fluid were taken from simulations for determining the GL coexistence region with maxwell construction (cf. chapter 6) in a density range of  $\rho = 0.001, \dots, 0.3$ . For  $\mu^2 = 30$  and  $36$  were special simulations done for  $\rho = 0.001, 0.01$  and  $0.05$ , since for the original particle number  $N = 2048$  the finite size effects for the scaling law were too close to the transition point. The scaling of radius of gyration of the observed clusters with particle number is not dependent on density, only the range of observed chain lengths vary. The different critical parameters are given in table 5.1. Here  $\nu_1$  denotes the critical

Table 5.1: Critical parameters for the radius of gyration scaling.

$\mu^2$	$\nu_1$	$\nu_2$
0	-	0.446
5	-	0.489
16	0.690	0.470
30	0.688	0.462
36	0.710	0.451
60	0.644	-
7.563 (DSS)	0.752	-

parameter for the scaling law in the short chain length range,  $\nu_2$  denotes it in the long chain length range. The parameters are averaged over several temperatures, only the values for  $\mu^2 = 60$  and  $\mu_{DSS}^2 = 7.563$  are for one temperature. The critical parameters are not dependent on the temperature, only the absolute value of  $R_g$  and the transition points are.

The values lie in the range of  $\nu_1 = 0.644 - 0.752$  and  $\nu_2 = 0.446 - 0.489$  without tendency for increasing dipole strength. We can explain this behaviour of  $\nu$  with the conclusions we came to for the behaviour of single clusters with particle number and dipole strength in subsection 5.3.1. ST particles with high dipole strength and DSS particles form chains with a certain stiffness. So short chains for these systems are most likely linear chains, rings or chain like mutants as shown in figure 5.10. The critical parameters of the scaling law for these systems should lie somewhere in the range between the parameter  $\nu_{XY} = 0.67$ , describing head-to-tail rings, and  $\nu_{ccd} = 0.75$ , derived by cluster-cluster aggregation for

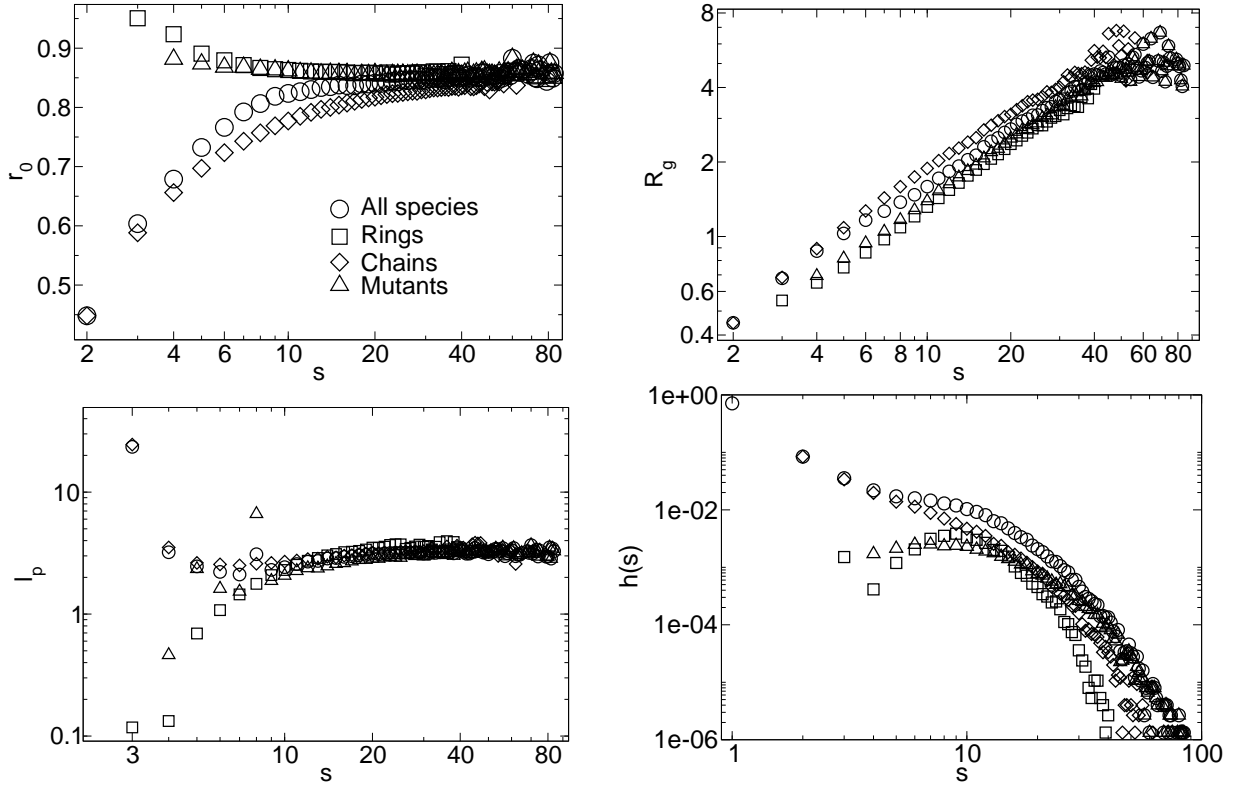


Figure 5.13: The average bond length,  $r_0$ , radius of gyration,  $R_g$ , persistence length,  $l_p$ , and fraction number,  $h(n)$ , per cluster size,  $n$ , for  $\mu^2 = 36$ ,  $T = 9.31$ ,  $N = 2048$  and  $\rho = 0.003$ . The circles are the values for clusters of certain size, the other the contributions of the particular species.

head-to-tail dipolar clusters in the zero temperature limit. All observed parameters  $\nu_1$  lie in or close to this range as expected for rigid chains and rings. It is also in good accordance with van Workum and Douglas who found  $\nu = 0.68$  for  $\mu^2 = 36$  [14].

For small dipole moments like  $\mu^2 = 5$  and long clusters of high dipole moments, the observed parameters  $\nu_2$  are in accordance with the parameters obtained from simulation  $\nu_{LJ} = 0.4 - 0.5$  in literature [17–19] for the LJ fluid, including this work (cf. table 5.1). The parameter for the LJ fluid  $\nu_{LJ}$  is larger than the one for a compact spherical shape  $\nu_s = 1/3$ , meaning there is a fractal structure inside the cluster. Here the transition from one scaling law to the other is a smooth one, different to the single cluster simulations, where we saw a 'collapse' of the structure for a certain particle number (cf. figure 5.6).

Figure 5.12 shows the transition chain length  $n_{ch}$  for the gyration scaling and persistence length  $l_p$  for long clusters ( $n > 100$ ) depend on the reciprocal temperature  $\beta$ . For dipole moments  $\mu^2 = 30$  and  $36$  we see a clear correlation between  $s_{ch}$  of the transition and  $l_p$ . Both depend linear on the reciprocal temperature with a larger scattering for  $s_{ch}$ . We can't make a judgement for  $\mu^2 = 16$ , since the scattering for  $s_{ch}$  is so large, while  $l_p$  clearly depends linear on  $\beta$ , too. This correlation is quite reasonable, if we remember that

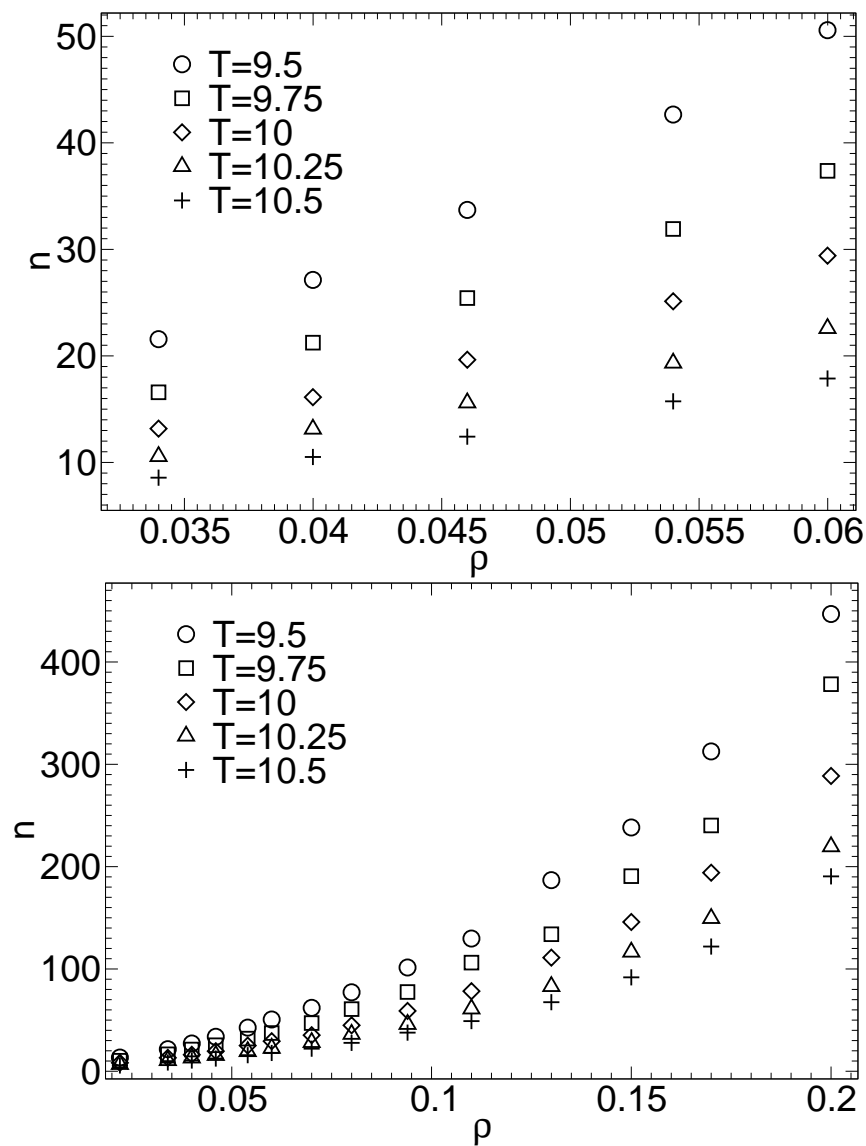


Figure 5.14: Average chain length  $n$  versus density for a system of  $N = 2048$  ST particles with  $\mu^2 = 36$  for different temperatures. Top: for a low density range the growth seems to be linear, cf. [14]. Bottom: on a larger density range the growth is rather exponential. The radius for determining neighbors was chosen as  $r_n = 1.5$ .

pieces of the chains shorter than the persistence length behave rather like flexible rods and pieces longer can only be described statistically, like a random walk. Van Workum and Douglas did not find a transition in the gyration scaling of the  $\mu^2 = 36$  system [14], since they give data in a chain length range ( $10 \leq s \leq 70$  for  $\beta \approx 0.11$ ) where we find a transition ( $s_{ch} \approx 45$ ).

In figure 5.14 some characteristic properties for a system with chain formation ( $\mu^2 = 36$ ,  $T = 9.31$ ,  $N = 2048$ ,  $\rho = 0.003$ ) are shown. The number fraction of chains with a certain length  $h(s)$  show that the total frequency of clusters is decreasing with chain length. If we take deeper insight at the frequency of species, we see that for short clusters with  $s \leq 6$  rings and mutants do not play a role, but become more important for  $6 < s < 30$ . For cluster lengths  $s \geq 30$  mutants become predominant, but these clusters are already very unlikely for these system parameters. For the radius of gyration we see no real difference in the scaling behaviour for the different species, only the absolute values differ. As expected in the range  $4 \leq s \leq 40$ , the radius of gyration of chains of certain length is the largest, the one of rings is the smallest and the one of mutants is intermediate. For cluster lengths  $s > 40$  the scattering is too big for this low density. The average bond length  $r_0$  differs for small clusters ( $s < 30$ ) until the large cluster limit is reached. The average bond length is monotonically decreasing to this limit for rings, for chains its monotonically increasing. This is clear since for a linear chain the dipolar are bigger than for a bended chain like a piece of a ring. This effect disappear for large rings, where small apertures look like linear chains. For chains its the other way, since very short chains are almost perfectly linear, while longer chains are a little bit bended. Mutants behave similar to rings. The persistence length  $l_p$  has a large cluster limit, too. For small clusters it is very large for chains, while for rings it is very short. This is consistent with the observations for the bond length.

Figure 5.14 shows the dependence of the average chain length  $n$  on the density for a system of  $N = 2048$  ST particles with  $\mu^2 = 36$  and different temperatures. The upper panel shows an amplification for the low density range. Here  $n$  seems to have a linear dependence of density like in [14], while for a larger density range (lower panel) the dependence seems to be exponential. With decreasing temperature the chains become longer on average.

## 5.4 Conclusion

We successfully compared our ST MD simulation program for low densities and intermediate dipole moments with a second-order virial expansion for the case with and without polarizability. A third-order virial expansion describes a system with intermediate dipole moment ( $\mu^2 = 3$ ) in the whole gas phase quite well, failing on entering the GL coexistence region, while for strongly dipolar systems ( $\mu^2 = 36$ ) it fails already for a very dilute system due to chain formation. By single droplet simulations we were able to confirm the vortex like arrangement of the dipole orientations inside the clusters predicted by [5]

and observed by [6–8]. We could also confirm the spherical shape in the low temperature limit for big clusters observed by [6, 7]. On the one hand we found no evidence neither for ferroelectric order [4] nor for a perpendicular orientation of the dipoles to the surface [9], on the other hand we found no evidence neither for a spheroidal [4] nor for a toroidal [5] shape. By simulating coexisting clusters, we found a transition in the scaling of the radius of gyration for clusters with strong dipoles as already investigated by [13]. While the size of clusters with intermediate dipole strength ( $\mu^2 \leq 5$ ) scale with particle number like LJ clusters, clusters with strong dipoles  $\mu^2 \geq 16$  scale like stiff rings or chains. This scaling shows a transition for large particle numbers, since the chains form globules with a more compact shape. A collapse was only observed by single droplet simulation in the low temperature limit. We showed the correlation between persistence length of the clusters and the transition point.

# Bibliography

- [1] V. Russier and M. Douzi. On the utilization of the Stockmayer model for ferrocolloids: Phase transition at zero external field. *Journal of Colloid and Interface Science*, 162:356–371, 1994.
- [2] C. Kriebel and J. Winkelmann. Thermodynamic properties of polarizable Stockmayer fluids: perturbation theory and simulation. *Molecular Physics*, 88(2):559–578, 1996.
- [3] J.S. Rowlinson. The critical constants of polar gases. *Journal of Chemical Physics*, 19(7):831–833, 1951.
- [4] H. Zhang and M. Widom. Global phase diagrams for dipolar fluids. *Physical Review E*, 49(5):3591–3593, 1994.
- [5] S. Banerjee and M. Widom. Shapes and textures of ferromagnetic liquid droplets. *Brazilian Journal of Physics*, 31(3):360–365, 2001.
- [6] H.B. Lavender, K.A. Iyer, and S.J. Singer. Global orientational order in model polar clusters. *Journal of Chemical Physics*, 101(9):7856–7867, 1994.
- [7] D. Lu and S.J. Singer. Orientational ordering and anisotropy in model polar clusters. *Journal of Chemical Physics*, 103(5):1913–1921, 1995.
- [8] A.P. Shreve, J.P.R.B. Walton, and K.E. Gubbins. Liquid drops of polar molecules. *Journal of Chemical Physics*, 85(4):2178–2186, 1986.
- [9] V. Talanquer and D.W. Oxtoby. Nucleation in dipolar fluids: Stockmayer fluids. *Journal of Chemical Physics*, 99(6):4670–4679, 1993.
- [10] Y. Zhou, M. Cook, and M. Karplus. Protein motions at zero-total angular momentum: The importance of long-range correlations. *Biophysical Journal*, 79(6):2902–2908, 2000.
- [11] W. Greiner. *Theoretische Physik*, volume 2. Verlag Harri Deutsch, 6 edition, 1998.
- [12] J.W. Eaton. GNU Octave version 2.1.73, <http://www.octave.org>.
- [13] P.R. ten Wolde, D.W. Oxtoby, and D. Frenkel. Coil-globule transition in gas-liquid nucleation of polar fluids. *Physical Review Letters*, 81(17):3695–3698, 1998.
- [14] K. van Workum and J.F. Douglas. Equilibrium polymerization in the Stockmayer fluid as a model of supermolecular self-organization. *Physical Review E*, 71(031502), 2005.

- 
- [15] J. H. Akao. Percolation in a self-avoiding vortex gas model of the  $\lambda$  transition in three dimensions. *Physical Review E*, 53(6):6048–6055, 1996.
- [16] N.K. Kultanov and Y.E. Lozovik. The critical behaviour of the 3d  $x - y$  model and its relation with fractal properties of the vortex excitations. *Physics Letters A*, 223:189–194, 1996.
- [17] D.M. Heyes. Percolation cluster statistics of Lennard-Jones fluids. *Molecular Physics*, 66(5):1057–1074, 1989.
- [18] V.P. Gregory and J.C. Schug. Clustering of Lennard-Jones particles below the critical temperature. *Molecular Physics*, 78(2):407–420, 1993.
- [19] N. Yoshii and S. Okazaki. A large-scale and long-time molecular dynamics study of supercritical Lennard-Jones fluid. an analysis of high temperature clusters. *Journal of Chemical Physics*, 107(6):2020–2033, 1997.
- [20] P.M. Mors, R. Botet, and R. Jullien. Cluster-cluster aggregation with dipolar interactions. *Journal of Physics A*, 20(15):L975–L980, 1987.
- [21] F. Pesth. Flüssig-Gas-Koexistenz in Stockmayer-Fluiden mittels Computersimulation. Diploma thesis, Bergische Universität Wuppertal, April 2006.
- [22] M.J. Stevens and G.S. Grest. Phase coexistence of a Stockmayer fluid in an applied field. *Physical Review E*, 51(6):5976 – 5983, 1995.

# 6 Gas-liquid coexistence in the Stockmayer fluid via computer simulation

## 6.1 Introduction

The ST model does exhibit GL phase separation readily for small dipole strengths, because of the LJ part of its potential. In this chapter we want to trace the GL coexistence curves of the ST fluid via computer simulation. The equation of state of a one component system depends in general on the quantities  $P, V, T$  of which two can be chosen independently (cf. equation (5.2.1))<sup>1</sup>. Figure 6.1 shows a schematic illustration of the phase diagram of a one component system like the LJ system<sup>2</sup>. The left figure shows the phase behaviour in the  $P$ - $T$  plane where the GL phase transition is indicated by a line, the vaporization curve, on which GL coexistence exists only. If we adjust pressure and temperature of a system (NPT ensemble) we will find no stable phase coexistence of the gas and liquid phase, the transition is happening immediately if we pass the borderline. The vaporization curve terminates at the critical point for high temperatures and pressures, beyond which no GL transition exists any more, and by the triple point for low temperatures and pressures, where three phases coexist: gas, liquid and solid. For smaller temperatures and pressures than the triple point there is the sublimation curve indicating the gas-solid transition. We focus on the region between the critical and the triple point. Looking at the phase diagram in the  $P$ - $V$  plane (right figure), we see that there is no sudden transition from gas to liquid by changing volume or pressure, there is rather a region where both phases coexist. The dashed lines indicate isotherms. Compressing the system in a pure phase causes an increase in pressure. In the coexistence regions the isotherms are flat and the pressure is constant. The critical isotherm has an inflection point at the critical volume. Notice that the slope of the isotherms is negative in pure phase regions,  $\partial P/\partial V|_T < 0$ , due to the stability condition  $\kappa_T > 0$  for the compressibility at constant temperature. The borderline of the GL phase coexistence region is called binodal. On an isotherm in the coexistence region, the pressure and the chemical potential of both

---

<sup>1</sup>Here we do not consider the interaction with external fields.

<sup>2</sup>In general full phase diagrams, even for one component systems, are much more complex (e.g. water)

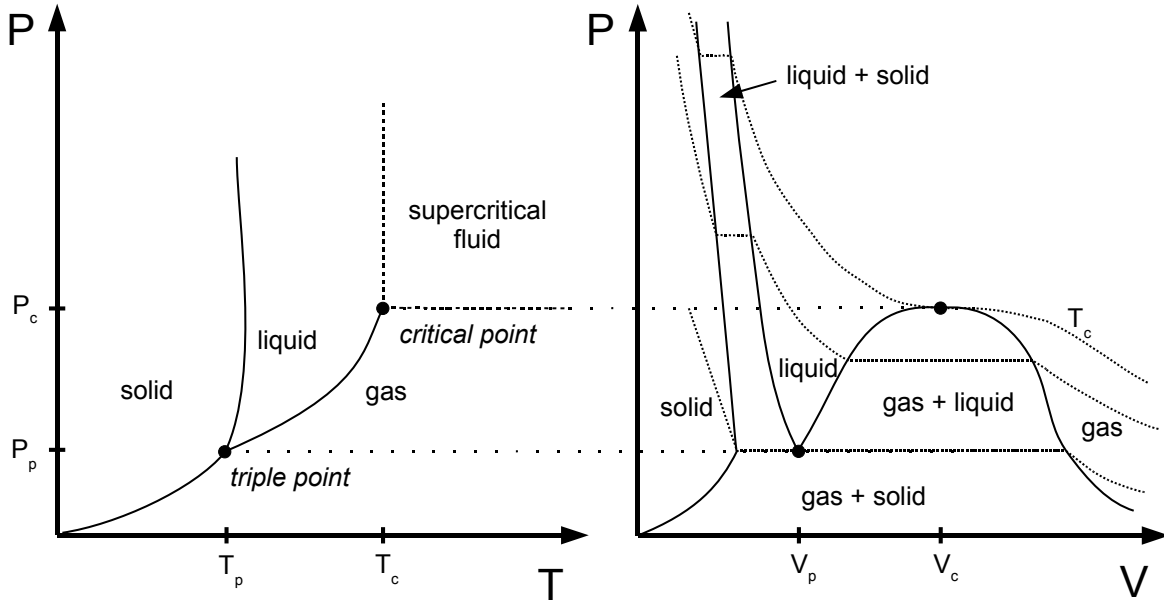


Figure 6.1: Schematic illustration of the phase diagram for a simple one component system in the  $P$ - $T$  and the  $P$ - $V$  plane. The dashed lines in the  $P$ - $V$  plane are isotherms.

phases remain constant. GL and gas-solid coexisting lines can be theoretically obtained from the Clausius-Clapeyron equation, based on the equality of the chemical potentials of both phases and the continuity of the Gibbs free energy. A detailed introduction to the physics of phase transitions can be found in [1–3].

The phase diagram of the ST fluid is more complicated than the one shown here, because it includes orientational ordering of the dipoles. Actually, the global phase diagram of the ST fluid is still unknown [4, 5]. For increasing dipole strength the ST fluid shows reversibly assembling chains in the gas phase<sup>3</sup>. Due to this chain formation GL separation was previously believed to disappear above a certain threshold of dipole strength. The conclusion that this threshold should be close to  $\mu^2 \approx 25$  is based on work by van Leeuwen and Smit [7], which is quoted frequently in the subsequent literature (e.g, [4, 8–13]). Van Leeuwen and Smit used the GEMC technique to study the modified ST potential.

In this work we report GL phase coexistence curves of the ST fluid including equilibrium polymerization and ferroelectric order. In particular we report phase coexistence between an isotropic gas and an isotropic liquid for dipole strengths up to  $\mu^2 = 60$ , which is significantly above the limit proposed previously beyond which no GL transition should exist. We also present GL coexistence curves of the polarizable ST fluid for point polarizabilities  $\alpha$  in the range  $0 \leq \alpha \leq 0.08$  and dipole strengths  $\mu^2 = 1.0, 2.0$  and  $3.0$ . Finally we investigate possible GL phase transition in the DSS fluid for selected parameters.

<sup>3</sup>The formation of chains in colloidal systems due to dipolar interaction was first predicted by Pincus and de Gennes [6].

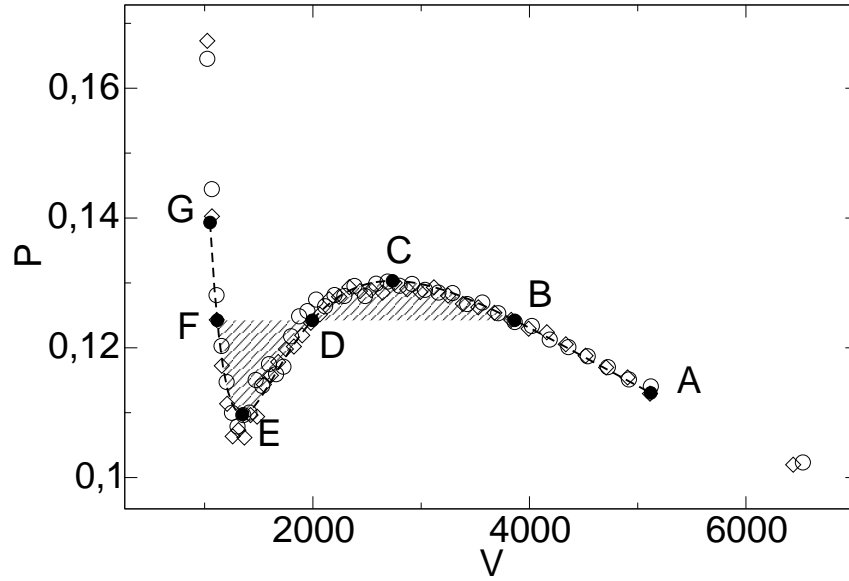


Figure 6.2: Illustration of the Maxwell construction method for a typical van der Waals isotherm. The symbols are the results of NVT-MD simulations for  $\mu^2 = 5$ ,  $T = 2.26$ ,  $N = 512$ . Open circles: results obtained during compression; open diamonds: results obtained during subsequent expansion. The dashed line represents a fit using a simple approximate equation of state. The shading highlights the equal areas.

## 6.2 Determination of gas-liquid coexistence curves

### 6.2.1 The Maxwell construction method

GL phase coexistence curves in this work are obtained primarily via Maxwell construction, a method to determine equilibrium states for instance for the van der Waals equation. The van der Waals equation

$$P = \frac{NT}{V-b} - \frac{a}{V^2} \quad (6.2.1)$$

was in history the first attempt of an equation of state which reproduces many of the important features of the GL phase transition. A shortcoming of the van der Waals theory is the phase coexistence region, where isotherms of real systems should be flat due to phase separation (cf. Fig 6.1). The van der Waals equation behaves different, like the isotherm shown in figure 6.2, and exhibits in this region a so called van der Waals loop. Phase separation is not included in the theory due to its mean field character, describing a homogeneous fluid. One compression path for a van der Waals system follows the points ABCDEFG, while in equilibrium the path would be ABDFG. Following the path of the van der Waals loop, we start in the pure gas phase A compressing the system until we reach the binodal B. Entering the coexistence region, for a real gas in equilibrium the pressure

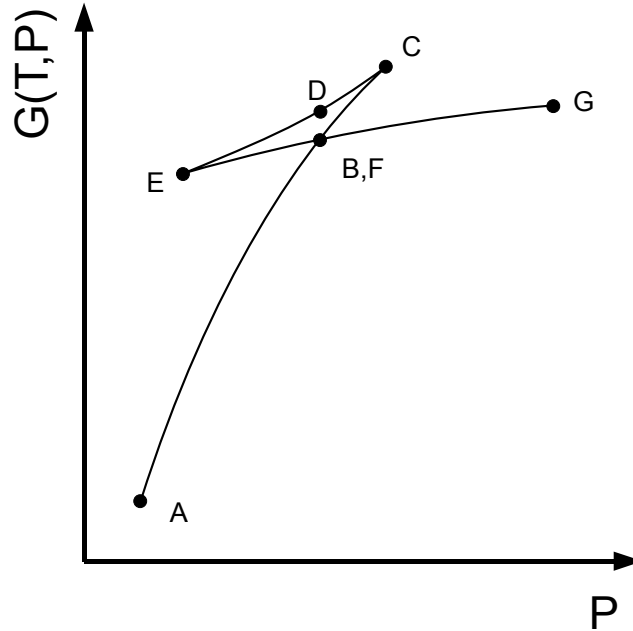


Figure 6.3: Gibbs free energy versus pressure for the van der Waals isotherm in figure 6.2. In equilibrium the compression/expansion path would be ABG. The paths BC and EF are metastable, the path CDE is mechanical unstable, since  $G(T, P)$  is convex.

would not increase by compressing the system until the pure liquid phase is reached. For the van der Waals system the pressure continues to increase until point C, marking the spinodal. Region BC is metastable, since phase separation is driven by nucleation assisted by impurities or external disturbances, and conforms to a supercooled gas which can be realized in the laboratory for very pure samples. Comparing with figure 6.3, showing the molar Gibbs free energy dependent on pressure for the isotherm in figure 6.2, we see that the region BC is not equilibrium, because it no longer corresponds to the minimum of free energy. This applies also for the region EF which conforms to a metastable superheated liquid. With the path CDE the system passes the region where spinodal decomposition proceeds [14]. Spinodal decomposition does not depend on the formation of nucleation sites, it is rather started immediately by fluctuations in density with infinitesimal amplitude and long wave length which grow and result in phases of different density. The van der Waals equation predicts here positive slope  $\partial P/\partial V|_T > 0$  and therefore a negative compressibility  $\kappa_T < 0$ , an unphysical effect. This corresponds to mechanical unstable states, since the Gibbs free energy is convex in this region violating the requirements of stability. The points E and F correspond again to the spinodal and binodal, respectively, before we reach the pure liquid phase G. At the critical temperature and beyond the van der Waals equation will behave like real systems with an inflection point at the critical point. However, aim of the Maxwell construction is to remove the unphysical parts from the isotherms.

Equilibrium requirements for GL phase coexistence of a one component system are equality of both the pressures and the chemical potentials of the coexisting phases

$$P_s = P_g = P_l , \quad (6.2.2)$$

$$\mu_s = \mu_g = \mu_l . \quad (6.2.3)$$

Here  $P_g$  ( $P_l$ ) indicates the pressure of the gas (liquid) phase and  $\mu_g$  ( $\mu_l$ ) the chemical potential of both, the  $s$  indicates saturation pressure (chemical potential). Equation (6.2.3) corresponds to a constant Gibbs free energy

$$G = N\mu = F + PV \quad (6.2.4)$$

along an isotherm in the GL coexistence region ( $dG = 0$ ). Here  $F$  indicates the Helmholtz free energy. For the difference of the Gibbs free energies of the pure phases on the coexistence curve we get

$$0 = N(\mu_l - \mu_g) = F_l - F_g + P_s(V_l - V_g) . \quad (6.2.5)$$

and by integrating the relation  $P = -\partial F/\partial V|_T$  along the isotherm we obtain the difference of the Helmholtz free energies

$$F(V_l, T) - F(V_g, T) = - \int_{V_g}^{V_l} P(V, T) dV . \quad (6.2.6)$$

Here  $P(V, T)$  is the particular equation of state not the equilibrium pressure. Adopting this into equation (6.2.5) we get the system of equations from which we can practically calculate the equilibrium pressure  $P_s$ , and the coexisting volumes  $V_g$  and  $V_l$

$$P_s = P_g = P_l$$

$$\int_{V_g}^{V_l} P(V, T) dV = P_s(V_l - V_g) . \quad (6.2.7)$$

The justification of the Maxwell construction was given by Griffiths [15] with his suggested 'hypothesis of analyticity' for deriving equilibrium. The Helmholtz free energy is analytic everywhere except on the phase boundaries. Only Maxwell's equal-areas construction satisfies this condition. An attempt to place the horizontal part of the isotherm in any other position inevitably leads to some sort of phase transition in the one phase region. To apply this method to simulation data we carry out a large number of NVT-simulations along an isotherm (cf. Fig. 6.2). The simulated systems exhibit the same behaviour in the coexistence region as the van der Waals fluid, because they are too small to show phase separation. Cross-sections of simulation snapshots for huge ST systems are shown in Figure 6.4 for  $\mu^2 = 3$  and 36 at critical density and below critical temperature. Both systems evince phase separation, we can see regions with higher and lower density. For

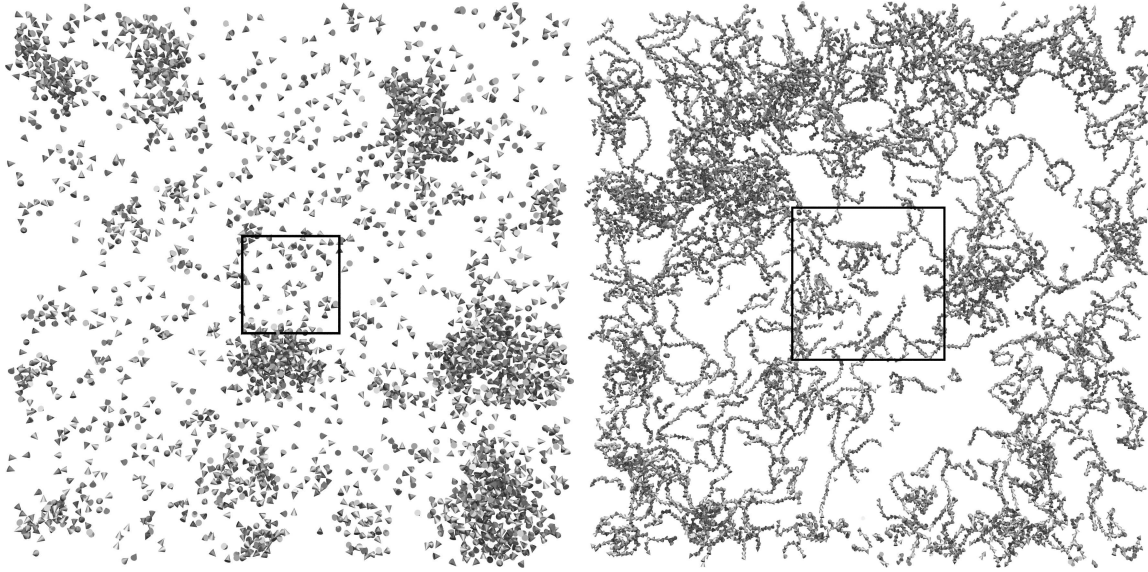


Figure 6.4: Phase separation in huge ST systems with  $\mu^2 = 3$ ,  $T \approx 1.49$ ,  $\rho \approx 0.3$  (left) and  $\mu^2 = 36$ ,  $T \approx 8.3$ ,  $\rho \approx 0.09$  (right), both with particle number  $N = 100000$ . For illustration cross-sections with thickness of some LJ units were taken. The squares indicates the box sizes of simulations done for Maxwell construction.

comparison the size of the simulation boxes, used for Maxwell construction, are indicated by the squares. We can see that the spatial range of the density fluctuation due to phase separation exceed the size of the small boxes, so phase separation cannot proceed. We start with simulations in the very dilute gas phase. Here we have to check carefully if equilibrium is really reached, since this can take more time than getting good averages if chain association occurs. Then the system is compressed gradually and the pressure is averaged after a long enough equilibration time. This is continued till the liquid phase is reached. To preclude hysteresis effects, this procedure is repeated during expansion of the system from the liquid phase to the gas phase. If both van der Waals loops are approximately equal, we do not report the results separately, but average them to get better results. We obtain the analytical equation of state by fitting an adequate function, in general a modification of the van der Waals equation, to the simulation data. For some fitting functions there are no exact solutions of (6.2.7), so we solve the system of equations numerically using Mathematica [16]. Repeating this procedure for a series of temperatures yields the GL coexistence curve.

## 6.2.2 Kofke's thermodynamic integration method

As soon as we have determined the coexistence points for a system of one single temperature, we can also proceed with Kofke's thermodynamic integration method [17, 18] to

determine the phase coexistence curves. With given conditions at a single state point, simultaneous but independent NPT simulations of each phase are performed in succession along the saturation line. In each of both simulations the pressure is adjusted to satisfy the chemical potential equality, according to the Gibbs-Duhem equation for pure substances (gas or liquid) which may be written as

$$N_{g,l} (\beta d\mu_{g,l} + \mu_{g,l} d\beta) = H_{g,l} d\beta + \beta V_{g,l} dP_{g,l}, \quad (6.2.8)$$

where  $N_{g,l}$  is the number of particles,  $\mu_{g,l}$  is the chemical potential,  $H_{g,l}$  the enthalpy,  $V_{g,l}$  the volume and  $P_{g,l}$  the pressure of the respective phases. The reciprocal temperature is given by  $\beta = 1/T$ . If the temperature for two coexisting phases is changed, to remain in equilibrium, the pressure must change in a manner ( $dP_s = dP_g = dP_l$ ) that maintains chemical potential equality between them ( $d\mu_s = d\mu_g = d\mu_l$ ). The required change is obtained by subtracting the two Gibbs-Duhem equations (6.2.8) for the pure phases at the borders of the phase coexistence region

$$0 = (H_g - H_l) d\beta + (V_g - V_l) \beta dP_s, \quad (6.2.9)$$

resulting in the Clausius-Clapeyron relation

$$\frac{dP_s}{d\beta} = -\frac{\Delta H}{\beta \Delta V} \quad (6.2.10)$$

with  $\Delta H = H_g - H_l$  and  $\Delta V = V_g - V_l$ . The subscript  $s$  indicates that the derivative is taken along the saturation line. Practically, for the Kofke integration the equivalent equation

$$\frac{d \ln P_s}{d\beta} = -\frac{\Delta H}{\beta P \Delta V} = f(\beta, P) \quad (6.2.11)$$

is used, because any integration scheme applied would benefit from the slowly varying integrand  $f(\beta, P)$ . We will follow Kofke and use a predictor-corrector integration scheme solving the differential equation  $y' = f(\beta, P)$  with  $y = \ln P$ . Depending on how many former state points are available we will employ the formula from table 6.1 with the best accuracy. As initial values for Kofke integration we use a single state point on the phase coexistence curve obtained by Maxwell construction and do the first integration step with the trapezoid-rule predictor yielding

$$P = P_0 e^{f_0 \Delta \beta}. \quad (6.2.12)$$

Here  $\Delta \beta$  is the step size for the integration scheme in reciprocal temperature. We proceed with two independent NPT simulations at the same pressure, one in the gas phase and one in the liquid phase. The difference in Volumes  $\Delta V$  can be directly obtained from the simulation, the difference in enthalpies  $\Delta H$  can be obtained via the relation

$$H = E + PV, \quad (6.2.13)$$

where  $E$  is the internal energy. For every state point we apply one predictor and one corrector, since these two are already in quite good agreement for the chosen temperature

Table 6.1: Predictor-corrector formulas for the Kofke integration method

Name	Type	n	Formula
Trapezoid	P	1	$y_{i+1} = y_i + \Delta\beta f_i$
	C	1	$y_{i+1} = y_i + \frac{\Delta\beta}{2} (f_{i+1} + f_i)$
Midpoint	P	2	$y_{i+1} = y_{i-1} + 2\Delta\beta f_i$
	C	2	$y_{i+1} = y_{i-1} + \frac{\Delta\beta}{3} (f_{i+1} + 4f_i + f_{i-1})$
Adams	P	4	$y_{i+1} = y_i + \frac{\Delta\beta}{24} (55f_i - 59f_{i-1} + 37f_{i-2} - 9f_{i-3})$
	C	3	$y_{i+1} = y_i + \frac{\Delta\beta}{24} (9f_{i+1} + 19f_i - 5f_{i-1} + f_{i-2})$

steps. In principle the corrector can be applied as often as needed for desired accuracy. After this we can proceed for the next step applying the midpoint-rule, because we have knowledge of two state points along the coexistence curve and so on.

The most successful approach was to start with Kofke integration scheme at an intermediate temperature of the phase coexistence diagram and than calculating two integration paths, one for decreasing temperature and one for increasing temperature towards the critical point.

### 6.2.3 Scaling laws for the critical point

The discussed methods to determine state points on the GL phase coexistence curves both do suffer both from problems near the critical point. In close proximity of the critical point fluctuations, especially in the pressure, become very large. So in the case of the Maxwell construction near the critical temperature, we have to perform very long simulations to get adequate averages for the pressure, at some point this becomes infeasible. A similar problem occurs for the Kofke integration. The large fluctuations in pressure cause large fluctuations in the volumes of the NPT simulations and the instantaneous volume differences  $\Delta V$  of the pure phases can become very small, consequential the simulation volume can jump between both. This can be precluded by increasing the system size, because this increases  $\Delta V$ . The disadvantage of *NPT* simulations of huge particle numbers, however, is the very slow volume averaging which becomes infeasible, too. But even if we are not able to get good results in the vicinity of the critical point, we are able to estimate the location of the critical point based on the coexistence curve as explained below.

This estimate is based on suitable scaling laws [19]. Systems in same universality classes, according to their critical exponents, behave similar at continuous phase transitions, which

can be described by an order parameter, vanishing in the unordered phase and growing spontaneously on approach of the critical point. The different order parameters obey the same scaling functions with the same critical exponents, except for the system dependent amplitudes that relate mathematical scaling laws to physical laws. Fluids near the GL critical point are expected to belong to the universality class of the three dimensional Ising model. This is reasonable, since we can describe a fluid quite well by a lattice model, equivalent to the Ising model, where an up-spin represents lattice sites with microscopic droplets and a down-spin microscopic cavities. These are systems with short-ranged forces and scalar order parameters, here  $\rho_l - \rho_g$ , vanishing at the critical temperature  $T_c$ . Below  $T_c$ ,  $\rho_l - \rho_g$  increases monotonously. Some thermodynamic quantities diverge at the critical point like in this case the heat capacity at constant temperature  $C_v$ .

The scaling laws can be obtained from renormalization group (RG) theory [2, 20]. The critical point is a fixed point with a characteristic 'range of attraction' meaning a range of starting points within which convergence will occur to the particular root. Each fixed point corresponds to one universality class and Hamiltonians with a wide range of parameters will converge to the same fixed point. The RG is a transformation of the original Hamiltonian of a system into a new one with reduced correlation length of the density fluctuations and reduced number of degrees of freedom. The transformation is chosen that the partition function is preserved.

We analyze the phase coexistence data to get an estimate of the critical point using the scaling relations

$$\rho_L - \rho_G \approx A_0 |t|^\beta + A_1 |t|^{\beta+\Delta} \quad (6.2.14)$$

$$(\rho_L + \rho_G)/2 \approx \rho_c + D_0 |t|^{1-\alpha} + D_1 |t| \quad (6.2.15)$$

$$P - P_c \approx P_0 |t| + P_1 |t|^{2-\alpha} + P_2 |t|^2, \quad (6.2.16)$$

with  $t = (T - T_c)/T_c$  [21], in conjunction with the 3D-Ising values of the critical exponents  $\alpha \approx 0.110$ ,  $\beta \approx 0.326$  and  $\Delta \approx 0.5$  [22] to extract the critical point parameters.

## 6.3 Results for gas-liquid coexistence from molecular dynamics

### 6.3.1 The non polarizable case

In Figure 6.5 we compare results for GL coexistence curves obtained by Maxwell construction for this work with data obtained by GEMC in [23–25] for the ST fluid with dipole strengths in the range  $\mu^2 = 1$  to 5. For  $\mu^2 = 1$  to 4 we simulated  $N = 216$  particles, for  $\mu^2 = 5$  both  $N = 216$  and  $N = 512$  (large symbols). We chose a time step of  $t = 0.006$  and cut off radius  $r_{cut} = 3$ , except for  $\mu^2 = 5$  and  $N = 512$  where we chose  $r_{cut} = 4.5$  which

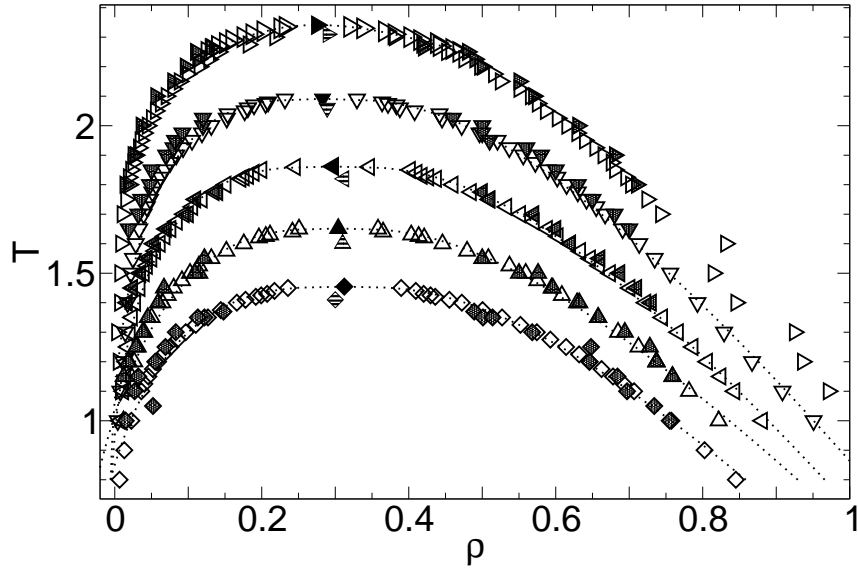


Figure 6.5: Comparison of the results for GL coexistence curves in the  $T$ - $\rho$  plane from the Maxwell construction method (hollow symbols) with results from the GEMC method [23–25] (shaded symbols) for dipole strengths  $\mu^2 = 1$  (diamonds), 2 (up-triangles), 3 (left-triangles), 4 (down-triangles) and 5 (right-triangles). The solid symbols indicate the critical points obtained from Maxwell construction and the striped symbols the ones obtained from GEMC.

changed the results only slightly. The GEMC results were obtained by simulations with particle numbers  $N = 216$  and  $N = 512$ , comparable to the ones we have chosen. Long-range corrections were calculated with Ewald summation, contrary to the reaction field method we used. Nevertheless the results are in good agreement with each other. Only in the gas phase the densities of GEMC seem to be systematically lower, but they are still in an acceptable range. The critical temperatures obtained by the GEMC data with the same scaling laws we employed, are systematically lower than the critical points obtained by Maxwell construction. This is rather an effect of the low temperatures used for the critical point scaling in GEMC, with the NVT simulations for Maxwell construction we were able to approach much closer to the critical temperature. It is worth mentioning that all simulation methods may suffer from problems in the vicinity of the critical point due to the finite size of the simulation box, which may suppress critical fluctuations.

Furthermore, in figure 6.6 we compare the results from Maxwell construction for  $\mu^2 = 5$  and 16 to corresponding results obtained via thermodynamic integration using Kofke's method. In addition we vary the system size  $N$  and in the case of thermodynamic integration the temperature increment  $\Delta T$ . The coexistence curves thus obtained for selected fixed dipole strengths are in close accord. Systems with  $\mu^2 = 16$  were simulated with a time step  $t = 0.004$  and cut off radius  $r_{cut} = 5$ . For this dipole strength we were able to determine coexistence curves by Kofke's method for much lower temperatures than with

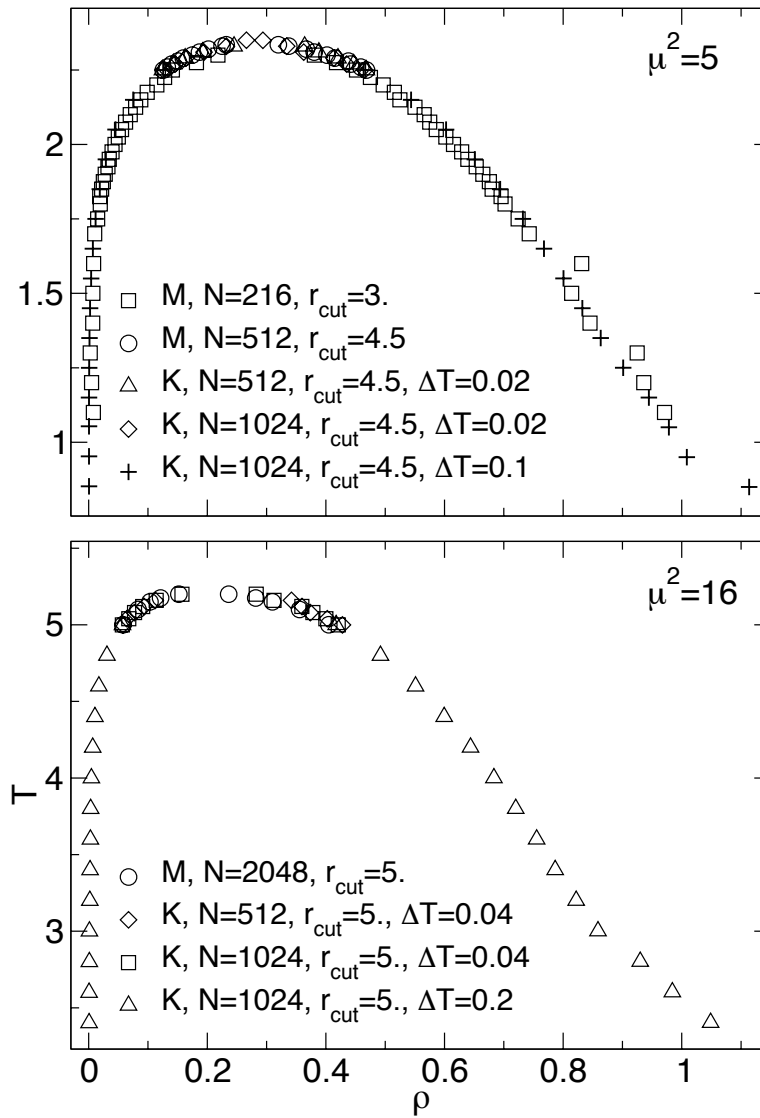


Figure 6.6: Binodal lines in the  $T$ - $\rho$  plane for  $\mu^2 = 5$  (top) and 16 (bottom). Comparison of Maxwell construction (M) and Kofke Integration (K) for different particle numbers  $N$  and in the case of Kofke integration different temperatures increments  $\Delta T$ .

Maxwell construction. Figure 6.7 shows the logarithmic saturation pressure for these

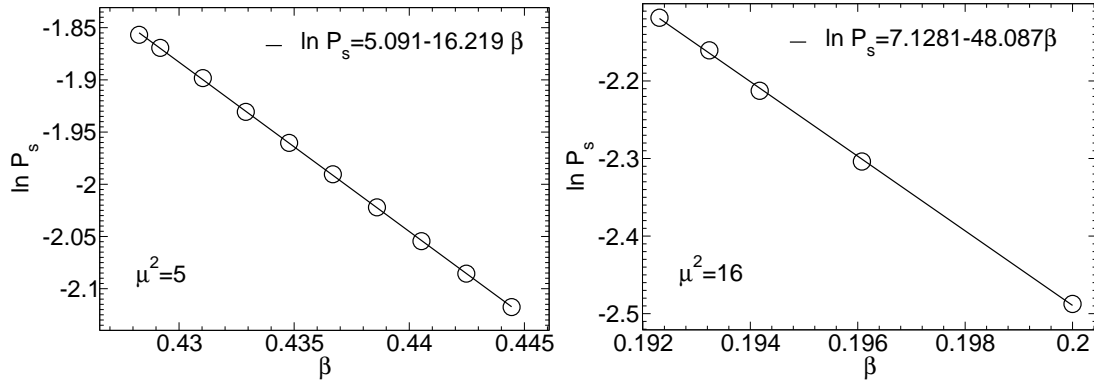


Figure 6.7: Logarithmic saturation pressure  $\ln P_s$  versus reciprocal temperature  $\beta$  for  $\mu^2 = 5$ ,  $N = 512$ ,  $r_{cut} = 4.5$  (left) and  $\mu^2 = 16$ ,  $N = 2048$ ,  $r_{cut} = 5$  (right) obtained from Maxwell construction. The indicated formulas are fits to the data and used to calculate initial pressures for Kofke integration.

systems obtained from Maxwell construction. Initial values for Kofke integration are calculated from the indicated formulas, which are linear fits to the data, to get more averaged values than only from one Maxwell construction. Additionally, this gives a justification of the use of the logarithmic form of the Clausius-Clapeyron equation (6.2.11). The logarithmic saturation pressure depends linear on the reciprocal temperature  $\beta$ . The nematic order parameter  $q_{nem}$  from Kofke integration for the coexistence curve on the liquid side is shown in figure 6.8. For decreasing temperature  $q_{nem}$  raises at  $T/T_c \lesssim 0.55$ . Notice that here  $T_c$  is again the GL critical temperature. The reduced transition temperature seems to be universal.

We tried also to obtain results for coexistence curves via Kofke integration for  $\mu^2 = 30$  and 36, but this turned out to be impracticable, because averaging the volumes from NPT simulations for systems with long chains turned out to be prohibitively time consuming.

Figure 6.9 compiles coexistence curves for dipole strengths in the range from  $\mu^2 = 0$  to 36 in LJ and in the range from  $\mu^2 = 0$  to 60 in critical units obtained via Maxwell construction. Numerical values for critical temperatures and densities are listed in Table 6.2. Simulations for  $\mu^2 = 30$  and 36 were performed with  $N = 2048$ ,  $t = 0.002$  and  $r_{cut} = 7$ , simulations for  $\mu^2 = 60$  with  $N = 2048$ ,  $t = 0.002$  and  $r_{cut} = 10.5$  unless stated otherwise. As fit function for the van der Waals loop was used in the range  $\mu^2 = 0$  to 4

$$P = \frac{NT}{V-b} - \frac{a}{V^{2-\nu}}, \quad (6.3.1)$$

in the range  $\mu^2 = 5$  to 36

$$P = \frac{NT}{V-b} - \frac{a}{V^{2-\nu}} + c \quad (6.3.2)$$

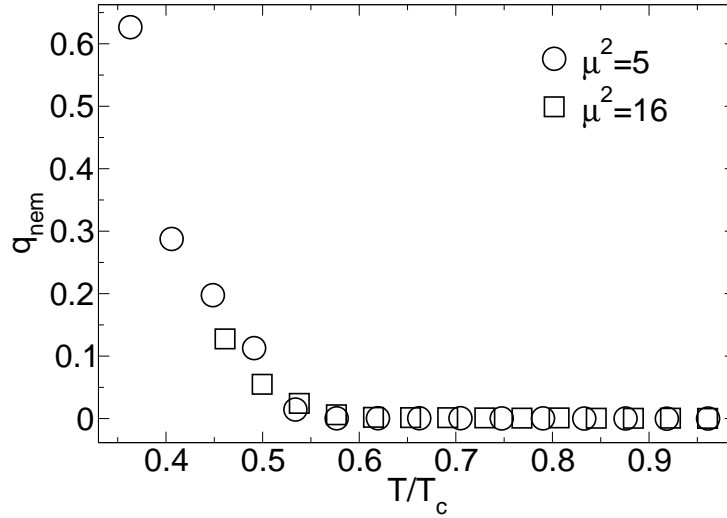


Figure 6.8: Nematic order parameter  $q_{nem}$  from simulations for Kofke integration with  $\mu^2 = 5$ ,  $N = 1024$  and  $\mu^2 = 16$ ,  $N = 1024$  in the liquid phase. For decreasing temperature ( $T/T_c \lesssim 0.55$ )  $q_{nem}$  is increasing.

and for  $\mu^2 = 60$

$$P = \frac{NT}{(V-b)^d} - \frac{a}{V^{2-\nu}}. \quad (6.3.3)$$

Here  $a$ ,  $b$ ,  $c$ ,  $d$  and  $\nu$  are fit parameters. The dashed coexistence curves in figure 6.9 are obtained by the fits for the critical point (cf. equation (6.2.14) and (6.2.15)) with

$$\rho_g = \rho_c - \frac{1}{2}A_0 t^\beta - \frac{1}{2}A_1 t^{\beta+\Delta} + D_0 t^{1-\alpha} + D_1 t \quad (6.3.4)$$

$$\rho_l = \rho_c + \frac{1}{2}A_0 t^\beta + \frac{1}{2}A_1 t^{\beta+\Delta} + D_0 t^{1-\alpha} + D_1 t. \quad (6.3.5)$$

We notice that the critical temperature obtained for the LJ system is slightly higher than most values found in literature (between 1.31 to 1.32). Possibly the equal area construction based on a simple equation of state, like the van der Waals equation or modifications of the van der Waals equation, overemphasizes the occurrence of the pressure loop. On the other hand with the NVT simulations we are able to get results much closer to the critical temperature than with with the GEMC method, because two box simulation methods suffer from switching phases in the boxes in the vicinity of the critical point. This can be avoided by increasing the system size, as done for the Kofke integrations. Nevertheless, this effect is small compared to the dependence of the GL critical temperature on  $\mu^2$  in the range studied. The bottom panel in figure 6.9 shows the coexistence curves in critical units  $T/T_c$  and  $\rho/\rho_c$  to point out the deviation from the principle of corresponding states, which claims that all substances obey the same equation of state if expressed in critical units [26], with increasing dipole strength. We can confirm the observations in [25] for  $\mu^2 = 0$  to 5 that the deviation from corresponding states behaviour for the ST fluid is

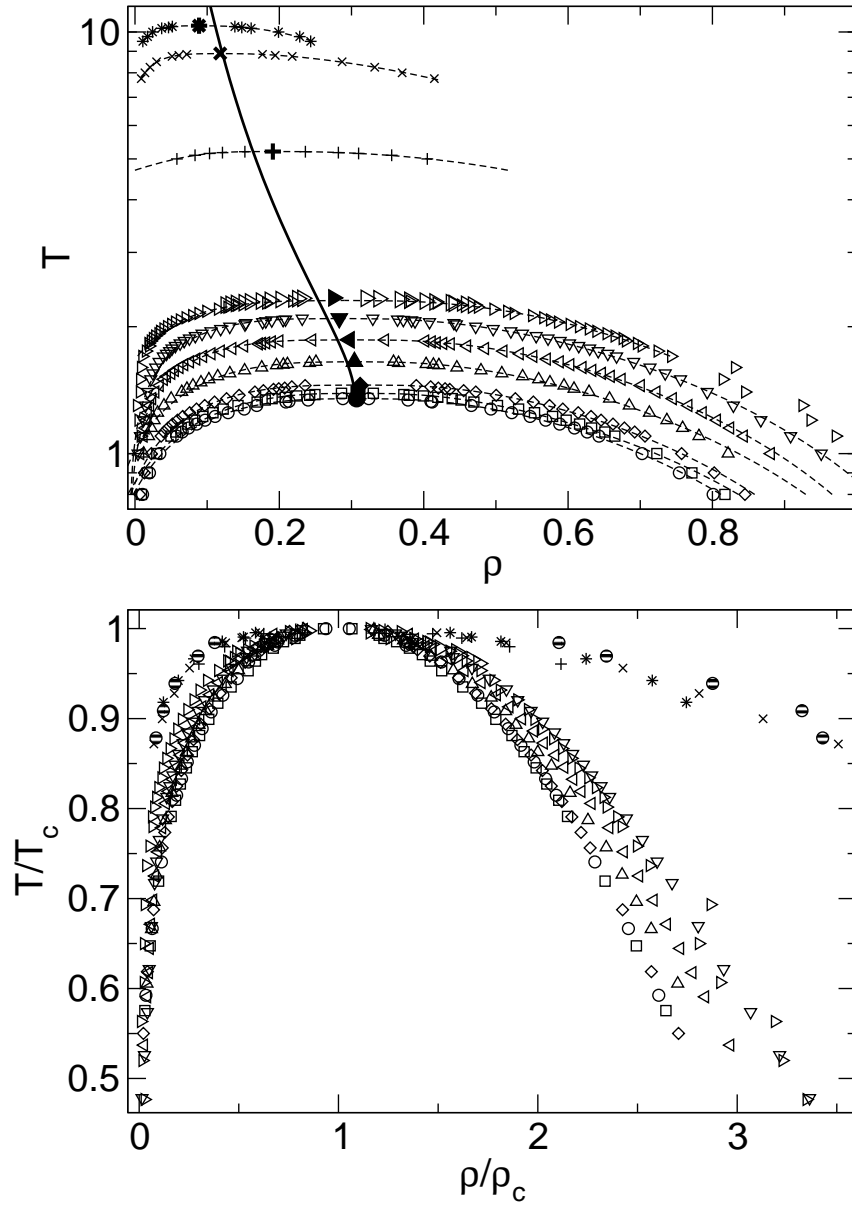


Figure 6.9: GL coexistence curves in the  $T$ - $\rho$  plane obtained by Maxwell Construction for  $\mu^2 = 0$  (hollow circles), 0.5 (squares), 1.0 (diamonds), 2.0 (up-triangles), 3.0 (left-triangles), 4.0 (down-triangles), 5.0 (right-triangles), 16 (pluses), 30 (crosses), 36 (stars) and 60 (striped circles). In the top panel fat symbols indicate the position of the critical point. The dashed lines are fits obtained via equations (6.3.4) and (6.3.5). The solid line shows the shift of the critical point as obtained by a lattice theory, discussed in chapter 7. Bottom: Same as above in critical units to show the deviation from the principle of corresponding states with increasing dipole strength.

Table 6.2: GL critical parameters for the ST system and the pST system obtained by the scaling relations (6.2.14)-(6.2.16).

$\mu^2$	$\alpha$	$T_c$	$\rho_c$	$P_c$
0	0.00	1.35	0.307	0.147
0.5	0.00	1.39	0.309	0.156
1	0.00	1.45	0.3123	0.158
2	0.00	1.65	0.304	0.168
3	0.00	1.86	0.297	0.170
4	0.00	2.09	0.283	0.170
5	0.00	2.34	0.275	0.159
16	0.00	5.20	0.191	0.121
30	0.00	8.89	0.118	0.0668
36	0.00	10.35	0.089	0.0439
60	0.00	16.51	0.0249	0.0133
1	0.02	1.48	0.297	0.160
1	0.04	1.50	0.308	0.160
1	0.06	1.53	0.307	0.162
1	0.08	1.58	0.308	0.175
2	0.02	1.69	0.307	0.164
2	0.04	1.76	0.316	0.174
2	0.06	1.85	0.310	0.189
2	0.08	1.95	0.321	0.203
3	0.02	1.95	0.297	0.175
3	0.04	2.07	0.303	0.186
3	0.06	2.22	0.304	0.210
3	0.08	2.43	0.322	0.240

in the direction of higher liquid densities and near the critical region in the direction of slightly lower gas densities. The stronger the dipole moment, the larger is the deviation. Beyond the observations in [25], it seems that for large dipole strengths there is a limiting curve, at least on the gas side, since the results for  $\mu^2 = 16, 30, 36$  and  $60$  appear to scatter around the same line. On the liquid side the investigated density range is too small to make a judgement.

Figure 6.10 shows the coexistence curves for  $\mu^2 = 30, 36$  (top panel) and  $60$  (bottom panel) in detail. For increasing dipole strength the maximum around the critical point becomes much sharper in density. Contrary to smaller dipole strengths the coexistence curve for  $\mu^2 = 36$  seems to intersect in its extension with the one for  $\mu^2 = 30$ . To justify the choice of the cut off radius  $r_{cut} = 10.5$  used for  $\mu^2 = 60$ , we show in figure 6.11 the DD correlation function  $\langle \vec{\mu}(0) \cdot \vec{\mu}(r) \rangle / \mu^2$  and the radial pair distribution function  $g_2(r)$  for densities  $\rho = 0.0005$  (start of the isotherm for Maxwell construction) and  $\rho = 0.14$

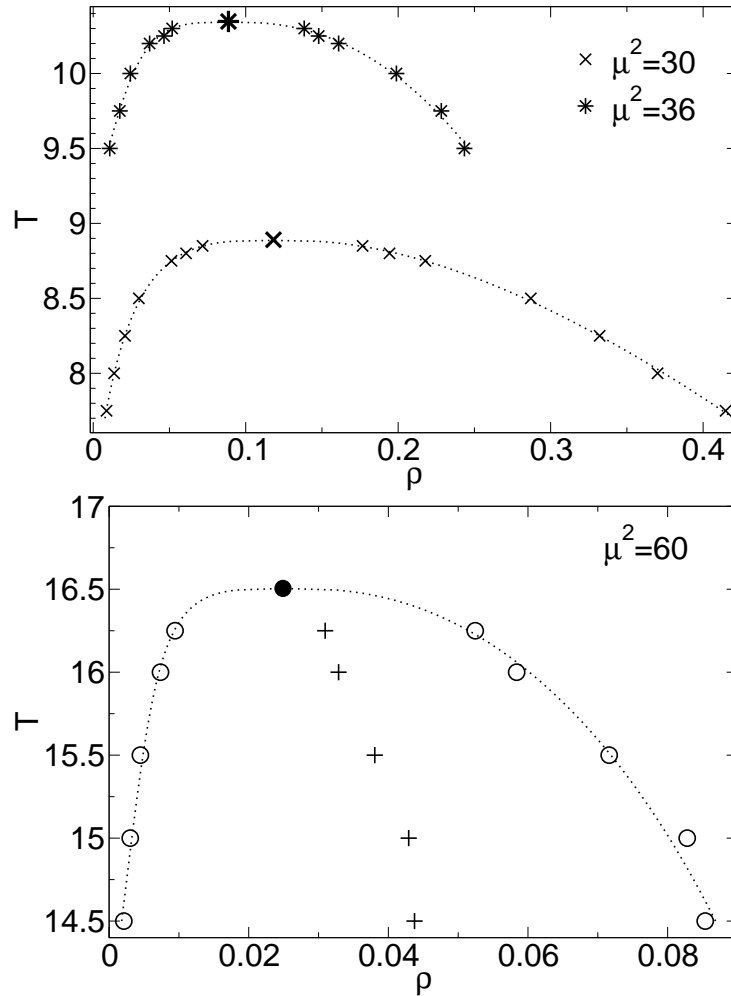


Figure 6.10: GL coexistence curves for  $\mu^2 = 30, 36$  (top) and  $60$  (bottom) from Maxwell construction in detail. The pluses in the bottom figure indicate  $(\rho_g + \rho_l)/2$ .

(end of the isotherm) at temperature  $T = 14.5$ . For the higher density the cut off is much larger than the correlation length in both the dipole orientations and radial pair distribution. Contrary, in the very dilute phase the correlation lengths are similar to  $10.5$ . The slowly declining tail of the radial pair distribution is typical for clusters of comparable size as the correlation length. The negative tail of the DD correlation function is a consequence of rings as predominant cluster species (cf. figure 6.12). For an ideal ring the DD correlation of particles on opposite sites is negative. This behaviour was not observed for the other dipole strengths. Figure 6.13 shows a check of an isotherm with  $\mu^2 = 60$  for finite size effects. For different particle numbers,  $N = 2048$  and  $10000$ , the pressure must be printed versus density to compare the systems, since the volume is not invariant under particle number changes. The solid line is a fit obtained for  $N = 2048$  via equation (6.3.3). We see no significant deviations of the two curves which cannot

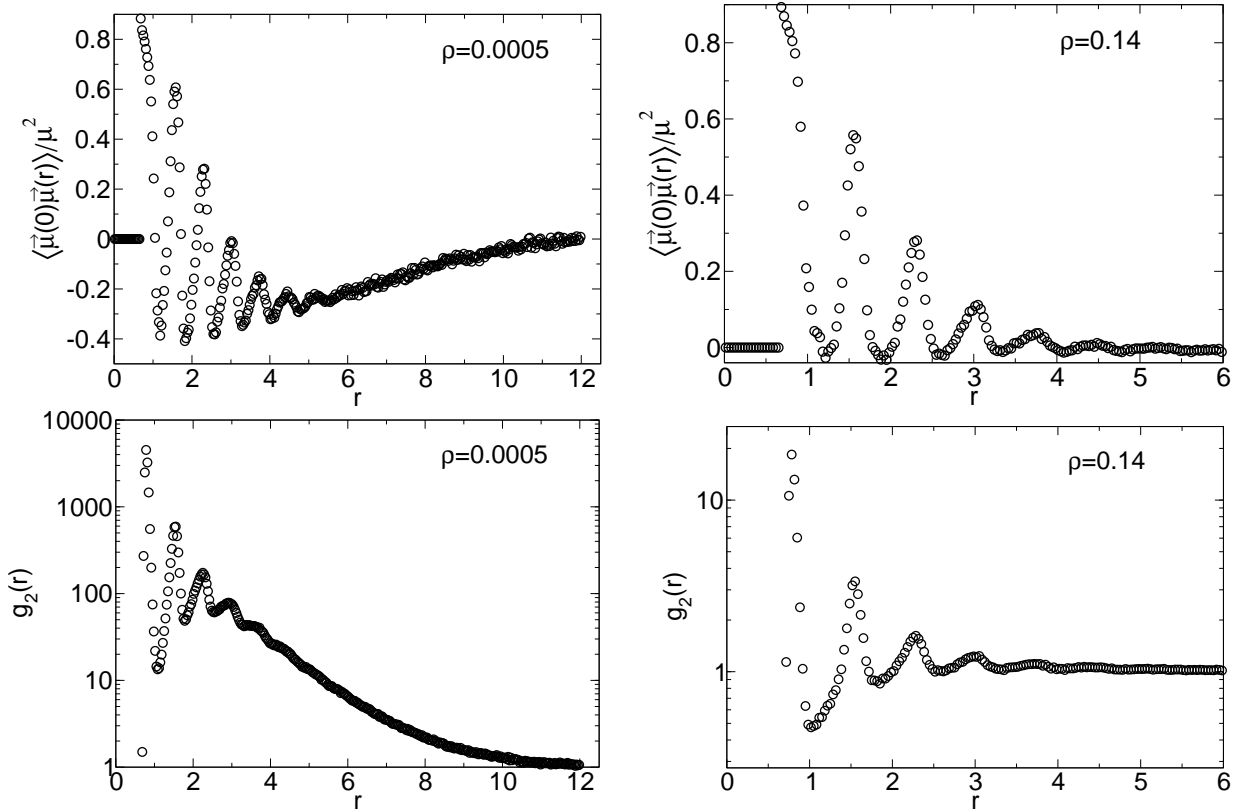


Figure 6.11: DD correlation  $\langle \vec{\mu}(0) \cdot \vec{\mu}(r) \rangle / \mu^2$  (top) and radial pair distribution function  $g_2(r)$  (bottom) for  $\mu^2 = 60$  and the indicated densities  $\rho$  at  $T = 14.5$ . The choice of  $r_{cut} = 10.5$  seems to be sufficient for the correlation functions. In the very dilute phase the correlations seem to be more long-ranged due to chain formation.

be explained with statistical scattering. To perform simulations with  $N = 10000$  and  $\mu^2 = 60$  is an enormous computational task. Getting good averages for the 6 points with  $N = 10000$  took even longer time than simulating the whole isotherm for  $N = 2048$ . A number of isotherms for ST systems with  $\mu^2 = 5, 16, 30, 36$  and  $60$  obtained from NVT simulations are shown in figure 6.14. For  $\mu^2 = 5$  the system with particle number  $N = 512$  is presented, the rest for parameters already mentioned above. The symbols indicate the simulation results, the solid lines the fits to equations (6.3.2) and (6.3.3). For some systems there are large deviations of the fitting and simulation data in the very dilute phase. This is for our purpose irrelevant, since for Maxwell construction we need a good fit only in the phase coexistence region. For increasing temperature the pressure is also increasing as indicated by the arrows. The plotted isotherms correspond to temperatures  $T = 2.25, 2.26, 2.27, 2.28, 2.29, 2.3, 2.31, 2.32, 2.33, 2.335, 2.34$  for  $\mu^2 = 5$ ,  $T = 5, 5.1, 5.15, 5.175, 5.2, 5.225, 5.25, 5.3$  for  $\mu^2 = 16$ ,  $T = 7.75, 8, 8.25, 8.5, 8.75, 8.8, 8.85, 9, 9.25$  for  $\mu^2 = 30$ ,  $T = 9.5, 9.75, 10, 10.2, 10.25, 10.3, 10.5$  for  $\mu^2 = 36$  and  $T = 14.5, 15, 15.5, 16, 16.25, 16.5$  for  $\mu^2 = 60$ .

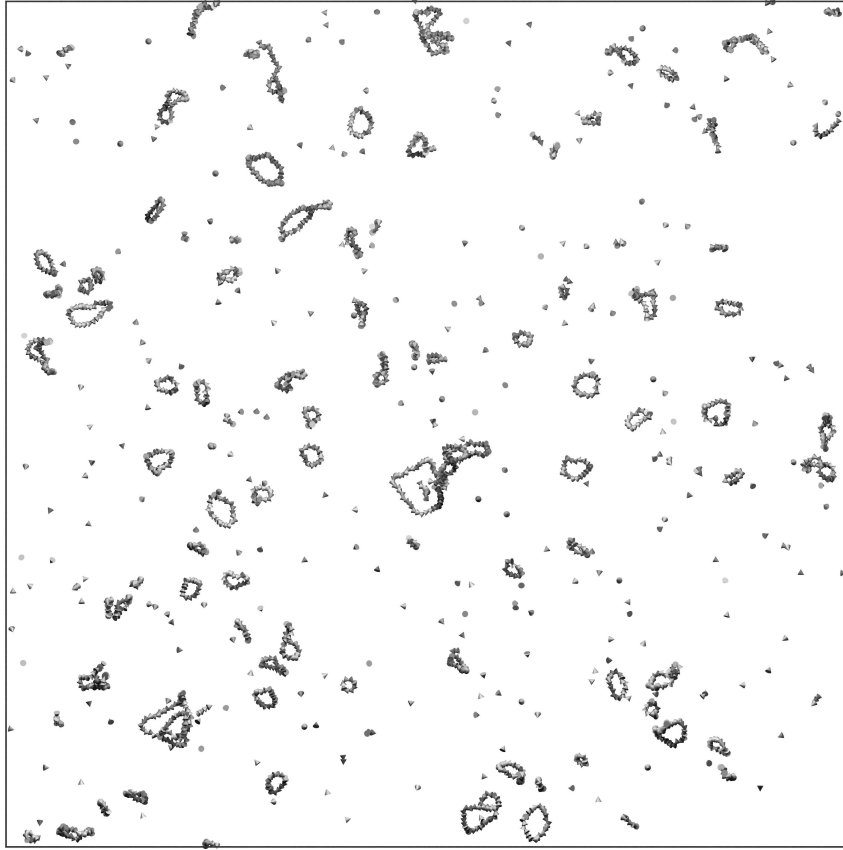


Figure 6.12: Simulation snapshot for a system with  $\mu^2 = 60$ ,  $\rho = 0.0005$  and  $T = 14.5$ . At these system parameters rings are the predominant cluster species. Contrary to other snapshots shown in this work, perspective depth has been removed due to the huge simulation box.

The nematic order parameter  $q_{nem}$  versus density  $\rho$  of isotherms for a system with  $\mu^2 = 4$  and  $N = 216$  are shown in figure 6.15. The arrow indicates increasing temperature. The binodal lies for  $T = 1$  at  $\rho_l \approx 0.95$ . With Maxwell construction we reach only state points on the binodal with beginning ferroelectric ordering. The two lower panels show the radial pair distribution function  $g_2(r)$  and the DD correlation function  $\langle \vec{\mu}(0) \cdot \vec{\mu}(r) \rangle / \mu^2$  for this system at density  $\rho = 1$  and particle number  $N = 2048$  for three temperatures:  $T = 1$  with the largest appearing  $q_{nem}$ ,  $T = 1.5$  with a very small  $q_{nem}$  and from the not in the top panel given temperature  $T = 2$ , where the average of  $q_{nem}$  is exactly zero. For the correlation functions we chose simulations with larger particle number to be able to print  $g_2(r)$  and  $\langle \vec{\mu}(0) \cdot \vec{\mu}(r) \rangle / \mu^2$  for a larger range of separations. The radial distribution function looks similar for all temperatures with only small deviations in the amplitude of the maxima and minima. The DD correlation function behaves different. Here we can see clearly the increasing correlation for decreasing temperature. For  $T = 1$ , where we find  $q_{nem} \approx 0.24$ , the DD correlation is not longer vanishing for the long-range limit. The

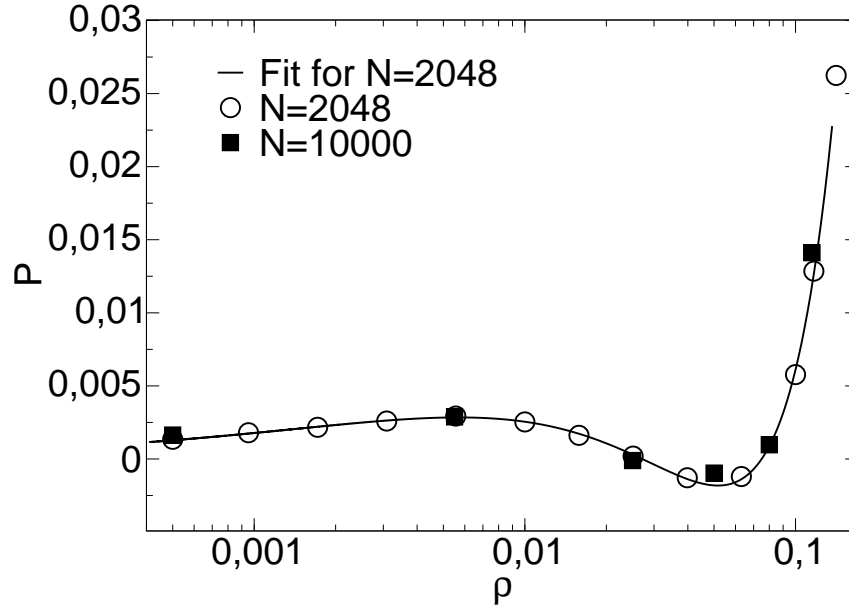


Figure 6.13: Isotherm for  $\mu^2 = 60$  for different particle numbers. Here pressure versus density is plotted, since the volume is not invariant under particle number changes. The fit is obtained via equation (6.3.3)

correlations are propagating through the whole simulation box. For large dipole moments  $\mu^2 = 16, 30$  and  $36$  the Maxwell construction fails for parameters where ferroelectric ordering should appear. To determine the ferroelectric transition on the binodal, the Kofke integration seems to be the method of choice (cf. fig. 6.8), but this becomes difficult for large dipole moments ( $\mu^2 = 16$ ), too.

### 6.3.2 Checking the cut off radius

Up to now we have chosen different cut offs  $r_{cut}$  for systems with different dipole strengths without justifying the particular choice, except for the radial pair distribution function and the DD correlation. In practice we have chosen some single state points and increased  $r_{cut}$  until the pressure reached a limit. By this method we have shown that the cut off is sufficient at this particular state point, but we cannot assume that this holds for the whole coexistence region offhand. So we investigate the influence of the cut off on one isotherm in some more detail. Figure 6.16 shows isotherms for a system with  $\mu^2 = 30$  and  $N = 2048$  at temperature  $T = 8.75$  for three different cut offs  $r_{cut} = 4, 7$  and  $9$ . The smallest cut off,  $r_{cut} = 4$ , is definitely not sufficient to calculate the phase boundaries. The cut offs  $r_{cut} = 7$  and  $9$  are in good accordance in the pure phases and metastable regions ( $\partial P/\partial \rho|_T > 0$ ), in the mechanical unstable region ( $\partial P/\partial \rho|_T < 0$ ) they differ.

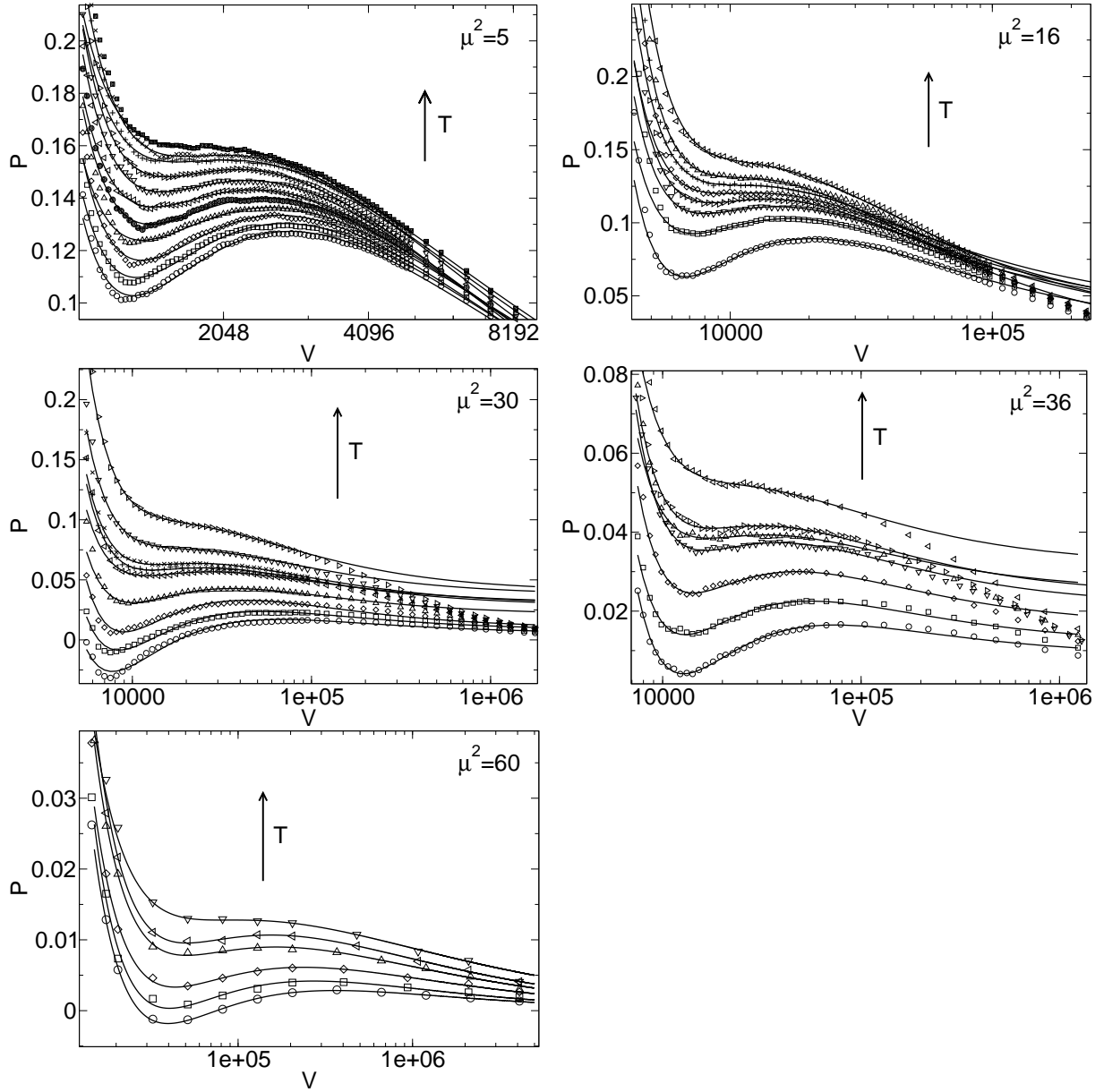


Figure 6.14: Isotherms (pressure vs. volume) for dipole strengths  $\mu^2 = 5, 16, 30, 36$  and  $60$  from NVT simulations from which phase boundaries are determined via Maxwell construction. The solid lines are fits to the simulation data corresponding to equation (6.3.1) to (6.3.3). The arrows indicate direction of increasing temperature. The deviations of the fits to the simulation data in the very dilute phase are irrelevant, since we are only interested in the phase coexistence region.

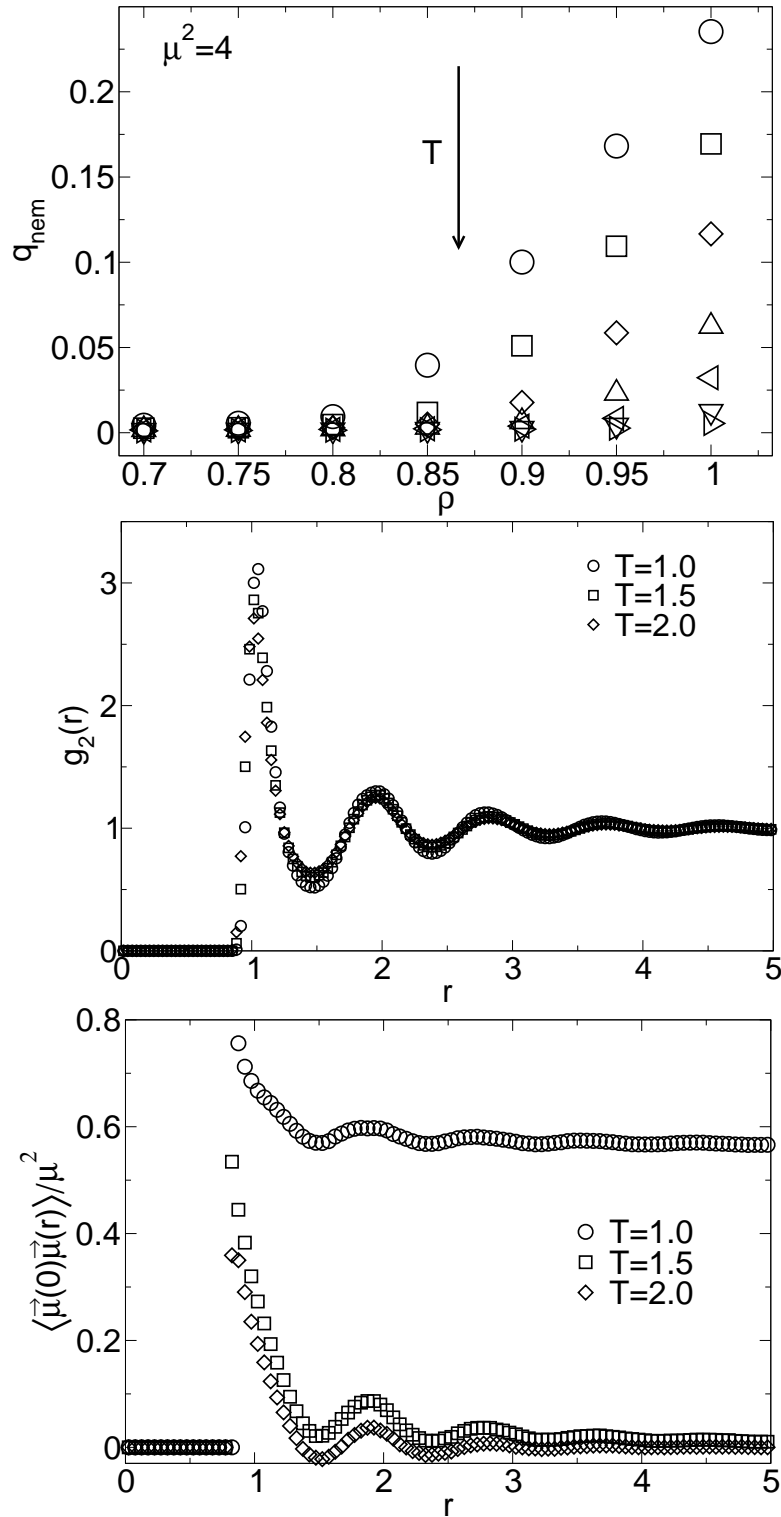


Figure 6.15: Nematic order parameter  $q_{nem}$  versus particle number density  $\rho$  for  $\mu^2 = 4$  and  $N = 216$ . The radial distribution function  $g_2(r)$  and DD correlation  $\langle \vec{\mu}(0) \cdot \vec{\mu}(r) \rangle / \mu^2$  are shown for  $N = 2048$ . In the top panel the arrow indicates increasing temperature  $T = 1, 1.1, 1.2, 1.3, 1.4, 1.5$  and  $1.6$ . The to lower panels are obtained from simulations for  $\rho = 1$ .

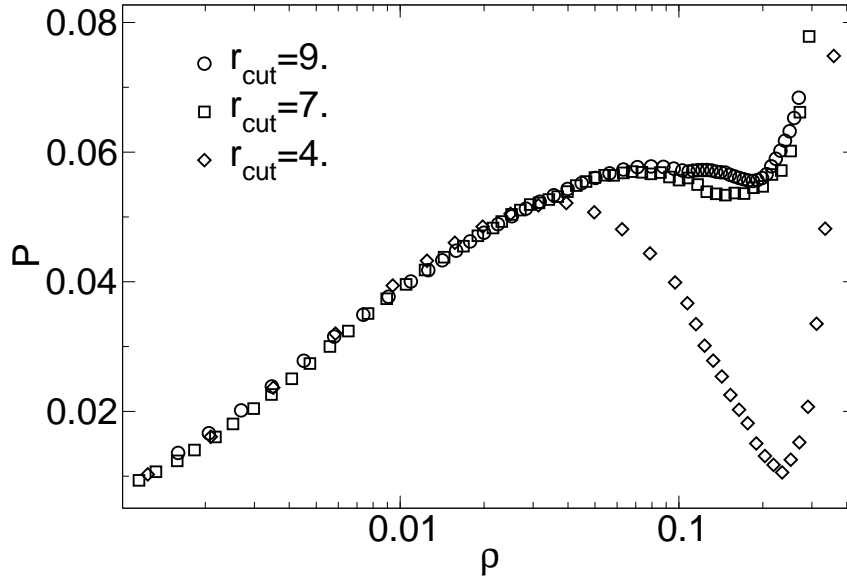


Figure 6.16: Comparison of isotherms for a system with  $\mu^2 = 30$ ,  $N = 2048$  and  $T = 8.75$  for different cut offs  $r_{cut} = 4, 7$  and  $9$

This difference appears a little bit shady, the van der Waals loop for  $r_{cut} = 7$  looks better than for  $r_{cut} = 9$  whose shape looks untypical. This can be due to equilibration problems, the simulation of the isotherm for  $r_{cut} = 9$  took several times as long as for  $r_{cut} = 7$ . In figure 6.17 we compare the radial distribution function  $g_2(r)$  and the DD correlation for the different cut offs at density  $\rho = 0.001$ . There are no noticeable deviations. So to check the correlation functions is not enough to choose a sufficient cut off. In figure 6.18 we compare the average chain lengths  $n$  and fraction numbers  $h$  of species for cut offs  $r_{cut} = 4, 7$  and  $9$ . Here we can see no significant deviations, too. The choice of the cut off has no effect on the cluster structure of the system, in all linear chains are predominant. We can conclude that the choice of the cut off has no influence on the structure of the system. We see deviations in pressure for the cut off which we used to calculate the phase boundaries and a larger one in the mechanical unstable region. We were not able to investigate this in more detail due to the enormous computational effort necessary for  $r_{cut} = 9$ . To find out if  $r_{cut} = 7$  for  $\mu^2 = 30$  and  $36$  is sufficient or not to determine the phase boundaries adequately, may be a task for the future.

### 6.3.3 The polarizable case

Figure 6.19 compiles GL coexistence curves for the pST model, we obtained at fixed dipole moment  $\mu^2 = 1$  and point polarizabilities  $\alpha = 0, 0.02, 0.04, 0.06$  and  $0.08$  using again the Maxwell construction method, in comparison with data obtained by GCMC in [27]. For

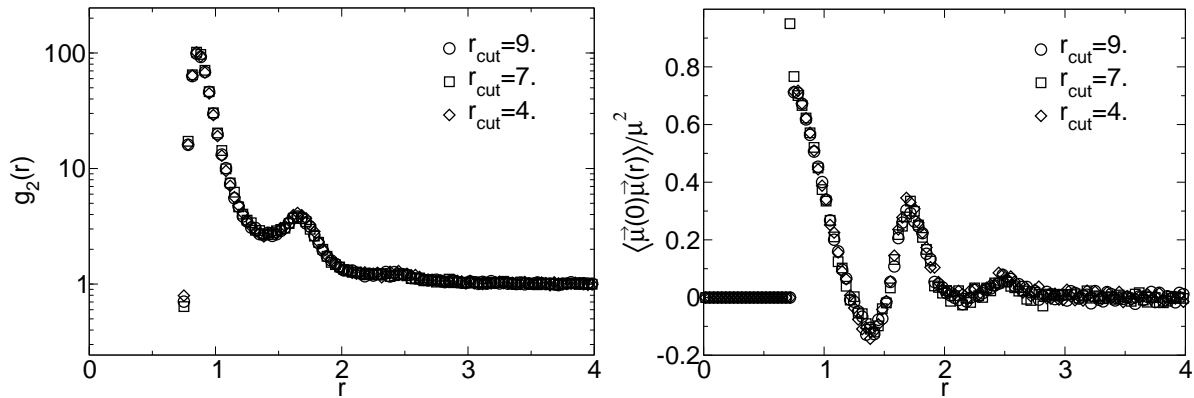


Figure 6.17: The radial pair distribution function  $g_2(r)$  and the DD correlation function  $\langle \vec{\mu}(0) \cdot \vec{\mu}(r) \rangle / \mu^2$  for  $\mu^2 = 30$ ,  $N = 2048$ ,  $T = 8.75$  and  $\rho = 0.001$  for different cut offs  $r_{cut} = 4, 7$  and  $9$ .

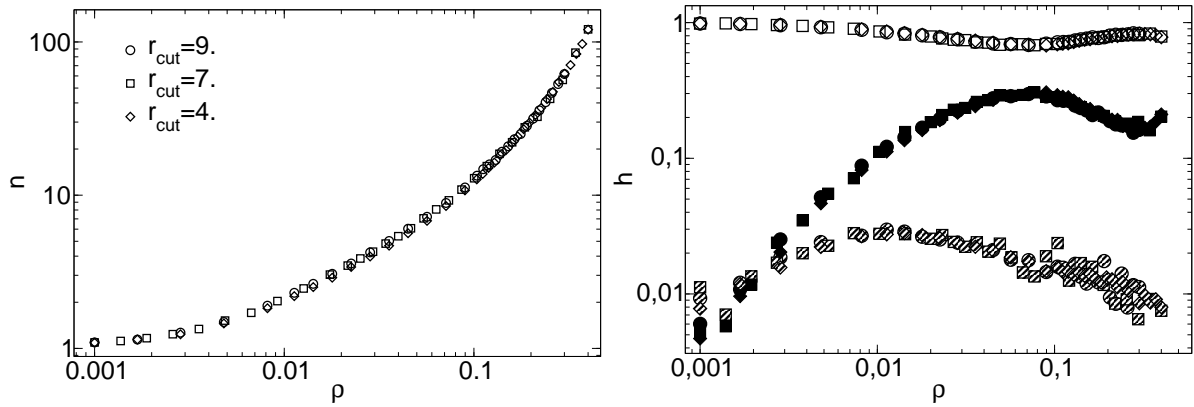


Figure 6.18: Average chain length  $n$  and number fraction of the different species  $h$  vs. density for  $\mu^2 = 30$ ,  $N = 2048$ ,  $T = 8.75$  and different cut off distances  $r_{cut} = 4, 7$  and  $9$ . In the right panel the hollow symbols indicate chains, the striped symbols rings and the filled symbols mutants.

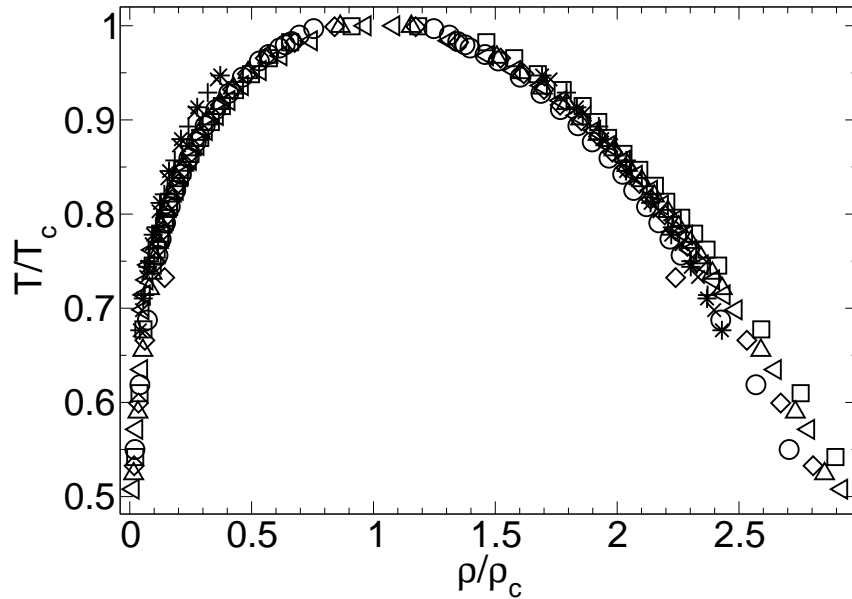


Figure 6.19: GL coexistence curves in critical units for the pST fluid with  $\mu^2 = 1$  and polarizabilities  $\alpha = 0$  (circles), 0.02 (squares), 0.04 (diamonds), 0.06 (up-triangles), 0.08 (left-triangles) via Maxwell construction in comparison with data from GCMC [27] for  $\alpha = 0$  (Pluses),  $\alpha = 0.03$  (crosses) and  $\alpha = 0.06$  (stars).

this case we give the phase diagram only in critical units since the deviations for different polarizabilities are too small. For our data there seems to be no deviations from the principle of corresponding states larger than the statistical scattering for different values of  $\alpha$ . Our data differs slightly from the data given in [27] in the gas phase. This is most likely due to the different critical points which are given for the GCMC data by  $T_c = 1.4$ ,  $\rho_c = 0.318$  for  $\alpha = 0$ ,  $T_c = 1.432$ ,  $\rho_c = 0.322$  for  $\alpha = 0.03$  and  $T_c = 1.478$ ,  $\rho_c = 0.328$  for  $\alpha = 0.06$ . We provide data much closer to the the critical point, so differences in the fits for the critical points are not surprising. For  $\mu^2 = 2$  and 3 the coexistence curves are shown in figure 6.20 in LJ and critical units. Here the polarization causes no obvious deviations from the principle of corresponding states, too, despite the polarizability causes a strong increase of the critical temperatures for  $\mu^2 = 2$  and 3. A possible reason for this may be the isotropic form of the polarizability. On the other hand the range of investigated densities and temperatures may be too small for significant deviations. The critical parameters are listed in Table 6.2.

### 6.3.4 Gas-liquid transition for the dipolar soft sphere fluid

In this subsection we will have a short look at the phase behaviour of the DSS fluid. Whether or not the similar DHS fluid exhibits a GL phase transition has been discussed

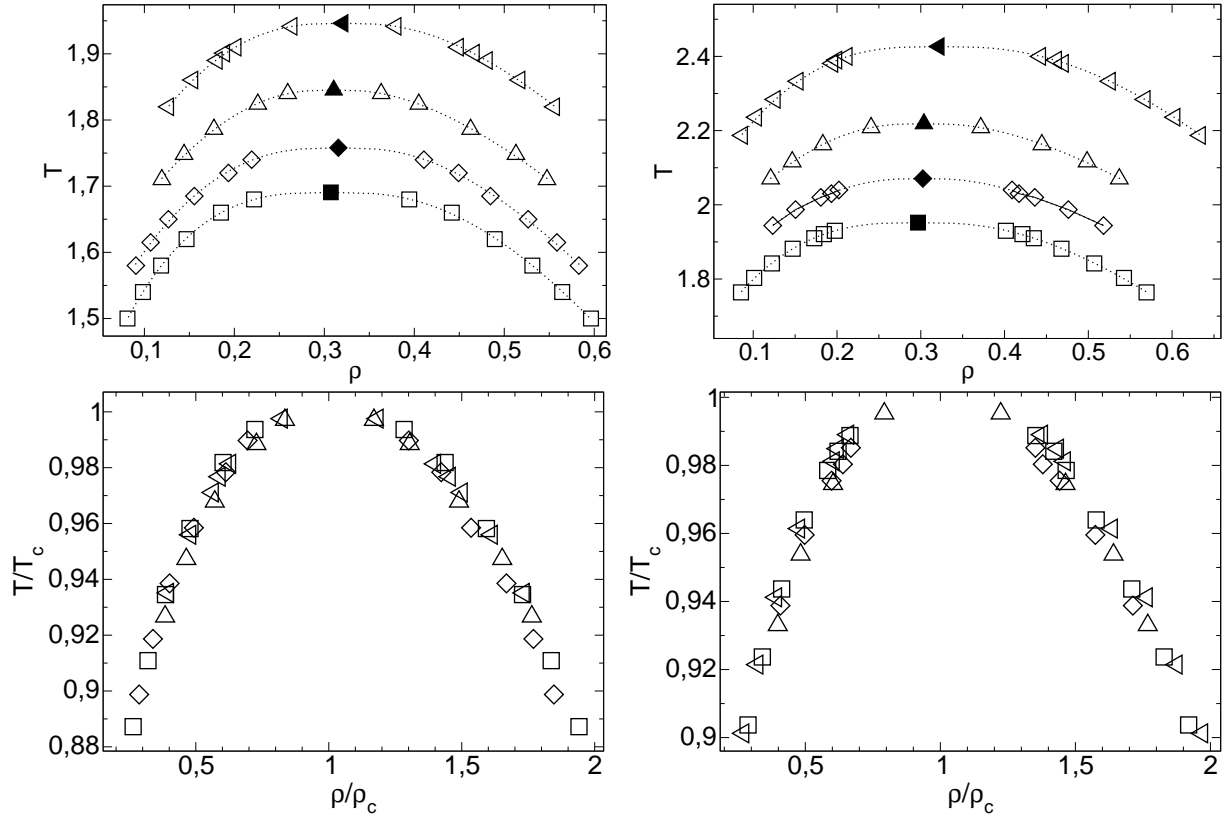


Figure 6.20: GL coexistence curves for the pST fluid for  $\mu^2 = 2$  (left) and 3 (right). The different polarizabilities  $\alpha$  are indicated by the same symbols as in figure 6.19. Filled symbols indicate the critical point. The bottom figures are in critical units and show the principal of corresponding states.

frequently in literature [9, 28–32] and is still a matter of debate [4, 5]. We will investigate isotherms of the DSS fluid in a region where a GL phase transition for the DHS fluid was claimed based on NPT and GCMC simulations. The critical point for a DHS fluid should lie in our units at  $T_c \approx 1.14$  and  $\rho_c \approx 0.1$  for  $\mu^2 = 7.563$  [31, 32].

Figure 6.21 shows in the top panel isotherms (pressure vs. density) at temperature  $T = 1$ , clearly below the expected critical temperature, for the DSS fluid with  $\mu^2 = 7.563$  for different cut off distances  $r_{cut}$  and different particle numbers  $N$ . We see that the isotherms do not depend on the particle number. For  $N = 512$  and 2048 with the same cut off the isotherms are in good agreement. Contrary, the isotherms of the DSS fluid depend strongly on the chosen cut off at the given simulation parameters. While the isotherms for  $r_{cut} = 7$  show an obvious van der Waals loop, the isotherms for  $r_{cut} = 9$  show only an inflection point or perhaps a very weak van der Waals loop, the isotherm for  $r_{cut} = 11$  shows no van der Waals loop at all. So for these parameters the occurrence of a van der Waals loop seems to be a cut off effect. The lower panel of Figure 6.21 shows again no significant deviations in the average chain length of the system for different cut

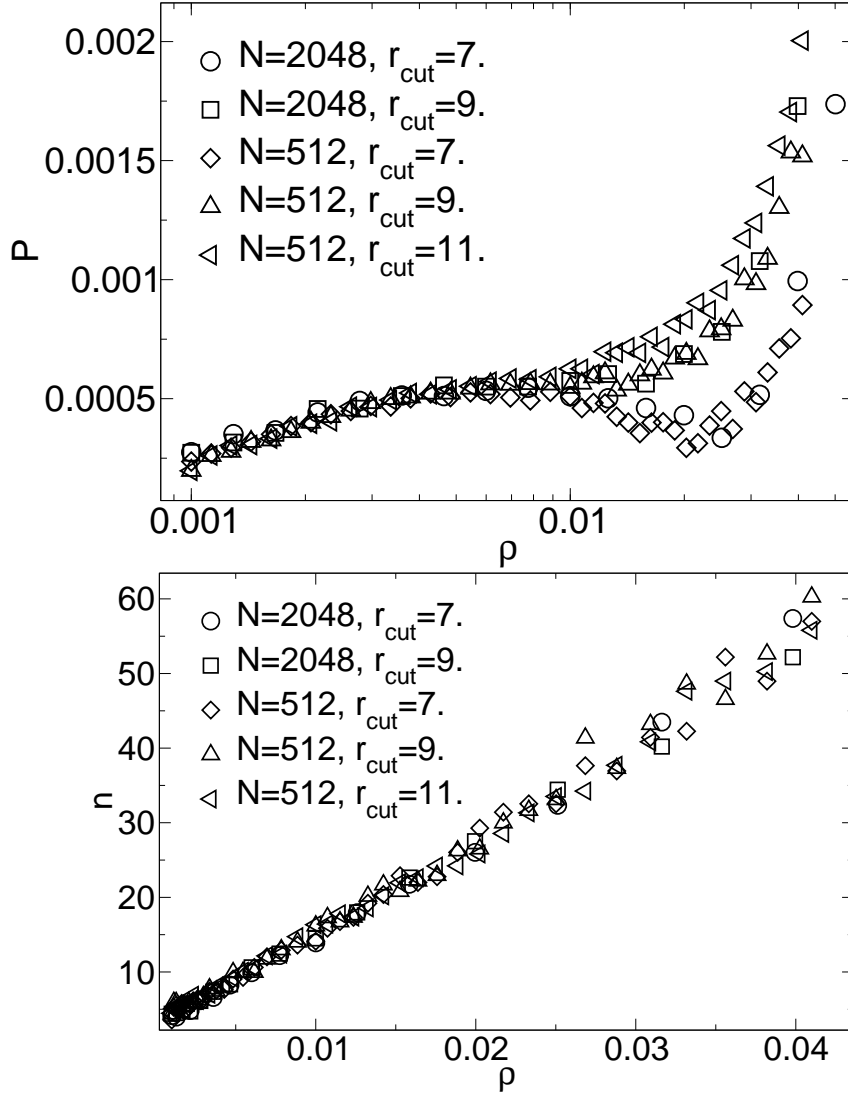


Figure 6.21: Top: pressure versus density for the DSS fluid with  $\mu^2 = 7.563$  for different cut offs and particle numbers as indicated at temperature  $T = 1$ . For sufficient large cut offs ( $r_{\text{cut}} \gtrsim 9$ ) the van der Waals loop disappears and the equation of state shows no phase transition. Bottom: the average chain length  $n$  for the different systems. Besides statistic uncertainties there seems to be no deviations for different cut offs and particle numbers.

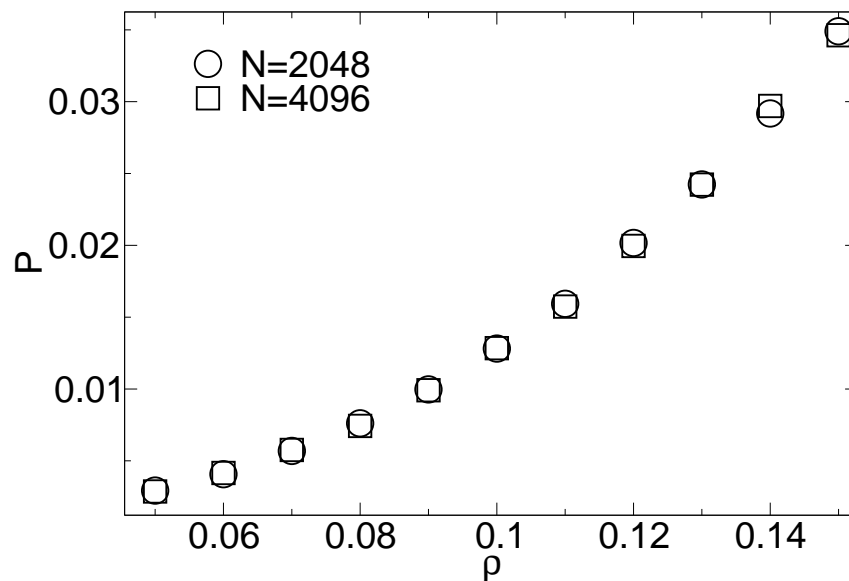


Figure 6.22: Pressure versus density for the DSS fluid ( $\mu^2 = 7.563$ ,  $r_{cut} = 11$ ,  $T = 1$ ) with particle numbers  $N = 2048$  and  $4096$ , in a region where Camp *et al.* observed a phase transition for the DHS fluid [31]. There is evidence neither for a phase transition nor for significant finite size effects in the DSS fluid.

offs and particle numbers, as already observed for the ST fluid. So differences in cluster structure should be no reason for the differences in pressure. It is remarkable that if we look at the particular systems with van der Waals loop ( $N = 512$  and  $2048$ ,  $r_{cut} = 7$ ), we expect for them the border to the liquid phase to lie in the region  $\rho_l \approx 0.03$ , even this is much below the expected critical density  $\rho_c \approx 0.1$  for the DHS fluid obtained in [31, 32]. In reference [32] Ganzenmüller and Camp argue that the GL phase transition of the DHS fluid may disappear in simulation due to finite-size effects. In figure 6.22 we show isotherms around the expected critical density for two relative large systems ( $N = 2048$  and  $4096$ ,  $r_{cut} = 11$ ,  $T = 1$ ). Here we see evidence neither for a phase transition nor for significant finite-size effects.

For comparison, we show in figure 6.23 the influence of particle number and cut off for a ST system with  $\mu^2 = 7.563$  at temperature  $T = 2.8$ . The critical temperature of this system is expected to be approximately  $T_c \approx 2.96$ , obtained from a linear fit for the critical temperatures (cf. chapter 7). Here systems with ( $N = 512$ ,  $r_{cut} = 3, 4$  and  $5$ ), ( $N = 1372$ ,  $r_{cut} = 5, 6$  and  $7$ ) and ( $N = 2700$ ,  $r_{cut} = 5$  and  $7$ ) are shown. We see that for the smallest particle number the limiting curve is still not reached, first with  $N = 1372$  and  $r_{cut} = 5$  it is. Nevertheless, the finite-size and cut off effects for the ST with these parameters are small compared with the ones observed for the investigated DSS fluid. We note that the DHS system differ from the DSS system discussed here due to the distinct length scale of the repulsive interaction which the power law repulsion does not possess. But we can at least state that at parameters where the DHS is expected to show a GL

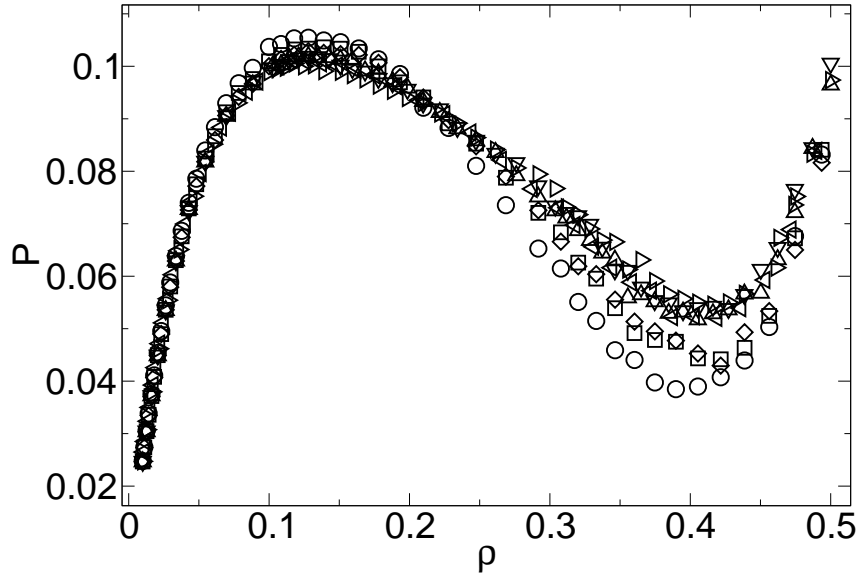


Figure 6.23: For comparison a ST fluid with  $\mu^2 = 7.563$  and  $T = 2.8$ . For  $N = 512$  the cut offs  $r_{cut} = 3$  (circles), 4 (squares), 5 (diamonds) were simulated, for  $N = 1372$   $r_{cut} = 5$  (up-triangles), 7 (left-triangles) and for  $N = 2700$   $r_{cut} = 5$  (down-triangles), 7 (right-triangles). There are finite size effects, but the limiting curve shows still a phase transition.

phase transition [31,32] we found no evidence for the DSS to show a GL phase transition. Nevertheless, we cannot argue with our existing data on the DSS that it exhibits no GL phase transition at all, but in chapter 7 we will show that the non-existence of GL phase separation is consistent with the existing data on the GL critical point of the ST fluid.

## 6.4 Conclusion

While the results from Maxwell construction for our NVT simulations are in close accord with previous GEMC works for dipole strengths  $\mu^2 \leq 5$  [23–25] we do find phase coexistence also for the larger dipole strengths. This disagrees with the GEMC work by van Leeuwen and Smit [7], which is responsible for the widely accepted believe that the ST system should not exhibit a GL critical point above  $\mu^2 \approx 25$ . Van Leeuwen and Smit attribute the observed disappearance of the critical point to the formation of reversible dipole chains. However, we do find coexistence of the isotropic gas and the isotropic liquid for all dipole strengths studied, i.e.  $0 \leq \mu^2 \leq 60$ . We found that the deviation from the principle of corresponding states increases with increasing dipole moment. On the other hand there seems to be a limiting curve for large dipole moments, at least on the gas side of the coexistence curve.

For dipole strengths  $\mu^2 = 5$  and 16 Kofke's integration method turned out to be a good alternative to Maxwell construction. We were able to determine the binodal to much lower temperatures and observed nematic order for reduced temperature  $T/T_c \lesssim 0.55$ . For the large dipole moments  $\mu^2 = 30$  and 36 Kofke's method turned out to be impracticable. In the region where these systems were investigated by NVT simulations no nematic order was found.

For the pST fluid we showed that our results are in good accord with results obtained by GCMC [27]. At fixed dipole moment and various polarizabilities the principle of corresponding states was fulfilled almost perfectly.

Finally we showed that for a particular DSS system the GL transition is an effect of a too short cut off, while the structure of the fluid is almost not dependent on the cut off. For parameters where the DHS fluid is expected to show a phase transition [31, 32] we found evidence neither for a phase transition nor for finite-size effects with Maxwell construction. Due to the strong similarity between the DSS and the DHS system, we expect the same conclusion to hold for DHS. For comparable ST fluids smaller cut offs are sufficient.



# Bibliography

- [1] L.E. Reichl. *A Modern Course in Statistical Physics*. John Wiley & Sons, 2 edition, 1998.
- [2] C. Domb. *The Critical Point*. Taylor & Francis, 1996.
- [3] W. Gebhardt and U. Krey. *Phasenübergänge und kritische Phänomene*. Friedr. Vieweg & Sohn, 1980.
- [4] P.I.C. Teixeira, J.M. Tavares, and M.M. Telo da Gama. The effect of dipolar forces on the structure and thermodynamics of classical fluids. *Journal of Physics: Condensed Matter*, (33):R411–R434, 2000.
- [5] B. Huke and M. Lücke. Magnetic properties of colloidal suspensions of interacting magnetic particles. *Reports on Progress in Physics*, 67:1731–1768, 2004.
- [6] P.G. de Gennes and P.A. Pincus. Pair correlations in a ferromagnetic colloid. *Zeitschrift für Physik B*, 11(3):189–198, 1970.
- [7] M.E. van Leeuwen and B. Smit. What makes a polar liquid a liquid? *Physical Review Letters*, 71(24):3991–3994, 1993.
- [8] M.J. Stevens and G.S. Grest. Structure of soft-sphere dipolar fluids. *Physical Review E*, 51(6):5962 – 5975, 1995.
- [9] R.P. Sear. Low-density fluid phase of dipolar hard spheres. *Physical Review Letters*, 76(13):2310–2313, 1996.
- [10] R. van Roij. Theory of chain association versus liquid condensation. *Physical Review Letters*, 76(18):3348–3351, 1996.
- [11] J.M. Tavares, M.M. Telo da Gama, and M.A. Osipov. Criticality of dipolar fluids: Liquid-vapor condensation versus phase separation in systems of living polymers. *Physical Review E*, 56(6):6252–6255, 1997.
- [12] J.M. Tavares, J.J. Weis, and M.M. Telo da Gama. Strongly dipolar fluids at low densities compared to living polymers. *Physical Review E*, 59(4):4388–4395, 1999.
- [13] K. van Workum and J.F. Douglas. Equilibrium polymerization in the Stockmayer fluid as a model of supermolecular self-organization. *Physical Review E*, 71(031502), 2005.
- [14] H. Kabrede and R. Hentschke. Spinodal decomposition in a 3d lennard-jones system. *Physica A*, 361(2):485–493, 2006.

- 
- [15] R.B. Griffiths. Thermodynamic functions for fluids and ferromagnets near the critical point. *Physical Review*, 158(1):176–187, 1967.
- [16] Wolfram Research, Inc. Mathematica version 5.1.1, <http://www.wolfram.com>.
- [17] D.A. Kofke. Direct evaluation of phase coexistence by molecular simulation via integration along the saturation line. *The Journal of chemical physics*, 98(5):4149–4162, 1993.
- [18] D.A. Kofke. Gibbs-duhem integration: a new method for direct evaluation of phase coexistence by molecular simulation. *Molecular physics*, 78(6):1331–1336, 1993.
- [19] J.V. Sengers and J.M.H. Levelt Sengers. Thermodynamic behaviour of fluids near the critical point. *Annual Reviews of Physical Chemistry*, 37:189–222, 1986.
- [20] M.E. Fisher. The renormalization group in the theory of critical behavior. *Review of Modern Physics*, 46(4):597–615, 1974.
- [21] M. Ley-Koo and M.S. Green. Consequences of the renormalization group for the thermodynamics of fluids near the critical point. *Physical Review A*, 23(5):2650–2659, 1981.
- [22] A. Pelissetto and E. Vicari. Critical phenomena and renormalization-group theory. *Physics Reports*, 368(6):549–727, 2002.
- [23] B. Smit, C.P. Williams, E.M. Hendriks, and S.W. de Leeuw. Vapour-liquid equilibria for Stockmayer fluids. *Molecular Physics*, 68(3):765–769, 1989.
- [24] M.E. van Leeuwen, B. Smit, and E.M. Hendriks. Vapour-liquid equilibria of Stockmayer fluids, computersimulations and perturbation theory. *Molecular Physics*, 78(2):271–283, 1993.
- [25] M.E. van Leeuwen. Deviation from corresponding-states behaviour for polar fluids. *Molecular Physics*, 82(2):383–392, 1994.
- [26] J.O. Hirschfelder, C.F. Curtiss, and R.B. Bird. *Molecular Theory of Gases and Liquids*. John Wiley & Sons, Inc., 8 edition, 1964.
- [27] K. Kiyohara, K.E. Gubbins, and A.Z. Panagiotopoulos. Phase coexistence properties of polarizable Stockmayer fluids. *Journal of Chemical Physics*, 106(8):3338–3347, 1997.
- [28] K.-C. Ng, J.P. Valleau, G.M. Torrie, and G.N. Patey. Liquid-vapour co-existence of dipolar hard spheres. *Molecular Physics*, 38(3):781–788, 1979.
- [29] J.-M. Caillol. Search of the gas-liquid transition of dipolar hard spheres. *Journal of Chemical Physics*, 98(12):9835–9849, 1993.
- [30] M.A. Osipov, P.I.C. Teixeira, and M.M. Telo da Gama. Structure of strongly dipolar fluids at low densities. *Physical Review E*, 54(3):2597–2609, 1996.
- [31] P.J. Camp, J.C. Shelley, and G.N. Patey. Isotropic fluid phases of dipolar hard spheres. *Physical Review Letters*, 84(1):115–118, 2000.

- [32] G. Ganzenmüller and P.J. Camp. Vapor-liquid coexistence in fluids of charged hard dumbbells. *Journal of Chemical Physics*, 126:191104, 2007.



# 7 Equilibrium polymerization and gas-liquid critical behavior in the Stockmayer fluid

## 7.1 Introduction

Dipolar interaction may lead to the reversible formation of polydisperse chains from molecules or colloidal particles [1,2] whose physical behavior is similar to ordinary polymer systems [3]. The ST fluid, as already discussed in the chapters 5 and 6, shows this kind of chain formation. The chain formation in turn strongly affects the behavior of the monomer systems. This coupling together with the special problems caused by long-range interaction thus far has prevented a complete theory, particularly for computing the phase diagram of dipolar liquids [4]. While it was widely accepted that the ordinary SF will not show GL phase separation for dipole moments exceeding  $\mu^2 \approx 25$  [5,6], attributed to the formation of reversible dipole chains, Dudowicz, Freed and Douglas reached a different conclusion [7]. They mapped the Stockmayer fluid onto a Flory-Huggins (FH) mean field lattice model and studied the interplay between chain formation and GL phase separation. Their theory implies that the GL critical point exists for all dipole strengths.

In this chapter we develop a simple theory to explain the dependence of the GL critical point in the ST fluid on dipole strength, in particular the coupling between GL critical behaviour and the formation of reversible dipole chains. The theory is based on the FH lattice description for polymer systems in conjunction with a transfer matrix model for isolated chains of reversibly assembled dipolar particles. The basis of our theory, i.e. the FH lattice description, is the same as in references [7–11]. However, we choose a different mapping between the lattice model's direct interaction parameters and the ST fluid, cf. in particular [7,11]. Our approach allows to directly relate the shift of the GL critical point to the details of the underlying interactions. We also stress the similarity between the mean field critical behavior of reversibly formed dipole chains in comparison to ordinary systems of linear polymers, in particular  $n$ -alkanes. It is this similarity which also makes the disappearance of the GL critical point in the ST system due to chain formation highly suspicious. As the alignment of the dipoles tangential to the chain strongly diminishes the DD interaction between chains, the remaining LJ interaction makes the chains very much alkane-like.

On the other hand the DD interaction may give rise to long-range orientational order, and the attending transition from the isotropic fluid to an anisotropic liquid may interfere with the isotropic gas-to-isotropic liquid transition. Zhang and Widom [12] have studied the interplay between isotropic van der Waals type interaction and anisotropic dipolar interaction using a simple mean field model. The difference to the model used in this work is the neglect of chain formation. The authors obtain a sequence of phase diagrams which indicate a vanishing of the GL critical point due to the instability of the isotropic liquid in comparison to the anisotropic liquid. The parameter which drives this behavior is the reduction of the GL critical temperature. Similar results were obtained via DFT by Groh and Dietrich [13, 14]. The ST model has been shown to exhibit ferroelectric liquid order under suitable conditions (cf. chapter 8). To some extent we also include a discussion of the transition from the isotropic liquid to the ferroelectric liquid and employ the FH model to describe entire GL coexistence curves, including possible ferroelectric order.

## 7.2 Flory-Huggins lattice model for reversibly assembling polymers

### 7.2.1 The Helmholtz free energy

According to the FH-approach polymers are described by paths on a regular lattice. A schematic illustration for a mixture of polydispers polymers on such a lattice is given in figure 7.1 for two dimensions. Each lattice site may represent one monomer, here corresponding to one ST particle. Polymers, i.e. dipole chains, are indicated by the lines between monomers, monomers without lines are single particles. We derive the Helmholtz free energy

$$F_L = E_L - TS_L \quad (7.2.1)$$

for a lattice model including self assembly of particles and free lattice sites, corresponding to free space. This model has been introduced for a different system in references [15, 16]. In equation (7.2.1)  $E_L$  is the lattice energy, caused by the interactions between the monomers arranged on the lattice, and  $S_L$  the packing entropy of the lattice. In equilibrium the Helmholtz free energy is minimal and from this condition thermodynamic quantities like for instance the mean chain length or the pressure may be obtained.

#### The lattice interaction energy

First we will calculate the lattice energy  $E_L$ . We distinguish interactions between monomers of different clusters or single particles with interaction energy  $\varepsilon T$  per contact, and interac-

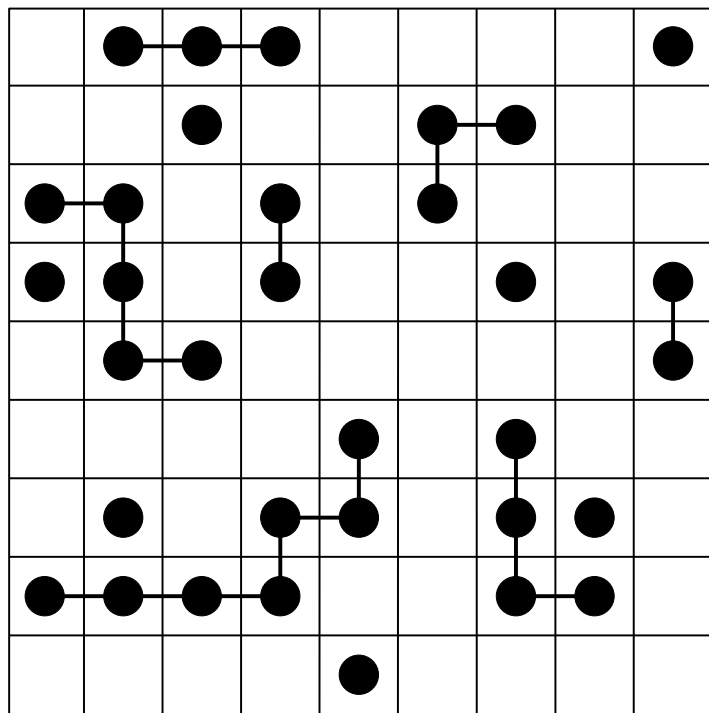


Figure 7.1: Schematic illustration of the FH lattice model for polydispers polymers in two dimensions. The monomers (circles) are allocated randomly to the lattice. Polymers are indicated by paths of connected balls. Isolated balls correspond to single particles, while free cells correspond to free space.

tions between monomers within the same aggregate (chain) with interaction energy  $\varepsilon_i T$ . We assume the single particles and aggregates to be distributed randomly on the lattice. If we look at any lattice site the probability for finding here a monomer, belonging to an aggregate of length  $s$  ( $s$ -mer), is given by the volume fraction

$$\phi_s = \frac{b_0 s N_s}{V}. \quad (7.2.2)$$

Here  $b_0$  denotes the volume of one lattice site, or the particle respectively,  $N_s$  the number of aggregates consisting of  $s$  monomers and  $V$  the volume of the whole considered lattice. The probability that a site is occupied by a monomer, part of whatever kind of aggregate, is given by the volume fraction

$$\phi = \sum_{i=1}^{\infty} \phi_s = \frac{b_0}{V} \sum_{i=1}^{\infty} s N_s, \quad (7.2.3)$$

which is related to the number density via  $\phi = b_0 \rho$ . We will call interactions between monomers belonging to different clusters inter-aggregate interaction, interactions between monomers within the same cluster intra-aggregate interaction. For randomly distributed

configurations the mean number of inter-aggregate interactions between monomers of  $s$ -mers and monomers of  $s'$ -mers ( $s \neq s'$ ) is given by

$$\approx \phi_s \phi_{s'} N_L q, \quad (7.2.4)$$

where

$$N_L = \sum_{s=1}^{\infty} s N_s + N_{empty} = \frac{V}{b_0} \quad (7.2.5)$$

is the total number of lattice sites not to be confused with the total number of monomers  $N = \sum_{s=1}^{\infty} s N_s$ ,  $N_{empty}$  is the number of free lattice sites and  $q$  is the coordination number of the lattice. In three dimensions  $q = 6$ , while in two dimensions as in figure 7.1,  $q = 4$ . The average number of inter-aggregate interactions between monomers of aggregates with same length is given by

$$\approx \frac{1}{2} \phi_s^2 N_L q. \quad (7.2.6)$$

The factor  $1/2$  prevents double counting. In both cases we neglect that monomers inside and at the end of aggregates have a reduced number of possible nearest neighbors from other clusters and assume  $q-2 \approx q-1 \approx q$ . So the total lattice inter-aggregate interaction energy is

$$E_{inter} = T \left( \sum_{s < s'} \varepsilon \phi_s \phi_{s'} + \frac{1}{2} \sum_{s=1}^{\infty} \varepsilon \phi_s^2 \right) N_L q. \quad (7.2.7)$$

The total intra-aggregate interaction energy is given by

$$E_{intra} = T \sum_{s=2}^{\infty} \varepsilon_i (s-1) N_s, \quad (7.2.8)$$

if we assume all clusters to be linear chains, since a linear chain of length  $s$  has  $s-1$  bonds. This yields the total lattice energy

$$E_L = E_{inter} + E_{intra} \quad (7.2.9)$$

$$= T \left[ \left( \sum_{s < s'} \phi_s \phi_{s'} + \frac{1}{2} \sum_{s=1}^{\infty} \phi_s^2 \right) \varepsilon N_L q + \frac{V}{b_0} \sum_{s=2}^{\infty} \varepsilon_i (s-1) N_s \right] \quad (7.2.10)$$

$$= T \left( \frac{1}{2} \varepsilon N_L q \phi^2 + \frac{\varepsilon_i V}{b_0} \sum_{s=2}^{\infty} \frac{s-1}{s} \phi_s \right). \quad (7.2.11)$$

For the last transformation we have used

$$\phi^2 = \left( \sum_{s=1}^{\infty} \phi_s \right)^2 = \sum_{s=1}^{\infty} \sum_{s'=1}^{\infty} \phi_s \phi_{s'} = \sum_{s=1}^{\infty} \phi_s^2 + 2 \sum_{s < s'}^{\infty} \phi_s \phi_{s'} \quad (7.2.12)$$

and  $N_s = V \phi_s / (b_0 s)$ .

### The lattice packing entropy

Deriving the packing entropy takes more effort and requires additional approximations [17–19]. The packing entropy of a lattice with polydispers aggregates is given by

$$S_L = \ln \left[ \prod_{s=1}^{\infty} \Omega_s(N_s) \right], \quad (7.2.13)$$

where

$$\Omega_s(N_s) = \frac{1}{N_s!} \prod_{i=0}^{N_s-1} \omega_{s,i+1} \quad (7.2.14)$$

is the number of possibilities to arrange the  $s$ -mers sequentially on the lattice on which the  $s'$ -mers with  $s' < s$  are already arranged. Here  $N_s!$  accommodates the in-distinguishability of the particles.  $\omega_{s,i+1}$  is the number of possibilities to arrange the  $(i+1)$ th  $s$ -mer on the lattice, already filled with  $i$   $s$ -mers and all shorter aggregates. To determine a general term for  $\omega_{s,i+1}$  we consider an empty lattice and fill it with aggregates with increasing chain length starting with single particles ( $s = 1$ ).

$s = 1$  :

$$\omega_{1,i+1} = N_L - i \quad (7.2.15)$$

To insert the  $(i+1)$ th single particle, the number of available lattice sites  $N_L$  is reduced by  $i$  already inserted single particles.

$s = 2$  :

$$\omega_{2,i+1} = \underbrace{(N_L - N_1 - 2i)}_{T1} \underbrace{q \left( 1 - \frac{N_1 + 2i}{N_L} \right)}_{T2} \quad (7.2.16)$$

Here  $T1$  determines the number of possibilities to insert the first unit of the  $(i+1)$ th dimer on the lattice, already filled with  $N_1$  single particles and  $i$  dimers. The first unit of each dimer has  $q$  nearest neighbor sites of which  $T2$  are empty on average, since  $f_{2,i}/N_L = (N_1 + 2i)/N_L$  is the number fraction of filled sites. Due to this treatment of particle insertions the FH model has the character of a mean field theory.

$s = 3$  :

$$\omega_{3,i+1} = \underbrace{(N_L - N_1 - 2N_2 - 3i)}_{T1} \underbrace{q \left( 1 - \frac{N_1 + 2N_2 + 3i}{N_L} \right)}_{T2} \times \underbrace{(q-1) \left( 1 - \frac{N_1 + 2N_2 + 3i}{N_L} \right)}_{T3} \quad (7.2.17)$$

Insertion of the first two units of the 3-mers following the same reasoning as above. Here the second units have only  $(q - 1)$  nearest neighbor sites. We assume that the number fraction of filled sites remain the same for all units of the same aggregate. For every additional unit for  $s$ -mers with  $s > 3$  we make the approximation that these also each have  $T3$  insertion possibilities.

$s$  : With the former approximations we can now give a general term for  $s$ -mers

$$\omega_{s,i+1} = (N_L - f_{s,i}) (q - 1)^{s-1} \left(1 - \frac{f_{s,i}}{N_L}\right)^{s-1} \quad (7.2.18)$$

$$= (N_L - f_{s,i})^s \left(\frac{q - 1}{N_L}\right)^{s-1} \quad (7.2.19)$$

with the number fraction of filled sites

$$\frac{f_{s,i}}{N_L} = \frac{1}{N_L} \left( \sum_{k=1}^s k N_k - s N_s + s i \right) \quad (7.2.20)$$

and the additional approximation  $q \approx q - 1$ .

Now we possess the information necessary to calculate the packing entropy of the lattice, i.e.

$$S_L = \ln \left[ \prod_{s=1}^{\infty} \Omega_s(N_s) \right] = \ln \left[ \prod_{s=1}^{\infty} \frac{1}{N_s!} \prod_{i=0}^{N_s-1} \omega_{s,i+1} \right] \quad (7.2.21)$$

$$= \sum_{s=1}^{\infty} \ln \left[ \frac{1}{N_s!} \prod_{i=0}^{N_s-1} \omega_{s,i+1} \right] = \sum_{s=1}^{\infty} \left( -\ln [N_s!] + \sum_{i=0}^{N_s-1} \ln \omega_{s,i+1} \right) \quad (7.2.22)$$

$$= \sum_{s=1}^{\infty} \left( -N_s \ln N_s + N_s + \sum_{i=0}^{N_s-1} \left( s \ln [N_L - f_{s,i}] + (s - 1) \ln \left[ \frac{q - 1}{N_L} \right] \right) \right), \quad (7.2.23)$$

where we have used the Stirling approximation  $\ln[N!] \approx N \ln N - N$ . Using equation (7.2.2) to replace the  $N_s$ 's we obtain for the first term of the sum

$$\sum_{s=1}^{\infty} (-N_s \ln N_s + N_s) = \frac{V}{b_0} \sum_{s=1}^{\infty} \left( \frac{\phi_s}{s} - \frac{\phi_s}{s} \ln \left[ \frac{V \phi_s}{b_0 s} \right] \right) \quad (7.2.24)$$

$$= \frac{V}{b_0} \left( \sum_{s=1}^{\infty} \frac{\phi_s}{s} - \sum_{s=1}^{\infty} \frac{\phi_s}{s} \ln \left[ \frac{\phi_s}{s} \right] - \ln \left[ \frac{V}{b_0} \right] \sum_{s=1}^{\infty} \frac{\phi_s}{s} \right). \quad (7.2.25)$$

For the second term we approximate the inner sum via integration, i.e.

$$\sum_{s=1}^{\infty} \sum_{i=0}^{N_s-1} s \ln(N_L - f_{s,i}) \quad (7.2.26)$$

$$\approx \sum_{s=1}^{\infty} \int_0^{N_s} di s \ln(N_L - f_{s,i}) = \sum_{s=1}^{\infty} \int_{x(N_s)}^{x(0)} dx(i) \ln x(i) \quad (7.2.27)$$

$$= \sum_{s=1}^{\infty} (x(0) \ln x(0) - x(0) - x(N_s) \ln x(N_s) + x(N_s)) \quad (7.2.28)$$

$$= \sum_{s=1}^{\infty} \left( N_L - \sum_{k=1}^s k N_k - s N_s \right) \ln \left[ N_L - \sum_{k=1}^s k N_k - s N_s \right] \quad (7.2.29)$$

$$- \sum_{s=1}^{\infty} \left( N_L - \sum_{k=1}^s k N_k \right) \ln \left[ N_L - \sum_{k=1}^s k N_k \right] - \sum_{s=1}^{\infty} s N_s$$

$$= N_L \ln N_L - \left( N_L - \sum_{s=1}^{\infty} s N_s \right) \ln \left[ N_L - \sum_{s=1}^{\infty} s N_s \right] - \sum_{s=1}^{\infty} s N_s \quad (7.2.30)$$

$$= N_L \ln N_L - N_{empty} \ln N_{empty} - \sum_{s=1}^{\infty} s N_s \quad (7.2.31)$$

$$= \frac{V}{b_0} \left[ \left( \ln \left[ \frac{V}{b_0} \right] - 1 \right) \phi - (1 - \phi) \ln [1 - \phi] \right], \quad (7.2.32)$$

In equation (7.2.27) we have used the substitution  $x(i) = N_L - f_{s,i}$ . Notice that for any finite lattice there exists a  $s_{max}$  with  $N_{s'} = 0$  for all  $s' > s_{max}$ . So all terms in equation (7.2.29) of the first two sums cancel each other except for the very first of the first sum and the very last non-vanishing term of the second sum. From equation (7.2.30) to (7.2.32) we have used  $N_L = V/b_0$  and

$$N_{empty} = N_L - \sum_{s=1}^{\infty} s N_s = \frac{V}{b_0} (1 - \phi). \quad (7.2.33)$$

For the last term of equation (7.2.23) we can simply evaluate the inner sum

$$\sum_{s=1}^{\infty} \sum_{i=0}^{N_s-1} (s-1) \ln \left[ \frac{q-1}{N_L} \right] \quad (7.2.34)$$

$$= \sum_{s=2}^{\infty} (s-1) N_s \ln \left[ \frac{q-1}{N_L} \right] \quad (7.2.35)$$

$$= \frac{V}{b_0} \left( \ln [q-1] \sum_{s=2}^{\infty} \frac{s-1}{s} \phi_s - \ln \left[ \frac{V}{b_0} \right] \sum_{s=2}^{\infty} \frac{s-1}{s} \phi_s \right). \quad (7.2.36)$$

Combining equation (7.2.25), (7.2.32) and (7.2.36) we get the packing entropy of the lattice dependent on the volume fractions  $\phi_s$  and  $\phi$

$$\frac{b_0 S_L}{V} = (\ln[q-1] - 1) \sum_{s=2}^{\infty} \frac{s-1}{s} \phi_s - \sum_{s=1}^{\infty} \frac{\phi_s}{s} \ln \left[ \frac{\phi_s}{s} \right] - (1-\phi) \ln[1-\phi]. \quad (7.2.37)$$

Inserting equation (7.2.37) and (7.2.11) in (7.2.1) we get an expression for the Helmholtz free energy of the lattice

$$\frac{b_0 F_L}{VT} = \frac{1}{2} \varepsilon q \phi^2 + (c+1) \sum_{s=2}^{\infty} \frac{s-1}{s} \phi_s + \sum_{s=1}^{\infty} \frac{\phi_s}{s} \ln \left[ \frac{\phi_s}{s} \right] + (1-\phi) \ln[1-\phi] \quad (7.2.38)$$

with  $c = \varepsilon_i - \ln[q-1]$ . Note that this is a special case of

$$\begin{aligned} \frac{b_0 F_L}{VT} &= \frac{1}{2} q \varepsilon_{MM} \phi_1^2 + \frac{1}{2} q \varepsilon_{AA} \phi_{agg}^2 + q \varepsilon_{MA} \phi_1 \phi_{agg} \\ &+ (c+1) \sum_{s=2}^{\infty} \frac{s-1}{s} \phi_s + \sum_{s=1}^{\infty} \frac{\phi_s}{s} \ln \left[ \frac{\phi_s}{s} \right] + (1-\phi) \ln[1-\phi], \end{aligned} \quad (7.2.39)$$

introduced in references [15, 16], where  $\varepsilon_{MM}$  is the parameter for interactions between free monomers,  $\varepsilon_{AA}$  for interactions between monomers bound in aggregates and  $\varepsilon_{MA}$  for interactions between free monomers and monomers bound in aggregates.  $\phi_1$  is the volume fraction for free monomers and  $\phi_{agg} = \sum_{s=2}^{\infty} \phi_s$  for aggregates with  $s > 1$ . The remaining variables are the same as we used here. This equation reduces to our with  $\varepsilon_{MM} = \varepsilon_{MA} = \varepsilon_{AA} = \varepsilon$ .

## 7.2.2 Calculating critical properties from the lattice model

### Mean chain length

To be able to determine the critical properties for our lattice model, we first calculate the mean chain length of the aggregates. Using the equilibrium condition for reversible aggregation  $\mu_s = s\mu_1$ , where

$$\frac{\mu_s}{T} = \frac{1}{T} \left. \frac{\partial F_L}{\partial N_s} \right|_{T, V, N_{s'} (s' \neq s)} = \frac{b_0 s}{VT} \left. \frac{\partial F_L}{\partial \phi_s} \right|_{T, V, \phi_{s'} (s' \neq s)} \quad (7.2.40)$$

$$= s \varepsilon q \phi + c(s-1) + \ln \left[ \frac{\phi_s}{s} \right] - s \ln[1-\phi] \quad (7.2.41)$$

is the chemical potential of an  $s$ -mer, we obtain  $\phi_s = s\beta^s e^c$  with  $\beta = \phi_1 e^{-c}$ . We get the mean chain length from

$$n = \frac{\sum_{s=1}^{\infty} s N_s}{\sum_{s=1}^{\infty} N_s} = \frac{\sum_{s=1}^{\infty} \phi_s}{\sum_{s=1}^{\infty} \frac{\phi_s}{s}} = \frac{1}{1-\beta}, \quad (7.2.42)$$

where we have used

$$\phi = \sum_{s=1}^{\infty} \phi_s = \sum_{s=1}^{\infty} s\beta^s e^c = \frac{\beta e^c}{(\beta - 1)^2} \quad (7.2.43)$$

$$\sum_{s=1}^{\infty} \frac{\phi_s}{s} = \sum_{s=1}^{\infty} \beta^s e^c = \frac{\beta e^c}{1 - \beta}, \quad (7.2.44)$$

obtained by the limit of the geometric series and  $\sum_{s=1}^{\infty} s\beta^s = (\beta d/d\beta) \sum_{s=1}^{\infty} \beta^s$ . Insertion of  $\beta = (1 - n^{-1})$  in (7.2.43) yields the mean chain length expressed via  $\phi$

$$n = \frac{1}{2} + \frac{1}{2} \sqrt{1 + 4\phi e^{-c}} \quad (7.2.45)$$

$$= \frac{1}{2} + \frac{1}{2} \sqrt{1 + 4(q-1)\phi e^{-\varepsilon_i}}. \quad (7.2.46)$$

Now we can rewrite the Helmholtz free energy as function of  $\phi$  and mean chain length  $n$  only

$$\frac{b_0 F_L}{TV} = \frac{1}{2} q \varepsilon \phi^2 + \phi \ln \phi + (1 - \phi) \ln [1 - \phi] + \left(1 - \frac{1}{n} - 2 \ln [n]\right) \phi, \quad (7.2.47)$$

where we have used  $\sum_{s=1}^{\infty} \phi_s/s = \phi/n$ , obtained by combining equations (7.2.42), (7.2.43) and (7.2.44). Here, however,  $n$  is a function of  $\phi$ .

### The equation of state and critical point

Using the relations

$$\left. \frac{\partial \frac{\phi_s}{s}}{\partial V} \right|_{T, N_s} = -\frac{1}{V} \frac{\phi_s}{s} \quad \text{and} \quad \left. \frac{\partial \phi}{\partial V} \right|_{T, N_s} = -\frac{1}{V} \phi \quad (7.2.48)$$

we are able to calculate the equation of state from equation (7.2.38), i.e.

$$\frac{b_0 P}{T} = -\frac{b_0}{T} \left. \frac{\partial F_L}{\partial V} \right|_{T, N_s} = \frac{1}{2} \varepsilon q \phi^2 - \ln [1 - \phi] - \phi + \sum_{s=1}^{\infty} \frac{\phi_s}{s} \quad (7.2.49)$$

$$= \frac{1}{2} \varepsilon q \phi^2 - \ln [1 - \phi] - \left(1 - \frac{1}{n}\right) \phi, \quad (7.2.50)$$

Analog to reference [11] we obtain the virial expansion for the pressure. First we consider the ordinary simple liquid limit (SL) without aggregation. For this we set  $n = 1$  in equation (7.2.50). We derive the virial expansion by substituting  $\ln [1 - \phi]$  in equation (7.2.50) by the power series expansion

$$\ln [1 - \phi] = -\phi - \frac{1}{2} \phi^2 - \frac{1}{3} \phi^3 - \mathcal{O}(\phi^4) \quad (7.2.51)$$

with respect to  $\phi$  for the limit  $\phi \rightarrow 0$ . This yields

$$P_{SL} = \frac{T\phi}{b_0} \left( 1 + \frac{b_0}{2} (\varepsilon q + 1) \frac{\phi}{b_0} + \frac{b_0^2}{3} \frac{\phi^2}{b_0^2} + \mathcal{O}(\phi^3) \right) \quad (7.2.52)$$

and by comparison with equation (5.2.1) we get for the second and third virial coefficients

$$B_{2,SL}(T) = \frac{b_0}{2} (\varepsilon q + 1) \quad (7.2.53)$$

$$B_{3,SL}(T) = \frac{b_0^2}{3}. \quad (7.2.54)$$

Via  $B_{2,SL}(T_{Boyle,SL}) = 0$  we obtain the Boyle temperature

$$T_{Boyle,SL} = -\varepsilon_0 q \quad (7.2.55)$$

for a system of monomers, where  $\varepsilon_0 = \varepsilon T$ . For the case with aggregation we have to expand additionally the reciprocal mean chain length

$$\frac{1}{n} = 1 - e^{-c}\phi + 2e^{-2c}\phi^2 - 5e^{-3c}\phi^3 + \mathcal{O}(\phi^4), \quad (7.2.56)$$

inserted in equation (7.2.50) this yields

$$P = \frac{T\phi}{b_0} \left[ 1 + \frac{b_0}{2} (\varepsilon q + 1 - 2e^{-c}) \frac{\phi}{b_0} + b_0^2 \left( \frac{1}{3} + 2e^{-2c} \right) \frac{\phi^2}{b_0^2} + \mathcal{O}(\phi^3) \right] \quad (7.2.57)$$

and we get for the virial coefficients

$$B_2(T) = \frac{b_0}{2} (\varepsilon q + 1 - 2e^{-c}) \quad (7.2.58)$$

$$B_3(T) = b_0^3 \left( \frac{1}{3} + 2e^{-2c} \right). \quad (7.2.59)$$

For the Boyle temperature with aggregation we get

$$T_{Boyle} = \frac{\varepsilon_0 q}{2e^{-c} - 1}. \quad (7.2.60)$$

The GL critical properties expressed via the mean chain length at the critical point  $n_c$  can be obtained by solving the system of equations

$$\left. \frac{\partial P}{\partial V} \right|_T = \left. \frac{\partial^2 P}{\partial V^2} \right|_T = 0 \quad (7.2.61)$$

employing Mathematica [20]. We obtain for the GL critical point by power series expansion of the solution with respect to  $n_c$

$$\phi_c = f_\rho(n_c) = \begin{cases} \frac{1}{2} - \frac{3}{4}(n_c - 1)^2 + \mathcal{O}((n_c - 1)^3) & n_c \rightarrow 1 \\ \frac{\sqrt{3}}{2} \frac{1}{\sqrt{n_c}} - \frac{3}{4} \frac{1}{n_c} + \mathcal{O}\left(\frac{1}{n_c^{3/2}}\right) & n_c \rightarrow \infty \end{cases}, \quad (7.2.62)$$

$$T_c = -q\varepsilon_0 f_T(n_c) = \begin{cases} -\frac{q\varepsilon_0}{4} [1 + (n_c - 1) + \mathcal{O}((n_c - 1)^2)] & n_c \rightarrow 1 \\ -q\varepsilon_0 \left(1 - \frac{5}{2\sqrt{3}} \frac{1}{\sqrt{n_c}} + \mathcal{O}\left(\frac{1}{n_c}\right)\right) & n_c \rightarrow \infty \end{cases}, \quad (7.2.63)$$

and

$$b_0 P_c = \begin{cases} -q\varepsilon_0 \left[\left(\frac{\ln 2}{4} - \frac{1}{8}\right) + \mathcal{O}(n_c - 1)\right] & n_c \rightarrow 1 \\ -q\varepsilon_0 \left[\frac{5\sqrt{3}}{16} \frac{1}{n_c^{3/2}} - \frac{77}{64} \frac{1}{n_c^2} + \mathcal{O}\left(\frac{1}{n_c^{5/2}}\right)\right] & n_c \rightarrow \infty \end{cases}. \quad (7.2.64)$$

Here  $\varepsilon = \varepsilon_0/T$ ,  $n_c = n(\phi_c, \varepsilon_i(T_c))$ ,

$$f_\rho(n) \equiv \left(1 + \sqrt{\frac{m^3}{K}}\right)^{-1}, \quad (7.2.65)$$

where  $m = 2n - 1$  and  $K = 6n(n - 1) + 1$ , and

$$f_T(n) \equiv \frac{1}{2} \left(\frac{n}{m} + [K - n(n - 1)] \sqrt{\frac{1}{Km^3}}\right)^{-1}. \quad (7.2.66)$$

The equations (7.2.62) to (7.2.64) include the GL critical point in the limit of a system consisting of monomers only ( $n_c \rightarrow 1$ ), as well as in the limit of a system consisting of long monodisperse polymers ( $n_c \rightarrow \infty$ ). For large  $n_c$  the critical density vanishes as  $\sim n_c^{-1/2}$ , whereas the critical temperature approaches a constant value, which coincides with the Boyle temperature of the monomer system in the SL.

In this theory reversible association is promoted by the quantity  $\varepsilon_i$ . In particular  $\varepsilon_i = 0$  describes the SL. For  $\varepsilon_i = 0$  and  $q = 6$ , however, one obtains  $n_c = (\sqrt{11} + 1)/2 \approx 2.158$  and not  $n_c = 1$  as one may expect. This theory reaches the limit  $n_c = 1$  only if  $\exp[-c] = 0$ . But this means that  $n_c = 1$  under all circumstances, i.e. no association occurs even if  $\varepsilon_i \neq 0$ . The effect is due to the inability of the lattice theory to distinguish between adjacent unassociated and reversibly bound lattice sites. Because of this we must redefine the SL, i.e.  $\varepsilon_i = 0$ , via the simultaneous solution of equations (7.2.46) and (7.2.62) given by  $n_{c,SL} \approx 2.0142$  and  $\phi_{c,SL} = f_\rho(n_{c,SL}) \approx 0.4086$ . The attendant critical temperature is  $T_{c,SL} = -q\varepsilon_{0,SL} f_T(n_{c,SL}) \approx -0.4002q\varepsilon_{0,SL}$ , where  $\varepsilon_{0,SL}$  is the pair interaction for the SL. Note that in the case of the ST fluid the SL compiles to the LJ fluid. For the virial expansion of  $P_{SL}$  we avoided this problem by first setting  $n = 1$ .

### Dipolar long-range contribution to the pressure

Up to now this theory can explain the decrease of the critical density with increasing dipole strength  $\mu^2$  in terms of an increasing mean chain length  $n$ . Thus we must find a link between  $\mu^2$  and  $n$ . We may introduce the dipole strength on the level of the equation of state by including the pressure contribution due to long-range dipolar attractive

interaction. The thermally averaged DD interaction can be calculated analog to equation (3.7.2) via

$$\langle u_{DD} \rangle = \frac{1}{4\pi^2} \int \int d\Omega_i d\Omega_j u_{DD}(\vec{r}_{ij}, \vec{\mu}_i, \vec{\mu}_j) g_{DD}(r_{ij}, \vec{\mu}_i, \vec{\mu}_j) \quad (7.2.67)$$

with the solid angle elements  $d\Omega_i = d\varphi_i d\theta_i \sin\theta_i$ , the DD pair interaction  $u_{DD}(\vec{r}_{ij}, \vec{\mu}_i, \vec{\mu}_j)$  (cf. equation (2.1.4)) and the pair distribution function of the mutual orientations of the dipoles  $g_{DD}(r_{ij}, \vec{\mu}_i, \vec{\mu}_j)$  which can be approximated by

$$g_{DD}(r_{ij}, \vec{\mu}_i, \vec{\mu}_j) \approx \exp \left[ -\frac{u_{DD}(\vec{r}_{ij}, \vec{\mu}_i, \vec{\mu}_j)}{T} \right] \approx 1 - \frac{u_{DD}(\vec{r}_{ij}, \vec{\mu}_i, \vec{\mu}_j)}{T} \quad (7.2.68)$$

$$= 1 - \frac{\mu^2}{r_{ij}^3 T} f(\theta_i, \theta_j, \varphi_i - \varphi_j), \quad (7.2.69)$$

resulting in

$$\langle u_{DD} \rangle = -\frac{2\mu^4}{3T r^6}. \quad (7.2.70)$$

From this we get the long-range contribution to the pressure

$$P_{DD} \approx -\frac{1}{6} \rho^2 \int_{r \geq R} d^3 r r \frac{\partial \langle u_{DD} \rangle}{\partial r} = -\frac{8\pi}{9} \frac{\mu^4 \rho^2}{T R^3}, \quad (7.2.71)$$

where  $r$  is the DD separation and  $R$  is a suitable cut off. This approximation holds only for  $-\mu^2/(Tr^3) \ll 1$ , cf. equation (7.2.69). Specifically we integrate this contribution into the equation of state (7.2.50) via the substitution

$$\varepsilon_0 = \varepsilon_{0,SL} - \frac{16\pi}{9qb_0 R^3} \frac{\mu^4}{T} \quad (7.2.72)$$

and by substitution of  $\varepsilon_{0,SL}$  in terms of

$$T_{c,SL} = -\frac{q\varepsilon_0}{4} \quad (7.2.73)$$

from equation (7.2.63) for  $n_c \rightarrow 1$ , we get for the inter-aggregate particle-particle interaction parameter

$$\varepsilon q = -\frac{4T_{c,SL}}{T} - \frac{16\pi}{9b_0 R^3} \frac{\mu^4}{T^2}. \quad (7.2.74)$$

Here the SL complies again with the LJ fluid in the case of the ST system. Insertion of equation (7.2.72) into equation (7.2.63) yields

$$\begin{aligned} T_c(\mu) &= T_{c,SL} & \text{for } \mu^2 &= 0, \\ T_c(\mu) &\propto \mu^2 & \text{for } \mu^2 &\rightarrow \infty \end{aligned} \quad (7.2.75)$$

and fixed critical mean chain length  $n_c$ . This is in reassuring agreement with simulation data (cf. figure 7.5). We note that the applicability of equation (7.2.71) rests on the premise that the individual dipoles retain sufficient rotational freedom even as part of a reversible chain. So in the case of aggregation the persistence length of the chains should fulfill the condition  $l_p < R$ .

### Transfer matrix model for an isolated chain

To give an estimation of the intra-aggregate interaction parameter  $\varepsilon_i$ , we employ the transfer matrix model which is useful to calculate canonical partition functions for which  $\exp[-\beta\mathcal{H}]$  can be separated in factors of identical form. We get the lattice free energy in the limit of a single infinitely long chain ( $s \rightarrow \infty$ ), vanishing  $\phi$  and  $N_s = 1$  from equation (7.2.38)

$$\frac{F_L}{sT} = \varepsilon_i - \ln[q - 1]. \quad (7.2.76)$$

In order to find an approximate expression for  $\varepsilon_i = \varepsilon_i(\mu^2)$  we estimate the configuration free energy of an isolated chain consisting of  $s$  ST dipoles based on the potential energy

$$U_{conf}^{(chain)} = \sum_{i=1}^{s-1} \left( u_{LJ}(r_{i,i+1}) + \vec{\mu}_i \underset{\sim}{\mathbb{T}} \vec{\mu}_{i+1} \right), \quad (7.2.77)$$

where  $u_{LJ}$  is the LJ pair potential (2.1.1) and  $\underset{\sim}{\mathbb{T}}$  the dipole tensor (2.1.13). The summation includes the interactions of nearest neighbors only, which in the one-dimensional case is not unreasonable. In addition we assume a uniform "bond length"  $r = |\vec{r}_{i,i+1}|$ . The canonical configurational partition function now becomes

$$Q_{conf}^{(chain)} = \int d\{\Omega_{\vec{r}}\} d\{\Omega_{\vec{\mu}}\} \exp \left[ -\frac{1}{T} U_{conf}^{(chain)} \right], \quad (7.2.78)$$

where  $\int d\{\Omega_{\vec{r}}\} d\{\Omega_{\vec{\mu}}\}$  denotes the integration over all possible paths and dipole orientations of the chain. We want to evaluate the integration on a simple cubic lattice, i.e.

$$\int d\{\Omega_{\vec{r}}\} d\{\Omega_{\vec{\mu}}\} \approx \left( \frac{4\pi}{q} \right)^{2s-1} \sum_{\{\Omega_{\vec{r}}\}, \{\Omega_{\vec{\mu}}\}}. \quad (7.2.79)$$

Note that there are  $s$  dipole moments connected by  $s - 1$  "bonds". The chain becomes a path on the cubic lattice ( $q = 6$ ). Every lattice site on the path is occupied by a dipole  $\vec{\mu}_i$  oriented along one of six possible lattice directions. The possible orientations are given by the vectors  $\vec{e}^{(1)} = (1, 0, 0)$ ,  $\vec{e}^{(2)} = (0, 1, 0)$ ,  $\vec{e}^{(3)} = (0, 0, 1)$ ,  $\vec{e}^{(4)} = -\vec{e}^{(1)}$ ,  $\vec{e}^{(5)} = -\vec{e}^{(2)}$ , and  $\vec{e}^{(6)} = -\vec{e}^{(3)}$ , i.e.  $\vec{\mu}^{(k)} = \mu \vec{e}^{(k)}$ . Because every segment along the chain contributes the same to the total LJ interaction we may write this factor in front of the sum and expand

the exponential function

$$Q_{conf}^{(chain)} = \left(\frac{4\pi}{q}\right)^{2s-1} \exp\left[-\frac{(s-1)u_{LJ}(r)}{T}\right] \quad (7.2.80)$$

$$\times \sum_{\{\Omega_{\vec{r}}\}, \{\Omega_{\vec{\mu}}\}} \langle \mu_1 | \tilde{\mathbb{M}} | \mu_2 \rangle \langle \mu_2 | \tilde{\mathbb{M}} | \mu_3 \rangle \dots \langle \mu_{s-1} | \tilde{\mathbb{M}} | \mu_s \rangle \langle \mu_s | \tilde{\mathbb{M}}_0 | \mu_1 \rangle \quad (7.2.81)$$

$$= \left(\frac{4\pi}{q}\right)^{2s-1} \exp\left[-\frac{(s-1)u_{LJ}(r)}{T}\right] \sum_{\{\Omega_{\vec{r}}\}, \{\Omega_{\vec{\mu}}\}} \langle \mu_1 | \tilde{\mathbb{M}}^{s-1} \tilde{\mathbb{M}}_0 | \mu_1 \rangle \quad (7.2.82)$$

$$= \left(\frac{4\pi}{q}\right)^{2s-1} \exp\left[-\frac{(s-1)u_{LJ}(r)}{T}\right] \text{Tr} \left( \tilde{\mathbb{M}}^{s-1} \tilde{\mathbb{M}}_0 \right), \quad (7.2.83)$$

with  $|\mu_i\rangle = \vec{\mu}_i$  and

$$\sum_{\{\Omega_{\vec{r}}\}, \{\Omega_{\vec{\mu}}\}} |\mu_i\rangle \langle \mu_i| = \mathbb{1}. \quad (7.2.84)$$

The elements of the transfer matrix  $\tilde{\mathbb{M}}$  are given by

$$\tilde{\mathbb{M}}_{kl} = \sum_{\nu=1}^6 \exp\left[-\frac{1}{T} \sum_{\alpha, \beta} \mu_{\alpha}^{(k)} \mathbb{T}_{\alpha\beta}^{(\nu)} \mu_{\beta}^{(l)}\right] \quad (7.2.85)$$

( $k, l = 1, \dots, 6$ ) and  $\mathbb{T}_{\alpha\beta}^{(\nu)}$  are the components of the dipole tensor

$$\mathbb{T}_{\alpha\beta}^{(\nu)} = \frac{1}{r^3} (\delta_{\alpha\beta} - 3e_{\alpha}^{(\nu)} e_{\beta}^{(\nu)}), \quad (7.2.86)$$

cf. equation (2.1.14). The orientations of the dipole moments are indicated by ( $k$ ), ( $l$ ) and the direction of the intermolecular axis by ( $\nu$ ). The elements of the matrix  $\tilde{\mathbb{M}}_0$  are simply all equal to 1, since we consider chains with open non-interacting ends. Note that the trace is independent from the basis, hence we can write

$$\text{Tr} \left( \tilde{\mathbb{M}}^{s-1} \right) = \sum_i \lambda_i^{s-1}, \quad (7.2.87)$$

where  $\lambda_i$  are the eigenvalues of  $\tilde{\mathbb{M}}$ . Approximating  $\text{Tr} \left( \tilde{\mathbb{M}}^{s-1} \right) \approx \lambda_{max}^{s-1}$ , where

$$\lambda_{max}(r) = 2e^{2a}(1 + 2e^{-a} + 12e^{-2a} + 2e^{-3a} + e^{-4a}) \quad (7.2.88)$$

is the largest eigenvalue of  $\tilde{\mathbb{M}}$  with  $a = \mu^2/(Tr^3)$ , we obtain for the configuration free energy of the chain

$$\frac{1}{sT} F_{conf}^{(chain)} = -\frac{1}{s} \ln Q_{conf}^{(chain)} \quad (7.2.89)$$

$$\approx \frac{s-1}{s} \min_r \left( \frac{u_{LJ}(r)}{T} - \ln \left[ \frac{\lambda_{max}(r)}{q^2} \right] \right) - \frac{2s-1}{s} \ln[4\pi], \quad (7.2.90)$$

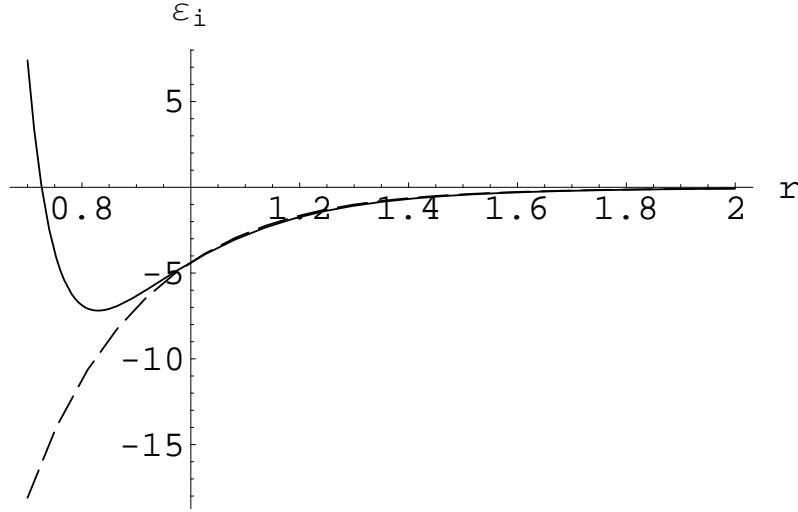


Figure 7.2: Comparison of the intra-aggregate interaction parameter  $\epsilon_i$  according to the expression in square brackets in equation (7.2.91) (solid line) to  $\epsilon_i$  according to the expression in square brackets in equation (7.2.92) (dashed line) plotted vs. "bond length"  $r$  for  $T = 10$  and  $\mu^2 = 36$ . Note that  $\epsilon_i(\mu^2/(Tr_0^3)) \approx -9.7$  (using equation (7.2.92)) and  $r_0 \approx 0.73$  in this special case.

Note that  $\min_r$  accounts for the fact that  $r$  is a variable parameter and the free energy becomes minimal in equilibrium. Comparing equation (7.2.76) with equation (7.2.90) we find that  $\epsilon_i$  is given by

$$\epsilon_i \approx \left[ \frac{u_{LJ}(r)}{T} - \ln \lambda_{max}(r) + 2 \ln q \right]_{r=r_{min}}, \quad (7.2.91)$$

where we have replaced  $(s-1)/s$  by unity. Here  $r_{min}$  is the separation for which the expression (7.2.91) acquires its minimum. Note also that the term  $(2s-1)/s \ln[4\pi]$  which appears in equation (7.2.90) is missing here. This is because a factor  $s \ln[4\pi]$ , corresponding to the dipole orientation, is not present in the lattice free energy. The remaining part,  $(s-1) \ln[4\pi]$  corresponds to the orientation of the bonds in the off lattice case, which in the lattice model is replaced by the term  $\ln[q-1]$ . Notice that for  $\mu^2 = 0$  we find  $\epsilon_i \approx u_{LJ}(r_{min})/T$ . Because the LJ fluid is our SL we must not use (7.2.91) directly but rather

$$\epsilon_i \approx [-\ln \lambda_{max}(r_{min}) + 2 \ln q]_{r=r_{min}}, \quad (7.2.92)$$

where  $r_{min}$  is the optimal monomer separation within a chain computed via minimization of expression (7.2.91).

The last ingredient to our theory of the  $\mu^2$  dependence of the critical point is the relation

$$b_0 \approx b_{0,SL} \frac{r_0}{r_{0,SL}}. \quad (7.2.93)$$

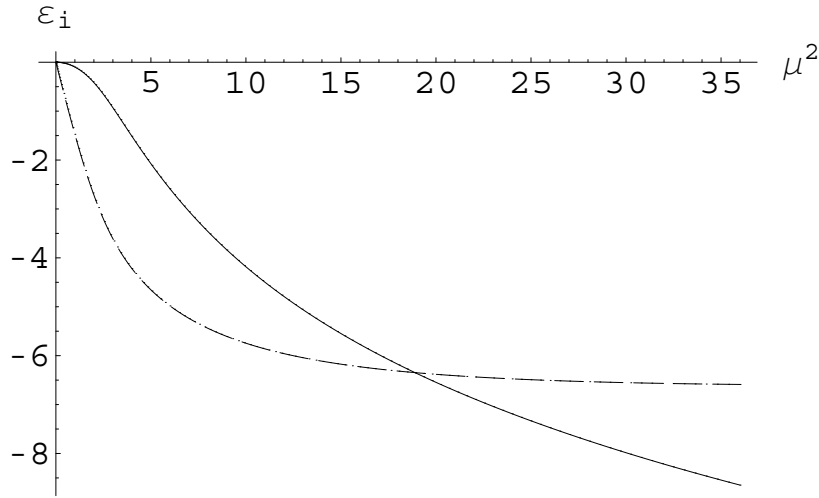


Figure 7.3: Based on the theoretical curves shown in figure 7.5 this plot compares intra-aggregate interaction parameter  $\varepsilon_i(\mu^2/(T_c r_0^3))$  (solid line) at the critical point with the simple approximation  $-2\mu^2/T_c$  (dashed line).

Here  $r_0$  is the root of expression (7.2.91), and  $r_{0,SL} = 1$  is the root of the same expression in the limit  $\mu^2 = 0$ . Because the dipolar interaction within a chain leads to an attraction increasing with increasing  $\mu^2$  we see from equation (7.2.62) that at constant  $n_c$  this leads to an increase of the critical monomer number density  $\rho_c = \phi_c/b_0$ . However, if  $n_c$  is increasing with increasing  $\mu^2$  then the competition of the two effects will determine  $\rho_c(\mu^2)$ .

The two quantities  $r_{min}$  and  $r_0$  are illustrated in figure 7.2, which shows the dependence of the expression (7.2.91) on  $r$  for  $T = 10$  and  $\mu^2 = 36$ . The minimum of this expression (solid line) is  $r_{min}$  and the function  $-\ln \lambda_{max}(r) + 2 \ln q$  (dashed line) evaluated at  $r = r_{min}$  is  $\varepsilon_i(\mu^2/(T r_{min}^3)) \approx -9.7$  for this temperature and dipole strength. In addition  $r_0 \approx 0.73$  is the root of expression (7.2.91) in this special case. Figure 7.3 shows the comparison of  $\varepsilon_i(\mu^2/(T_c r_{min}^3))$  plotted vs. dipole strength with the simple approximation  $-2\mu^2/T_c$ . We note that the simple approximation comes close to being constant for  $\mu^2 > 10$ .

In order to compute the critical point shift as function of  $\mu^2$  together with the critical aggregation number  $n_c$ , we need to solve the equations (7.2.46), (7.2.62), and (7.2.63) using (7.2.72), (7.2.92), and (7.2.93). Introducing the definitions  $x_\rho \equiv \rho_c/\rho_{c,SL}$  and  $x_T \equiv T_c/T_{c,SL}$  we may rewrite the above set of equations, i.e. equations (7.2.46), (7.2.62), and

(7.2.63), in a more transparent form:

$$n_c = \frac{1}{2} + \frac{1}{2} \sqrt{1 + 4(q-1)e^{-\varepsilon_i} f_\rho(n_c)} \quad (7.2.94)$$

$$x_\rho \approx \frac{f_\rho(n_c)}{r_0 f_\rho(n_{c,SL})} \quad (7.2.95)$$

$$\frac{1}{x_T} \left( 1 + \frac{\kappa \mu^4}{r_0} \frac{1}{x_T} \right) \approx \frac{f_T(n_{c,SL})}{f_T(n_c)}, \quad (7.2.96)$$

where

$$\kappa = \frac{16\pi \rho_{c,SL} f_T(n_{c,SL})}{9R^3 T_{c,SL}^2 f_\rho(n_{c,SL})}, \quad (7.2.97)$$

$r_0 = r_0(\mu^2, T_c)$  and  $\varepsilon_i = \varepsilon_i(\mu^2/(T_c r_{min}^3))$ . Here  $\rho_{c,SL}$  and  $T_{c,SL}$  are the respective values for the LJ system.

Assuming for the moment constant  $r_{min}$  and  $r_0$ , we observe that  $x_\rho$  or  $\rho_c$  will simply decrease if the average critical chain length increases at  $T_c$ . We do expect an increase of  $n_c$ , because for small dipole strength  $\mu^2$  increases faster than  $T_c$  as equation (7.2.96) shows. However, for long chains  $f_T(n_c)$  approaches 1 and  $T_c \propto \mu^2$ . This in turn implies that  $\varepsilon_i$  becomes constant, which means that  $n_c$  and thus also  $\rho_c$  approaches a constant. This basic behavior, i.e. an initial slow increase of  $T_c$ , as function of  $\mu^2$ , which subsequently becomes steeper and proportional to  $\mu^2$  and the decrease of  $\rho_c$  which then levels off as soon as  $T_c \propto \mu^2$ , is modified by the  $\mu^2$ -dependence of  $r_{min}$  and  $r_0$ . A decrease of  $r_{min}$  with increasing  $\mu^2$  promotes growth because it tends to increase  $\varepsilon_i$ . This will decrease  $f_\rho(n_c)$  causing  $\rho_c$  to decrease. On the other hand the factor  $1/r_0$  in equation (7.2.95) will counteract this decrease to some extent.

### 7.2.3 Including ferroelectric order

This model does not yet include ferroelectric order. A mean field description for the orientational potential energy can be derived by using Debye's approximation [21] of the local field

$$\vec{E}_{loc}^{(D)} = \frac{4\pi\rho}{3} \frac{\epsilon + 2}{\epsilon - 1} \langle \vec{\mu} \rangle, \quad (7.2.98)$$

experienced by a point dipole in the center of a spherical cavity inside a dielectric medium with static dielectric constant  $\epsilon$ . Here  $\langle \vec{\mu} \rangle$  is the mean dipole moment of the sample (mean field!). We will discuss this description in chapter 8 in more detail. Employing Debye's approximation we derive the orientational potential energy

$$U_{orient} = -\frac{1}{2} \sum_{i=1}^N \vec{E}_{loc}^{(D)} \cdot \vec{\mu}_i \quad (7.2.99)$$

for a system of  $N$  point dipoles. This leads to the canonical orientation partition function

$$Q_{orient} = \frac{N!}{\prod_{\nu} N_{\nu}! \left(\frac{4\pi}{\Delta\Omega}\right)^N} \exp \left[ \frac{1}{2T} \sum_{i=1}^N \vec{E}_{loc}^{(D)} \cdot \vec{\mu}_i \right] \quad (7.2.100)$$

$$= \frac{N!}{\prod_{\nu} N_{\nu}! \left(\frac{4\pi}{\Delta\Omega}\right)^N} \exp \left[ \frac{\mu}{2T} \sum_{\nu} N_{\nu} \vec{E}_{loc}^{(D)} \cdot \vec{e}_{\nu} \right]. \quad (7.2.101)$$

Here  $N_{\nu}$  is the number of indistinguishable dipoles pointing into a solid angle element  $\Delta\Omega_{\nu} = \Delta\Omega$  with  $N = \sum_{\nu} N_{\nu}$  and  $(4\pi/\Delta\Omega)^N$  is the total number of orientational states [22]. The unit vector  $\vec{e}_{\nu}$  points into  $\Delta\Omega_{\nu}$ . The factor  $N!/\prod_{\nu} N_{\nu}!$  is the number of distinguishable distributions of the dipole orientations to the solid angle elements. The attending orientational free energy is

$$\frac{b_0 F_{orient}}{VT} = -\frac{b_0}{V} \ln Q_{orient} \quad (7.2.102)$$

$$= \frac{b_0}{V} \left( -N \ln N + N + \sum_{\nu} \left( N_{\nu} \ln N_{\nu} - N_{\nu} \frac{4\pi\rho}{6T} \mu^2 d \cos \theta_{\nu} \right) + N \ln \left[ \frac{4\pi}{\Delta\Omega} \right] \right) \quad (7.2.103)$$

$$= \phi \left[ \left( \frac{3}{2} - \frac{2\pi\rho\mu^2}{3T} \right) d^2 + \frac{9}{20} d^4 + \frac{99}{350} d^6 + \frac{1539}{7000} d^8 \dots \right], \quad (7.2.104)$$

where  $\mu d$  is the average dipole moment along the director and  $\theta_{\nu} = \angle(\langle \vec{\mu} \rangle, \vec{e}_{\nu})$ . In addition  $(\epsilon + 2)/(\epsilon - 1)$  is set equal to unity. The route from equation (7.2.103) to (7.2.104) is analogous to the calculation of the free energy for classical spins by the mean field approach and is presented in section 6.1 of reference [19]. Here  $d$  is an order parameter for the transition from the isotropic to the ferroelectric liquid. When the coefficient of the leading term in equation (7.2.104) changes sign an orientationally ordered phase becomes stable compared to the isotropic fluid or vice versa. The condition

$$\frac{3}{2} - \frac{2\pi\rho\mu^2}{3T_{cf}^{(D)}} = 0 \quad (7.2.105)$$

yields an isotropic-ferroelectric transition temperature  $T_{c,f}^{(D)} = (4\pi/9)\rho\mu^2$  for Debye's approach. An example for  $F_{orient}/(NT)$ , dependend on the order parameter  $d$ , is given in figure 7.4 ( $\mu^2 = 1$ ,  $\rho = 1$ ) for temperatures  $T < T_{cf}$ ,  $T = T_{cf}$  and  $T > T_{cf}$ . For temperatures higher than the critical temperature  $T_{cf}$  the orientational free energy is monotonously increasing and has its minimum at  $d = 0$ . The minimum of the free energy determines equilibrium, thus we can state that there is no ferroelectric phase stable. For  $T < T_{cf}$  the free energy has its minimum at  $d \neq 0$ , meaning there is a non vanishing orientation of the dipoles and an ferroelectric phase becomes stable. The equilibrium value

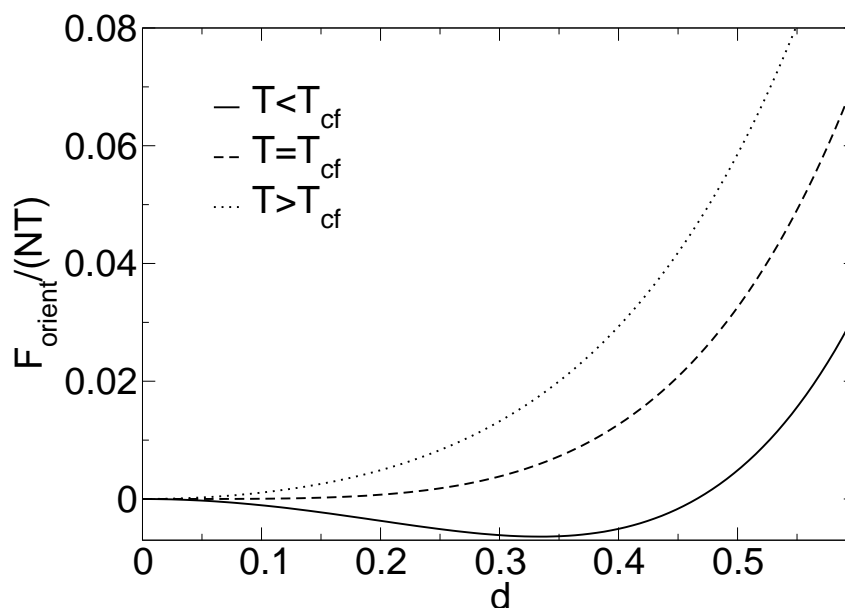


Figure 7.4: The orientational free energy  $F_{orient}/(NT)$  from the Debye approach vs. the order parameter for the ferroelectric phase  $d$ . For  $T > T_{cf}$  there is no orientational order in equilibrium. For  $T < T_{cf}$  the orientational free energy has its minimum for non vanishing  $d$ .

of  $d$  in equation (7.2.104), i.e.  $d^{(0)}$ , is determined by the minimum of the free energy

$$\left. \frac{b_0}{VT} \frac{\partial F_{orient}}{\partial d} \right|_{T,\phi} = 0. \quad (7.2.106)$$

However, the critical temperature predicted by Debye's approach is considerably too high, compared to simulation data (cf. chapter 8). Here we account for these simulation results by scaling the Debye transition temperature,  $T_{cf}^{(D)}$  via

$$T_{cf} = \kappa T_{cf}^{(D)}, \quad (7.2.107)$$

where  $\kappa \approx 0.1361$  is chosen to reproduce the transition temperature  $T_{cf}^{(ST)}$  obtained on the basis of previous simulation work<sup>1</sup>.

Thus the combined free energy is

$$F = F_L + F_{orient}(d^{(0)}) \quad (7.2.108)$$

and the combined pressure

$$P = P_L + P_{orient}(d^{(0)}), \quad (7.2.109)$$

<sup>1</sup>Note that this  $\kappa$  is not related to  $\kappa$  in equation (7.2.97)

where

$$\frac{b_0 P_{orient}}{T} = - \left. \frac{b_0}{T} \frac{\partial F_{orient}}{\partial V} \right|_{T, N_s} = - \frac{2\pi\phi^2 \mu^2}{3T} (d^{(0)})^2. \quad (7.2.110)$$

Note that  $\phi = b_0 N/V$  and  $\rho = N/V$  in (7.2.104) are both dependent on volume. With the exception of possible chain formation this model has been used before by Zhang and Widom [12] to investigate the global phase diagram of dipolar fluids (Zhang and Widom use the van der Waals free energy to model  $F_{config}$ ).

With the knowledge of the equation of state (7.2.109) and the Helmholtz free energy (7.2.108) we are able to determine the GL coexistence curves from the lattice theory. For this we solve simultaneously

$$P(T, \phi_g) = P(T, \phi_l) \quad (7.2.111)$$

$$\mu(T, \phi_g) = \mu(T, \phi_l), \quad (7.2.112)$$

where

$$\mu = \frac{G}{N} = \frac{F}{N} + \frac{b_0 P}{\phi} \quad (7.2.113)$$

using the computer algebra package Mathematica [20]. Here  $\phi_g$  and  $\phi_l$  are the coexisting volume fractions of gas (g) and liquid (l).

## 7.3 Comparison to molecular dynamics simulation results

### 7.3.1 Gas-liquid critical behaviour

#### The Stockmayer fluid

In this section we want to compare the data for critical points and GL coexistence curves obtained by simulation for the ST fluid, reported in section 6.3, with the results from lattice theory developed in section 7.2. Figure 7.5 compiles and compares simulation results for the GL critical temperature  $T_c$  and the critical density  $\rho_c$  of the ST fluid plotted versus dipole strength  $\mu^2$ . The filled circles denote data points obtained by this work using MD simulations in conjunction with the Maxwell construction method to determine the coexisting GL densities, shown in table 6.2. The hollow circles denote data points obtained by Florian Pesth [25] via the same method, but slightly different long-range corrections. He calculated the reaction field from the Onsager equation [26]. All other symbols denote previously published data by other groups [5, 6, 23, 24]. Notice that the data for the vLS system taken from reference [5] were mapped via the relations (2.2.3), (2.2.4) and (2.2.5) to the ST system. The dotted line in the upper panel of figure 7.5 is a linear fit to the critical temperature  $T_c = b + m\mu^2$  (with  $b = 1.0815$ ,  $m = 0.25761$ )

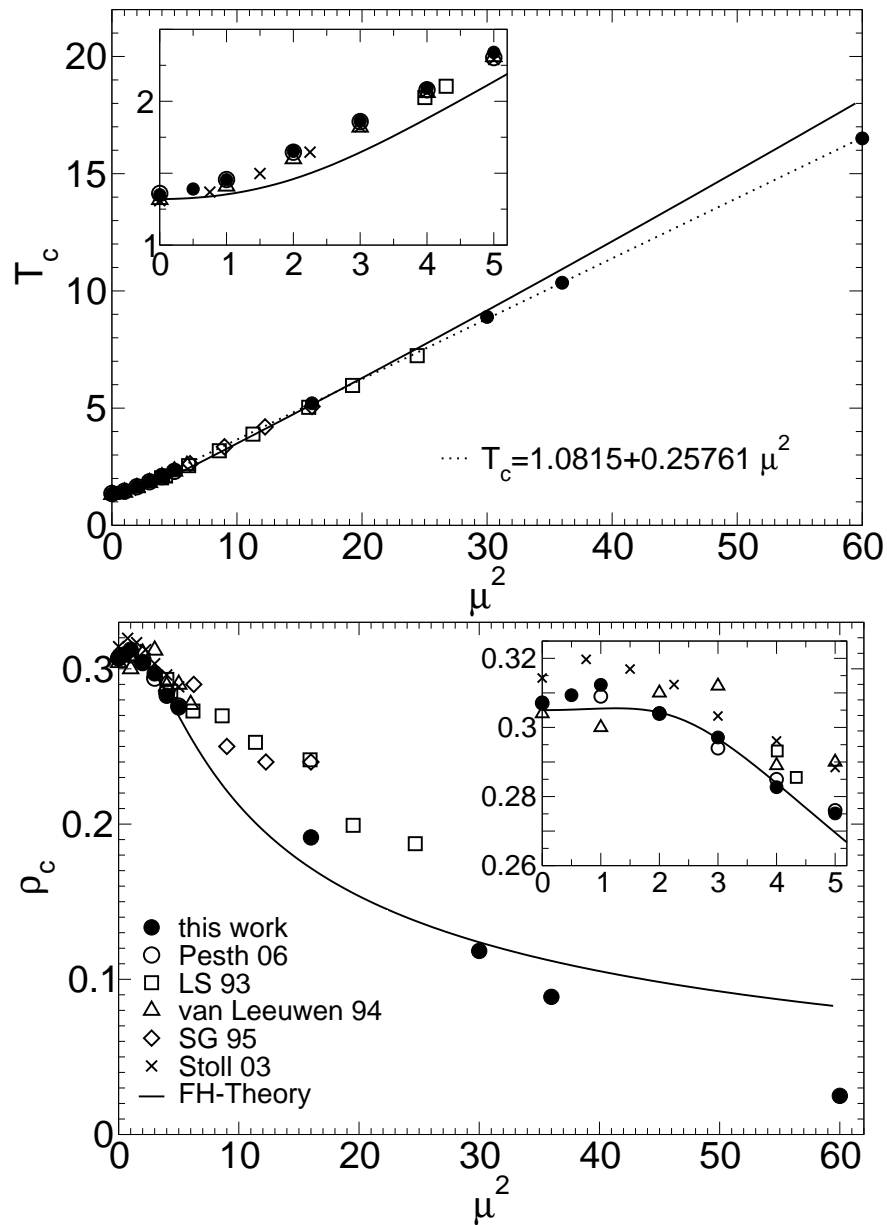


Figure 7.5: Top: GL critical temperature  $T_c$  of the ST fluid versus dipole strength  $\mu^2$ . Symbols indicate computer simulation results (this work and references [5,6,23–25]). Bottom: GL critical density  $\rho_c$  of the ST fluid vs. dipole strength  $\mu^2$ . The solid lines are the theoretical results obtained from the FH model for  $R = 4.1$ . The insets are magnifications of the small dipole strength range.

including data only for  $\mu^2 \geq 3$ . The theoretical curves (solid lines) are obtained by numerical solution of equations (7.2.94) to (7.2.96) computing  $\varepsilon_i$  according to equation (7.2.92) using  $r_{min}$  obtained via the minimization condition (7.2.91). Here we use the LJ critical constants  $\rho_{c,SL} = 0.305$  and  $T_{c,SL} = 1.32$ . The only adjustable parameter is the cut off radius  $R$  which is set to  $R = 4.1$ . The resulting agreement with the simulation results for the critical temperature  $T_c$  versus dipole strength  $\mu^2$  shown in the top panel of figure 7.5 is excellent in the range of dipole strength  $\mu^2 \leq 36$ . For  $\mu^2 = 60$  there is an obvious deviation, but the error of  $\sim 10\%$  is still small. The bottom panel shows the theoretical results for the critical density  $\rho_c$  versus  $\mu^2$  in comparison to the simulation results. We do find quite reasonable agreement between the theory and our simulations over the range of dipole strengths  $\mu^2 \leq 36$ . Here for  $\mu^2 = 60$  the deviations become quite large. The reason for this disagreement may be the choice of  $R = 4.1$ . Since  $R$  is the cut off for the long-range contribution for thermally averaged dipole orientations, cf. equation (7.2.71), the persistence length for chains should be smaller than  $R$  ( $l_p < R$ ). From figure 5.12 we know that this holds for  $\mu^2 = 36$ , but the persistence length has not yet been investigated for  $\mu^2 = 60$ . However, both our theory and the simulations yield critical densities which are systematically lower than the values obtained previously with the GEMC method in the range  $\mu^2 > 5$ . In addition, and more important, we do observe GL criticality for  $\mu^2 = 30, 36$  and  $60$ . This is well above the limit  $\mu^2 \approx 25$  beyond which the critical point should disappear. The path of the critical point obtained by lattice theory in the  $T$ - $\rho$  plane parameterized by the dipole moment, is the solid line in figure 6.9 (top panel).

It is worth pointing out that an equally good result for  $T_c$  versus  $\mu^2$  may be obtained by adding the pressure long-range contribution (7.2.71) to any simple monomer equation of state (for instance equation (7.2.50) with  $n = 1$  or the van der Waals equation (6.2.1)). It is the decrease of the critical density with increasing  $\mu^2$  which presents a challenge. In the case of equation (7.2.50) with  $n = 1$  or the van der Waals equation the critical density is inversely proportional to the monomer volume. In order for the critical density to drop this volume must effectively increase. The reversible aggregation of monomers into linear chains offers a simple mechanism as shown by equation (7.2.62). Even though the FH type lattice model employed here is not difficult, there is an even simpler way to understand this point intuitively. Let  $b$  describe the volume parameter in the van der Waals equation. Then, as just mentioned, the critical chain number density  $\rho_c^{(chain)}$  is proportional to  $b^{-1}$ , i.e.  $\rho_c^{chain} \propto b^{-1}$ . If now a reversible chain consisting of  $n$  monomers can be treated as an "ideal coil" or "blob" with a mean diameter  $\sim n^{1/2}$  and therefore with  $b \sim n^{3/2}$  interacting with other such "blobs" the resulting critical density of this fluid of "blobs" obeys  $\rho_c^{chain} \sim n^{-3/2}$ . Multiplying  $\rho_c^{chain}$  with  $n$  we obtain for the monomer number density  $\rho_c \sim n^{-1/2}$ . This is exactly the same scaling behavior as in equation (7.2.62) for large  $n_c$ . The problem with this simple van der Waals picture is that there usually is significant overlap between "blobs" at the densities of interest. For instance, we can extend the scaling argument to the critical temperature, which in the van der Waals case is proportional to  $a/b$ , where  $a$  is the attraction parameter. Using  $a \propto n^2$  we obtain  $T_c \propto n^{1/2}$ , i. e. the critical temperature does not approach a finite value as  $n \rightarrow \infty$ . In the case at hand this yields a exaggerated rise of  $T_c$  with increasing  $\mu^2$ .

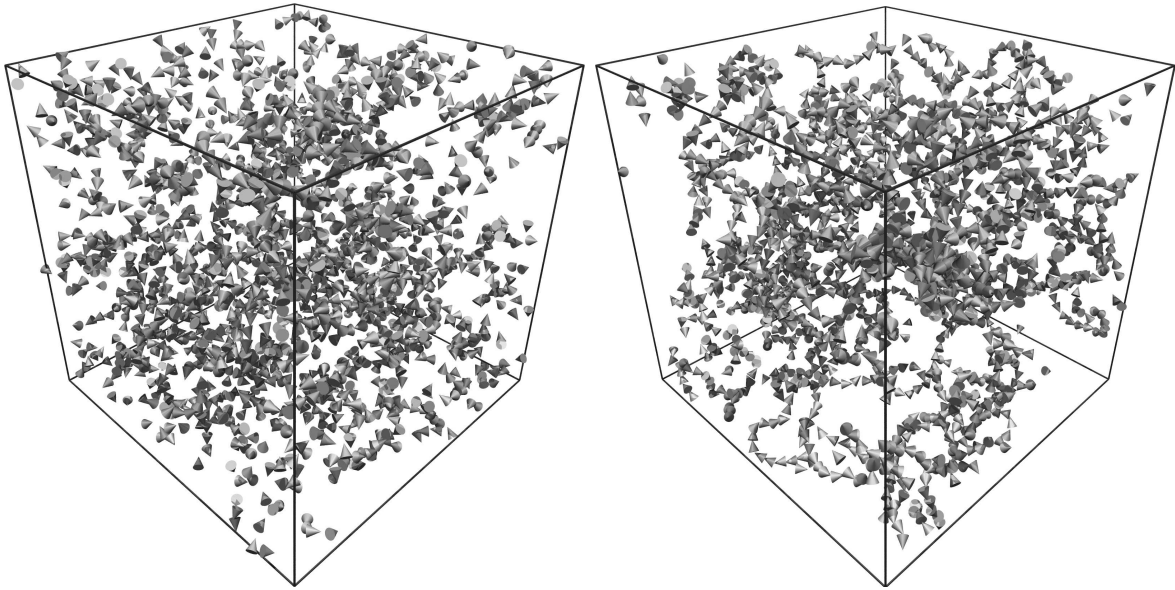


Figure 7.6: Snapshots taken during a MD computer simulation of 2048 ST particles with  $\mu^2 = 36$  at  $\rho = 0.099 (\approx \rho_c)$ . Left:  $T = 14.0$ ; right:  $T \approx T_c$ . At the critical temperature the particles form obvious chains. Considerably above the critical temperature the snapshot shows a more homogeneous gas of monomers.

The existence of chains near the GL critical point is illustrated pictorially in figure 7.6. The figure shows two snapshots taken during a molecular dynamics simulation of 2048 ST particles with  $\mu^2 = 36$  near the critical density. The left panel shows a system configuration at a temperature high enough to suppress the formation of long chains. The system looks more like a homogeneous gas of monomers. The right panel corresponds to  $T \approx T_c$ . In this case chain segments are clearly discernible. The preceding theoretical analysis of the critical point shift attributes the decreasing critical density to a corresponding increase of the average chain lengths. In order to support this point figure 7.7 shows the dependence of the average chain length at criticality obtained from MD simulations on dipole strength. Two ST particles are considered to be neighbors along a chain, if their distance is less than  $r_n$  (cf. subsection 5.3.2). Consequently the average chain length depends considerably on the value of  $r_n$  in the not very dilute phase. Nevertheless, we do observe a significant increase of the average chain length regardless of the specific  $r_n$ -value supporting our above premise. In addition to the simulation results the figure includes the theoretical dependence of  $n_c$  on  $\mu^2$  (corresponding to the solid lines in Fig. 7.5). The agreement between theory and simulation is qualitative. The theoretical  $n_c$  is plagued by a strong dependence on the details of the interaction between the Stockmayer particles. Quantitative agreement between theory and simulation can for instance be improved if an additional factor is introduced reducing the numerical value of  $\varepsilon_i$  in equation (7.2.92). However, this procedure does not yield additional physical insight beyond the level of the present one-parameter theory.

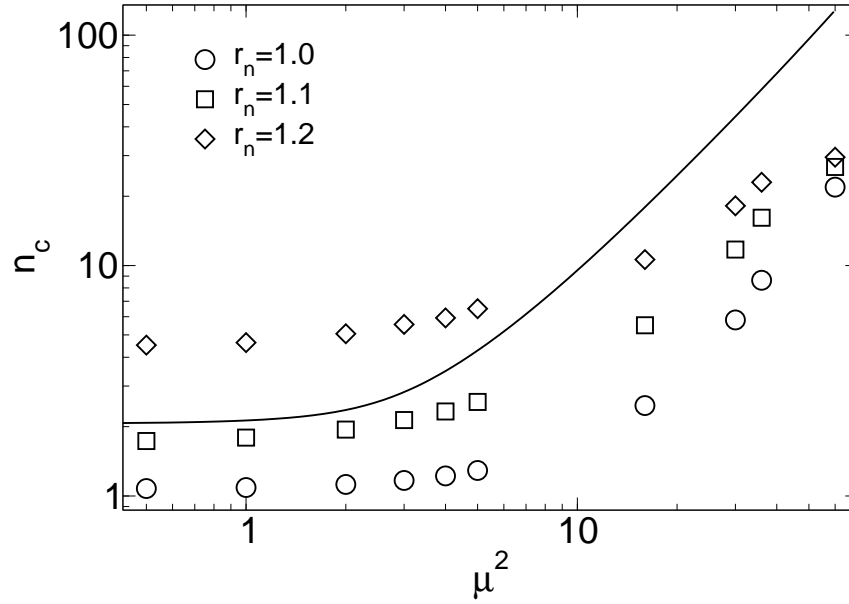


Figure 7.7: Mean aggregation number at the critical point  $n_c$  versus dipole strength  $\mu^2$ . Symbols: MD simulation point analyzed with the parameter  $r_n = 1.0, 1.1$  and  $1.2$  as described in subsection 5.3.2; solid line: theoretical results corresponding to the theoretical curves in figure 7.5.

### Comparison to gas-liquid criticality of alkanes

Here we want to draw a more explicit correspondence between the FH lattice description and an ordinary system of chain molecules at GL criticality. Figure 7.8 shows experimental critical point data for  $n$ -alkanes versus chain length  $n$ , i.e. their number of methylene groups. The solid curves are well known results following from the equation of state (7.2.50) [3], i.e.  $T_c = T_c^\infty n / (1 + \sqrt{n})^2$  with  $T_c^\infty = T_{Boyle}$ , the critical temperature for a system of infinitely long chains,  $\phi_c = 1 / (1 + \sqrt{n})$  and  $P_c$  accordingly. We emphasize that this is not an attempt to describe the critical data for  $n$ -alkanes quantitatively. This has been done elsewhere [27–29]. In addition, corrections to the FH critical point shift at large  $n$ , where  $n$  is the monodisperse chain length in pure polymer systems or in polymer-solvent mixtures also have been discussed (e.g., [30, 31]). Instead, the main purpose of figure 7.8 is to highlight similarities between the ST system near GL criticality and an ordinary fluid of linear polymer or polymerlike molecules. Notice that  $T_c^\infty$  is not known for  $n$ -alkanes. In the literature a rather wide range of values is discussed, e.g. 1100 K to 1700 K in Ref. [27]. Here we use  $T_c^\infty = 1300\text{K}$ . Notice that the function  $f_T(n)$  in equation (7.2.63) also approaches a constant value in the limit  $n \rightarrow \infty$ . It is the factor (7.2.74) which yields the  $\mu^2$ -dependence of  $T_c$  in the ST system. In the case of  $\rho_c$  we use  $\rho_c = m_0^{(n)} / b_0^{(n)} \phi_c$  simply setting  $m_0^{(n)} / b_0^{(n)} = 1$ . Here  $b_0^{(n)}$  is the volume per carbon subunit and  $m_0^{(n)}$  is its mass. The important point to note is that both

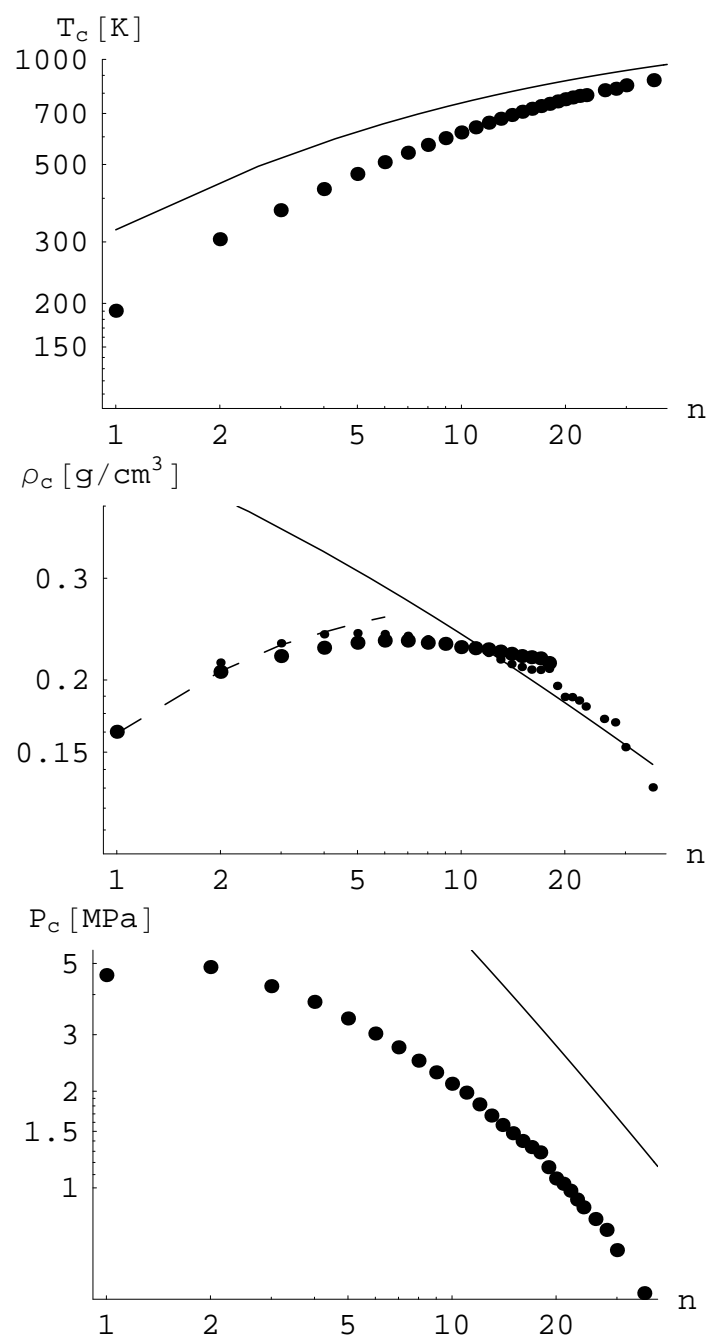


Figure 7.8: The critical point of  $n$ -alkanes as function of chain length  $n$ , i.e. the number of methylene groups. Large Dots: Experimental critical point data for  $n$ -alkanes taken from Table 2 in reference [27] vs. chain length  $n$ ; small dots: critical density computed via  $\rho_c = 6.718nP_c/T_c$ ; solid lines: FH theory with  $T_c^\infty = 1300\text{K}$  and  $b_0 = 1$  in the units used here; dashed line: density based on MP2-calculations of the all-trans molecular volume.

quantities depend on  $n$ . This is demonstrated by the dashed line in the middle panel of figure 7.8. The line connects the values  $(m_0^{(n)}/b_0^{(n)})/(m_0^{(1)}/b_0^{(1)})\rho_c^{methane}$  obtained for  $n = 1, 2, \dots, 6$  using the experimental critical density of methane.  $m_0^{(n)}/b_0^{(n)}$  is obtained by dividing the mass of the respective  $n$ -alkane by its volume computed via the quantum chemistry program Spartan [32] using second order Møller-Plesset perturbation theory (6-31G\* basis set) applied to all-trans conformations (for  $n > 4$ ). Notice that the initial rise of the critical density with  $n$  is the consequence of a shrinking volume per C-subunit essentially due to dispersion attraction. This is the motivation to include the relation (7.2.93) into the above theory, even though the maximum exhibited by  $\rho_c$  in figure 7.5 is much less pronounced in comparison to the maximum of the critical mass density in figure 7.8. In order to extend the available data for  $\rho_c$  to larger  $n$ -values we have assumed the relation  $\rho_c = 6.718nP_c/T_c$ . Data values obtained via this relation are represented by the smaller dots. Notice that  $P_c/(\rho_c T_c) = const$  is a fairly good approximation for  $n \leq 18$ , where  $\rho_c$  is known independently. For  $n > 18$  the scatter is considerable. But the extrapolation suggests that the experimental  $\rho_c$  may decrease in reasonable accord with the FH prediction. Finally, the solid line in the bottom panel of figure 7.8 is plotted using  $T_c^\infty = 1300\text{K}$  and  $b_0 = b_0^{(n)} = 1$  allowing a rough comparison between the slope of  $P_c$  for large  $n$  as obtained experimentally in comparison to the FH result.

### The modified Stockmayer fluid

Here we want to discuss the critical behaviour of the vLS system with the interaction energy, given by equation (2.3.1), at fixed dipole moment  $\mu_{vLS}^2$  and variable  $\lambda$ . Notice that the factor  $\lambda$  adjusts the strength of the dispersion attraction. Therefore we may infer the critical behaviour of purely dipolar systems without dispersion attraction, since the vLS potential includes the DSS potential in the limit  $\lambda \rightarrow 0$ . In recent research it is still a matter of debate, if purely dipolar systems exhibit a GL phase transition or not, as already discussed in subsection 6.3.4. Applying the scaling relations (2.2.3), (2.2.4) and (2.2.5) we map the data obtained for the ST system obtained by simulation and theory to the vLS system with fixed dipole strength  $\mu_{vLS}^2 = 4$  originally investigated by van Leeuwen and Smit [5]. Figure 7.9 shows the same critical data as in figure 7.5 converted via the above mentioned scaling relations to  $T_{c,vLS}$  versus  $\lambda$  as well as  $\rho_{c,vLS}$  versus  $\lambda$ . The dotted line in the upper panel is obtained by inserting the straight fit from figure 7.5, here  $T_{c,vLS} = b\lambda^2 + m\lambda^{1/2}$  (with  $b = 1.0815$ ,  $m = 0.25761$ ). Notice that the agreement with the simulation data is excellent for  $\lambda \leq 1.21$ . For  $\lambda > 1.21$  the deviation is expected, because this corresponds to  $\mu^2 < 3$  for the ST fluid in figure 7.5, where the dependence of  $T_c$  on  $\mu^2$  is not linear for the ST fluid. Notice also that  $T_{c,vLS} \sim \lambda^{1/2} \rightarrow 0$  for  $\lambda \rightarrow 0$  at fixed  $\mu_{vLS}^2$  corresponds to  $\mu^2 \rightarrow \infty$  for the ST system. Thus according to the scaling argument presented here, there should be no finite GL critical temperature in the DSS system ( $\lambda = 0$ ). For the critical density of the vLS system  $\rho_{c,vLS}$  (lower panel in figure 7.5) we do expect that it also vanishes for small  $\lambda$ , since the simulations yield a

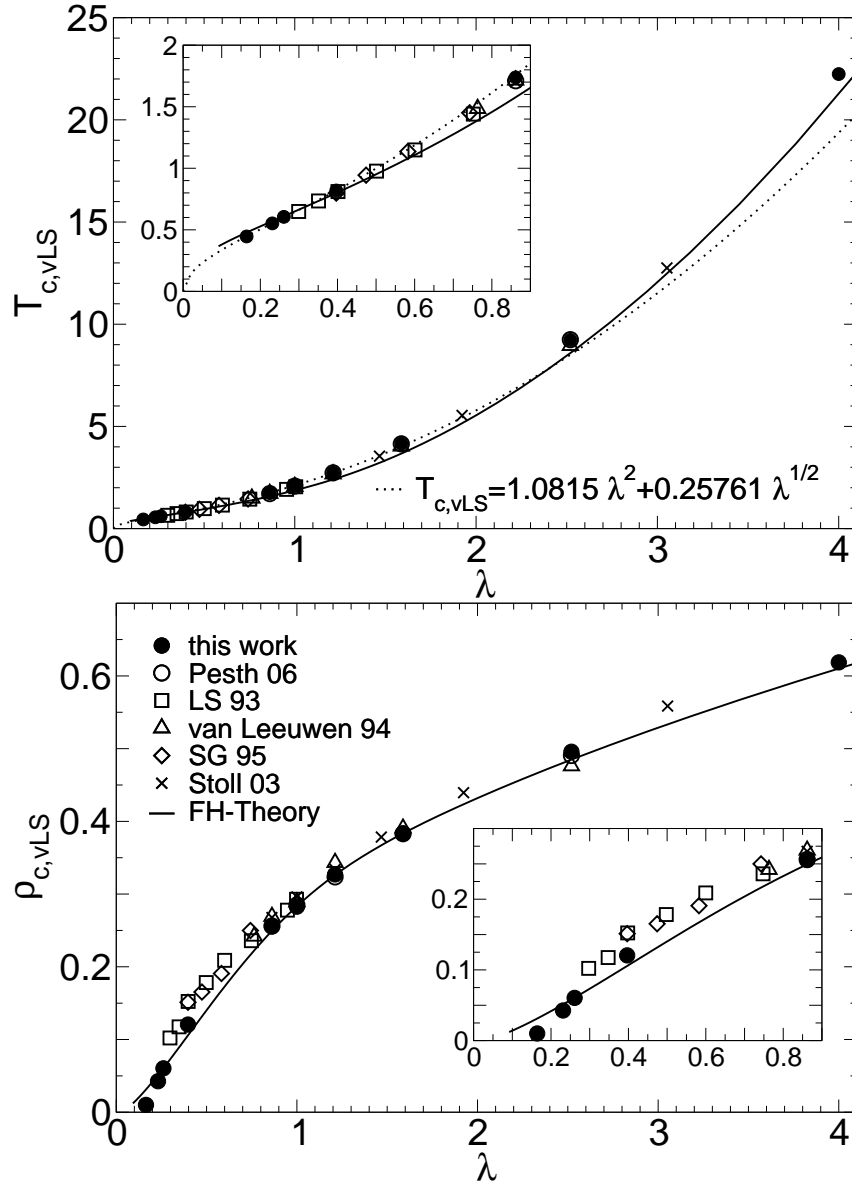


Figure 7.9: The critical properties of the ST system shown in figure 7.5 converted to the vLS system with  $\mu_{vLS}^2 = 4$ . Symbols indicate simulation results, the solid line is the result obtained via lattice theory and the dotted line corresponds to the linear approximation of  $T_{c,ST}$  shown in figure 7.5. Top: GL critical temperature  $T_{c,vLS}$  versus  $\lambda$ ; bottom: GL critical density  $\rho_{c,vLS}$  versus  $\lambda$ . The insets are magnifications for the small  $\lambda$  range.

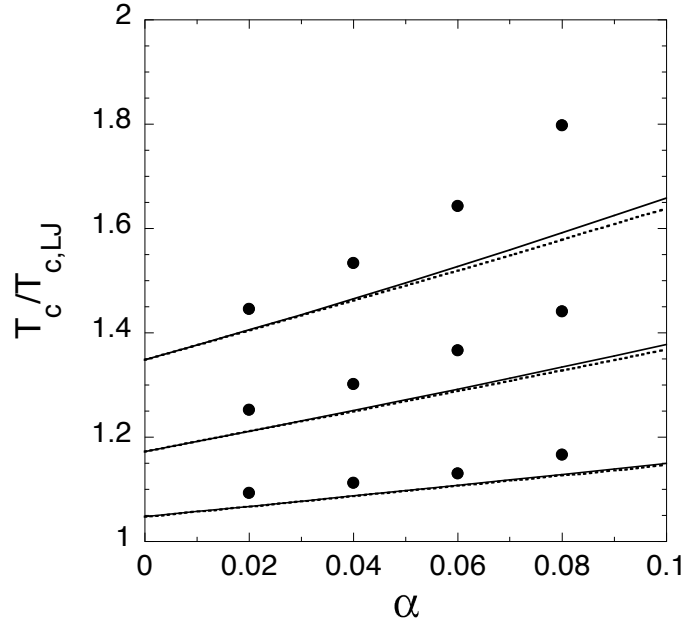


Figure 7.10: GL critical temperature  $T_c$  in units of the LJ GL critical temperature  $T_{c,LJ}$  vs. polarizability  $\alpha$ . From bottom to top:  $\mu^2 = 1, 2$  and  $3$ . The symbols are simulation data taken from table 6.2. Solid lines show the theoretical results including the second order in  $\alpha$ ; dotted lines show the theoretical results including the first order in  $\alpha$ .

monotonous decrease of  $\rho_c$  for the ST fluid with increasing  $\mu^2$ . The lattice theory in fact yields  $\rho_{c,vLS} \rightarrow 0$  for  $\lambda \rightarrow 0$ .

Therefore we conclude that in the DSS limit a vanishing GL critical temperature and a simultaneously vanishing GL critical density is consistent with the simulation data obtained thus far for the ST and vLS models. In principle of course there may be other types of phases and phase transitions intervening before the limit is reached, which are not included at present. However, the result for a vanishing critical point for  $\lambda \rightarrow 0$  is consistent with direct simulations on the DSS fluid reported in subsection 6.3.4.

### The polarizable Stockmayer fluid

Figure 7.10 shows the  $\alpha$ -dependence of the critical temperature for  $\mu^2 = 1, 2$ , and  $3$  of the pST. Symbols indicate results from simulation, the solid and dotted lines are theoretical results including the second and first order respectively (cf. appendix A). For the

theoretical results the ratio  $T_c/T_{c,LJ}$  is estimated using its relation

$$\frac{T_c}{T_{c,LJ}} = \frac{T_{Boyle}}{T_{Boyle,LJ}} \quad (7.3.1)$$

to the Boyle temperature  $T_{Boyle}$ . The index LJ always refers to the same quantity in the LJ system. If we assume that the investigated systems exhibit no chain formation, which is reasonable because the dipole strength is low, we get  $T_c$  and  $T_{Boyle}$  from lattice theory for mean chain length  $n = 1$ , coinciding with the SL and equations (7.2.55) and (7.2.73) apply. Comparing equations (7.2.55) and (7.2.73) yields  $T_{Boyle} = 4T_c$ . The Boyle temperature is obtained by the root of the second virial coefficient  $B_2(T_{Boyle}, \mu, \alpha) = 0$  which we calculate in appendix A. Notice that this estimate of  $T_c$  in terms of  $T_{Boyle}$  is close to the corresponding result obtained from other simple equations of state like the Dieterici or van der Waals equations of state. The resulting estimate of  $T_c$  via  $T_{Boyle}$  is in qualitative agreement with the simulation data.

### 7.3.2 Gas-liquid coexistence curves and ferroelectric order

Here we compare the theoretical results for the GL coexistence curves for the ST system, obtained by lattice theory including possible ferroelectric order by using our mean field model, with computer simulation results already discussed in chapter 6. Coexistence curves for dipole strengths  $\mu^2 = 1, 5, 16$  and  $36$  are compiled in figure 7.11. Symbols are simulation results, whereas hollow symbols are obtained by Maxwell construction and filled ones by Kofke integration, the solid lines are GL coexistence curves obtained by lattice theory by solving equations (7.2.111) and (7.2.112) simultaneously and the thick-dashed lines indicate the transition from the isotropic to ferroelectric liquid. Our mean field theory contains two adjustable parameters. The parameter  $R = 4.1$  introduced in equation (7.2.72) is fixed by the rise of the GL critical temperature shown in figure 7.5. The second parameter is  $\kappa$  which reduces the Debye transition temperature to the ferroelectric state, which is too high, to the value obtained by simulation (cf. chapter 8). Obviously the transition to the ferroelectric state occurs at rather low temperatures. Of the three typical phase diagrams discussed by Zhang and Widom [12] in their figure 2 only the topmost diagram appears to be realized in the ST system, except for the only coexistence of an isotropic gas and a ferroelectric ordered liquid for temperatures below the triple point for isotropic gas-isotropic liquid-ferroelectric ordered liquid coexistence. We reported already in figure 6.15 a strong decrease of the nematic order parameter in the GL coexistence region with decreasing density and the simple droplet simulations in subsection 5.3.1 showed no evidence for ferroelectric order in droplets at very low temperatures. So the only coexistence of an isotropic gas and a ferroelectric liquid below a certain temperature seems to be rather unlikely. We also note that the other phase diagrams obtained by Zhang and Widom in their figure 3 do follow from our mean field model if the parameter  $\kappa$  is increased. However, this is not appropriate for the ST system.

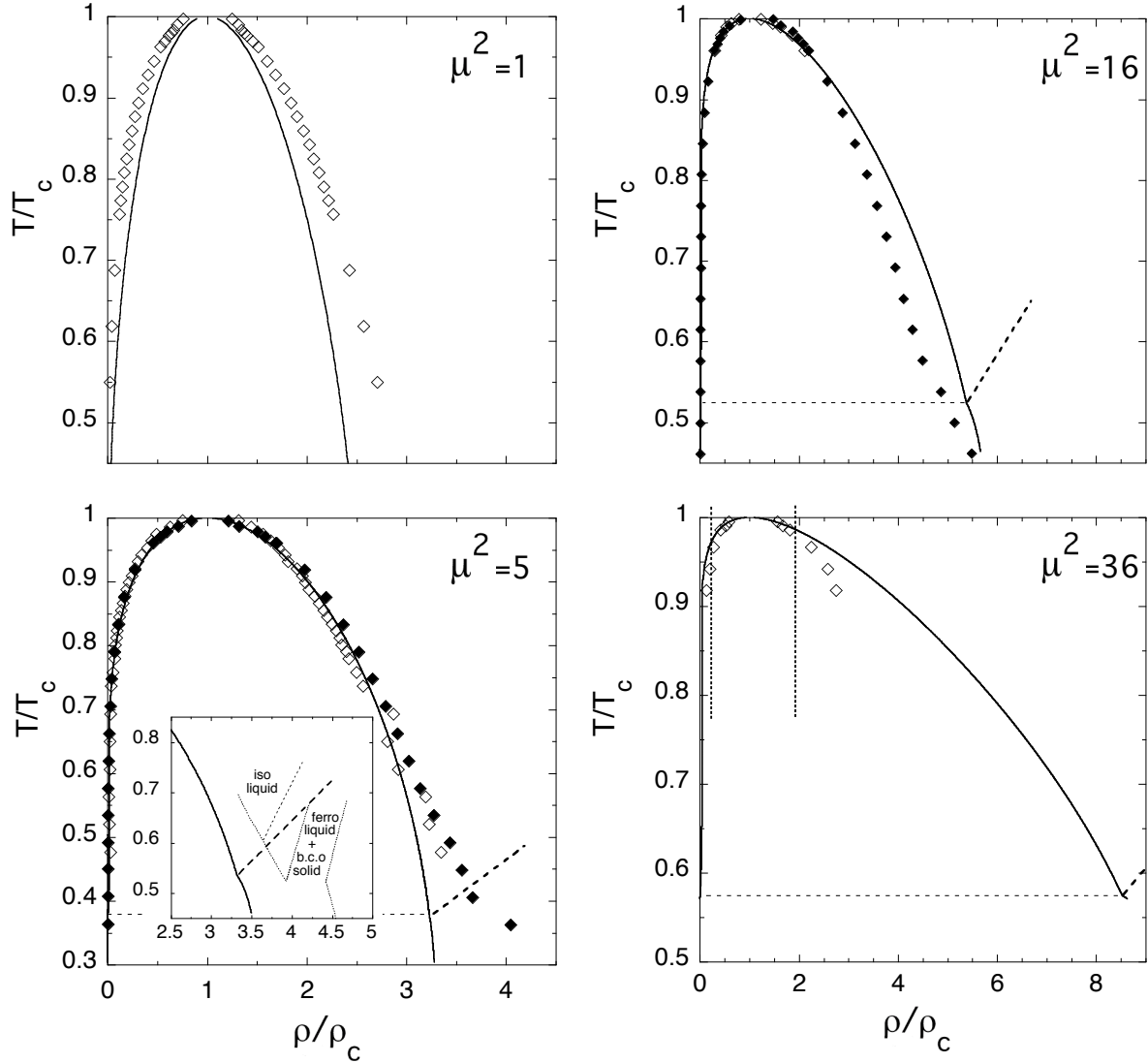


Figure 7.11: Comparison between GL coexistence curves obtained by simulation (symbols) and lattice theory (lines) for the indicated dipole strength. Hollow symbols: Maxwell construction; filled symbols: Kofke integration. The thick-dashed line indicates the transition from the isotropic to the ferroelectric liquid. The inset shows a comparison between the lattice theory for  $\mu^2 = 6.25$  and the corresponding section of the phase diagram obtained via simulation in reference [33] (dotted and short dashed lines). The vertical dotted lines in plot for  $\mu^2 = 36$  are explained in the text.

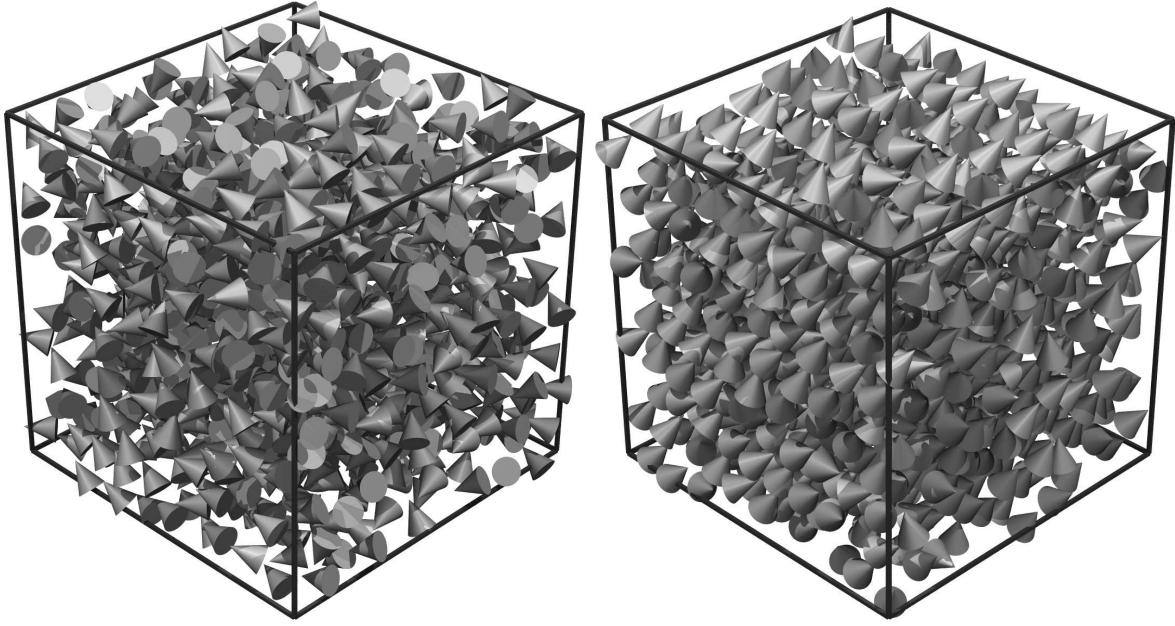


Figure 7.12: Simulation snapshots of the  $\mu^2 = 5$ -system. Left:  $T/T_c \approx 0.49$ . Orientational order of the dipoles is still not obvious. Right:  $T/T_c \approx 0.36$ . Here the nematic order parameter has increased to  $q_{nem} \approx 0.6$ . The mean orientation of the dipoles is visible.

Notice that the inset in the panel for  $\mu^2 = 5$  of figure 7.11 shows a partial phase diagram obtained for  $\mu^2 = 6.25$  and a slightly increased value of  $\kappa$  ( $\kappa = 0.186$ ) in comparison to a partial phase diagram obtained via simulation by Gao and Zeng [33]. These authors primarily have studied the additional transition to the solid state not studied in this work. The nematic order parameter computed during the simulations with  $\mu^2 = 5$  and 16 increases significantly above zero for liquid densities at low temperatures, i.e.  $T/T_c \lesssim 0.55$ , cf. figure 6.8. With increasing nematic order parameter these liquid densities appear to deviate from the extrapolated coexistence curve based on the densities at higher  $T/T_c$ . This is illustrated for  $\mu^2 = 5$  by the two simulation snapshots shown in figure 7.12. The right panel depicting a system configuration at  $T/T_c \approx 0.36$  exhibits visible orientational order, while at  $T/T_c \approx 0.49$  (left panel) orientational order is still not obvious despite of an already increasing nematic order parameter.

In summary, it is unlikely that the transition to ferroelectric order will cause the GL critical point to disappear for the benefit of a tricritical point as found by Zhang and Widom [12]. Certainly this is not the case in the range of dipole strengths considered here. Note also that even though, according to the Debye theory, the ferroelectric transition temperature  $T_{cf}$ , increases proportional to  $\mu^2$  at fixed  $\rho$ , the same dependence, i.e.  $T_c \propto \mu^2$  for large  $\mu$ , is found for the GL critical temperature (cf. equation 7.2.75). In addition the GL critical point "escapes" to lower densities.

Ferroelectric order, as considered thus far, is induced by the particle's dipole moments.

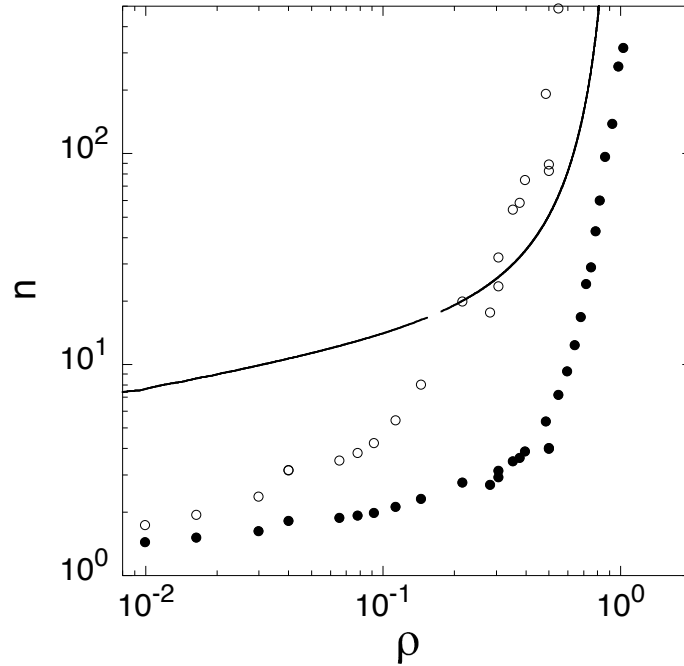


Figure 7.13: Mean aggregation number  $n$  versus particle number density  $\rho$  along the GL coexistence curve for  $\mu^2 = 16$ . Symbols: simulation result obtained with  $r_n = 1.0$  (filled circles) and  $r_n = 1.2$  (hollow circles); solid line: lattice theory. Note that the gap in this curve indicates the critical point.

Another cause for possible orientational order, at least theoretically, is shape induced interaction between reversible chains akin to the isotropic-to-nematic phase transition studied originally by Onsager for rigid monodisperse rods or rodlike polyelectrolytes [34]. The transition to the nematic state occurs for volume fractions proportional to  $\sigma_r/L$ , where  $\sigma_r$  is an effective rod-diameter and  $L$  is the rod length. For large  $L$  the transition therefore occurs at small densities. Onsager's approach can be extended to semiflexible polymers [35,36] and to rod-like micelles [37]. In these theories an orientationally ordered phase occurs for volume fractions proportional to  $\sigma_r/l_p$ , where  $l_p$  is the persistence length. Notice that  $l_p$  depends on temperature. The fact that such a transition is not observed in ST systems with chain formation may be understood in terms of the small persistence length, but for other models of equilibrium polymers this may be relevant [38,39].

Figure 7.13 shows the average chain length  $n$  along the GL coexistence curve obtained for  $\mu^2 = 16$ . The symbols are simulation results, whereas the solid line is the theoretical result. Here  $r_n$  is again the separation within which two particles are considered to be part of the same cluster. We note that there is qualitative agreement between the lattice theory and the simulation similar to the case of the average chain length at criticality shown in figure 7.7.

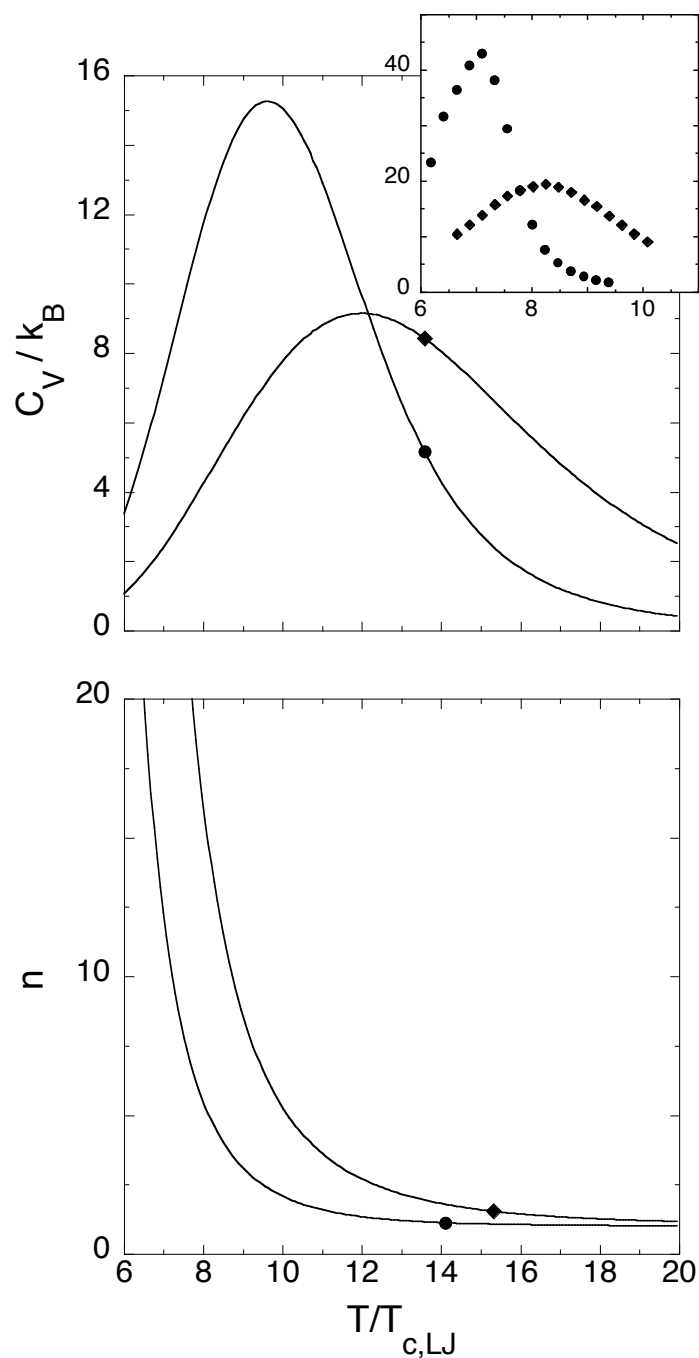


Figure 7.14: Top: Heat capacity at constant volume  $C_V$  vs. reduced temperature  $T/T_{c,LJ}$ . Diamond:  $\rho/\rho_{c,LJ} = 0.0637$ ; circle:  $\rho/\rho_{c,LJ} = 0.00637$ .  $T_{c,LJ}$  and  $\rho_{c,LJ}$  are critical quantities of the LJ system. Inset: Corresponding heat capacity via canonical Monte Carlo simulation taken from reference [40] (figure 4). Bottom: Corresponding average chain length  $n$ .

In figure 7.14 we compare the temperature dependence of the isochoric heat capacity per particle  $C_V$  (omitting the contributions from the kinetic degrees of freedom) obtained via canonical MC simulation in reference [40] for  $\mu^2 = 36$ , to the lattice theory, calculated via

$$-\frac{1}{T}C_V = \left. \frac{\partial^2 F_L}{\partial T^2} \right|_{V, N_s}. \quad (7.3.2)$$

Again there is qualitative agreement. It is important to note that our theoretical treatment neglects the reversible formation of rings. In reference [40] it is shown, however, that there may be a large fraction of rings at the thermodynamic conditions considered here. Notice in this context that the theoretical  $C_V$  is almost exclusively determined by the last term in equation (7.2.47) ( $b_0$  and therefore  $\phi$  is slightly dependent on temperature via equation (7.2.93), i.e.  $C_V$  is determined by the temperature dependence of the average chain length  $n$ ). The latter is shown in the bottom panel. The strongest curvature of  $n$  as function of  $T$ , i.e. the onset of aggregation, corresponds to the maximum of the heat capacity. As explained in subsection 7.2.2 the no-aggregation limit of the lattice theory is not  $n = 1$  but  $n \approx 2$ . We also note that the authors of reference [40] apparently do not notice phase coexistence even though their isochors cross from the one-phase into the coexistence region found in our simulations (as indicated by the vertical dotted lines in the bottom panel of figure 7.11).

### 7.3.3 Relative Stability of chains and rings

Finally, we want briefly return to the issue of relative stability of chains and rings mentioned above. The probability for an ideal wormlike chain containing  $N$  dipoles to form a ring is

$$p_{ring} = \frac{1}{4\pi} \left( \frac{3}{2\pi N} \right)^{\frac{3}{2}}, \quad (7.3.3)$$

cf. reference [41]. Notice that a random path maps out a sphere of radius  $\sim N^{1/2}$  and volume  $\sim N^{3/2}$ . The factor  $1/(4\pi)$  accounts for the smoothness of the chain at the junction point. The remaining factor results from the normalization of the random path's probability distribution. Using  $p_{chain} = 1 - p_{ring}$  we obtain the entropy loss due to ring closure

$$\Delta S = S_{ring} - S_{chain} = \ln \left[ \frac{p_{ring}}{p_{chain}} \right]. \quad (7.3.4)$$

The corresponding change of the free energy is

$$\Delta F = T\epsilon_i - T \ln \left[ \frac{p_{ring}}{p_{chain}} \right], \quad (7.3.5)$$

where  $T\epsilon_i$  is the contribution of the contact interaction to the free energy (cf. equation (7.2.92)). The condition  $\Delta F = 0$  thus defines the cross over length,  $N_x \sim \exp(-2\epsilon_i/3)$ , for

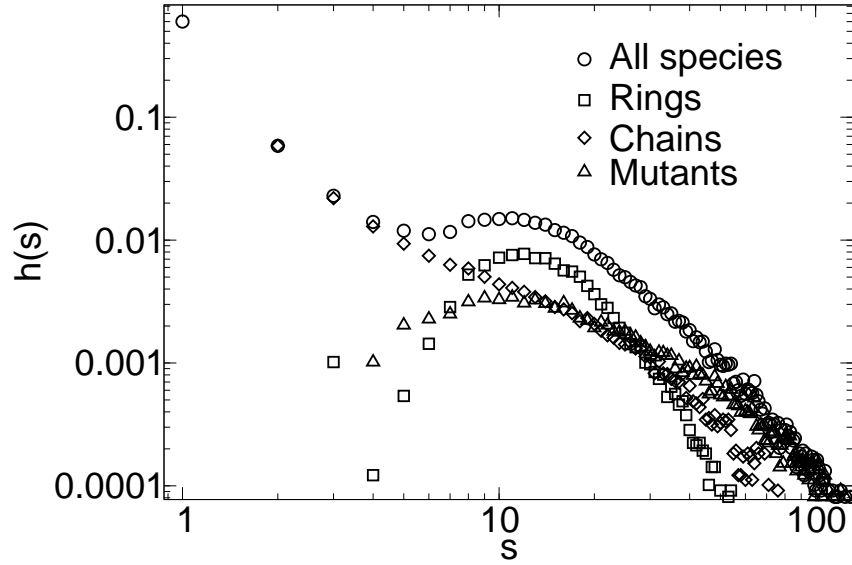


Figure 7.15: Number fraction  $h(s)$  of clusters of different species and chain lengths for a system with  $\mu^2 = 60$ ,  $N = 2048$ ,  $T = 16.5 (\approx T_c)$  and  $\rho \approx 0.005$  from simulation. Here in a certain chain length range ( $8 \lesssim s \lesssim 30$ ) rings are the most likely clusters.

sufficiently large  $N$ . This means that for  $N > N_x$  the chain is more stable than the ring, whereas for  $N < N_x$  the ring is more stable than the chain. On the other hand, according to equation (7.2.46), the lattice model yields a mean chain length  $n \sim \phi^{1/2} \exp(-\epsilon_i/2)$ . If we are interested in the relative stability of chains versus rings close to GL criticality we can make use of  $\phi_c \sim n_c^{-1/2}$  (cf. equation (7.2.62) for large  $n_c$  corresponding to large  $\mu^2$ ). Therefore we find  $n_c \sim N_x^{3/5}$ , which means close to the GL critical point, for sufficiently large  $\mu^2$  and therefore large  $n_c$  (cf. figure 7.7), rings are more stable than chains. This is consistent with figure 7.15. Here simulation results for the number fraction of clusters of different species and cluster lengths for a ST system with  $\mu^2 = 60$ ,  $N = 2048$ ,  $T = 16.5$  and  $\rho \approx 0.005$  are shown. The considered temperature is close to the critical one, but the density is much lower than the critical one, since at critical density the cluster size is already limited by the chosen simulation box size. Contrary to results for smaller dipole strength (cf. figure 5.13 and 6.18) rings become in the range of clusters size  $8 \lesssim s \lesssim 30$  dominant compared to chains. For larger cluster sizes mutants become predominant which we did not include in our considerations. This is quite reasonable, since the larger a cluster is the higher is the probability for knots or contacts to other clusters. Some examples for small clusters are shown in figure 7.16. Even at high dipole strength threefold coordinated crosslinks, as considered by Tlustý and Safran [42], seem to be rare. The mutants seem to be rather chains or rings with knots. With increasing density the clusters appear to be more and more interlooped. Notice that the formation of rings is not yet included in our lattice theory. This may be a reason for the poor accordance between critical density obtained by theory and simulation besides the choice of the cut off distance  $R$

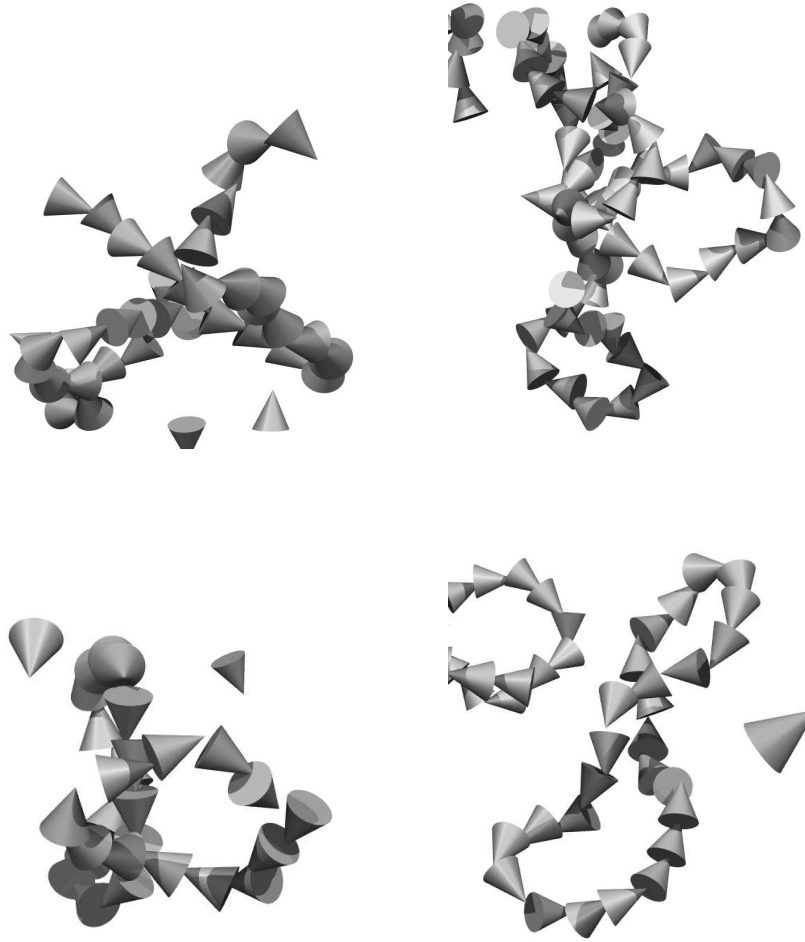


Figure 7.16: Snapshots of mutants from a simulation with  $\mu^2 = 60$ ,  $\rho = 0.0025$  and  $T = 16.5$ . The mutants look rather like knotted chains or rings, than like branched ones. There are no obvious threefold coordinated crosslinks.

for the long-range contribution of the dipolar interactions. However, an additional phase transition driven by the formation of rings and chains appears to be unlikely, since there is no compelling reason to expect that rings and chains should phase separate under the considered conditions.

## 7.4 Conclusion

In this chapter we adopted the FH like lattice theory for reversible assembled particles, developed in [15, 16], to the ST system. We do find coexistence of the isotropic gas and

the isotropic liquid for all dipole strengths studied, i.e.  $0 \leq \mu^2 \leq 60$ . Systems with large dipole strengths  $\mu^2 \gtrsim 25$  were believed previously to show no GL coexistence. With the theory developed here we are able to explain quite reasonably the dependence of the GL critical point in the ST fluid on  $\mu^2$ . The shift of the critical point to lower densities and higher temperatures as function of dipole strength closely resembles the critical point shift as function of chain length in ordinary linear polymer systems. The dependence of the critical temperature on dipole strength may be explained without particle association, but this explanation does not include the shift of the critical density. In particular the increase of the critical density with increasing dipole strength is a consequence of the existence of reversible chains near criticality. Contrary to the case of ordinary linear polymer systems, where the Flory approach yields a finite critical temperature for infinite chain length, the critical temperature continues to increase proportional to  $\mu^2$  even for large average chain length. In addition we do not find evidence, in neither simulation nor theory for an abrupt disappearance of the GL critical point found to occur in earlier simulation work. It is worth noting that the possible transition to ferroelectric liquid order is not expected to interfere with this conclusion, a possibility that has been discussed in theories of phase behaviour in dipolar fluids (e.g. [12, 13]).

Investigating the vLS system at fixed dipole strength with varying parameter  $\lambda$ , we found that the nonvanishing GL phase transition for the ST fluid with large dipole strength is consistent with the nonexistence of GL phase separation in the DSS fluid. At fixed dipole moment  $\mu_{vLS}^2 = const$ ,  $\lambda \rightarrow 0$  implies  $\mu^2 \rightarrow \infty$  in the ST system. With the mapping between ST and vLS systems and  $T_c \sim \mu^2$  for large dipole strengths in the ST system, we obtain  $T_{c,vLS} \sim \lambda^{1/2} \rightarrow 0$  for  $\lambda \rightarrow 0$  at fixed dipole strength in the vLS system. Since the simulations yield a monotonous decrease of the critical density with increasing dipole strength in the ST system, we do expect a vanishing critical density  $\rho_{c,vLS} = \lambda^{1/2}$  for  $\lambda \rightarrow 0$  in the vLS system. Lattice theory in fact yields  $\rho_{c,vLS} \rightarrow 0$  for  $\lambda \rightarrow 0$ . Therefore we conclude that in the DSS limit a vanishing GL critical temperature and a simultaneously vanishing GL critical density is in accordance with simulation and theoretical data obtained thus far for the ST and vLS system.

Nevertheless there may be, for the ST and DSS system, other types of phases and phase transitions. We showed that for dipole strength  $\mu^2 = 60$  in a certain chain length region rings become dominant, which is not yet included in the lattice theory and may explain the large deviation of the critical density from theory and simulation for this dipole strength. A different suggestion is due to Tlustý and Safran [42] who argued that reversible chains may form reversible networks. The chain ends may participate in reversible, threefold coordinated crosslinks or may be free. The authors construct a free energy based solely on the network defects, i.e. the free ends and the crosslinks. They find that phase separation into a free end-rich and a free end-poor phase can occur. The whole idea is developed on the basis of the DHS model. The model is a much simplified theory for a (reversible) polymer network. Other types of defects may be present and important, e.g. physical crosslinks. In particular, as the authors remark themselves, a crucial prerequisite is the observation of dipolar networks. However, the simulations presented in this work as well as a number of exploratory simulations for  $\mu^2 = 100$  at  $T = 26.5$  do not reveal

the formation of dipolar networks in the ST fluid. At very low densities the systems seem to consist only of chains and rings which combine to mutants from time to time. At higher densities the number fraction of mutants becomes much higher, but the interaction between the linear chain-like sections of the mutants appear rather to be driven by the LJ interaction or they appear simply to be interlooped. Real threefold coordinated crosslinks have been observed very rarely even for very high dipole moments.

# Bibliography

- [1] P.G. de Gennes and P.A. Pincus. Pair correlations in a ferromagnetic colloid. *Zeitschrift für Physik B*, 11(3):189–198, 1970.
- [2] P.I.C. Teixeira, J.M. Tavares, and M.M. Telo da Gama. The effect of dipolar forces on the structure and thermodynamics of classical fluids. *Journal of Physics: Condensed Matter*, (33):R411–R434, 2000.
- [3] P.J. Flory. *Principles of Polymer Chemistry*. Cornell University Press, Ithaca, 1953.
- [4] B. Huke and M. Lücke. Magnetic properties of colloidal suspensions of interacting magnetic particles. *Reports on Progress in Physics*, 67:1731–1768, 2004.
- [5] M.E. van Leeuwen and B. Smit. What makes a polar liquid a liquid? *Physical Review Letters*, 71(24):3991–3994, 1993.
- [6] M.J. Stevens and G.S. Grest. Phase coexistence of a Stockmayer fluid in an applied field. *Physical Review E*, 51(6):5976 – 5983, 1995.
- [7] J. Dudowicz, K.F. Freed, and J.F. Douglas. Flory-Huggins model of equilibrium polymerization and phase separation in the Stockmayer fluid. *Physical Review Letters*, 92(4):045502, 2004.
- [8] J. Dudowicz, K.F. Freed, and J.F. Douglas. Lattice model of living polymerization. I. Basic thermodynamic properties. *Journal of Chemical Physics*, 111(15):7116–7130, 1999.
- [9] J. Dudowicz, K.F. Freed, and J.F. Douglas. Lattice model of living polymerization. II. Interplay between polymerization and phase stability. *Journal of Chemical Physics*, 112(2):1002–1010, 2000.
- [10] J. Dudowicz, K.F. Freed, and J.F. Douglas. Lattice model of living polymerization. III. Evidence for particle clustering from phase separation properties and "rounding" of the dynamical clustering transition. *Journal of Chemical Physics*, 113(1):434–446.
- [11] J. Dudowicz, K.F. Freed, and J.F. Douglas. Lattice model of equilibrium polymerization. IV. Influence of activation, chemical initiation, chain scission and fusion, and chain stiffness on polymerization and phase separation. *Journal of Chemical Physics*, 119(23):12645–12666, 2003.
- [12] H. Zhang and M. Widom. Global phase diagrams for dipolar fluids. *Physical Review E*, 49(5):3591–3593, 1994.

- [13] B. Groh and S. Dietrich. Ferroelectric phase in Stockmayer fluids. *Physical Review E*, 50(5):3814–3833, 1994.
- [14] B. Groh and S. Dietrich. Long-ranged orientational order in dipolar fluids. *Physical Review Letters*, 72(15):2422–2425, 1994.
- [15] P.B. Lenz and R. Hentschke. Concentration dependent size of reversibly assembling polymers in solution: A mean-field lattice theory. *Journal of Chemical Physics*, 121(21):10809–10813, 2004.
- [16] P.B. Lenz. *Gleichgewichtspolymere: Gittertheorie und Computersimulation*. PhD thesis, Bergische Universität Wuppertal, 2005.
- [17] T.L. Hill. *An Introduction to Statistical Thermodynamics*, volume 2. Addison-Wesley, 1962.
- [18] P.G. de Gennes. *Scaling concepts in polymer physics*. Cornell University Press, 1979.
- [19] R. Hentschke. *Statistische Mechanik*. Wiley-VCH, 2004.
- [20] Wolfram Research, Inc. Mathematica version 5.1.1, <http://www.wolfram.com>.
- [21] P. Debye. *Polare Molekeln*. S. Hirzel, Leipzig, 1929.
- [22] R. Zwanzig. First-order phase transition in a gas of long thin rods. *Journal of Chemical Physics*, 39(7):1714–1721, 1963.
- [23] M.E. van Leeuwen. Deviation from corresponding-states behaviour for polar fluids. *Molecular Physics*, 82(2):383–392, 1994.
- [24] J. Stoll, J. Vrabec, and Hans Hasse. Comprehensive study of the vapour-liquid equilibria of the pure two-centre Lennard-Jones plus pointdipole fluid. *Fluid Phase Equilibria*, 209:29–30, 2003.
- [25] F. Pesth. Flüssig-Gas-Koexistenz in Stockmayer-Fluiden mittels Computersimulation. Diploma thesis, Bergische Universität Wuppertal, April 2006.
- [26] H. Fröhlich. *Theory of Dielectrics*. Clarendon Press, 1949.
- [27] E.D. Nikitin. The critical properties of thermally unstable substances: measurement methods, some results and correlations. *High Temperature*, 36(2):305–318, 1998.
- [28] E.W. Lemmon and A.R.H. Goodwin. Critical properties and vapour pressure equation for alkanes  $C_nH_{2n+2}$ : Normal alkanes with  $n \leq 36$  and isomers for  $n=4$  through  $n=9$ . *Journal of Physical and Chemical Reference Data*, 29(1):1–39, 2000.
- [29] J.C. Pamies and L.F. Vega. Critical properties of homopolymer fluids studied by a Lennard-Jones statistical associating fluid theory. *Molecular Physics*, 100(15):2519–2529, 2002.
- [30] H. Frauenkron and P. Grassberger. Critical unmixing of polymer solutions. *Journal of Chemical Physics*, 107(22):9599–9608, 1997.
- [31] L.V. Yelash, T. Kraska, A.R. Imre, and S.J. Rzoska. Apparent exponents for the chain length dependence of the volume fraction in critical polymer solutions. *Journal of Chemical Physics*, 118(13):6110–6119, 2003.

- 
- [32] *Spartan '04 Macintosh (v1.0.3)*.
- [33] G.T. Gao and X.C. Zeng. Freezing transition of a strongly dipolar simple fluid. *Physical Review E*, 61(3):R2188 – R2191, 2000.
- [34] L. Onsager. The effects of shape on the interaction of colloidal particles. *Annals of the New York Academy of Sciences*, 51(4):627–659, 1949.
- [35] A.Y. Grossberg and A.R. Khokhlov. Physics of phase transitions in solutions of macromolecules. *Soviet Scientific Reviews, Physics Reviews*, 8:5–156, 1987.
- [36] A.N. Semenov and A.R. Khokhlov. Statistical physics of liquid-crystalline polymers. *Soviet Physics Uspekhi*, 31:988–1014, 1988.
- [37] T. Odijk. Ordered phases of elongated micelles. *Current Opinion in Colloid & Interface Science*, 1:337, 1996.
- [38] J.T. Kindt and W.M. Gelbart. Chain self-assembly and phase transitions in semi-flexible polymer systems. *Journal of Chemical Physics*, 114(3):1432–1439, 2001.
- [39] R. Hentschke, P. Lenz, and B. Fodi. *Supramolecular Polymers*, chapter A. Cifferri (Ed.). Taylor & Francis, Boca Raton, 2005.
- [40] K. van Workum and J.F. Douglas. Equilibrium polymerization in the Stockmayer fluid as a model of supermolecular self-organization. *Physical Review E*, 71(031502), 2005.
- [41] H. Yamakawa and W.H. Stockmayer. Statistical mechanics of wormlike chains. II. Excluded volume effects. *Journal of Chemical Physics*, 57(7):2843–2854, 1972.
- [42] T. Tlusty and S.A. Safran. Defect-induced phase separation in dipolar fluids. *Science*, 290(5495):1328–1331, 2000.



# 8 Dielectric properties and the ferroelectric transition of the Stockmayer fluid via computer simulation

## 8.1 Introduction

In this chapter we report extensive MD simulations of the ST and pST fluid aiming to estimate the location of the transition from the isotropic fluid to the ferroelectric ordered fluid via the divergence of the static dielectric constant. The dependence of the transition on dipole strength  $\mu^2$ , temperature  $T$  and system size is investigated. The results are compared to a large number of previous simulations in the literature on the ST as well as DSS and DHS systems and Debye's and Onsager's approaches to calculate the static dielectric constant. We also relate our findings to recent experiments in nitromethane/nitrobenzene solutions containing ferroelectric domains under ambient conditions. In addition we study the local field in relation to the structure and dynamics of the liquid phase as function of temperature, dipole strength, and polarizability. These results include the significantly less studied pST fluid. First we want to give a short historical overview of approaches to calculate the static dielectric constant of materials from their molecular characteristics and the evidence for a ferroelectric transition in fluids.

### A historical overview

In 1912 Debye published an equation relating the static dielectric constant  $\epsilon$  of gases and liquids to their permanent molecular dipole moments  $\mu$  and isotropic polarizabilities  $\alpha$  (a detailed discussion can be found in [1]). His formula can be found in every textbook on physical chemistry. Applied properly the Debye formula is a valid means to determine the aforementioned molecular quantities from bulk measurements of the static dielectric constant. He assumed that the electrostatic interaction of a molecule with its surrounding can be described by a point dipole in the center of a spherical cavity, embedded in a

homogeneous dielectric. More precisely, the standard derivation of Debye's equation (cf. section 4.5 in [2]) assumes that molecules in the immediate vicinity of the central molecule do not contribute to its local electric field. These molecules are therefore omitted and the cavity becomes much larger. However, the radius of the cavity is never specified because it does not enter into the final result. The entire argument is lacking transparency and rigor and so Debye's approach has been criticized and improved. A major contribution is due to Onsager [3]. His main criticism centers on the ferroelectric Curie point, indicating the transition from the isotropic liquid to the ferroelectric ordered liquid, predicted by Debye's equation. Especially the lack of experimental evidence for this transition to a large extent [4] motivated Onsager to a new approach. In his analysis he still assumes a point dipole placed in the center of a spherical cavity surrounded by a macroscopic dielectric, but the orienting field is separated in a cavity field contributing to the alignment of the permanent dipoles and a reaction field which does not. In his idea the spherical cavity is a result from the volume expansion of the molecule itself. The result is an equation akin to Debye's, which in fact does not show a transition at finite temperature. It is worth remarking that even though Onsager's derivation is more transparent and, over a wide range, his equation is a better approximation than the (linearized) Debye formula it does not appear in any of the standard textbooks. The history of the Onsager equation in relation to Debye's equation is discussed in reference [5].

Shortly after Onsager's paper Kirkwood published an extension of this work [6]. His treatment combines continuum electrostatics with a statistical mechanical calculation of the average dipole moment of a macroscopic volume containing polar molecules enclosed in a homogeneous dielectric. Subsequently various additions and improvements were made (see in particular reference [7]). Kirkwood's approach became especially relevant when the increasing power of computing machines allowed the simulation of simple polar liquids, in particular the (polarizable) ST fluid (cf. [8] for MD or [9] for MC). Initial confusion regarding the proper handling of the long-range electrostatic interactions was resolved over the years in a series of papers (e.g. [10–15]). The precise determination of the dielectric constant of a liquid via computer simulation according to the above method requires to compute the fluctuation correlation function of the vector sum of dipole moments contributed by a large number of molecules. Because this is computationally very demanding, simulation results for dielectric (and thermodynamic) properties of polar and especially polarizable model fluids continue to be interesting.

Although we found Onsager's approach to be more transparent than Debye's, simulation work by Wei and Patey [16] and Stevens and Grest [17] on the DSS fluid, Weis and Levesque [18, 19] and Camp and Patey [20] on the DHS fluid, Houssa et al. on dipolar Gay-Berne molecules [21], Stevens and Grest [17] and Gao and Zeng [22] on ST particles provides evidence for a transition from the isotropic liquid to the ferroelectric liquid phase. A fair number of theoretical studies, also reach the conclusion that the above liquid-to-liquid orientational ordering transition should occur. For a comparative discussion of the various approaches the reader is referred to reference [23]. Nevertheless, the experimental verification remains a challenging problem. A number of experimental groups have studied the temperature dependence of the initial susceptibility in magnetic fluids (either in

suspensions of coated magnetite [24–26] or cobalt particles [27].). None of these studies do find Curie-Weiss behavior nor an isotropic-to-nematic transition. However, the experiments are plagued by polydispersity of the particle size, aggregation and solidification. The more recent study on iron-nitride magnetic fluids by Mamiya et al. [28] thus far is the only one which convincingly suggests that a transition to a ferromagnetic fluid phase does exist in this system. However, these systems are not molecular fluids, but on the other hand the ST model is not restricted to these. In this respect recent hyper-Rayleigh scattering studies by Shelton [29] on nitromethane-nitrobenzene mixtures are of special interest. From his data Shelton draws the conclusion that at ambient conditions (temperature is 300K) his samples contain ferroelectric domains whose typical volume is  $20\text{nm}^3$ . For neat nitromethane he finds an order parameter of around 0.9. With increasing mole fraction of nitrobenzene this order parameter decreases to about 0.25 in pure nitrobenzene. The two molecules are small and rather compact and thus the ST potential may not be a bad approximation of intermolecular interaction. Shelton and Quine found similar behaviour for liquid nitrobenzene doped with triflic acid [30].

## 8.2 Methods for determining the static dielectric constant in fluids

It is useful to briefly discuss the simple prototypical models for calculating  $\epsilon$  due to Debye and Onsager in relation to the usual approach employed in computer modeling. All three approaches have in common that spheres with different characteristics are embedded in an infinite homogeneous dielectric.

### 8.2.1 The Onsager equation

Onsager considers in his approach a single point dipole  $\vec{m}$  at the center of a spherical cavity inside the dielectric. The spherical cavity here is a result of the volume expansion of the particle itself, different to the point of view in subsection 3.7.3, where we considered the cut off sphere embedded in a dielectric medium. This is a rough approximation, since this implies that the dipolar short range interaction energy between neighboring dipoles is negligible and only long-range forces will be considered. We have already shown that this is rather unlikely for system parameters for the ST fluid chosen in the former chapters, since we have observed a strong DD correlation between nearest neighbored dipoles (cf. figure 6.15 for instance). The local field at the position of the dipole  $\vec{m}$  (excluding the dipole's own field) is the sum of the cavity field

$$\vec{E}_{cav} = \frac{3\epsilon}{2\epsilon + 1} \vec{E}_{ext}, \quad (8.2.1)$$

arose in a spherical cavity in the dielectric with dielectric constant  $\epsilon$  due to an external field  $\vec{E}_{ext}$  and the reaction field

$$\vec{E}_R = \frac{2(\epsilon - 1)}{(2\epsilon + 1)a^3} \vec{m} = g\vec{m}, \quad (8.2.2)$$

due to the polarization of the surrounding dielectric by the dipole  $\vec{m}$ , where  $a$  is the radius of the cavity with only one dipole in its center, contrary to the considerations for equation (3.7.12). Both fields can be obtained by applying the continuity relations of the tangential component of the electric field and the normal component of the dielectric displacement field at the surface of the cavity. The sum of both fields yields the local electric field at the position of the dipole  $\vec{m}$

$$\vec{E}_{loc} = \vec{E}_{cav} + \vec{E}_R \quad (8.2.3)$$

$$= \frac{3\epsilon}{2\epsilon + 1} \vec{E}_{ext} + g\vec{m}. \quad (8.2.4)$$

Note that we called the electric field calculated for MD simulation acting on one point dipole  $\vec{E}'(\vec{r}_i)$ . Not to get confused we will call this for the further theoretical considerations here the local electric field  $\vec{E}_{loc}$ . It is tempting to eliminate the unknown cavity radius in equation (8.2.2) via  $a^{-3} = (4\pi/3)\rho$ . However, this yields a qualitative incorrect dependence of  $\vec{E}_{loc}$  on  $\rho$  as we show below. Insertion of equation (8.2.4) into equation (2.1.10) yields

$$\vec{m} = \frac{3\epsilon}{2\epsilon + 1} \frac{\alpha}{1 - \alpha g} \vec{E}_{ext} + \frac{1}{1 - \alpha g} \vec{\mu} \quad (8.2.5)$$

and this inserted into equation (8.2.4) again yields

$$\vec{E}_{loc} = \frac{3\epsilon}{2\epsilon + 1} \frac{1}{1 - \alpha g} \vec{E}_{ext} + \frac{g}{1 - \alpha g} \vec{\mu}. \quad (8.2.6)$$

Onsager proceeds now by computing the thermal average  $\langle \vec{m} \rangle$  in order to tie the local polarization to the macroscopic polarization  $\vec{P}$  via

$$\rho \langle \vec{m} \rangle = \vec{P} = \frac{\epsilon - 1}{4\pi} \vec{E}_{ext}. \quad (8.2.7)$$

The particular significance of equation (8.2.5) is that in order to obtain  $\langle \vec{m} \rangle$  it is sufficient to compute  $\langle \vec{\mu} \rangle$  using the Boltzmann weight  $\exp[\beta \vec{\mu} \cdot \vec{E}_{loc}]$ , with reciprocal temperature

$\beta$ , via

$$\langle \vec{\mu} \rangle = \mu \langle \cos \theta \rangle \frac{\vec{E}_{ext}}{|\vec{E}_{ext}|} \quad (8.2.8)$$

$$= \mu \frac{\vec{E}_{ext}}{|\vec{E}_{ext}|} \frac{\int_0^\pi d\theta \sin \theta \cos \theta e^{\beta \vec{\mu} \cdot \vec{E}_{loc}}}{\int_0^\pi d\theta \sin \theta e^{\beta \vec{\mu} \cdot \vec{E}_{loc}}} \quad (8.2.9)$$

$$= \mu \frac{\vec{E}_{ext}}{|\vec{E}_{ext}|} \mathcal{L}(\beta \mu E_{loc}) \quad (8.2.10)$$

$$\approx \frac{3\epsilon}{2\epsilon + 1} \frac{\mu^2}{3T(1 - \alpha g)} \vec{E}_{ext}, \quad (8.2.11)$$

where we have used  $\langle \vec{\mu} \rangle \parallel \vec{E}_{ext}$ ,  $\theta = \angle(\vec{\mu}, \vec{E}_{loc})$  and  $\mathcal{L}(x) \approx x/3$  for  $x \rightarrow 0$ . Note that  $\mathcal{L}(x)$  is the Langevin function. Combining this result with the thermal average of equation (8.2.5) yields

$$\langle \vec{m} \rangle = \frac{3\epsilon}{2\epsilon + 1} \left( \frac{\mu^2}{3T(1 - \alpha g)^2} + \frac{\alpha}{1 - \alpha g} \right) \vec{E}_{ext}. \quad (8.2.12)$$

and insertion into equation (8.2.7) yields for vanishing external field,  $\vec{E}_{ext} \rightarrow 0$ , Onsager's equation (OE)

$$\frac{3}{4\pi\rho} \frac{(\epsilon - 1)(2\epsilon + 1)}{9\epsilon} = \frac{1}{3T} \left( \frac{\mu}{1 - \alpha g} \right)^2 + \frac{\alpha}{1 - \alpha g}. \quad (8.2.13)$$

Setting  $\vec{\mu} = 0$  or in the limit  $1/T \rightarrow 0$  we obtain the usual Clausius-Mossotti relation (3.7.14) between  $\alpha$  and  $\epsilon$  (or better  $\epsilon_\infty$ ).

## 8.2.2 The Debye equation

The approach underlying the Debye equation is different. He calculates the local field in the center of the cavity by the Lorentz method

$$\vec{E}_{loc}^{(D)} = \vec{E}_{ext} + \vec{E}_{pol} + \vec{E}_{neigh}, \quad (8.2.14)$$

where  $\vec{E}_{ext}$  is again the field due to external sources,  $\vec{E}_{pol}$  is the field due to the polarization charge distribution on the surface on the cavity and  $\vec{E}_{neigh}$  is the field due to the nearest neighbors inside the cavity. By geometric considerations it is argued that for aligned dipoles arranged on a regular lattice inside the cavity their contribution to the local field vanishes, implying  $\vec{E}_{neigh} = 0$ , thus this should hold even for less symmetric cases (see for details section 4.5 in [2]). Comparable to Onsager's approach the aforementioned DD

correlation of nearest neighbors shows that this rough approximation does not hold in general. The field due to the polarization charge distribution is given by

$$\vec{E}_{pol} = \oint \frac{\sigma_{pol} d\vec{A}}{a^2} = \frac{4\pi}{3} \vec{P}, \quad (8.2.15)$$

where  $\sigma_{pol}$  is the array charge density,  $d\vec{A}$  is an array element pointing to the center of the cavity and  $a$  the radius of the cavity. This yields the local electric field in the center of the cavity

$$\vec{E}_{loc}^{(D)} = \vec{E}_{ext} + \frac{4\pi}{3} \vec{P} = \frac{4\pi}{3} \frac{\epsilon + 2}{\epsilon - 1} \vec{P}, \quad (8.2.16)$$

where we have used again equation (8.2.7) to substitute the external field  $\vec{E}_{ext}$  by the macroscopic polarization  $\vec{P}$ . We employed this approach already in the former chapter for a simple theory for the ferroelectric phase transition, cf. equation (7.2.98). The difference between this and Onsager's local field becomes clear if we rewrite equation (8.2.16) in the Onsager form, i.e.

$$\vec{E}_{loc}^{(D)} = \frac{3\epsilon}{2\epsilon + 1} \vec{E}_{ext} + ga^3 \frac{4\pi\rho}{3} \langle \vec{m} \rangle. \quad (8.2.17)$$

Onsager's local field is an instantaneous field, explicitly depending on the instantaneous value of  $\vec{m}$ , which is present even for vanishing external field  $\vec{E}_{ext} = 0$ . Here the local field depends on the thermal average of  $\vec{m}$  instead, and it vanishes if  $\vec{E}_{ext} = 0$  unless  $\langle \vec{m} \rangle \neq 0$ . Onsager's local field virtually neglects the orientation correlation between the  $\vec{\mu}$ , whereas here their orientation correlation is overestimated. We proceed via

$$\vec{P} = \rho \langle \vec{m} \rangle = \rho \langle \vec{\mu} \rangle + \rho \alpha \vec{E}_{loc}^{(D)}, \quad (8.2.18)$$

where  $\langle \vec{\mu} \rangle$  is again given by equation (8.2.10). Thus we obtain the well known equation

$$\frac{3}{4\pi\rho} \frac{\epsilon - 1}{\epsilon + 2} = \frac{\mu \mathcal{L}(\beta\mu E_{loc}^{(D)})}{E_{loc}^{(D)}} + \alpha \approx \frac{1}{3T} \mu^2 + \alpha. \quad (8.2.19)$$

For the purpose of reference we call the linear approximation (LDE) as opposed to the full Debye equation (FDE). Note that in the limit  $\mu^2/T \rightarrow 0$  equations (8.2.13) and (8.2.19) coincide.

Already the LDE predicts the divergence of the dielectric constant, i.e. we can write the linearized version of equation (8.2.19) for  $\alpha = 0$  as

$$\frac{1}{\chi} = 3 \left( T_r - \frac{4\pi}{9} \right), \quad (8.2.20)$$

where

$$\chi = \frac{\epsilon - 1}{4\pi} \quad (8.2.21)$$

is the susceptibility, and  $T_r = T/(\rho\mu^2)$  is the reduced temperature. The same result may be obtained in a more insightful manner via the canonical orientation partition function

(7.2.101) for Debye's approach, where  $\vec{E}_{loc}^{(D)}$  is given by equation (8.2.17). The attending orientation free energy is given by equation (7.2.104), where  $ga^3$  in the local field (8.2.17) is set equal to unity. When the coefficient of the leading term changes sign an orientationally ordered phase becomes stable compared to the isotropic fluid or vice versa (cf. subsection 7.2.3).

### 8.2.3 The fluctuation equation

The usual approach to compute  $\epsilon$  via computer simulation, initially discussed by Kirkwood [6] and later refined by Mandel and Mazur [7], consists of two steps. We consider a system like in our approach for the reaction field (cf. figure 3.2 and subsection 3.7.3). The homogeneous polarization  $\vec{P}_{sphere}$  inside a large spherical volume  $V_{sphere}$  containing  $N_{sphere}$  molecules is related to a constant external field  $\vec{E}_{ext}$ , using equation (3.7.7) and (8.2.7), via

$$\frac{\rho}{N_{sphere}} \langle \vec{M}_{sphere} \rangle = \frac{\epsilon - 1}{4\pi} \vec{E}_i, \quad (8.2.22)$$

where  $\vec{M}_{sphere}$  is the total dipole moment of the sphere, and  $\vec{E}_i$  is the internal field inside the sphere. Note that the dipole density  $\rho = N_{sphere}/V_{sphere} = N/V$  is constant for the whole system. Applying again the continuity relations for the electric field and the dielectric displacement field, we get for a spherical sample embedded in a homogeneous dielectric with the same dielectric constant  $\epsilon$  ( $\epsilon_i = \epsilon_a = \epsilon$  in figure 3.2)

$$\vec{E}_i = \frac{2\epsilon + 1}{3\epsilon} \vec{E}_{ext}. \quad (8.2.23)$$

Thus insertion in equation (8.2.22) yields

$$\langle \vec{M}_{sphere} \rangle = \frac{3N_{sphere}}{4\pi\rho} \frac{(\epsilon - 1)(2\epsilon + 1)}{9\epsilon} \vec{E}_{ext} \quad (8.2.24)$$

The second step is the calculation of  $\langle \vec{M}_{sphere} \rangle$  from statistical mechanics via

$$\langle \vec{M}_{sphere} \rangle = \frac{\int d\Gamma \vec{M}_{sphere} e^{-\beta\mathcal{H}}}{\int d\Gamma e^{-\beta\mathcal{H}}}. \quad (8.2.25)$$

Note that  $d\Gamma$  is the configurational phase space volume element,  $\beta$  the reciprocal temperature and  $\mathcal{H}$  the configurational Hamiltonian. Since we want only to sketch the derivation of  $\langle \vec{M}_{sphere} \rangle$  phenomenologically, we may write the Hamiltonian in the form

$$\mathcal{H} \approx \mathcal{H}_0 - \vec{M}_0 \cdot \vec{E}_{ext} - \frac{1}{2} \alpha_{sample} \vec{E}_{ext}^2, \quad (8.2.26)$$

where  $\mathcal{H}_0$  is the Hamiltonian in the absence of an external field and  $\alpha_{sample}$  the macroscopic polarizability of the whole sample. Here  $\vec{M}_0$  denotes the total dipole moment of the entire

simulation box in the absence of an external field. For a more accurate derivation of  $\langle \vec{M}_{sphere} \rangle$  see references [7, 11, 15]. In principle care has to be taken that the Boltzmann weight used to calculate the average is consistent with the Hamiltonian actually used in the simulation from which the necessary averages are later obtained [15]. In the present case  $\mathcal{H}$  refers to the electrostatic potential energy of the cubic simulation cell (using reaction field boundary conditions for the electrostatic interactions). Using

$$\vec{M}_{sphere} \approx \vec{M}_{0,sphere} + \alpha_{sphere} \vec{E}_{ext} \quad (8.2.27)$$

we can write equation (8.2.25) including terms linear in  $\vec{E}_{ext}$  only

$$\langle \vec{M}_{sphere} \rangle_0 \approx \left\langle \left( \vec{M}_{0,sphere} + \alpha_{sphere} \vec{E}_{ext} \right) \left( 1 + \beta \vec{M}_0 \cdot \vec{E}_{ext} \right) \right\rangle_0 \quad (8.2.28)$$

$$= \langle \vec{M}_{0,sphere} \rangle_0 + \alpha_{sphere} \vec{E}_{ext} + \left\langle \beta \vec{M}_{0,sphere} \vec{M}_0 \cdot \vec{E}_{ext} \right\rangle_0. \quad (8.2.29)$$

The subscript 0 refers to the limit for vanishing external field  $\vec{E}_{ext} \rightarrow 0$ . Note that  $\langle \vec{M}_{0,sphere} \rangle_0 = 0$  due to the missing preferential orientation and

$$\left\langle \vec{M}_{0,sphere} \vec{M}_0 \cdot \vec{E}_{ext} \right\rangle_0 = \left\langle \left( \vec{M}_{0,sphere} \right)_z \left( \vec{M}_0 \right)_z \right\rangle_0 \vec{E}_{ext} \quad (8.2.30)$$

$$= \frac{1}{3} \left\langle \vec{M}_{0,sphere} \cdot \vec{M}_0 \right\rangle_0 \vec{E}_{ext} \quad (8.2.31)$$

for  $\vec{E}_{ext} \parallel \vec{e}_z$ . This yields in the limit of small polarizability

$$\langle \vec{M}_{sphere} \rangle = \frac{1}{3T} \langle \vec{M}_{0,sphere} \cdot \vec{M}_0 \rangle \vec{E}_{ext} + \alpha_{sphere} \vec{E}_{ext}. \quad (8.2.32)$$

Insertion in equation (8.2.24), using  $\alpha_{sphere} \approx N_{sphere} \alpha$  and  $\vec{M}_{0,sphere} \rightarrow \vec{M}_{sphere}$ ,  $\vec{M}_0 \rightarrow \vec{M}$  for  $\vec{E}_{ext} \rightarrow 0$

$$\frac{3}{4\pi\rho} \frac{(\epsilon - 1)(2\epsilon + 1)}{3\epsilon} \vec{E}_{ext} = \frac{\langle \vec{M}_{sphere} \cdot \vec{M} \rangle_0}{TN_{sphere}} \vec{E}_{ext} + \alpha \vec{E}_{ext}. \quad (8.2.33)$$

Using the Clausius-Mossotti like relation (3.7.15) yields the fluctuation equation (FE)

$$\frac{3}{4\pi\rho} \frac{(\epsilon - 1)(2\epsilon + 1)}{3\epsilon} = \frac{\langle \vec{M}_{sphere} \cdot \vec{M} \rangle_0}{TN_{sphere}} + \frac{3}{4\pi\rho} \frac{(\epsilon_\infty - 1)(2\epsilon_\infty + 1)}{9\epsilon_\infty}. \quad (8.2.34)$$

Even though de Leeuw *et al.* [15] argue quite convincingly that  $\langle \vec{M}_{sphere} \cdot \vec{M} \rangle_0$  should be used recent simulation work frequently is based on  $\langle \vec{M}^2 \rangle_0$  instead (e.g. [31, 32]). This point has also been dealt with in reference [33].

Notice that the radius of the spherical sample for calculating the dielectric constant has to be chosen equal to the cut off radius  $r_{cut}$  of the system [15]. In practise, to accelerate the computation of the dielectric constant, we place several spheres with radius  $r_{cut}$  at random

positions in the simulation box and calculate its total dipole moment  $\vec{M}_{sphere}$  in order to calculate the fluctuations  $\langle \vec{M}_{sphere} \cdot \vec{M} \rangle_0$ . Since the reaction field corrections depend on the dielectric constant (cf. equation (3.7.12)) we use for these, as already mentioned, the cumulative average of the dielectric constant obtained by the FE.

It is useful to emphasize the similarity between this and Onsager's equation. Writing

$$\langle \vec{M}_{sphere} \cdot \vec{M} \rangle_0 = \left\langle \sum_{i \in sphere} \sum_{j \in box} \vec{m}_i \cdot \vec{m}_j \right\rangle_0 \quad (8.2.35)$$

$$\approx N_{sphere} \left\langle \vec{m}_1 \cdot \sum_{j \in box} \vec{m}_j \right\rangle_0 \quad (8.2.36)$$

$$\approx N_{sphere} m_0^2 \left( 1 + \left\langle \sum_{\substack{j \in box \\ j \neq 1}} \cos \theta_{1,j} \right\rangle_0 \right). \quad (8.2.37)$$

Here  $\theta_{1,j}$  is the angle between the dipole moment 1 in the center of the sphere and another dipole  $j$ .  $m_0^2$  is the mean square average of  $\vec{m}_1$  in the absence of the external field. A further approximation is the substitution of  $\langle \sum_{j \in box} \cos \theta_{1,j} \rangle_0$  by the average number of dipoles in the nearest neighbor shell of a particle  $z$  times  $\langle \cos \theta \rangle_{nn,o}$ , where  $\theta$  is the angle between this dipole and a nearest neighbor dipole. The index  $nn$  indicates that the average is over nearest neighbors only. Using

$$\vec{m}_0 = \frac{1}{1 - \alpha g} \vec{\mu} \quad (8.2.38)$$

from Onsager's approach we may expect an improvement of Onsager's equation if  $\mu^2$  in equation (8.2.13) is replaced by  $\mu^2(1 + z \langle \cos \theta \rangle_{nn,o})$  [6]. Here we will indicate this modification of Onsager's equation by the acronym EOE. In our system the factor  $(1 + z \langle \cos \theta \rangle_{nn,o})$  will lead to an increase of the predicted dielectric constant compared to Onsager's equation.

## 8.3 Results for vanishing polarizability

### 8.3.1 Static dielectric constant from different approaches

Figure 8.1 shows the dependence of the static dielectric constant  $\epsilon$  on temperature  $T$  for different dipole strengths,  $\mu^2 = 0.5, 1.0, \text{ and } 3.0$ . Here we used the parameters  $N = 500$ ,  $\rho = 0.8$ , and  $r_{cut} = 3$  throughout unless stated otherwise. The left panel of figure 8.1 illustrates the effect on  $\epsilon$  when  $\langle \vec{M}_{sphere} \cdot \vec{M} \rangle_0$  'box-and-sphere' in the FE (8.2.34) is

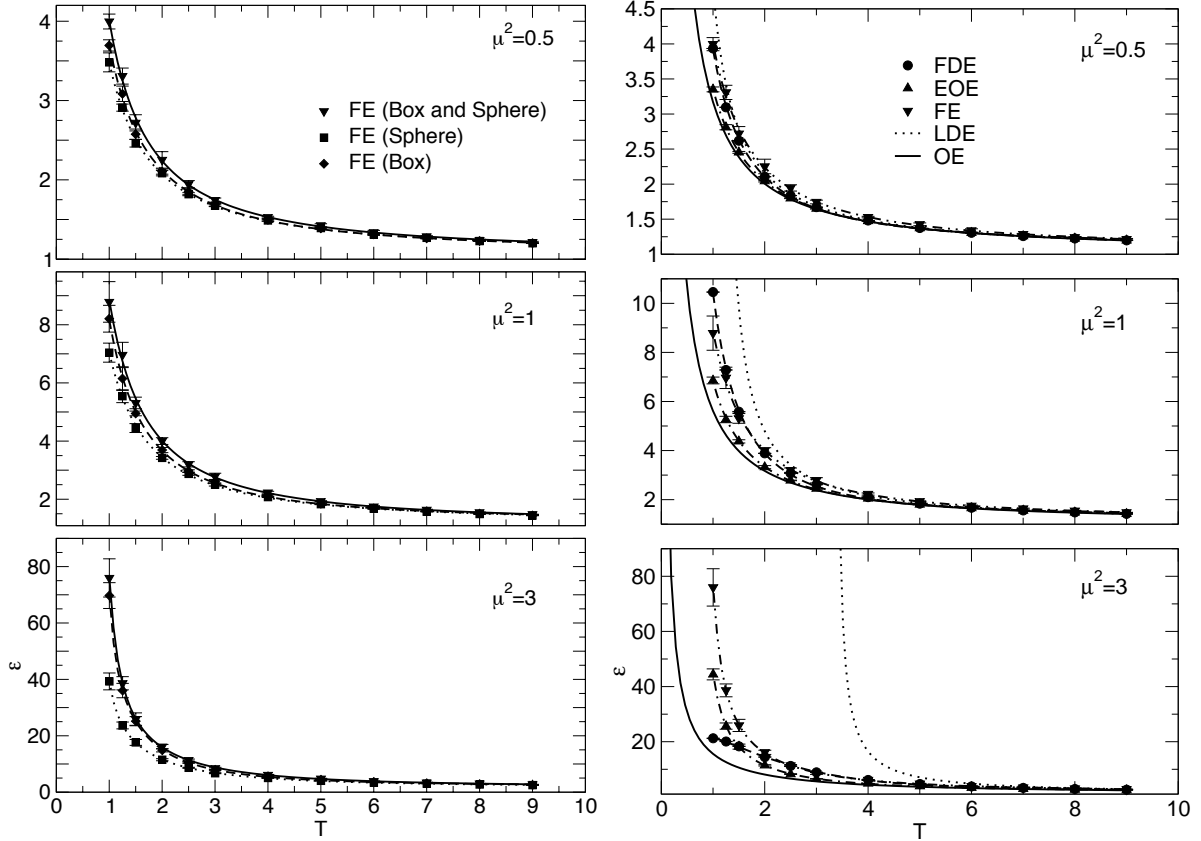


Figure 8.1: The static dielectric constant  $\epsilon$  from the different approaches versus temperature  $T$  for dipole strength  $\mu^2 = 0.5, 1$  and  $3$  ( $N = 500, \rho = 0.8, r_{cut} = 3$ ). Left: Comparison of FE 'box-and-sphere' to FE 'box' and FE 'sphere' from simulation. For high temperatures the deviations for the different equations diminish. For large dipole strengths and low temperatures the deviations between 'sphere' on the one hand and 'box-and-sphere'/'box' on the other hand become significant. Right: Comparison of results from the FE 'box-and-sphere' to results from the approaches of Debye (FDE, LDE) and Onsager (EOE, OE). For the smallest dipole strength ( $\mu^2 = 0.5$ ) all computation methods are in good agreement. For higher dipole strengths ( $\mu^2 = 1$  and  $3$ ) the range of accordance is shifted to higher temperatures.

replaced by  $\langle \vec{M}^2 \rangle_0$  'box' and  $\langle \vec{M}_{sphere}^2 \rangle_0$  'sphere', respectively. The deviations are rather minor. In particular they appear to diminish for 'box-and-sphere' and 'box' on a relative scale as the dipole strength increases. Only the deviations of these to 'sphere' at large dipole strength and low temperature become very significant. These differences, as is discussed in reference [33], are system size dependent and reduce as the system size is increased. The following results are 'box-and-sphere' results, since it appears that this is the adequate form for our simulations.

In the right panel of figure 8.1 we compare the static dielectric constant  $\epsilon$  from the FE 'box-and-sphere' to the approaches from Debye (FDE, LDE) and Onsager (EOE, OE) for same system parameters as in the left panel. For the smallest dipole moment  $\mu^2 = 0.5$  all methods of calculation are in good accordance, especially the LDE is close to the data points for FE. Notice that the LDE is calculated from equation (8.2.19) without usage of simulation data. Thus for simulations with small dipole moments only, computational effort can be saved by applying the LDE to calculate the static dielectric constant for the reaction field corrections from equation (3.7.12). For dipole strength  $\mu^2 = 1$  the LDE and OE hold only for very high temperatures. Here the FDE, using the local field  $E_{loc}$  obtained by simulation, yields good accordance to the FE in the whole considered temperature range. Usage of the FDE instead of the FE still reduces the computational effort, since the local field has to be calculated for the torque anyway (cf. equation (3.2.5)). Furthermore, usage of the FDE yields faster good averages than usage of FE, as indicated by the error bars. This is due to the fact that quite good averages of the local field can be obtained already by one single configuration. For the fluctuation of the total dipole moment we have to respect a long-range of the trajectory of the system in phase space. For  $\mu^2 = 3$  even the FDE is a valid approximation only for high temperatures above the GL critical temperature. Here for low temperatures the EOE yields better results. Nevertheless, the computational effort for applying the EOE is not less than for the FE itself.

### 8.3.2 Inverse susceptibility and the ferroelectric transition

#### Simulation results for the Stockmayer fluid

Figure 8.2 shows our simulation data on the static dielectric constant, expressed via the inverse susceptibility, together with 44 data points from previous simulations on ST fluids (notice that a number of symbols are masked by others.): reference [10] (table II; data shown as solid squares in figure 8.2), reference [12] (tables 2 and 5; solid down triangles), reference [14] (figure 1; solid circles), reference [15] (table 1; open square with filled triangle above diagonal), reference [36] (table 4; triangles pointing to the lower right), reference [37] (table 1; solid diamonds), reference [31] (table 3; solid up-triangle), reference [32] (figure 2; open squares with filled triangle below diagonal). Our own data include the following combination of simulation parameters ( $\mu^2$ ,  $N$ ,  $r_{cut}$ ,  $\rho$ ):

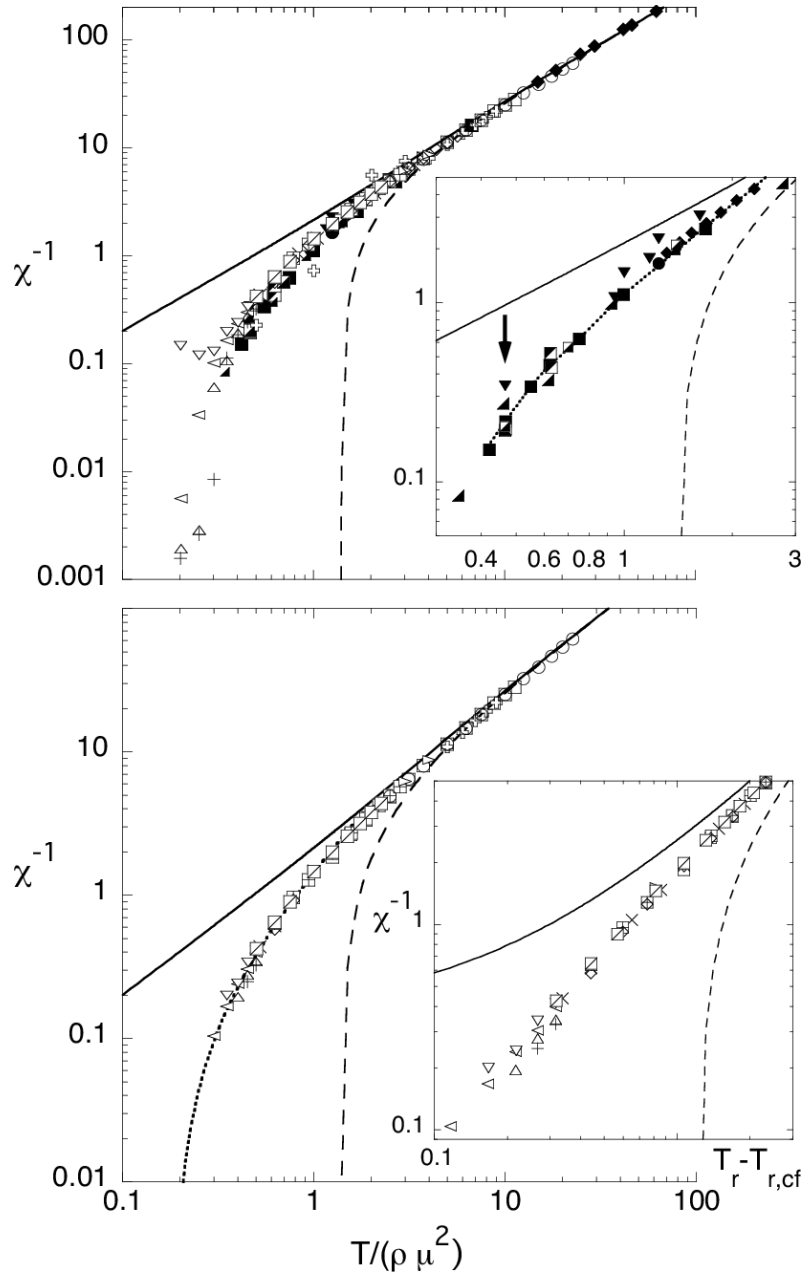


Figure 8.2: Top: Inverse susceptibility  $\chi^{-1}$  versus reduced temperature  $T_r = T/(\rho\mu^2)$ . The symbols represent simulation results from this work (hollow symbols, pluses and crosses) and the literature (solid and semi-solid symbols). The details are given in the text. Solid line: OE; dashed line: LDE. The inset magnifies a portion of the graph showing literature data only. The dotted line represents the RHNC theory result taken from table 2 in reference [34]. Another good theoretical description which provides a close form approximation for  $\chi^{-1}$  can be found in reference [35]. Bottom: The symbols represent a subset of the above data. Solid line: OE; dashed line: LDE; dotted line: power law approximation. The inset shows a magnified portion of the main graph. Notice that  $\chi^{-1}$  is plotted versus  $T_r - T_{r,cf}$  instead of  $T_r$ .

(0.5, 500, 3, 0.8; hollow circles), (1.0, 500, 3, 0.8; open squares), (2.0, 500, 3, 0.8; hollow diamonds), (3.0, 500, 3, 0.8; crosses), (4.0, 500, 3, 0.8; hollow squares with inscribed plus), (4.0, 2000, 5, 0.8; pluses), (5.0, 500, 3, 0.1; hollow crosses), (5.0, 500, 3, 0.5; hollow right triangles), (5.0, 500, 3, 0.8; hollow squares with diagonal line), (5.0, 2000, 5, 0.8; hollow up triangles), (10.0, 2000, 5, 0.8; hollow left triangles), (36.0, 2000, 5, 0.8; hollow down triangles). Our data were obtained at temperatures ranging from 1 to 10. The data in reference [37] were calculated along the gas-to-liquid binodal line covering the density range  $0.016 \leq \rho \leq 0.76$  and temperatures from 1.0 to 1.3 for  $\mu^2 = 1$ . Most of the other simulations cover somewhat smaller parameter ranges ( $T$  from 0.8 to 1.35,  $\mu^2$  between 0.25 and 4, and  $\rho$  between 0.8 and 0.85). However, overall there is a considerable range of values for  $T$ ,  $\mu^2$ , and  $\rho$  for which data are available. The approximate collapse of these data, collected over 25 years, on a common curve is quite remarkable. However, the reduction of the dependence of  $\chi^{-1}$  on  $\rho$ ,  $\mu^2$  and  $T$  to the quantity  $T/(\rho\mu^2)$  is not exact. See for instance the discussion by Joslin [38] on the third dielectric and pressure virial coefficients of dipolar hard sphere fluids or the more recent discussion of the static dielectric properties of polar fluids in reference [35]. Nevertheless, it appears to yield a rather good approximation in case of the ST potential. In particular it is difficult to separate out the individual effect of  $\rho$ ,  $\mu$ , and  $T$ , based on the simulation data published thus far because of considerable scatter especially at small  $\chi^{-1}$ . The arrow in the upper inset in figure 8.2 indicates four data points obtained in different works with exactly the same parameter values ( $\rho = 0.822$ ,  $\mu^2 = 3$ ,  $T = 1.15$ ; [12, 31, 32, 36]). The respective  $\chi^{-1}$ -values range from 0.19 to 0.34.

Our estimate of the ferroelectric transition is based on a subset of the data obtained in this work. We did exclude all data points under the GL binodal. An exception is the data set for  $\mu^2 = 36$ , where the peculiar increase of  $\chi^{-1}$  for  $T_r < 0.3$  still occurs in the one-phase region. In addition we did not find obvious difficulties during equilibration. At such large dipole strengths the particles easily form reversible linear aggregates which may interfere with the isotropic liquid-to-ferroelectric liquid transition. The conformation as well as orientation dynamics of equilibrium polymers depends on their length and thus may be extremely slow. However, at high densities chains are difficult to discern, and the dipole orientation correlation functions did not show evidence for the expected temporal or spatial increase of the correlation range. Nevertheless, this behavior may indicate the termination of the isotropic-to-nematic transition. Essentially, however, the reason for the above increase of  $\chi^{-1}$  remains unclear. The remaining data are shown in the lower panel of figure 8.2. The dotted line was obtained by fitting the data in the range  $\chi^{-1} < 1$  and  $T_r < 1$  to the power law

$$\frac{1}{\chi} = A(T_{r,cf} - T_r)^\gamma \quad (8.3.1)$$

assuming a second order transition. Here  $T_{r,cf}$  is the value of  $T_r$  at the ferroelectric transition. Setting  $\gamma = 1.37$ , this number is based on renormalization group work by Aharony and Bruce on the critical exponents of ferromagnets with dipolar interactions in addition to short range isotropic interactions on a cubic lattice (cf. the discussion in reference [39]), we treat  $A$  and  $T_{r,cf}$  as adjustable parameters, for which we obtain

$A \approx 1.91$  and  $T_{r,cf} \approx 0.19$ . Notice that this value for  $\gamma$  falls into the range of values for the same exponent of the classical Heisenberg model in 3D (cf. table 23 in reference [40]). This is reassuring in a way, because the aforementioned renormalization group calculation based on the analysis of a recursion relation near a certain fixed point was focused on GL criticality. It should be mentioned that the universality class of the long-range dipolar interactions still is a matter of debate [41, 42]. If we use the mean field value  $\gamma = 1$ , we obtain  $A \approx 1.75$  and  $T_{r,cf} \approx 0.27$ . The mean field value may be motivated by the suppression of long-range fluctuation near the transition. Nevertheless, decreasing  $\gamma$  from 1.37 to 1 is accompanied by a monotonous (but not severe) decrease of the quality of the fit. We note that the reduced set of data points to which we apply the power law (8.3.1) does include simulation data for  $\rho = 0.8$  only. Thus, we cannot infer information on the general dependence of  $T_{r,cf}$  on density for the ST fluid.

Previously Stevens and Grest [43] as well as Gao and Zeng [22] have observed the orientational ordering transition in the ST fluid. Stevens and Grest obtain  $T_{cf} = 1.5$ , where  $T_{cf}$  is the ferroelectric transition temperature, using  $N = 256$  and  $\mu^2 = 6.25$  for  $\rho = 0.9$ , i. e.  $T_{r,cf} \approx 0.27$ . Gao and Zeng use  $N \approx 500$ ,  $\mu^2 = 6.25$ . They determine three different  $T_{cf}$ , i.e.  $T_{cf} \approx 1.5, 1.7, 1.8$ , corresponding to  $\rho \approx 0.90, 0.95, 1.0$ . Here  $T_{r,cf}$  is between 0.27 and 0.29. Both groups locate the transition by the requirement that the orientation order parameter is close to 0.5 corresponding to half its value at perfect nematic order. Physically this value has no special relevance if we assume a second order transition, and therefore this method tends to yield larger transition temperatures. Nevertheless an estimate of the error is difficult.

### Comparison to simulation results for the dipolar soft sphere and dipolar hard sphere fluid

The same technique is employed in most studies on the related dipolar systems. Wei and Patey [16] obtain a transition to a liquid ferroelectric phase in a DSS fluid (for  $\mu^2 = 9$  at  $T = 1.0$  and  $T = 1.35$ ) via MD simulation at  $T_{r,cf} \approx 0.19$  (lower temperature) and 0.23 (higher temperature). The lower temperature is probably less reliable due to the difficult equilibration. Stevens and Grest [17] obtain somewhat higher values for  $T_{r,cf}$  for the same system, i.e.  $T_{r,cf} \approx 0.29$  ( $\mu^2 = 4, T = 1$ ),  $\approx 0.24$  ( $\mu^2 = 6.25, T = 1$ ) and  $\approx 0.2$  to 0.25 (due to hysteresis) ( $\mu^2 = 9, T = 1$ ). Weis and Levesque [18] find ferroelectric fluid order for a DHS system at  $T_r \approx 0.13$ . Subsequently they find  $T_{r,cf}$  bracketed by  $\approx 0.14$  and  $\approx 0.2$  varying the density at constant  $T/\mu^2$  [19]. Camp and Patey [20] locate the ferroelectric fluid transition at  $T_{r,cf} \approx 0.26$  ( $\mu^2 = 7.5, T \approx 1$ ) for the same system. Very recently Weiss [44] and Weis and Levesque [41] have applied a variation of the Binder cumulant method combined with histogram reweighting methods to precisely determine the ferroelectric transition in a DHS system. In the density range  $0.8 \leq \rho \leq 0.95$  they find a linear increase of  $T_{r,cf}$  from 0.265 to 0.33. They also deduce information on certain critical exponent ratios using finite size scaling. The resulting ratios are close to the same

quantities in the classical Heisenberg model.

### Comparison to theoretical results

Theoretical values for  $T_{r,cf}$  are significantly higher. From the simple LDE, i.e. equation (8.2.19) or (8.2.20) respectively, we directly obtain  $T_{r,cf} = 4\pi/9 \approx 1.4$ . Zhang and Widom [45] start from a mean field expression for the free energy of dipolar fluids composed of a van der Waals contribution plus the orientation free energy (7.2.104). The resulting  $T_{r,cf}$  is the same of course. Early DFT calculations of Groh and Dietrich [46] likewise yield  $T_{r,cf} \approx 1.5$ . We note that our simulations do not show evidence for a first order isotropic liquid-to-nematic liquid transition as predicted by the aforementioned theories under certain conditions. Among the best theories to date is the still earlier DFT work by Wei, Patey and Perara [47]. They derive results for the DHS and DSS fluid which are within a factor of 1.5 to 2 of the  $T_{r,cf}$  observed here. Nevertheless, considerable a priori information on the liquid structure is needed. A fairly extensive discussion of the present state of the theory discussed in this paragraph can be found in reference [23].

If we compare the  $\rho$ -dependence of  $T_{r,cf}$  found for the DHS system in references [41, 44] with the same quantity in the ST system, including our own result and the results in references [22, 43], we do find that  $T_{r,cf}^{(ST)} \approx T_{r,cf}^{(DHS)} - 0.06$ . Even though the transition from the isotropic liquid to the ferroelectric liquid is affected to lesser extent by the short range isotropic interactions as compared to the GL critical point, there is no reason why it should not change. While the critical exponents only depend on molecular detail as long as it does not alter symmetry, the transition temperature is not universal. The above theoretical work in particular shows that the neglect of molecular detail at short distances leads to severe deviations in comparison to simulation. Thus one may expect that the coupling between short range interaction and local order, which should be different in the ST and DHS-systems is responsible for the differences in  $T_{r,cf}$ .

### Comparison to experimental results

At this point we return to Shelton's experimental work on nitromethane-nitrobenzene solutions [29] and its relation to the ST system. For the sake of simplicity we concentrate on nitromethane. Nitromethane has a GL critical point at  $T_{exp,c} = 588\text{K}$  and  $\rho_{exp,c} = 0.353\text{g cm}^{-3}$  [48]. In order to compare this to the ST system we need to determine the LJ parameters  $\epsilon$  and  $\sigma$  explicitly. We have computed ab initio pair interaction energies to second order Møller-Plesset perturbation theory (6-31G\* basis set) using the program Spartan [49]. The C – N bonds of the two molecules were parallel and the intermolecular distance was the perpendicular distance between the C – N bonds. The resulting distance dependence of the interaction energy was fitted to the ST potential using  $\sigma \approx 4.7\text{\AA}$  determined from the calculated molecular volume (assumed spherical) and the likewise

calculated single molecule dipole moment  $\mu \approx 3.3$  D. The fit yields  $\epsilon \approx 1$  kJ/mol. The resulting dipole moment in the usual LJ units is  $\mu = \mu(\text{in Cm})/\sqrt{4\pi\epsilon_0\epsilon\sigma^3} \approx 2.5$ . The corresponding ST fluid has a GL critical point at  $T_c \approx 2.6$  and  $\rho_c \approx 0.28$  (e.g. [43]). Using the above values for  $\sigma$  and  $\epsilon$  to convert the experimental critical point data to LJ units we obtain  $T_c \approx 4.9$  and  $\rho_c \approx 0.36$ . Finally we may compute the reduced temperature  $T_r$  for nitromethane at the experimental conditions. The result is  $T_r \approx 0.33$ . Note that  $T_r$  does not depend on  $\sigma$  and  $\epsilon$ . Overall this mapping of nitromethane onto the ST fluid yields GL critical parameters and a value for  $T_r$  which are too large for ferroelectric order. But the discrepancy does not rule out such a mapping entirely. The dipole moment for nitromethane employed here, for instance, is the gas phase dipole moment. In the bulk liquid phase polarization may increase this value significantly. In water this increase appears to be 50 to 60% (e.g. [50]). If we repeat the above analysis with the nitromethane dipole moment increased by 25 % then  $\epsilon$  is raised to  $\approx 3$  kJ/mol. Consequently the nitromethane dipole moment in LJ units becomes  $\approx 1.76$ . The GL critical point for this ST fluid occurs at  $T_c \approx 1.86$  and  $\rho_c \approx 0.29$ . The GL critical point of nitromethane expressed in LJ units using this new  $\epsilon$ -value is shifted to  $T_c \approx 1.63$  and  $\rho \approx 0.36$ . In addition the reduced temperature for nitromethane with the increased dipole moment is  $T_r \approx 0.21$ . This value now is close to where ferroelectric order is expected based on the above analysis. Therefore an increase of the dipole moment due to polarization tends to bring the ST system in much closer accord with the experiment. However, needless to say that more careful analysis is needed.

### 8.3.3 The local electric field

We now return to simulation results on the local electric field inside the ST fluid. Figure 8.3 shows the contribution of a dipole's  $\vec{\mu}_i$  neighborhood to the magnitude of the instantaneous local electric field  $E_{loc}$ , i.e.  $E_{loc}(r)$  includes the contributions of neighbor dipoles inside a sphere of radius  $r$  for dipole strength  $\mu^2 = 0.5, 1, 2$  and  $3$  ( $T = 1$  and  $3$ ). Here  $E_{loc}$  is calculated via  $E_{loc} = \langle |\vec{E}'(\vec{r}_i)| \rangle$  from MD, where  $\vec{E}'(\vec{r}_i)$  is computed according to equation (3.7.16). Figure 8.3 shows that the first neighbor shell is the major contributor. Only as the dipole strength increases a second "step" appears contributed by the second nearest neighbor shell. In other words, the spatial range of DD correlation is limited to the first two neighbor shells for the dipole strengths and temperatures shown here. On the one hand this is in good accordance with the DD correlation function for  $\mu^2 = 4$ , shown in the lowest panel of figure 6.15, for the case without ferroelectric order. On the other hand this is in contradiction with Debye's assumption that the contribution of the nearest neighbors to the local electric field should vanish.

Figure 8.4 shows the density dependence of the instantaneous local field strength  $E_{loc}$ , for  $T = 8.0$  (solid circles),  $4.0$  (open squares),  $2.1$  (solid diamonds), and  $1.6$  (solid triangles) with  $\mu^2 = 4$  via MD. It is interesting to compare these simulations to Onsager's  $E_{loc}$ .

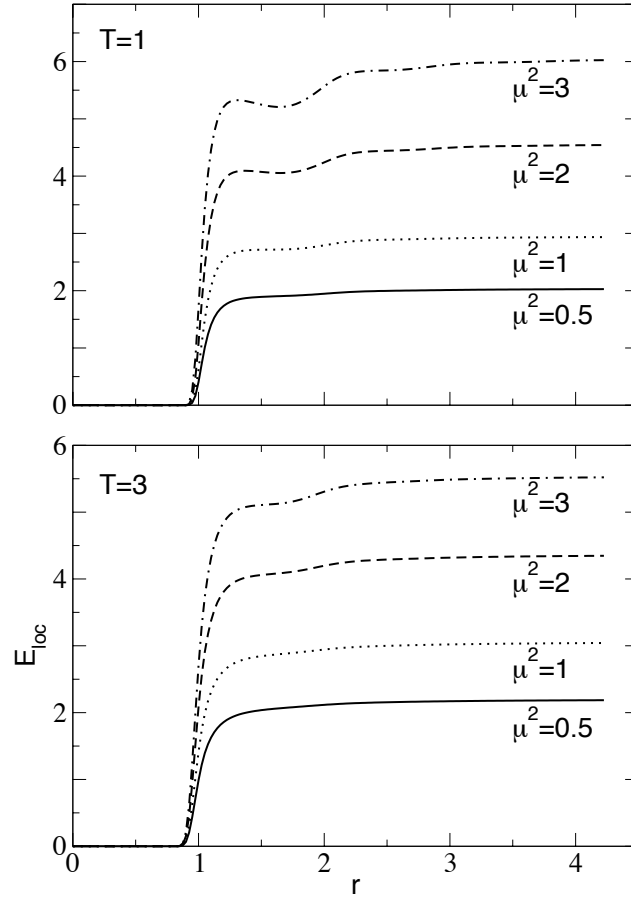


Figure 8.3: Average magnitude of the instantaneous local electric field  $E_{loc}$ , contributed by dipoles within a sphere of radius  $r$  centered on the reference point  $\vec{r}_i$  from simulation for temperature  $T = 1$  and  $3$ . The different line types distinguish the indicated dipole strengths  $\mu^2 = 0.5, 1, 2$  and  $3$ .

Combining equations (8.2.6) and (8.2.13) for  $\vec{E}_{ext} = 0$  we obtain

$$E_{loc} = \frac{(K - 4 + \sqrt{K^2 + 8})\mu}{(K + 2 + \sqrt{K^2 + 8})a^3} \quad (8.3.2)$$

with  $K = 1 + 4\pi/T_r$ . Here we obtain  $a = 0.66$  by fitting equation (8.3.2) to the simulation data for  $T = 1.6$  at low and intermediate concentrations. Thus  $E_{loc}(T = 1.6)$  is described quite well for densities below  $0.5$ . Higher densities correspond to the regime in which  $T_r < 1$ , where the Onsager theory significantly deviates from the simulation results for  $\chi^{-1}$ . However, a single fixed value for  $a$  merely yields qualitative agreement with the simulation (for  $T_r > 1$ ) as is illustrated by the second solid line drawn for  $T = 8$ . Notice also that with  $a^{-3} = 4\pi\rho/3$  the curvature of  $E_{loc}$  in the above equation changes. Expressing  $a$  in

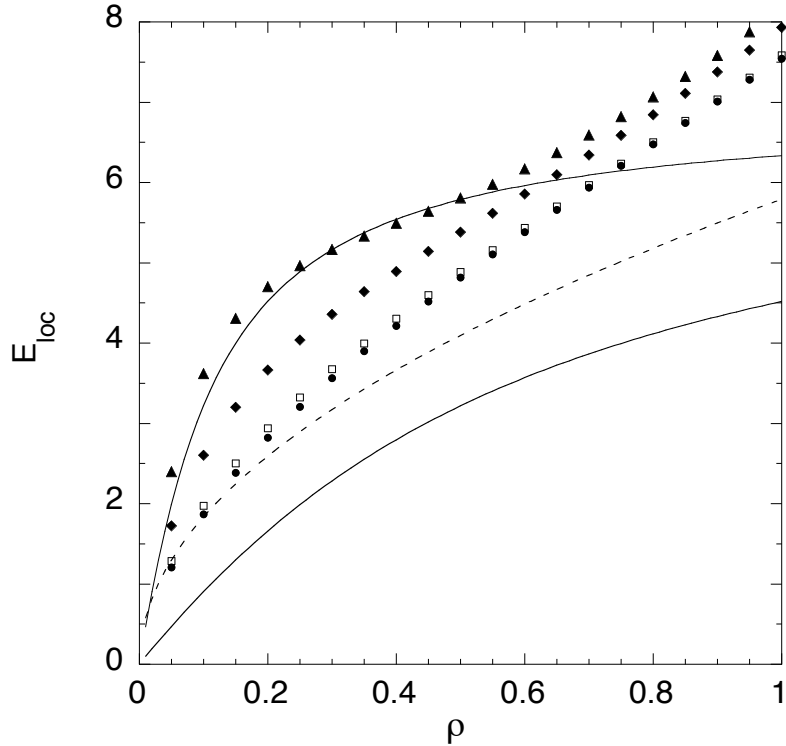


Figure 8.4: Magnitude of the instantaneous local field strength  $E_{loc}$  versus density  $\rho$  for  $T = 8$  (solid circles), 4 (open squares), 2.1 (solid diamonds), and 1.6 (solid triangles) with  $\mu^2 = 4$  via MD. Solid lines: Onsager's  $E_{loc}$  for  $T = 8$  and  $T = 1.6$  obtained with  $a = 0.66$ ; dashed line: simple approximation based on equation (8.3.11) for randomly orientated dipoles.

terms of  $\rho$  therefore is not appropriate.

Figure 8.5 shows the temperature dependence of the local field strength  $E_{loc} = \langle |\vec{E}'(\vec{r}_i)| \rangle$  for the same conditions as in figure 8.1 including  $\mu^2 = 10$ . The shape of these curves cannot be understood in terms of equation (8.3.2). This is because  $E_{loc}$  according to equation (8.3.2) decreases monotonically with increasing  $T$ , i. e. equation (8.3.2) yields the qualitative behavior for low temperatures only. Qualitatively the simulation results in figure 8.5 can be understood as follows. Instead of  $\langle |\vec{E}'(\vec{r}_i)| \rangle$  we consider the simpler but similar  $\langle (\vec{E}'(\vec{r}_i))^2 \rangle^{1/2}$ . We assume that we can calculate the electric field  $\vec{E}'(\vec{r}_i)$  exactly for

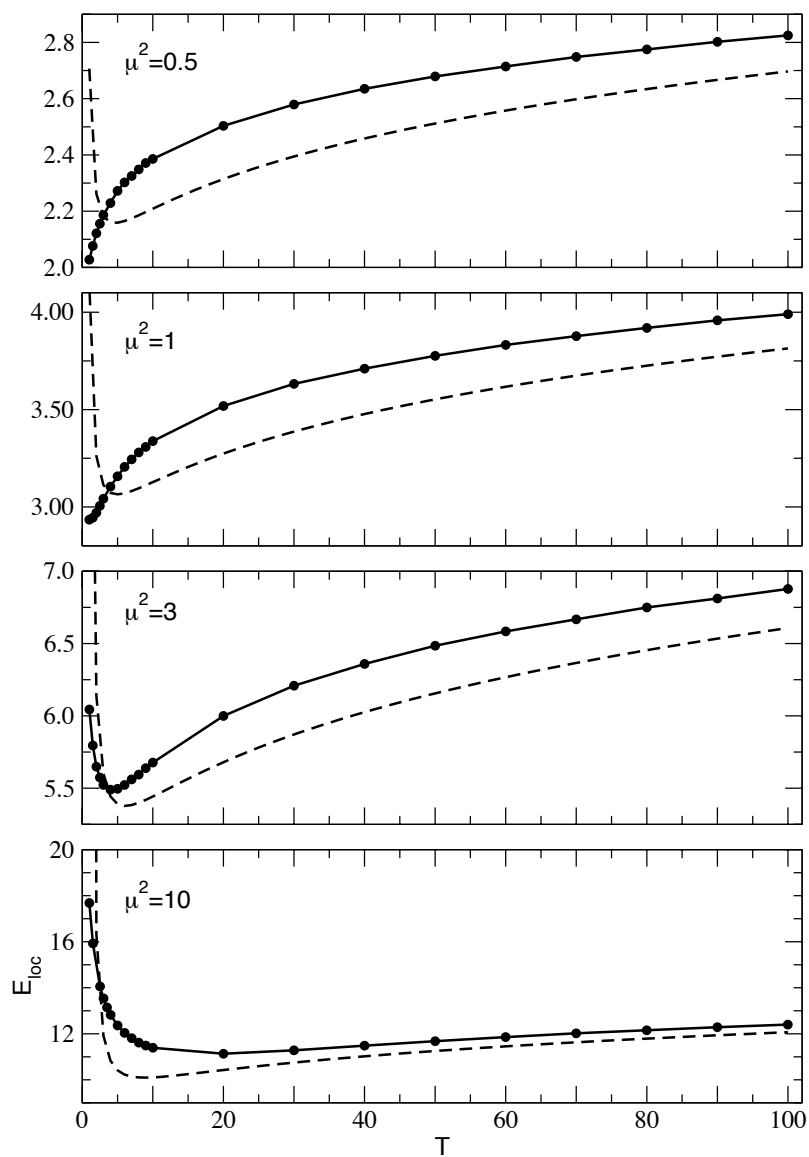


Figure 8.5: Instantaneous local field strength  $E_{loc}$  versus temperature  $T$  for  $\mu^2 = 0.5, 1, 3$  and 10. Circles: MD results; dashed lines: simple approximation based on equation (8.3.8) for randomly orientated dipoles.

all interactions via equation (2.1.25) without applying long-range corrections.

$$\vec{E}'(\vec{r}_i) \cdot \vec{E}'(\vec{r}_i) = \sum_{j \neq i} \sum_{k \neq i} \mathbb{T}_{ij} \vec{\mu}_j \cdot (\mathbb{T}_{ik} \vec{\mu}_k) \quad (8.3.3)$$

$$= \sum_{j \neq i} \sum_{k \neq i} \left( \frac{9 (\vec{r}_{ij} \cdot \vec{\mu}_j) (\vec{r}_{ik} \cdot \vec{\mu}_k) (\vec{r}_{ij} \cdot \vec{r}_{ik})}{r_{ij}^5 r_{ik}^5} - \frac{3 (\vec{r}_{ik} \cdot \vec{\mu}_k) (\vec{r}_{ik} \cdot \vec{\mu}_j)}{r_{ij}^3 r_{ik}^5} \right. \\ \left. - \frac{3 (\vec{r}_{ij} \cdot \vec{\mu}_j) (\vec{r}_{ij} \cdot \vec{\mu}_k)}{r_{ij}^5 r_{ik}^3} - \frac{\vec{\mu}_k \cdot \vec{\mu}_j}{r_{ij}^3 r_{ik}^3} \right) \quad (8.3.4)$$

$$= \sum_{j \neq i} \left( \frac{3 (\vec{r}_{ij} \cdot \vec{\mu}_j)^2}{r_{ij}^8} + \frac{\vec{\mu}_j^2}{r_{ij}^6} \right) + \sum_{\substack{j \neq i \\ j \neq k}} \sum_{\substack{k \neq i \\ k \neq j}} (\dots) \quad (8.3.5)$$

From equation (8.3.4) to (8.3.5) we have rearranged the double sum by factoring out the terms for  $j = k$ . Treating the orientation of the dipoles as random, the terms in the double sum of equation (8.3.5) can be omitted for the thermal average, since  $\langle \vec{r}_{ij} \cdot \vec{\mu}_j \rangle = 0$  and  $\langle \vec{\mu}_j \rangle = 0$  for random orientations. This assumption yields

$$\langle \vec{E}'(\vec{r}_i) \cdot \vec{E}'(\vec{r}_i) \rangle = \sum_{j \neq i} \left\langle \frac{3 (\vec{n}_{ij} \cdot \vec{\mu}_j)^2 + \vec{\mu}_j^2}{r_{ij}^6} \right\rangle = \mu^2 (N-1) \frac{3 \langle \cos^2 \theta \rangle + 1}{\langle r^6 \rangle}, \quad (8.3.6)$$

where  $\theta = \angle(\vec{n}, \vec{\mu})$ . Using

$$\langle \cos^2 \theta \rangle = \int_0^\pi d\theta \sin \theta \cos^2 \theta = \frac{1}{3} \quad (8.3.7)$$

for randomly orientated dipoles and employing equation (3.7.2) yields

$$\langle \vec{E}'(\vec{r}_i) \cdot \vec{E}'(\vec{r}_i) \rangle = 8\pi \mu^2 \rho \int_0^\infty dr \frac{1}{r^4} g_2(r) \quad (8.3.8)$$

In addition the pair correlation function is approximated via

$$g_2(r) \approx \exp[-(u_{LJ} - \langle u_{DD} \rangle)/T] \quad (8.3.9)$$

$$= \exp \left[ \left( -4 \left( \frac{1}{r^{12}} - \frac{1}{r^6} \right) + \frac{2}{3} \frac{\mu^2}{T r^6} \right) / T \right], \quad (8.3.10)$$

where we have used equation (7.2.70) for the thermally averaged DD interaction. Numerical integration yields the dashed lines in figure 8.5. We note that the qualitative agreement is quite good. The increase of the local field at high temperature requires the inclusion of repulsive interaction at small distances, which of course equation (8.3.2) does

not describe.

A further crude approximation, i.e. replacing  $g_2(r)$  by a step function, yields

$$E_{loc}^2 \sim 8\pi\rho \int_{a_0}^{\infty} dr \frac{1}{r^4} = \frac{8\pi\mu^2\rho}{3a_0^3}, \quad (8.3.11)$$

where  $a_0$  is a length equal to one. This expression produces the dashed line in figure 8.4. Inserting the values  $\mu^2 = 0.5, 1.0, 3.0$  and  $10.0$  from figure 8.5 yields  $E_{loc} \sim 1.8, 2.6, 4.5$  and  $8.2$ . These numbers are reasonably close to  $E_{loc}$  as obtained in the computer simulation in the temperature range most relevant for realistic systems. We note that inserting this expression for  $E_{loc}$  in the expansion of the Langevin function in equation (8.2.19) yields the condition  $8\pi\mu^4\rho/(45T^2) \ll 1$  for the validity of the LDE. For example, evaluating  $8\pi\mu^4\rho/(45T^2)$  for water ( $\mu = 1.85\text{D}$ ) at  $300\text{K}$  yields  $\sim 4$ , whereas for camphor ( $\mu = 1.34\text{D}$ ; this value is from an example on the application of the LDE in Atkins' textbook on physical chemistry. The larger values listed in some tables do not alter this argument.) we obtain  $\sim 0.02$ . For liquid water the LDE does not apply, whereas for camphor it does.

The left panel of figure 8.6 compares the autocorrelation of the local field  $E_{loc}^{-2} \langle \vec{E}_{loc}(0) \cdot \vec{E}_{loc}(t) \rangle$  to that of the individual dipole moments  $\mu^{-2} \langle \vec{\mu}(0) \cdot \vec{\mu}(t) \rangle$ . For autocorrelation functions  $\langle \dots \rangle$  indicates averaging of the respective quantity for all particles and for statistical independent time intervals. The relaxation of the local field is closely tied to the relaxation of the individual dipole moments. The same dynamical correlation is underlying Onsager's equation for the local field (cf. equation (8.2.6)). Apparently the relaxation times of the two quantities are closest at low temperatures. For comparison the right panel of figure 8.6 shows the normalized time-autocorrelation function of the total dipole moment of the simulation box

$$\frac{\langle \vec{M}(0) \vec{M}(t) \rangle}{\langle \vec{M}(0) \vec{M}(0) \rangle}.$$

Rotational relaxation, as expected, is slower at low temperatures and for large dipole moments. Even though there is no mean field in the usual sense for the dipoles to move in, the direct comparison of  $\langle \cos \sphericalangle(\vec{\mu}(t), \vec{E}_{loc}(t)) \rangle$  with  $\mathcal{L}(\mu E_{loc}/T)$  (where again  $E_{loc} = \langle |\vec{E}'(\vec{r}_i)| \rangle$ ) in figure 8.7 shows that the mean field average yields a good description. It is in this limited local sense that we have used  $E_{loc}$  computed above in equation (8.2.19).

### 8.3.4 The self diffusion coefficient

The self diffusion coefficient  $D$  can be calculated from simulation data via the Einstein relation

$$D = \frac{1}{6t} \langle |\vec{r}(t) - \vec{r}(0)|^2 \rangle, \quad (8.3.12)$$

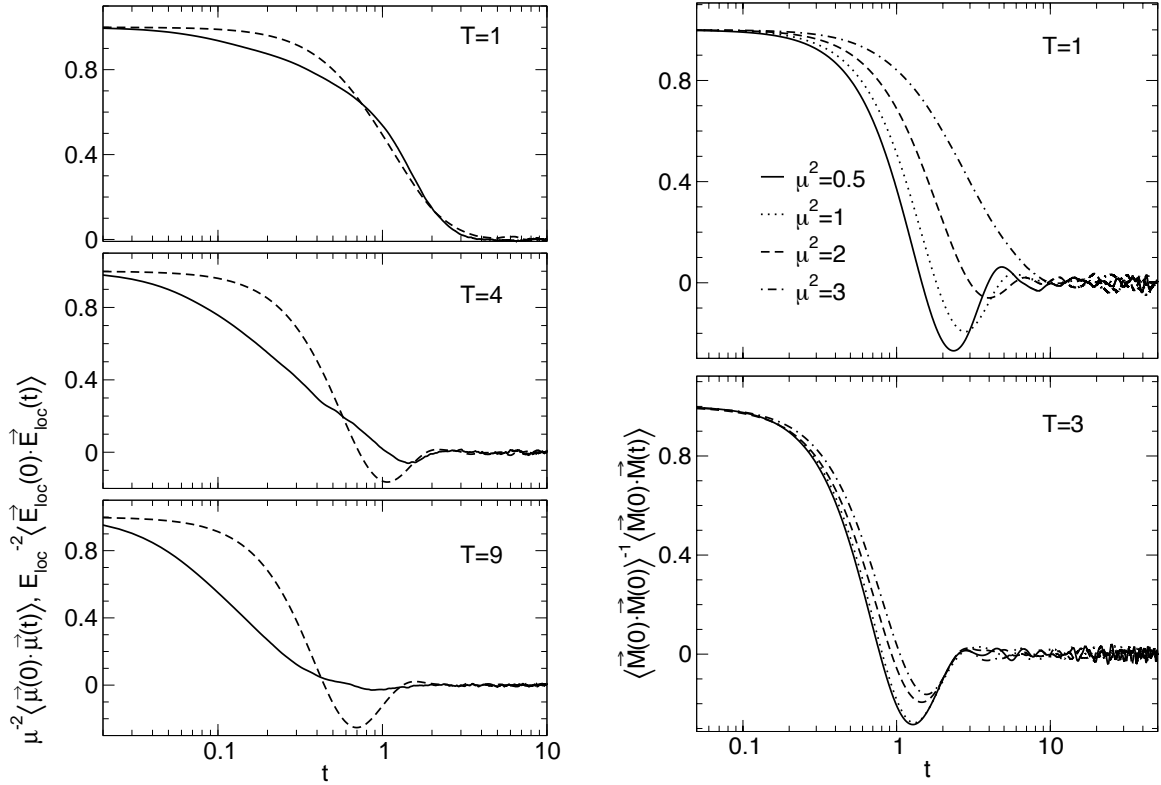


Figure 8.6: Left: Comparison of the autocorrelation functions  $\mu^{-2} \langle \vec{\mu}(0) \cdot \vec{\mu}(t) \rangle$  (dashed lines) and  $E_{loc}^{-2} \langle \vec{E}_{loc}(0) \cdot \vec{E}_{loc}(t) \rangle$  (solid lines) for dipole strength  $\mu^2 = 3$  and temperatures  $T = 1, 4$  and  $9$ . Right: Autocorrelation function of the total dipole moment for dipole strengths  $\mu^2 = 0.5, 1, 2$  and  $3$  and temperatures  $T = 1$  and  $3$ .

where  $\vec{r}(t)$  denotes the trajectory of any particle. The top panel of figure 8.8 shows an example for  $\mu^2 = 3$ ,  $N = 500$ ,  $\rho = 0.8$  and  $T = 1 \dots 9$ . The arrow in the plot indicates increasing temperature. The self diffusion coefficient is calculated from the slope of the lines. For small dipole strength (here  $\mu^2 = 3$ ) the statistical errors are rather minor, the lines are almost perfect straight lines. The bottom panel of figure 8.8 shows the self diffusion coefficient  $D$  computed as function of temperature for dipole strength  $\mu^2 = 0.5, 1, 3, 16$  and  $36$ . We note that for small dipole strength ( $\mu^2 = 0.5$  and  $1.0$ ) the result is in close accord with the temperature dependence of the self diffusion coefficient in the pure LJ fluid [51] (cf. figure 6 in the reference), which for high densities is close to linear. A close to linear dependence on temperature is observed for all dipole strengths considered. For  $\mu^2 = 36$  there is an apparent change of slope at  $T \approx 6$ . This temperature corresponds closely to the estimated transition temperature at  $0.19\rho\mu^2 \approx 6.3$  (even though we do not observe the expected divergence of the dielectric constant as discussed above). The significantly reduced diffusion coefficient indicates a structural change including chain formation. Overall the diffusion coefficient is reduced with increasing dipole strength.

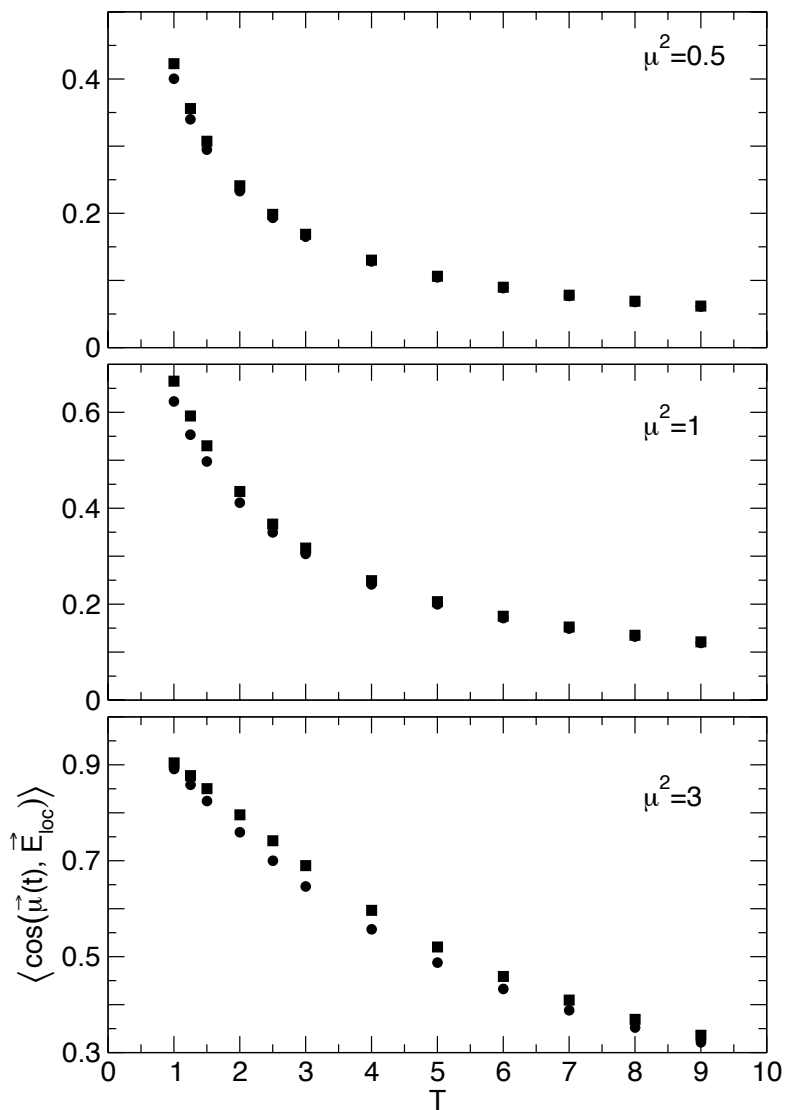


Figure 8.7: Direct comparison of  $\langle \cos(\vec{\mu}(t), \vec{E}_{loc}(t)) \rangle$  (spheres) with  $\mathcal{L}(\mu E_{loc}/T)$  (squares) as functions of temperature  $T$  for dipole strengths  $\mu^2 = 0.5, 1$  and  $3$ .

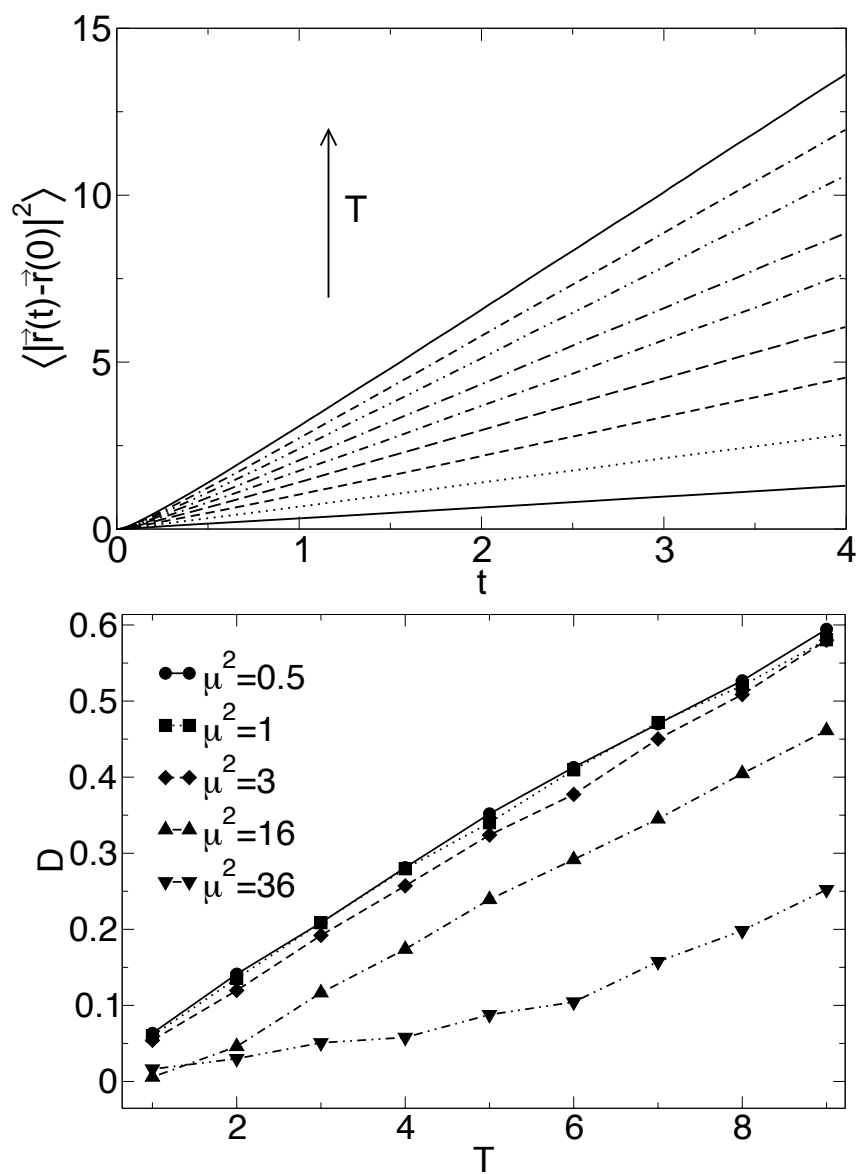


Figure 8.8: Top:  $\langle |\vec{r}(t) - \vec{r}(0)|^2 \rangle$  dependent on length of the time interval  $t$  for a system with  $\mu^2 = 3$ ,  $N = 500$ ,  $\rho = 0.8$  and  $T = 1 \dots 9$ , with unit increment. The arrow indicates increasing temperature. Bottom: Self diffusion coefficient  $D$  versus temperature  $T$  for different dipole strengths, i.e.  $\mu^2 = 0.5, 1.0, 3.0, 16$  and  $36$  ( $N = 500$ ,  $\rho = 0.8$ ).

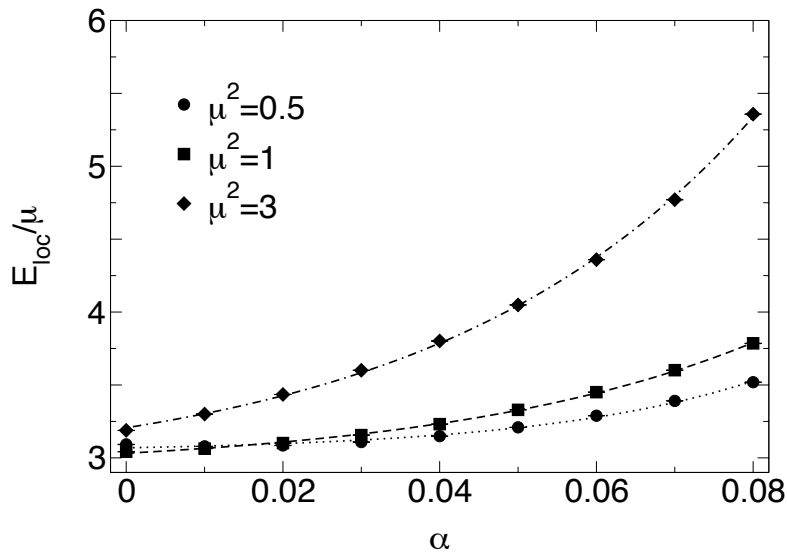


Figure 8.9: Magnitude of the reduced instantaneous local electric field  $\mu^{-1}E_{loc}$  versus polarizability  $\alpha$ . Temperature and density are  $T = 3.0$  and  $\rho = 0.8$ , respectively.

## 8.4 Results for positive polarizability

The following results are for the pST potential including a point polarizability  $\alpha$ . The dielectric properties of the pST fluid has been significantly less studied in the past than the ordinary ST fluid [31, 32]. Figure 8.9 shows the variation of the magnitude of the reduced instantaneous local field strength  $E_{loc}/\mu$  with polarizability  $\alpha$  for systems with dipole strengths  $\mu^2 = 0.5, 1$  and  $3$  at temperature  $T = 3$  and density  $\rho = 0.8$ . We notice the increasing dependence on polarizability with increasing permanent dipole moment. Finally, figure 8.10 shows the dependence of the static dielectric constant on  $\alpha$ . The conditions are the same as above. Again we compare with the simple approximations LDE and OE, which, as for the non polarizable case, bracket the results of the FE, FDE and EOE approaches. Notice that at this temperature and density ( $T = 3, \rho = 0.8$ ) the FE, FDE and EOE are in close accord in the non polarizable case. For the large  $\mu$ - and  $\alpha$ -values the deviations become significant. For  $\mu^2 = 3$  and polarizabilities in the range  $0.06 \leq \alpha \leq 0.08$  the approaches due to Debye and Onsager fail. In particular the FDE approach, which was shown to be in close accord to the FE over a wide range of parameters, breaks down for large dipole strength and polarizability. A reason why the FDE stops being useful when  $\epsilon$  becomes large may be due to the peculiar form of the rhs of equation (8.2.19). If we write this equation as  $(\epsilon - 1)/(\epsilon + 2) = K$  and if we assume that the standard error of  $K$  is  $\Delta K$ , then  $\Delta K$  is related to  $\Delta\epsilon$  via  $\Delta\epsilon \sim \epsilon^2 \Delta K$  when  $\epsilon$  becomes large. Again we recognize that the modification of Onsager's equation EOE, which includes the nearest neighbor shell correlations approximately, improves over the

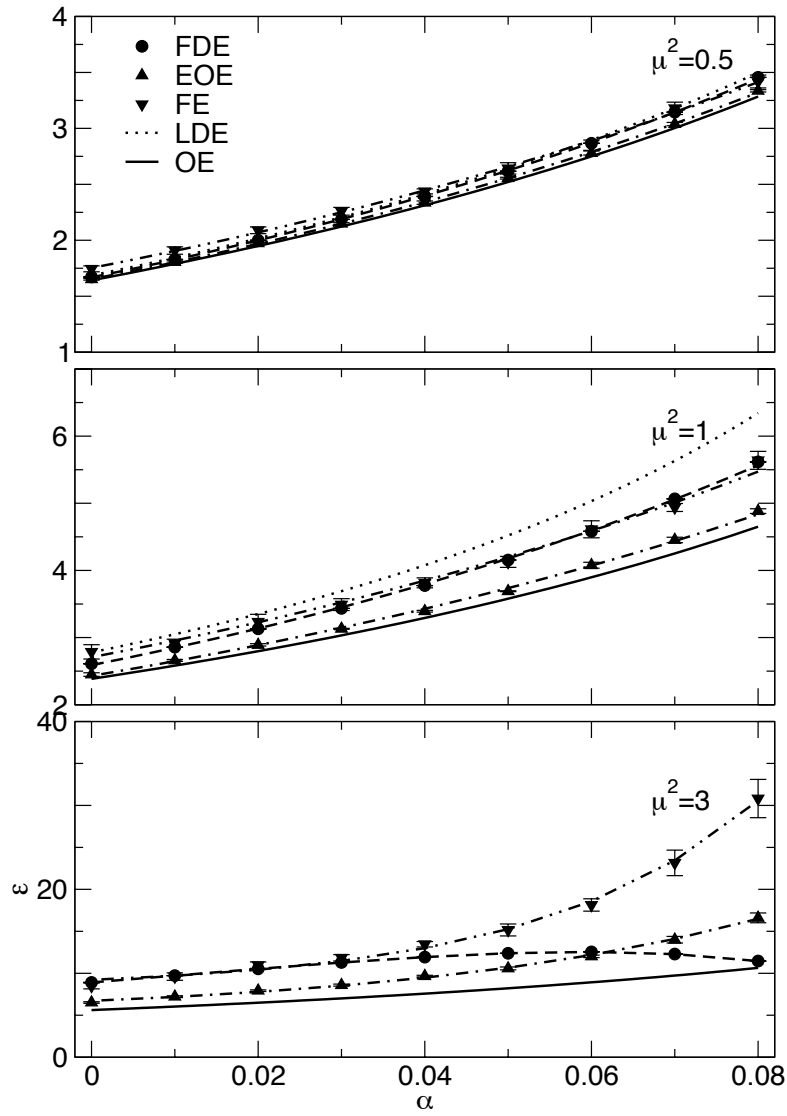


Figure 8.10: Static dielectric constant  $\epsilon$  versus polarizability  $\alpha$  for  $\mu^2 = 0.5, 1.0,$  and  $3.0$  ( $T = 3.0, \rho = 0.8$ ). Notice that for  $\mu^2 = 3.0$  the LDE approximation does not apply. For the non polarizable ST fluid the FDE and EOE are in close accord to the FE for all shown dipole strengths at this state point (cf. right panel of figure 8.1)

OE.

## 8.5 Conclusion

We found the FE with 'box-and-sphere' symmetry to be the adequate method to determine the static dielectric constant from MD computer simulation with reaction field long-range corrections. Nevertheless, the deviations to the in literature often used 'box' symmetry is rather minor. We compared these results to the approaches of Debye (LDE) and Onsager (OE) as well as two improved approaches FDE and EOE respectively. For small dipole moments ( $\mu^2 = 0.5$ ) all computation methods are in good accordance. For larger dipole moments the FDE and the EOE respectively yield well improvements compared to the LDE and OE. While the Onsager approach do not include ferroelectric order Debye's approach does. We obtained an estimate for the isotropic-to-ferroelectric transition in ST fluids from simulation in terms of the reduced temperature  $T_r = T/(\rho\mu^2)$  via the divergence of the inverse susceptibility  $\chi^{-1}$ . Even though the exclusive dependence of the transition on  $T_r$  is an approximation, we find that  $T_{r,cf} \approx 0.19$ , where  $T_{r,cf}$  is the value of  $T_r$  at the ferroelectric transition, for  $\rho = 0.8$  yields a good estimate for the location of the transition over a wide range of dipole strengths. Combination of this result with previous simulation results on the ferroelectric transition implies that  $T_{r,cf}$  increases with increasing  $\rho$  but lies below the same quantity found recently in DHS fluids. We were able to relate our results to experimental work of Shelton on ferroelectric domains in nitromethane-nitrobenzene solutions [29]. In addition we have studied the structural and dynamic dependence of the local electric field. In particular we have compared the instantaneous local field strength in the simulation with the corresponding quantity in Onsager's continuum approach. Finally, we investigated the self diffusion coefficient for the ST fluid dependend on temperature and dipole strength. For small dipole strength the self diffusion coefficient is in close accord to the one of the LJ fluid. With increasing dipole strength the diffusion coefficient is reduced, indicating structural changes including chain formation.



# Bibliography

- [1] P. Debye. *Polare Molekeln*. S. Hirzel, Leipzig, 1929.
- [2] J.D. Jackson. *Classical Electrodynamics*. Wiley & Sons, 1962.
- [3] L. Onsager. Electric moments of molecules in liquids. *Journal of the American Chemical Society*, 58:1486–1493, 1936.
- [4] J.S. Hoye and G. Stell. Ferroelectric phase transition in simple dipolar systems. *Molecular Physics*, 86(4):707–713, 1995.
- [5] P.C. Hemmer, H. Holden, and S. Kjelstrup Ratkje. *The Collected Works of Lars Onsager*. World Scientific, Singapore, 1996.
- [6] J.G. Kirkwood. The dielectric polarisation of polar liquids. *Journal of Chemical Physics*, 7:911–919, 1939.
- [7] M. Mandel and P. Mazur. On the molecular theory of dielectric polarization. *Physica*, 24:116–128, 1958.
- [8] F.J. Vesely. N-particle dynamics of polarizable Stockmayer-type molecules. *Journal of Computational Physics*, 24:361–371, 1976.
- [9] G.N. Patey, D. Levesque, and J.J. Weis. On the theory and computer simulation of dipolar fluids. *Molecular Physics*, 45(3):733–746, 1982.
- [10] E.L. Pollock and B.J. Alder. Static dielectric properties of Stockmayer fluids. *Physica A*, 102(1):1–21, 1980.
- [11] E.L. Pollock, B.J. Alder, and G.N. Patey. Static dielectric properties of polarizable Stockmayer fluids. *Physica A*, 108(1):14–26, 1981.
- [12] D.J. Adams. Static dielectric properties of the Stockmayer fluid from computer simulation. *Molecular Physics*, 42(4):907–926, 1981.
- [13] M. Neumann. Dipole moment fluctuation in computer simulations of polar systems. *Molecular Physics*, 50(4):841–858, 1983.
- [14] C.G. Gray, Y.S. Sainger, C.G. Joslin, P.T. Cummings, and S. Goldman. Computer simulation of dipolar fluids. Dependence of the dielectric constant on system size: A comparative study of Ewald sum and reaction field approaches. *Journal of Chemical Physics*, 85(3):1502–1504, 1986.

- [15] S.W. de Leeuw, J.W. Perram, and E.R. Smith. Computer simulation of the static dielectric constant of systems with permanent dipoles. *Annual Review of Physical Chemistry*, 37:245–270, 1986.
- [16] D. Wei and G.N. Patey. Ferroelectric liquid-crystal and solid phases formed by strongly interacting dipolar soft spheres. *Physical Review A*, 46(12):7783–7792, 1992.
- [17] M.J. Stevens and G.S. Grest. Phase coexistence of a Stockmayer fluid in an applied field. *Physical Review E*, 51(6):5976 – 5983, 1995.
- [18] J.J. Weis and D. Levesque. Ferroelectric phases of dipolar hard spheres. *Physical Review E*, 48(5):3728–3740, 1993.
- [19] D. Levesque and J.J. Weis. Orientational and structural order in strongly interacting dipolar hard spheres. *Physical Review E*, 49(6):5131–5140, 1994.
- [20] P.J. Camp and G.N. Patey. Structure and scattering in colloidal ferrofluids. *Physical Review E*, 62(4):5403–5408, 2000.
- [21] M. Houssa, L. Rull, and S.C. McGrother. Effect of dipolar interactions on the phase behavior of the gay-berne liquid crystal model. *Journal of Chemical Physics*, 109(21):9529–9542, 1998.
- [22] G.T. Gao and X.C. Zeng. Freezing transition of a strongly dipolar simple fluid. *Physical Review E*, 61(3):R2188 – R2191, 2000.
- [23] B. Huke and M. Lücke. Magnetic properties of colloidal suspensions of interacting magnetic particles. *Reports on Progress in Physics*, 67:1731–1768, 2004.
- [24] J. Popplewell, B. Abu Aisheh, and N.Y. Ayoub. The effect of particle interactions on Curie-Weiss behavior in ferrofluids. *Journal of Applied Physics*, 64(10):5852–5854, 1988.
- [25] M. Holmes, K. O’Grady, and J. Popplewell. A study of Curie-Weiss behaviour in ferrofluids. *Journal of Magnetism and Magnetic Materials*, 85(1-3):47–50, 1990.
- [26] H.D. Williams, K. O’Grady, S.W. Charles, and K.J. Davies. Curie-Weiss behaviour in ferrofluids: the effects of particle size and distribution. *Journal of Magnetism and Magnetic Materials*, 122(1-3):134–138, 1993.
- [27] K. O’Grady, A. Bradbury, S.W. Charles, S. Menear, J. Popplewell, and R.W. Chantrell. Curie-Weiss behavior in ferrofluids. *Journal of Magnetism and Magnetic Materials*, 31-34(2):958–960, 1983.
- [28] H. Mamiya, I. Nakatani, and T. Furubayashi. Phase transitions of iron-nitride magnetic fluids. *Physical Review Letters*, 84(26):6106–6109, 2000.
- [29] D.P. Shelton. Ferroelectric domains in nitrobenzene-nitromethane solutions measured by hyper-rayleigh scattering. *Journal of Chemical Physics*, 124:124509, 2006.
- [30] D.P. Shelton and Z. Quine. Doped liquid nitrobenzene is ferroelectric. *Journal of Chemical Physics*, 127:204503, 2007.

- [31] C. Millot, J.-C. Soetens, and M.T.C. Martins Costa. Static dielectric constant of the polarizable Stockmayer fluid. Comparison of the lattice summation and reaction field methods. *Molecular Simulation*, 18:367–383, 1997.
- [32] M. Valiskó, D. Boda, J. Liszi, and I. Szalai. A systematic Monte Carlo simulation and renormalized perturbation theoretical study of the dielectric constant of the polarizable Stockmayer fluid. *Molecular Physics*, 101(14):2309–2313, 2003.
- [33] P.G. Kusalik, M.E. Mandy, and I.M. Svishchev. The dielectric constant of polar fluids and the distribution of the total dipole moment. *Journal of Chemical Physics*, 100(10):7654–7664, 1994.
- [34] L.Y. Lee, P.H. Fries, and G.N. Patey. The solution of the reference hypernetted-chain approximation for Stockmayer fluids. *Molecular Physics*, 55(4):751–762, 1985.
- [35] A.O. Ivanov and O.B. Kuznetsova. Magnetic properties of dense ferrofluids: An influence of interparticle correlations. *Physical Review E*, 64(4):041405, 2001.
- [36] S.W. de Leeuw, B. Smit, and C.P. Williams. Molecular dynamics studies of polar/nonpolar fluid mixtures. I. Mixtures of Lennard-Jones and Stockmayer fluids. *Journal of Chemical Physics*, 93(4):2704–2714, 1990.
- [37] D. Boda, J. Liszi, and I. Szalai. Dielectric constant of a Stockmayer fluid along the vapour-liquid coexistence curve. *Molecular Physics*, 85(3):429–434, 1995.
- [38] C.G. Joslin. The third dielectric and pressure virial coefficients of dipolar hard sphere fluids. *Molecular Physics*, 42(6):1507–1518, 1981.
- [39] M.E. Fisher. The renormalization group in the theory of critical behavior. *Review of Modern Physics*, 46(4):597–615, 1974.
- [40] A. Pelissetto and E. Vicari. Critical phenomena and renormalization-group theory. *Physics Reports*, 368(6):549–727, 2002.
- [41] J.J. Weis and D. Levesque. Orientational order in high density dipolar hard sphere fluids. *Journal of Chemical Physics*, 125:034504, 2006.
- [42] Y. Levin. Criticality in strongly correlated fluids. *Journal of Physics: Condensed Matter*, 14:2303–2308, 2002.
- [43] M.J. Stevens and G.S. Grest. Structure of soft-sphere dipolar fluids. *Physical Review E*, 51(6):5962 – 5975, 1995.
- [44] J.J. Weis. The ferroelectric transition of dipolar hard spheres. *Journal of Chemical Physics*, 123:044503, 2005.
- [45] H. Zhang and M. Widom. Global phase diagrams for dipolar fluids. *Physical Review E*, 49(5):3591–3593, 1994.
- [46] B. Groh and S. Dietrich. Ferroelectric phase in Stockmayer fluids. *Physical Review E*, 50(5):3814–3833, 1994.

- 
- [47] D. Wei, G.N. Patey, and A. Perera. Orientational order in simple dipolar fluids: Density-functional theory and absolute-stability conditions. *Physical Review E*, 47(1):506–512, 1993.
- [48] D.R. Lide and H.V. Kehiaian. *CRC Handbook of Thermophysical and Thermochemical Data*. CRC Press, Boca Raton, 1994.
- [49] *Spartan '04 Macintosh (v1.0.3)*.
- [50] P.L. Silvestrelli and M. Parrinello. Water molecule dipole in the gas and in the liquid phase. *Physical Review Letters*, 82(16):3308–3311, 1999.
- [51] K. Meier, A. Laesecke, and S. Kabelac. Transport coefficients of the Lennard-Jones model fluid. I. Viscosity. *Journal of Chemical Physics*, 121(8):3671–3687.

## 9 Summary discussion

Here we want to briefly discuss the major results of this work and want to give an outlook on the outstanding problems and tasks. In this work we provided GL phase diagrams for dipolar fluids, in particular the ST fluid, including reversible chain formation and ferroelectric order which has not been published thus far [1]. For the low density structure of the ST fluid we showed, that a third-order virial expansion describes only systems with intermediate dipole moments ( $\mu^2 = 3$ ) in the whole gas phase well, for strongly dipolar systems ( $\mu^2 = 36$ ) this attempt fails due to chain formation. By single droplet simulations we were able to confirm the vortex like arrangement of the dipole orientations inside the clusters at low temperatures in agreement with references [2–5]. We found no evidence neither for ferroelectric order [6] nor for a perpendicular orientation of the dipoles to the surface [7]. In combination with the strongly decreasing nematic order parameter with decreasing density inside the GL coexistence region, we can conclude that a coexistence of an isotropic gas and a ferroelectric liquid, as supposed by reference [6], is rather unlikely. Nevertheless, it should be mentioned that the single cluster simulations holds many dangers due to metastable states and can only be taken as a low temperature limit. For more meaningful results the internal structure of coexisting clusters at higher temperatures should be investigated. By simulating coexisting clusters, we found a transition in the scaling law of the radius of gyration dependend on particle number for clusters with strong dipoles as already investigated by [8]. Clusters with strong dipoles ( $\mu^2 \geq 16$ ) scale like stiff rings or chains for small particle numbers and like LJ clusters for large particle numbers, due to the formation of globules with a more compact shape. We found the transition to be independent of density and the scaling parameters to be independent of temperature.

With the Maxwell construction we found a robust method to determine GL phase coexistence for dipolar fluids. While it is in close accord with previous GEMC works for dipole strengths  $\mu^2 \leq 5$  [9–11], it finds phase coexistence for dipole strengths  $\mu^2 \gtrsim 25$  for which GEMC fails due to reversible chain formation [12]. It seems that the determination of GL coexistence by Maxwell construction is only limited by the increasing computation effort for increasing dipole strength, due to the larger cut off distances and system sizes necessary. On the other hand Kofke’s integration method turned out to be infeasible for strong dipoles ( $\mu^2 \gtrsim 30$ ) due to the slowly convergence of the simulation volumes. Additionally, we adopted a FH like lattice theory for reversible assembled particles [13,14] to the ST system and included ferroelectric order by a simple Debye approximation. Comparison to GL coexistence curves and GL critical data from simulation showed good accordance,

in particular the non-vanishing GL critical point for  $\mu^2 \gtrsim 25$ , as already found by [15]. With this model we were able to explain the decreasing critical density with increasing dipole strength due to increasing chain length at the critical point, similar to ordinary linear polymer systems. Contrary to ordinary linear polymer systems the Flory approach yields no finite critical temperature for infinite chain length. For dipole strength  $\mu^2 = 60$  the results for the critical density from simulation and lattice theory differ, possibly due to predominant rings, which are not yet included in the lattice theory. On the other hand we recognized deviations in isotherms for  $\mu^2 = 30$  from simulation with larger cut off distances. With increasing computer power the influence of the cut off on the investigated systems should be studied in more detail. It is worth noting that the ferroelectric transition is not expected to interfere with the critical point, as discussed in [6, 16].

The mapping of the critical data of the ST system onto the vLS system at fixed dipole moment and varying dispersion interaction showed, that the non-vanishing GL critical point for the ST fluid with large dipole strength is consistent with the non-existence of the GL transition for vanishing dispersion interaction. From this we conclude that we expect a vanishing GL critical temperature and a simultaneously vanishing critical density in the DSS fluid. Direct simulation of the DSS fluid indicates that a GL transition may be an effect of a too short cut off distance. Nevertheless, simulations of other groups [17, 18] indicate a GL transition for the DHS fluid. For further investigations to solve this contradiction, it might be helpful to compare the behaviour of the DSS and DHS fluid directly by simulation. On the other hand there may be, for the ST and DSS system, other types of phases and phase transitions. Evidence for a separation in a phase with free end-rich chains and a phase with a free-end poor network, as suggested by [19], was not found. Threefold coordinated crosslinks as predicted for such a network were observed very rarely, even at very high dipole strength. To quantify this observation a more sophisticated detection of these crosslinks from simulation should be useful.

Investigating the dielectric properties of the ST fluid we found the FE with 'box-and-sphere' symmetry to be the adequate method to determine the static dielectric constant from MD computer simulation with reaction field long-range corrections. We compared the results to the approaches of Debye (LDE) and Onsager (OE) as well as two improved approaches FDE and EOE respectively. Both Debye's and Onsager's approach yield only good results for small dipole moments. We found an isotropic-to-ferroelectric transition in ST fluids via simulation and obtained an estimate of the transition temperature via the divergence of the inverse susceptibility  $\chi^{-1}$ . Even though the exclusive dependence of the transition on the reduced temperature  $T_r = T/(\rho\mu^2)$  is an approximation, we find that  $T_{r,cf} \approx 0.19$  for  $\rho = 0.8$  yields a good estimate for the location of the transition over a wide range of dipole strengths. On the other hand we found the nematic order parameter for  $\mu^2 = 5$  and  $\mu^2 = 16$  along the binodal only to be in good agreement if plotted versus the reduced temperature  $T/T_c$ , with  $T_c$  as the GL critical temperature. This should be evaluated for more dipole strengths and densities. Additionally, we were able to relate our results to experimental work of Shelton on ferroelectric domains in nitromethane-nitrobenzene solutions [20].

# Bibliography

- [1] B. Huke and M. Lücke. Magnetic properties of colloidal suspensions of interacting magnetic particles. *Reports on Progress in Physics*, 67:1731–1768, 2004.
- [2] S. Banerjee and M. Widom. Shapes and textures of ferromagnetic liquid droplets. *Brazilian Journal of Physics*, 31(3):360–365, 2001.
- [3] D. Lu and S.J. Singer. Orientational ordering and anisotropy in model polar clusters. *Journal of Chemical Physics*, 103(5):1913–1921, 1995.
- [4] H.B. Lavender, K.A. Iyer, and S.J. Singer. Global orientational order in model polar clusters. *Journal of Chemical Physics*, 101(9):7856–7867, 1994.
- [5] A.P. Shreve, J.P.R.B. Walton, and K.E. Gubbins. Liquid drops of polar molecules. *Journal of Chemical Physics*, 85(4):2178–2186, 1986.
- [6] H. Zhang and M. Widom. Global phase diagrams for dipolar fluids. *Physical Review E*, 49(5):3591–3593, 1994.
- [7] V. Talanquer and D.W. Oxtoby. Nucleation in dipolar fluids: Stockmayer fluids. *Journal of Chemical Physics*, 99(6):4670–4679, 1993.
- [8] P.R. ten Wolde, D.W. Oxtoby, and D. Frenkel. Coil-globule transition in gas-liquid nucleation of polar fluids. *Physical Review Letters*, 81(17):3695–3698, 1998.
- [9] B. Smit, C.P. Williams, E.M. Hendriks, and S.W. de Leeuw. Vapour-liquid equilibria for Stockmayer fluids. *Molecular Physics*, 68(3):765–769, 1989.
- [10] M.E. van Leeuwen, B. Smit, and E.M. Hendriks. Vapour-liquid equilibria of Stockmayer fluids, computersimulations and perturbation theory. *Molecular Physics*, 78(2):271–283, 1993.
- [11] M.E. van Leeuwen. Deviation from corresponding-states behaviour for polar fluids. *Molecular Physics*, 82(2):383–392, 1994.
- [12] M.E. van Leeuwen and B. Smit. What makes a polar liquid a liquid? *Physical Review Letters*, 71(24):3991–3994, 1993.
- [13] P.B. Lenz and R. Hentschke. Concentration dependent size of reversibly assembling polymers in solution: A mean-field lattice theory. *Journal of Chemical Physics*, 121(21):10809–10813, 2004.
- [14] P.B. Lenz. *Gleichgewichtspolymere: Gittertheorie und Computersimulation*. PhD thesis, Bergische Universität Wuppertal, 2005.

- 
- [15] J. Dudowicz, K.F. Freed, and J.F. Douglas. Flory-Huggins model of equilibrium polymerization and phase separation in the Stockmayer fluid. *Physical Review Letters*, 92(4):045502, 2004.
- [16] B. Groh and S. Dietrich. Ferroelectric phase in Stockmayer fluids. *Physical Review E*, 50(5):3814–3833, 1994.
- [17] P.J. Camp, J.C. Shelley, and G.N. Patey. Isotropic fluid phases of dipolar hard spheres. *Physical Review Letters*, 84(1):115–118, 2000.
- [18] G. Ganzenmüller and P.J. Camp. Vapor-liquid coexistence in fluids of charged hard dumbbells. *Journal of Chemical Physics*, 126:191104, 2007.
- [19] T. Tlusty and S.A. Safran. Defect-induced phase separation in dipolar fluids. *Science*, 290(5495):1328–1331, 2000.
- [20] D.P. Shelton. Ferroelectric domains in nitrobenzene-nitromethane solutions measured by hyper-rayleigh scattering. *Journal of Chemical Physics*, 124:124509, 2006.

# A Second virial coefficient for polarizable Stockmayer particles

The virial expansion of the equation of state for the ST system (cf. equation (5.2.1) for  $\alpha = 0$ ) is in literature a matter of common knowledge [1–5]. Here we want to derive the second and third virial coefficients of the equation of state for the pST model. The classical canonical partition function for a system of  $N$  ST dipoles is given by

$$Q = \frac{N!}{\prod_{\nu} N_{\nu}! \left(\frac{4\pi}{\Delta\Omega}\right)^N (2\pi\hbar)^{5N}} \int d\{q_i\} d\{p_i\} e^{-\beta\mathcal{H}}, \quad (\text{A.0.1})$$

where the prefactor is analog to the orientation partition function (7.2.100), the Hamiltonian  $\mathcal{H}$  is given by equation (3.5.17) and  $\int d\{q_i\} d\{p_i\}$  denotes integration over the whole phase space, i.e. all generalized coordinates (3.5.14) and momenta (3.5.15). We now proceed in standard fashion by transforming the integrations over the momenta conjugate to the Euler angles to the angular velocities  $\omega_j$  with respect to the major axes. Setting

$$\omega_{i_1} = \dot{\theta}_i \quad (\text{A.0.2})$$

$$\omega_{i_2} = \dot{\varphi}_i \sin \theta_i \quad (\text{A.0.3})$$

we obtain

$$dp_{\theta_i} dp_{\varphi_i} = \begin{vmatrix} \frac{\partial p_{\theta_i}}{\omega_{i_1}} & \frac{\partial p_{\theta_i}}{\omega_{i_2}} \\ \frac{\partial p_{\varphi_i}}{\omega_{i_1}} & \frac{\partial p_{\varphi_i}}{\omega_{i_2}} \end{vmatrix} = I^2 \sin \theta_i d\omega_{i_1} d\omega_{i_2}, \quad (\text{A.0.4})$$

cf. equations (3.5.12) and (3.5.13). Substitution of  $p_{\theta_i}$  and  $p_{\varphi_i}$  by  $\omega_{i_1}$  and  $\omega_{i_2}$  in equation (A.0.1) yields

$$\begin{aligned} -\ln Q &= -N \ln \left[ \frac{2\mathcal{I}}{\beta\hbar^2} \right] + N \ln \left[ \frac{4\pi\Lambda_T^3 \rho}{\Delta\Omega} \right] + \sum_{\nu} \left( N_{\nu} \ln \frac{N_{\nu}}{N} - N_{\nu} \right) \\ &\quad - \ln \int \frac{d\{\vec{r}_i\}}{V^N} d\{\varphi_i\} d\{\theta_i\} \{\sin \theta_i\} e^{-\beta U_{ST}} \end{aligned} \quad (\text{A.0.5})$$

(cf. reference [6]), where the first term is due to rotational and the second due to translational motion. Additionally, we have made use of the Stirling approximation for the  $N_{\nu}$ .

The quantity  $\Lambda_T$  is the thermal wavelength, and  $\rho$  is the dipole number density. A second order virial expansion yields the free energy

$$\frac{\beta F}{N} = -\ln \left[ \frac{8\pi\mathcal{I}}{\beta\hbar^2} \right] + \ln [\Lambda_T^3 \rho] - 1 + \int \frac{d\Omega}{4\pi} f(\Omega) \ln f(\Omega) + \rho B_2(T) + \mathcal{O}(\rho^2), \quad (\text{A.0.6})$$

where the second virial coefficient is given by

$$B_2(T) = -\frac{1}{2} \int \frac{d\Omega_i d\Omega_j}{(4\pi)^2} f(\Omega_i) f(\Omega_j) \int d^3r (e^{-\beta u_{pST}(\vec{r}, \Omega_i, \Omega_j)} - 1). \quad (\text{A.0.7})$$

Notice that  $\Omega_i$  denotes the dependence on  $\varphi_i$  and  $\theta_i$  ( $d\Omega_i = d\varphi_i d\theta_i \sin \theta_i$ ), and  $\Delta\Omega f(\Omega_\nu) = 4\pi N_\nu/N$  is the dipole orientation distribution function ( $\int d\Omega f/4\pi = 1$ ).

In the present case the pair interaction potential  $u_{pST}(\vec{r}, \Omega_i, \Omega_j)$  is given by equation (2.1.11). In the case for two particles only we can write

$$\vec{m}_i = \vec{\mu}_i - \alpha \mathbb{T} \vec{m}_j \quad \text{and} \quad \vec{m}_j = \vec{\mu}_j - \alpha \mathbb{T} \vec{m}_i, \quad (\text{A.0.8})$$

(cf. equation 2.1.10). Next we express  $u_{DD}$  entirely in terms of the permanent moments  $\mu$  and the point polarizability  $\alpha$ , we obtain

$$u_{DD} = \frac{1}{2} \left[ \left\{ \left( \mathbb{1} - \alpha^2 \mathbb{T}^2 \right)^{-1} \left( \vec{\mu}_i - \alpha \mathbb{T} \vec{\mu}_j \right) \right\} \mathbb{T} \vec{\mu}_j \right. \quad (\text{A.0.9})$$

$$\left. + \left\{ \left( \mathbb{1} - \alpha^2 \mathbb{T}^2 \right)^{-1} \left( \vec{\mu}_j - \alpha \mathbb{T} \vec{\mu}_i \right) \right\} \mathbb{T} \vec{\mu}_i \right]. \quad (\text{A.0.10})$$

Using

$$\vec{\mu}_i = \mu \begin{pmatrix} \sin \theta_i \cos \varphi_i \\ \sin \theta_i \sin \varphi_i \\ \cos \theta_i \end{pmatrix}. \quad (\text{A.0.11})$$

and expanding in small  $\alpha$  yields

$$\begin{aligned} \beta u_{DD} &= a (\cos \Delta\varphi \sin \theta_i \sin \theta_j - 2 \cos \theta_i \cos \theta_j) \quad (\text{A.0.12}) \\ &\quad - \frac{a}{r^3} (P_2(\cos \theta_i) + P_2(\cos \theta_j) + 2) \alpha + \\ &\quad + \frac{a}{r^6} (\cos \Delta\varphi \sin \theta_i \sin \theta_j - 8 \cos \theta_i \cos \theta_j) \alpha^2 + \mathcal{O}(\alpha^3), \end{aligned}$$

where  $a = \beta\mu^2/r^3$ ,  $\Delta\varphi = \varphi_i - \varphi_j$ , and  $P_2$  is the second order Legendre polynomial. We may now carry out the integrations over  $\varphi_i$  and  $\varphi_j$  analytically. The result may then be expanded in powers of  $a$  and the integration is carried out term by term. Notice that we assume  $f(\Omega) = 1$ , i.e. isotropic distribution of dipole orientations. Thus the second virial coefficient  $B_2(T, \mu^2, \alpha)$  becomes

$$\begin{aligned} B_2(T, \mu^2, \alpha) &= B_2^{(LJ)}(T) + \frac{x^2}{3} h_1 + \frac{x^4}{25} h_2 + \dots \quad (\text{A.0.13}) \\ &\quad + \left( 2x h_1 + \frac{4x^3}{5} h_2 + \dots \right) \alpha \\ &\quad + \left( \frac{21x^2}{5} h_2 + \frac{836x^4}{525} h_3 + \dots \right) \alpha^2 + \mathcal{O}(\alpha^3). \end{aligned}$$

Here  $x = \beta\mu^2$ ,

$$B_2^{(LJ)}(T) = -2\pi \int_0^\infty dr r^2 (\exp[-\beta u_{LJ}] - 1), \quad (\text{A.0.14})$$

and

$$h_j = -2\pi \int_0^\infty dr r^{2-6j} \exp[-\beta u_{LJ}]. \quad (\text{A.0.15})$$

Additional terms in equation (A.0.13) are listed in Table A.1.

Table A.1: Additional terms in the expression for  $B_2(T, \mu^2, \alpha)$  in equation (A.0.13)

$\mathcal{O}(\alpha^0)$	$\mathcal{O}(\alpha^1)$	$\mathcal{O}(\alpha^2)$
$\frac{x^2}{3} h_1$	$2x h_1$	$\frac{21x^2}{5} h_2$
$\frac{x^4}{25} h_2$	$\frac{4x^3}{5} h_2$	$\frac{836x^4}{525} h_3$
$\frac{29x^6}{11025} h_3$	$\frac{58x^5}{525} h_3$	$\frac{269x^6}{1225} h_4$
$\frac{11x^8}{99225} h_4$	$\frac{88x^7}{11025} h_4$	$\frac{5794x^8}{363825} h_5$
$\frac{13x^{10}}{4002075} h_5$	$\frac{26x^9}{72765} h_5$	$\frac{10139x^{10}}{14189175} h_6$
$\frac{17x^{12}}{243486243} h_6$	$\frac{68x^{11}}{6243237} h_6$	$\frac{73732x^{12}}{3381753375} h_7$
$\frac{523x^{14}}{456536705625} h_7$	$\frac{1046x^{13}}{4347968625} h_7$	$\frac{1246237x^{14}}{2587041331875} h_8$
...	...	...



# Bibliography

- [1] J.S. Rowlinson. The second virial coefficients of polar gases. *Transactions of the Faraday Society*, 45:974 – 984, 1949.
- [2] J.S. Rowlinson. The third virial coefficients of polar gases. *Journal of Chemical Physics*, 19(7):827–831, 1951.
- [3] J.O. Hirschfelder, C.F. Curtiss, and R.B. Bird. *Molecular Theory of Gases and Liquids*. John Wiley & Sons, Inc., 8 edition, 1964.
- [4] A. Yokozeki, H. Sato, and K. Watanabe. Ideal-gas heat capacities and virial coefficients of HFC refrigerants. *International Journal of Thermophysics*, 19(1):89–127, 1998.
- [5] K. van Workum and J.F. Douglas. Equilibrium polymerization in the Stockmayer fluid as a model of supermolecular self-organization. *Physical Review E*, 71(031502), 2005.
- [6] W. Pauli. *Statistical Mechanics*. Dover, Mineola, 1973.



## B Description of supplementary information and programs included on DVD

On the included DVD supplementary information on this work can be found. The  $\text{\LaTeX}$ -sources of this document can be found in the directory `diss`, including all figures in pdf format. The directory `diss_Bilder` provides some additional figures which were not included in the final version of this work. The directory `DPG-02-25-2008` contains sources of a talk held at the DPG conference in February of 2008 on topic of this work. In the directory `Literature`, publications related to this work can be found as well as the cited papers. In `Poster` the sources for two posters can be found. The first was presented at the DPG conference in 2005, the second was presented at the soft matter conference in 2007. The directory `Programs` contains the source codes of the most important simulation and analysis programs for this work.

The programs `PSTM_NPT.cpp` and `PSTM_NVT.cpp` were used for the MD simulations done for this work. The former is optimized for NPT simulation, the latter one for NVT simulations. Necessary for simulation is an additional `initfile` here `example.init` providing the simulation parameters. MD simulation is started by

```
./PSTM_NVT example.init.
```

The program writes thermodynamic quantities to `example_ausgabe.dat` and configurations files to `example_restart.conf`. Configuration files can be analyzed with `findcluster.cpp`. Is is executed by calling

```
./findcluster example.init example_restart.conf example_restart.xyz  
example_restart.dat example_restart_histo.dat.
```

`findcluster.cpp` converts the configuration file `example_restart.conf` to `example_restart.xyz`, a readable format for most visualization programs. `example_restart.dat` contain average values for single configurations like average chain length, radius of gyration and other quantities. In `example_restart_histo.dat`

quantities like radius of gyration, persistence length and so on are given dependent on chain length. For analysis of `example_ausgabe.dat`, `example_restart.dat` and `example_restart_histo.dat` there are plenty of scripts which are not explained in detail here.

The radial pair distribution function can be determined by

```
./PSTM_g2 example.init example_restart.conf example_g2.dat.
```

Here `example_g2.dat` is the file to which the radial pair distribution function dependent on separation is written. This works analog for the DD correlation function with

```
./PSTM_dipol_r example.init example_restart.conf example_dipol_r.dat.
```

The script

```
./makeinit_maxwell.sh patternfile
```

produces a row of parameter files along an isotherm. Parameters like start and end density or number of density steps have to be adjusted in the script, the remaining parameters are taken from the `patternfile`. A simulation cycle for Kofke integration is initiated by

```
./kofke,
```

which makes use of the `PSTM_NPT.cpp` program. This script needs two parameter files `phase_g_0_pre.init` and `phase_l_0_pre.init` in its directory with suitable parameters for one state point on the binodal on the gas side and one state point on the binodal on the liquid side. All parameters for the integration step are adjusted inside the script.

# Acknowledgments

Finally, I would like to thank all the helping hands without which this work would not have been possible. I am especially grateful to Prof. Dr. Reinhard Hentschke for admitting me to his group, the lot of helpful discussions, his patience, his support and his great contributions to this work, especially to the chapters 7 and 8. I would like to thank Christa Guse for the benefits of her preliminary works on the ST fluid. Since I was not experienced in this field of research when I started my work for this dissertation, I am grateful in particular to the former and present group members Hendrik Kabrede, Peter Lenz and Enno Oyen for teaching me the MD method and solving a lot of the initial problems to get a running MD simulation program. The later group members Henning Hörstermann, Florian Pesth and Dr. Wen-Ze Ouyang I would like for the many inspiring discussions and the helpfulness available at all times. Moreover, I would like to thank Heiko Braun, Nils Hojdis and the later along coming Ran Jia, who brought new oomph to the group. For her help in administrative matters and beyond this for the many interesting discussions, I would like to thank Susanne Christ. Besides these I thank my parents for their continuous support, my friends for the compensatory spare time and everybody that I have forgotten here.



# Index

- acceleration, 33
- alkane, 131, 154
- angular
  - acceleration, 32–34
  - momentum, 31, 32, 77
  - velocity, 32, 34, 42
- autocorrelation, 193, 194
- average
  - bond length, 93
  - chain length, 87, 138, 139, 162
- Berendsen
  - barostat, 43
  - thermostat, 41, 43
- binodal, 97
- Boltzmann weight, 28, 176, 180
- bond length, 143
- Boyle temperature, 140, 141, 159
- cavity field, 175
- cell list, 50, 52
- chain, 60, 74, 86, 90, 164
- charged hard dumbbell, 21
- chemical potential, 97, 138
- Clausius-Clapeyron equation, 98, 103, 108
- cluster, 60, 85, 87
- compressibility, 44, 97, 100
- constraint thermostat, 43
- coordination number, 134
- correlation length, 105
- critical
  - density, 141
  - exponent, 104
  - fluctuations, 106
  - point, 97, 139
  - temperature, 141
- Curie point, 174
- cut off radius, 44, 115
- DD correlation, 44, 46, 61, 111, 113, 114, 188
- Debye, 173
  - approximation, 147
  - equation, 177, 182, 184, 197
- density functional theory, 58, 77, 132
- dielectric, 176
  - constant, 47–49, 61, 173, 175, 178, 183
  - continuum, 44, 45, 47
  - displacement field, 47
- dilute-dense transition, 15, 59
- dipolar hard sphere model, 21, 28, 120
- dipolar soft sphere model, 21, 27, 28, 120, 156
- dipole
  - orientation distribution, 210
  - tensor, 26, 144
- dispersion, 22, 27, 57, 156
- droplet, 60, 71, 74
- Einstein relation, 193
- electric field, 22, 24, 47
- energy conservation, 43
- ensemble average, 37, 40, 45
- enthalpy, 37, 39, 103
- equal-areas construction, 101
- equation
  - of motion, 31–33
  - of state, 139, 209
- equilibrium polymerization, 60, 85, 98, 131
- equipartition theorem, 39

- ergodic hypothesis, 37
- ergodicity, 36, 37
- Euler method, 33
- Ewald summation, 49, 57, 58, 61
- Ewald-Kornfeld summation, 62
- external
  - field, 48, 176, 179
  - force, 40
  - virial, 41
- ferroelectric
  - order, 98, 147, 159, 161
  - phase, 47, 59
  - transition, 61, 173, 183
  - transition temperature, 148
- ferrofluid, 15, 59
- finite size effect, 36, 59, 112
- Flory-Huggins lattice theory, 60, 131
- fluctuation equation, 48, 179, 182, 197
- flying ice cube, 40
- force, 31–34, 41
  - field, 15
- friction, 43
- full Debye equation, 178, 182, 197
- gas-liquid
  - coexistence, 57, 97, 105
  - coexistence curve, 97–99, 102, 105, 106, 110, 112, 118, 120, 121, 159
  - critical density, 151, 157
  - critical parameters, 111
  - critical temperature, 151, 157, 158
- generalized
  - coordinate, 37, 39, 209
  - momentum, 37, 39, 209
- Gibbs
  - ensemble Monte Carlo, 57
  - free energy, 98, 100, 101
- Gibbs-Duhem equation, 103
- grand canonical Monte Carlo, 59
- Hamilton equation of motion, 39, 40
- Hamiltonian, 38, 179, 209
- hard
  - core repulsion, 28
  - rod, 21
  - spheroid, 21
- heat
  - bath, 42
  - capacity, 42, 60, 105, 164
  - current, 42
- Heisenberg model, 186
- Helmholtz free energy, 57, 101, 132, 139
- high-frequency dielectric constant, 48
- hypernetted-chain approximation, 62
- hypothesis of analyticity, 101
- ideal coil, 152
- induced dipole moment, 24, 49
- inter-aggregate interaction, 133
  - parameter, 142
- internal
  - energy, 37, 39, 46
  - force, 40
  - virial, 41, 46
- intra-aggregate interaction, 133
  - parameter, 143, 145, 146
- inverse susceptibility, 183, 184
- Ising model, 105
- isotherm, 97, 115, 116, 118
- kinetic energy, 33, 37, 41, 42
- Kirkwood, 174
  - factor, 61, 62
  - relation, 61
- Kofke integration, 43, 102
- Ladd lattice summation, 63
- Lagrangian, 38
- Langevin function, 177, 193
- lattice
  - energy, 132
  - entropy, 135
  - free energy, 143
- Lennard-Jones
  - potential, 15, 21, 22, 46
  - units, 22

- linearized Debye equation, 178, 182, 184, 197
- liquid crystal, 21
- local field, 175, 177, 188, 191
- long-range correction, 44–47
- Lorentz method, 177
  
- macroscopic quantities, 37
- many-body interaction, 26
- Maxwell construction, 99, 105
- mean dipole moment, 147
- metastable state, 37
- micelle, 16, 162
- microstate, 36
- minimum image convention, 35, 36
- modified Stockmayer model, 21, 27, 156
- molecular dynamics, 31
- moment of inertia, 32, 38
  - tensor, 77–80
- momentum, 31
- Monte Carlo, 36
- mutant, 86, 166
- Møller-Plesset perturbation theory, 156
  
- neighbor list, 50–52
- nematic order parameter, 84, 108, 114, 159
- nucleation, 100
- number fraction, 87
  
- Onsager, 174
  - equation, 150, 175, 181, 182, 184, 197
- order parameter, 105, 148
- orientation
  - function, 23, 24
  - partition function, 148
- orientational free energy, 148, 149
- Ornstein-Zernike integral equation, 62
  
- packing entropy, 132
- Padé approximation, 57, 58
- pair
  - correlation, 45, 58
  - distribution, 61, 62
  - interaction, 21
- partition function, 209
- Pauli exclusion principle, 22
- periodic boundary conditions, 35, 36
- permanent dipole moment, 24
- persistence length, 87, 91, 142
- perturbation theory, 57, 58
- phase space, 36, 37
  - density, 37, 46
  - trajectory, 39
- point dipole-point dipole pair interaction, 22
- point polarizability, 24
- polarizability, 197
- polarizable Stockmayer model, 21
- polarization, 47, 176, 179
- polymer, 133
- potential energy, 37
- predictor-corrector integration, 103
- pressure, 39, 41
- principal
  - axis of rotation, 81
  - moment of inertia, 77
- principle of corresponding states, 109, 120
  
- radial pair distribution, 44, 45, 61, 111, 113, 114
- radius of gyration, 79, 90
- reaction field, 47, 48, 58, 176
- relaxation time, 42, 44
- renormalization group theory, 105, 185
- ring, 86, 90, 164
- rotating block of ice, 77, 83
- rotational temperature, 40
- Runge-Kutta method, 33
  
- saturation
  - chemical potential, 101
  - pressure, 101, 108
- scaling law, 27, 104
- self diffusion, 193, 194, 199
- self-field, 48
- simple liquid limit, 139, 142
- single super chain approximation, 62

- Stockmayer
  - interaction potential, 21, 23
  - model, 21
- sublimation curve, 97
- supercooled gas, 100
- superheated liquid, 100
- surfactant, 15
- susceptibility, 174, 183, 184
  
- Taylor expansion, 33
- temperature, 39, 41
- thermodynamic
  - integration, 39, 102
  - state, 37
- thermostat, 41
- time
  - average, 37
  - reversibility, 33
- torque, 31, 32, 48
- total
  - dipole moment, 24, 47–49
  - electric field, 48
  - potential energy, 26
- transfer matrix, 131, 143, 144
- translational temperature, 40
- triple point, 97
  
- universality class, 104, 186
  
- van der Waals
  - equation, 99, 159
  - loop, 99, 122
- vaporization curve, 97
- velocity, 34, 41, 42
  - Verlet algorithm, 34
- Verlet
  - algorithm, 33, 34
  - neighbor list, 51
- virial, 41, 46
  - coefficient
    - first-order, 209
    - second-order, 209
  - equation of state, 58
  - expansion, 71, 72, 74, 139, 159, 209, 210
  - volume
    - bath, 44
    - current, 43
    - fraction, 133
  - vortex, 74